LOW PRESSURE PLASMA FOCUS FOR DEUTERON BEAM GENERATION

LIM LIAN KUANG

FACULTY OF SCIENCE
UNIVERSITY OF MALAYA
KUALA LUMPUR

2017

LOW PRESSURE PLASMA FOCUS FOR DEUTERON BEAM GENERATION

LIM LIAN KUANG

THESIS SUBMITTED IN FULFILMENT OF THE REQUIREMENTS FOR THE DEGREE OF DOCTOR OF PHILOSOPHY

**DEPARTMENT OF PHYSICS
FACULTY OF SCIENCE
UNIVERSITY OF MALAYA
KUALA LUMPUR**

2017

UNIVERSITY OF MALAYA
ORIGINAL LITERARY WORK DECLARATION

Name of Candidate: **LIM LIAN KUANG** [redacted]

Matric No: **SHC 120038**

Name of Degree: **DOCTOR OF PHILOSOPHY**

Title of Project Paper/Research Report/Dissertation/Thesis ("this Work"):

Low Pressure Plasma Focus for Deuteron Beam Generation

Field of Study: **Experimental Physics (Physics)**

I do solemnly and sincerely declare that:

(1) I am the sole author/writer of this Work;
(2) This Work is original;
(3) Any use of any work in which copyright exists was done by way of fair dealing and for permitted purposes and any excerpt or extract from, or reference to or reproduction of any copyright work has been disclosed expressly and sufficiently and the title of the Work and its authorship have been acknowledged in this Work;
(4) I do not have any actual knowledge nor do I ought reasonably to know that the making of this work constitutes an infringement of any copyright work;
(5) I hereby assign all and every rights in the copyright to this Work to the University of Malaya ("UM"), who henceforth shall be owner of the copyright in this Work and that any reproduction or use in any form or by any means whatsoever is prohibited without the written consent of UM having been first had and obtained;
(6) I am fully aware that if in the course of making this Work I have infringed any copyright whether intentionally or otherwise, I may be subject to legal action or any other action as may be determined by UM.

Ca[redacted] Date: 09/08/17

Subscribed and solemnly declared before,

Witness's Signature Date: 9. Aug 2017

[redacted]

ABSTRACT

The thesis presented an experimental investigations performed on the radiation (ion beam, neutrons and X-rays) emitted from a 2.7 kJ plasma focus device. With the aim to optimize for ion beam emission, the system has been modified with long electrode configuration operated at low pressures. Work has been carried out to find the best parameters while matching characteristic time of plasma focus. Diagnostics techniques including Faraday cup, biased ion collector and solid state nuclear track detectors were employed for the study of ion beams emission in terms of beam energies, their fluence (ions/m^2), number of ions and angular distribution of the emissions. Lee model code was configured to according to the system parameters and generate outputs at the experimental conditions. The results were compared with the experimental data. The study suggested that multiple current dips and prolong duration in the drop of discharge current signals corresponded to anomalous resistance played an important role in the ion beam emission. Significant ion beam emission with good reproducibility was obtained at operating pressure in the range of 0.1 – 0.5 mbar. The best condition is 0.2 mbar deuterium filling. Ion beams with energies in the range of 18 – 350 keV have been measured, while the discharge voltage was 13.5 kV. Ion beam fluence is estimated in the order of 10^{15} ions/m^2. The emission was highly anisotropic in the forward direction and spread out to about 30^{o}. The density of ion tracks measured to be 6.3 x 10^{10} ions/m^2 while in the velocity space they are in Maxwell-Boltzmann distribution. Electron temperature of the deuterium plasma was estimated as 3 – 5 keV. Correlation between the radiation emissions and pinch dynamics gave a clear picture that the ion beams were emitted at different instances during the pinch phase.

ABSTRAK

Tesis ini membentangkan penyelidikan atas hasilan sinaran (berkas ion, neutron dan Sinar-X) daripada 2.7 kJ peranti plasma fokus. Untuk tujuan pengeluaran berkas ion yang optimum, sistem telah diubahsuai untuk beroperasi pada tekanan rendah dengan menggunakan elektrod panjang. Penyelidikan dilaksanakan untuk mendapatkan parameter yang terbaik di samping memastikan masa cirian plasma fokus yang berpadanan. Teknik diagnostik termasuk mangkuk Faraday, pengesan ion dipincang dan pengesan jejak nuklear keadaan pepejal telah digunakan untuk kajian berkas ion dari segi tenaga, fluence (ion/m^2), bilangan ion dan taburan sudut ion. Kod model Lee telah dikonfigurasikan menggunakan parameter sistem dan menjanakan hasil keputusan seperti keadaan kajian eksperimen. Hasil keputusan itu telah dibandingkan dengan data eksperimen. Kajian tersebut mencadangkan bahawa arus dip (current dip) berbilang dan tempoh dip yang panjang dalam isyarat arus nyahcas adalah berkaitan dengan rintangan anomali yang memainkan peranan penting dalam pengeluaran berkas ion. Pengeluaran berkas ion yang ketara dengan kebolehulangan yang baik telah diperolehi pada tekanan operasi dalam julat 0.1 - 0.5 mbar. Keadaan terbaik adalah pada 0.2 mbar dengan pengisian deuterium. Berkas ion dengan tenaga dalam lingkungan 18 - 350 keV telah diukur dimana voltan nyahcas adalah 13.5 kV. Fluence berkas ion dianggarkan dalam urutan 10^{15} ion/m^2. Pengeluaran berkas ion itu sangat anisotropic pada arah hadapan dan tersebar lebih kurang 30^{o}. Kepadatan jejak ion diukur adalah 6.3 x 10^{10} ion/m^2 dalam taburan Maxwell-Boltzmann pada ruang halaju. Suhu elektron plasma deuterium dianggarkan adalah 3-5 keV. Korelasi antara pancaran sinaran dan dinamik cubitan (pinch) memberikan gambaran yang jelas bahawa berkas ion telah dihasilkan pada masa yang berbeza dalam fasa cubitan (pinch).

ACKNOWLEDGEMENTS

Foremost, I wish to convey my sincere gratitude and earnest thankfulness to my supervisor, associate professor Dr. Yap Seong Ling for her support and guidance with true enthusiasm throughout my research and thesis write-up. Dr. Yap is patient, supportive, available and inquisitive about her student's interests. Her enduring enthusiasm for plasma research is contagious to the point that she is able to ensnare her students into the difficult experimental work and hard thinking of relating observation and fundamental. With her positive influence in both my academic as well as future professional career I embrace new approaches and optimism to be a good physicist and researcher. I am very grateful to have such a wonderful and enriching experience to work with her which is also a great nourishment for my self-improvement and discovery. She will continue to be my esteemed role model in my scientific endeavor.

My sincere appreciations also goes to Emeritus Professor Dr. Lee Sing for his guidance, suggestions and discussions. Prof Lee inspires me with his enthusiasm and passion in plasma focus research and scientific paper writing. The privileged interaction with Prof Lee in several workshops and idea exchange through emails have been most beneficial to me.

My deepest gratitude goes to Mr. Jasbir Singh, who shared his engineering skills and technical experience of 30 years working on pulsed power and plasma experiments. There would be no replacement on his many suggestions in my experimental work. Not forgetting to thank all my colleagues in the Plasma Research Laboratory, particularly, Mr. Ngoi Siew Kien, Mr. Lee Ming Chuan, Mr. Ma Jian, Mr. Poh Hun Seng, Mr. Daryl Tan, Dr. Chan Li San and Ms. Lim Ling Hong for their help, idea sharing and fun discussion while we shared lab space, instruments and various facilities in the laboratories. It has been a very pleasant experience work in the team. To all my fellow friends who their names are not mentioned here I gratefully thank them for their moral support, encouragement, lovely friendship and assistance in all respect throughout my research period.

I am truly indebted and thankful to my beloved parents, in-laws and members of my family. Thank you for their trust and support, given me the opportunity to study, research, grow, fail, succeed, and have the best years of my life! I promise to make you proud in my future endeavors. I thank with love, my wife Wong Chiew Ing for her endless support, patient and understanding of my long working hour in the lab and forbearance during the completion of the study. She has always been helpful and I am truly blessed that we have overcome all the challenges.

Lastly, I record my appreciation to the Plasma Technology Research Centre, Department of Physics, University of Malaya and Ministry of Higher Education for the research facilities, grants and scholarships.

TABLE OF CONTENTS

LIST OF FIGURES

LIST OF TABLES

CHAPTER 1: INTRODUCTION

1.1 History of Plasma Physics Research: Fusion and Pinch Facilities

History on the plasma research is inseparable from the development of the work on electrical gaseous discharge in the late 19th century. Since then, research in discharge physics has been actively carried out, while a lot of useful information on elementary processes in gaseous discharge have been obtained from discharge tube experiments. The term of "plasma" was introduced by Irving Langmuir in the 1928 to describe the nature of the ionized gas and the way the electrified fluid carrying high velocity electrons, ions and impurities in a discharge tube. The important point of plasma is its unique and superior properties of exhibiting a range of phenomena of startling complexity for which has considerable practical utility and sometimes of great beauty.

Plasma being the fourth state of matter has been observed to exist pervasively in various forms around us in nature and is the most abundant form of known matter in the universe. The field of plasma physics was established to investigate and provide the scientific basis of the naturally occurring plasmas. Moreover, in furtherance of the pursuit for controlled nuclear fusion.

Science research has been developed in two ways:

i) Object of study was based on purely intellectual curiosity

ii) A goal was set and research was directed to resolve the inherent physical issues

The ultimate goal of the plasma research towards fusion falls into the latter category. It is therefore necessary to understand and control the plasma for practical application in generating fusion energy for the use of mankind. The dangers of global warming and energy crisis in the mid of twentieth century has raised the public consciousness due to anthropogenic emissions of carbon dioxide and depletion of non-renewable energy resources. A solution to long term demand of world energy supply is thus badly needed to allow the continuous progress of human civilization.

Most of today energy supplies were derived from utilization of finite earth resources mostly from fossil fuels: coals, natural gas and petroleum. Such energy resources are limited and supply trends will come to a critical point in a few decades from now. At this critical point, scientist has discovered the possibility of tapping energy from the nuclear fission reaction which leads to development of fission power reactor. Fission power plants since then provide a significant fraction of the electrical power in many countries and as high as 70 % in France. However, operation of nuclear fission power plant has some unsolved problems. This included the long-lived biological hazardous radioactive waste materials, creates possibilities for nuclear weapons proliferation and failure in engineering management where it was happened in Three-Mile Island, Chernobyl and recently, Fukushima.

In this regard, an alternative option of energy source is needed. A proposed solution to support the increasing human population is the development of a future limitless, greener, secure, safe, reliable, long-term and large-scale power plant: Nuclear fusion reactor. Nuclear fusion reaction uses inexhaustible fuel from seawater while not emitting any greenhouse gases. Controlled nuclear fusion is a concept of making an artificial Sun on Earth to duplicate the way our Sun that has powered the whole universe for several hundred million years now. The understanding of plasma confinement to harness fusion energy into a usable form will be a giant step for mankind which is not only imperative but necessary.

Fusion related research begins as early as in the year of 1929 when Atkinson & Houtermans (Atkinson & Houtermans, 1929) first proposed the concept and shown in calculation that the fusion reactions is the source that providing energy to the stars. 3 years later, the first fusion reaction was observed in the laboratory by Mark Oliphant et al. (Oliphant et al., 1934). In 1939, a more developed theory about the fusion reaction has been established by Bethe (Bethe, 1939). He was awarded the Nobel Prize in the year 1967 for his contribution in deriving fusion power cycle for the stars and discoveries associated to the energy production in stars.

It is then understood that for fusion reaction to take place in a laboratory scale, an extreme condition of temperature and pressure such as occurs in the Sun must be achieved. The most and hitherto challenge in nuclear fusion reaction lies in forcing two positively charged, mutually repelling, protons to fuse together. In order to do so, the kinetic energy required is of temperature of many millions Kelvin yet at very high density. Fortunately, such condition as in the Sun and needed in a nuclear fusion reactor can be engineered on Earth. This can be implemented through different approaches such as magnetic confinement, inertial confinement or electromagnetic pinch where these processes can generate hot and dense plasma for the nuclear fusion reaction.

The idea of inertial confinement is to compress and heat a fuel target within a very short period of time by its own inertial. The target is typically in the form of pellet of deuterium-tritium fuel. To achieve fusion, a larger amount of energy needed is delivered symmetrically and same at each point around the target using higher energy laser beam. For the purpose of study inertial confinement fusion, National Ignition Facility (NIF) has been built and it houses the world's largest and most powerful laser system with expensive electrical and optical equipment. The current research in inertial confinement is in the progress of improving the technique both scientifically and economically.

On the other hand, fusion scheme through magnetic confinement is based on the application of external magnetic field to confine the hot plasma out of contact with the walls of its container to undergo fusion reaction. Magnetic confinement device often has the shape of a torus (doughnut-shaped). The most advanced magnetic confinement device is the Tokamak where the world largest nuclear fusion research facility known as Joint European Torus (JET). JET has been successfully achieved fusion but the efficiency is only about 70 % which at present is still not quite economical. The notable achievement in JET has encouraged scientist and funding organizations to try something even bolder – the ITER.

ITER is an international project involved the governments of China, India, Japan, South Korea, Russia, the European Union and the United States for the support to design and build a larger experimental fusion reactor than the JET. The ITER agreement was officially signed on 21 November 2006 after two decades of discussion. Selecting the location for ITER was a long process that finally has reached a consensus to construct the facility in Cadarache, France in 2005. First plasma experiment is estimated to be demonstrated in 2025 using the fuel consists of deuterium and tritium. Despite the ultimate goal of ITER is to achieve breakeven yet it is not intended to be a viable reactor due to its size and cost. Instead, ITER play the role as a stepping-stone paves the way towards the economical use of fusion power.

Other than the megaproject like JET and ITER for the possible development towards fusion power, there is an alternative magnetic confinement scheme for the same purpose which uses the self-generated magnetic field to confine the plasma known as pinch effect. Z-pinch, for example, makes use of pinch effect to achieve high density plasma. In this device, a large current is flowed through the conducting gas medium (plasma) parallel to the axial in the *Z*-direction to generate an azimuthal magnetic field that create a force which tends to pulls or pinches the current filaments together. As a consequence, the gas is compressed and heated to generate a plasma of high temperature and density. The charged particles in the pinched plasma experience magnetic force due to self-generated magnetic field and gain sufficient thermal energy for fusion reaction to occur.

Z-pinches have a long history and are perhaps the oldest subject of study in plasma physics which has shown to be a most effective way of coupling stored magnetic energy into soft X-rays with a conversion of wall plug efficiency of about 15 % (Haines et al., 2005). Such efficient way of confining plasma has its great relevance devoted to the thermonuclear fusion power research.

The first *Z*-pinch was demonstrated by Martin Van Marum with an electrostatic generator at the end of 17^{th} century, which the instrument is now housed in the Teylers Museum. Since then numerous works were then carried out to understand the pinch effect by various researchers (Northrup, 1907; Pollock & Barraclough, 1905) with a major development by Bennet (Bennett, 1934) in deriving the pinch relation for the case of uniform charged particle streams having finite temperature. In 1946, Thomson and Blackman were devised the experiments on *Z*-pinch which lead to a patent on the concept of toroidal *Z*-pinch machine as a fusion reactor (Haines, 1996).

In recent advancement of the development in pulsed power technology capable of delivering MA current in a short duration (ns), new possibilities of X-ray generation for thermonuclear fusion has been actively explored. Deeney et al. (Deeney et al., 1998) obtained 1.8 MJ soft X-rays of 5 ns pulse width with peak power of 280 TW from 11 MJ *Z*-pinch device. The group employed a nested array of fine tungsten wires with the application of 20 MA and 150 ns rise time which implodes the wires to the axis by the pinch effect. This efficient and powerful X-ray source has been regarded as a potential candidate to energize a hohlraum for inertial confinement fusion (ICF).

Most notable variant form of *Z*-pinch is the compressional *Z*-pinch, exploding wire *Z*-pinch, gas puff *Z*-pinch, gas embedded *Z*-pinch, and plasma focus. Fusion neutron yield reported in 1976 (Decker & Wienecke, 1976) was 10^{12} at 1 MA current with 1 MJ input energy from Frascati plasma focus machine. The yield was greater than any other controlled fusion experiment at that time. Moreover plasma focus requires only a moderate pulsed power driver with microseconds' time scale instead of better than 100 ns time scale in other *Z*-pinch configuration. Its coaxial electrodes allow the magnetic energy to be stored inductively in the rundown phase prior to plasma pinch.

1.2 Scope/Motivation of The Research Project

Continuing efforts in plasma focus research on fusion related phenomena to both technological and industrial are most encouraging. Most of the plasma focus researches were conducted at pressure of several mbar or higher following the tradition with some good reasons, including the required gas filled for initial breakdown and formation of the current sheath. Therefore, there are very few results reported for plasma focus operated at very low pressure of less than 1 mbar.

Enhanced radiation output with peak axial current sheath speed lies within the range of 6 – 10 cm/μs as reported by Serban & Lee (Serban & Lee, 1998) has instigated us to operate the plasma focus with current sheath speed in this range. This was done by employing a longer electrode length to shift the pressure regime of a plasma focus device to operate in low pressure mode where a matching speed of 6-10 cm/μs can be achieved.

Excellent results in utilizing the pulsed ion beam emission for application in surface properties modification, ion implantation, thin film deposition and synthesis of nanoparticles has been demonstrated. It is worthwhile to mention also plasma focus with static inductance of more than 100 nH as is the case of our focus machine when operated at low pressure of less than 1 mbar showed the presence of anomalous resistance due to intensified plasma instabilities (Behbahani & Aghamir, 2012). The presence of such anomalous resistance was shown to increase the ion beam emission.

The main aim of this project was to investigate the radiation emission (ion beam, neutrons and X-rays) from a 2.7 kJ plasma focus device operated in deuterium at operating pressure of less than 1 mbar. Investigation of the pulsed radiation emission are crucial to have better understanding of the dynamics and physical process taking place in the hot plasma in order to extend the versatility of the plasma focus device as pulse radiation source for specific application. More intense ion beam emission has been obtained at low pressure compared to conventional pressure of several mbar. Various diagnostic techniques for time resolved and time integrated ion beam measurement were employed for this purpose.

In addition, the objectives are to achieve better understanding of the various phenomena taking place in the ion beam production (origins of the emission) and their correlation with the discharge parameters. Some numerical computation work using Lee model code to compare with the experimental data is also of interest in order to gain further insight of the physics during plasma pinch.

1.3 Organization of The Thesis

The thesis has been organized in following fashion. Some introductory of fusion research and the evolution of pinch devices related to fusion studies is given in Chapter 1. A brief discussion on the history of the evolution of dense plasma focus device and the versatility of the plasma focus device as a simple facility for the study of plasma fusion and dynamics is also given in this chapter. Followed is the motivation and objective of the research works.

In Chapter 2, the structure and dynamics of the plasma focus device are described. An overview of pinch dynamics at different phase of plasma focus evolution is presented and discussed. Chapter 3 presents some previous works on the pulsed radiation emission that has been done on by other researchers in the area mainly on ion beam emission. Review of some associated plasma phenomena and instabilities is outlined. The last part of the chapter discussed the various proposed neutron and ion beam production mechanism.

A detailed description of the experimental setup and diagnostic technique employed in this project is illustrated in Chapter 4. Chapter 5 discusses the results obtained and analysed. In this chapter also the correlation among the radiation emissions and with the discharge parameters are presented. A brief discussion of numerical simulation using Lee model and the interpretation of the discharge phenomena is also included. Finally, general conclusion of the experimental results is summarized in Chapter 6 followed by some suggestion for further works.

CHAPTER 2: PLASMA FOCUS DEVICE－STRUCTURE & DYNAMICS

2.1 Configuration & Working Principle

The innovation of the dense plasma focus configuration has enable the generation of a hot and dense plasma producing fusion neutron through the pinch effect. Pinch effect (Burkhardt et al., 1957) is one of the most efficient way of heating and confining the plasma in attaining fusion condition. The schematic electrode configuration of both the Filippov type and Mather type plasma focus device are shown in Figure 2.1 (Decker & Wienecke, 1976). In both device, the two coaxial electrodes comprised of inner and outer electrodes separated from each other with a distance of few centimeter of annular space by an insulator sleeve. Conventionally, the plasma focus is operated with the inner electrode as anode charged to high positive voltage and the outer electrode as cathode. It has been shown that reverse polarity of the electrodes caused a severe reduction in neutron production (Kubes et al., 2009).

The principle of operation for the two type of plasma focus both combines the feature of electromagnetic shock tube and pinch device. The essential difference between the two devices is in their aspect ratio which defined as the ratio of effective anode length to its diameter (Zhang et al., 2006). The Mather type plasma focus has the larger aspect ratio of greater than unity while less than unity for the case of Filippov type.

Despite many plasma focus devices have been built which is conformed to one of these aspect ratio, Mather type design was preferred as experimental tools to demonstrate the physics of the dense plasma due to its convenience in operation, compactness, flexibility in accessing different diagnostics, distinguishable phases of current sheath dynamics and more importantly the high neutron yield for the same input energy. In Filippov type operated at 37 kJ, neutron yield of 1.1 x 10^9 per shot was obtained (Goudarzi et al., 2005) whereas in Mather type operated at 12 kJ, neutron yield of 6.0 x 10^9 per shot has been measured (Lim et al., 2015).

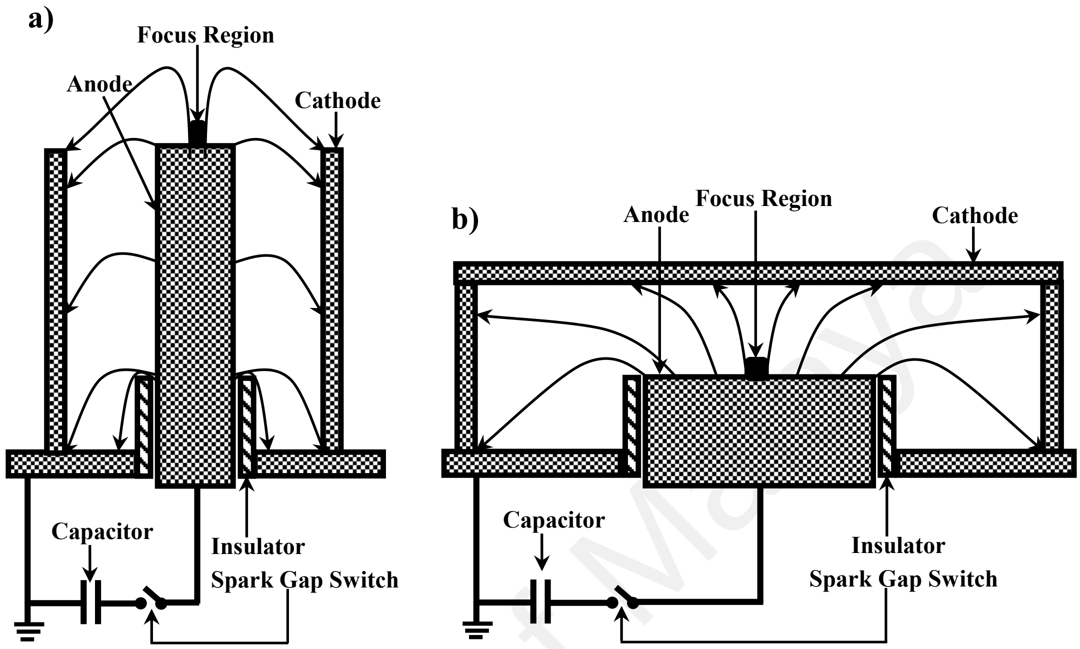

Figure 2.1: Schematic illustration of (a) Mather type and (b) Filippov type Plasma Focus

The plasma focus device has been operated in a wide energy range from 0.1 Joules to 1 Mega Joules. The operation of the plasma focus is first started by charging the capacitor to high voltages usually in the range of few tens of kilovolts. The capacitor is then discharged to the plasma focus tube by means of fast switches where the electrical energy stored in the capacitor is transferred in a transient manner. Electrical breakdown in the prefilled gas is initiated on the surface of insulator sleeve where a uniform layer of plasma sheath is formed. This layer of plasma sheath is also known as current sheath. The current sheath then gradually moves in an inverse pinch manner due to the Lorentz force from the region labeled 1 to 2 as illustrated in Figure 2.2.

Under the effect of Lorentz force, the current sheath are accelerated parallel to the electrode axis to high speed and continuously being heated up until the sheath collapses on axis to form a plasma column labeled as region 3. The speed of the current sheath in the region 3 is generally in the range of 2 – 2.5 times faster than the speed in region 2. The pinched plasma column formed by electromagnetic acceleration and compression is of very high temperature and density. Upon disruption of the plasma column by the onset of instabilities, an intense radiation is emitted.

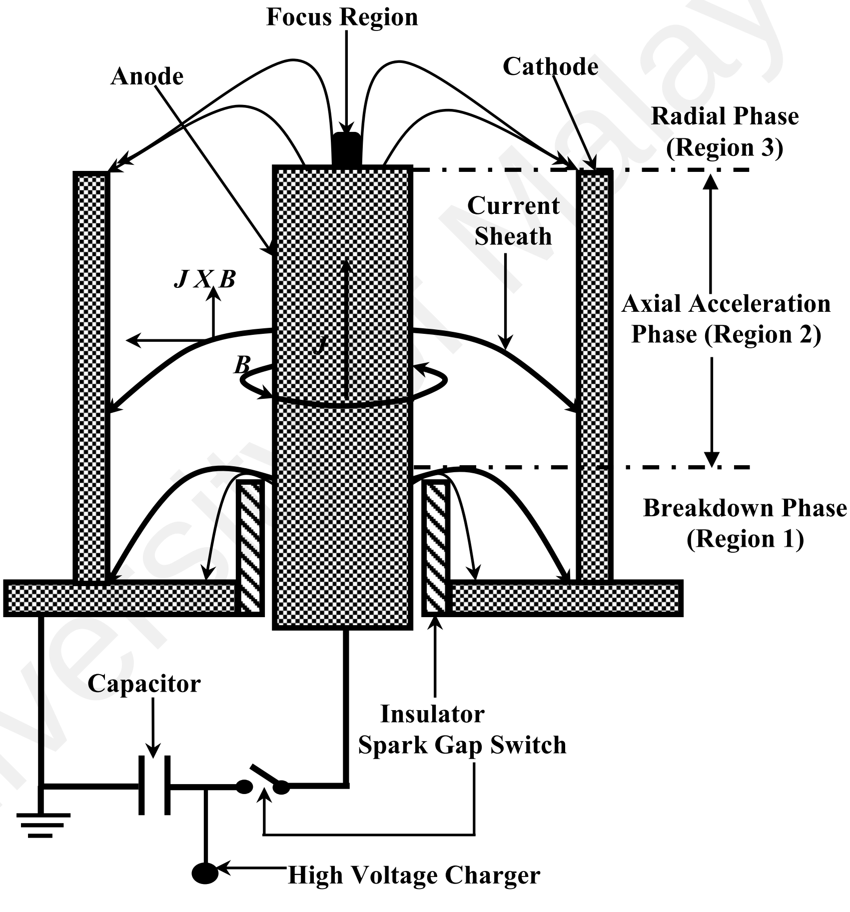

Figure 2.2: Schematic of current sheath motion under various phases of plasma focus operation

2.2 Dynamics of Plasma Focus Discharge

Plasma acceleration by $J \times B$ force from the early formation at the backwall to the final pinched plasma can be classified into three main phases. The initial or first phase of the discharge is called "breakdown phase" which refers to the initial gas breakdown and formation of parabolic current sheath. This is followed by the axial acceleration phase that accelerates the uniform axisymmetric current sheath towards the open end of the focus tube. This phase does not occur in the Filippov type plasma focus. The last and most important phase is the radial phase that confines (focus) azimuthally the axisymmetric current sheath toward the anode axis to form the pinched plasma. Details of each of the phases will be discussed in following subsections.

2.2.1 Breakdown & Inverse Pinch Phase

The first or breakdown phase played an important role in a focusing discharge (Krompholz et al., 1980). Upon breakdown, current sheath forms along the insulator sleeve surface. Breakdown dynamics in the plasma focus discharge is shown in Figure 2.3. The electrical breakdown can be enhanced with the use of a circular knife edge cathode (Donges et al., 1980). The reduction of the number of filaments in the discharge and enhancement in the gliding discharge was found to be favourable to form homogeneous and azimuthally symmetric current sheath. It has been reported that such uniform current sheath has increased the neutron yield by 20 % (Krompholz et al., 1980).

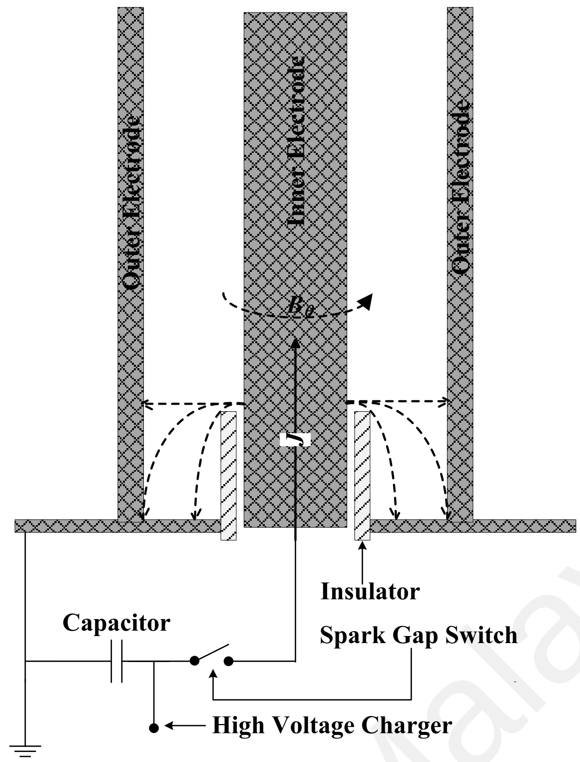

Figure 2.3: Schematic presentation of breakdown phase in plasma focus development

Number of current sheath layers and duration for the current sheath formation during breakdown phase was found to be dependent on the operating pressure (Bruzzone & Vieytes, 1993). A single and uniform current sheath was found to be an essential condition although not sufficient to optimize the performance of plasma focus discharge for good compression dynamics. Usually, a pressure of 1 mbar to 5 mbar was found to be favorable for a good focusing discharge. At too high pressure of 5 – 20 mbar, multi-layer current sheath with filamentary structure are more likely to occur. Too long attachment of the current sheath on the insulator surface was found to be detrimental to pinching quality as the heating effect leads to ablation of insulator material that can provide a path for current leakage. However, at too low pressure of 0.1 – 1.0 mbar a diffuse volumetric discharge may be developed to form a rather broad current sheath structure. The current during the breakdown phase is observed to flow concentrated near to the insulator (Bruzzone & Grondona, 1997) and a model has been developed to describe the complex phenomena occurring in the breakdown phase (Bruzzone et al., 2007).

2.2.2 Axial Acceleration Phase

The second phase also known as rundown phase is the acceleration of the current sheath along the focus tube as illustrated in Figure 2.4. The current sheath structure in this phase is not planar but canted backward from the anode to the cathode owing to the radial dependence of the magnetic pressure gradient. The radial component of the Lorentz force $(J \times B)_r$ accelerate the current sheath radially outwards towards the inner surface of the cathode. While, the axial component of the Lorentz force $(J \times B)_z$ accelerates the current sheath axially down the tube which varies with 1/r across the focus tube. As the results, the current sheath near the surface of the inner electrode is accelerated to higher velocity. Thus, the current sheath is usually slightly canted in the forward (*z*) direction at the inner electrode formed a parabolic shape of the current sheath structure (Chow et al., 1972).

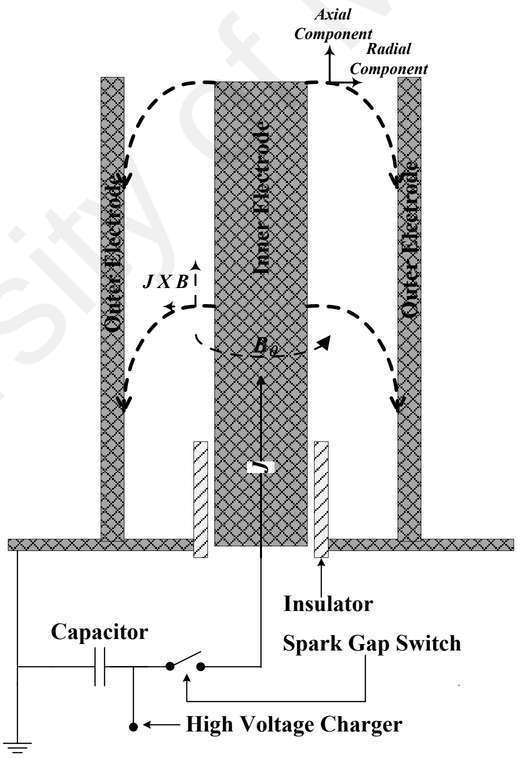

Figure 2.4: Schematic presentation of the dynamics of axial acceleration phase

Due to the slightly canted structure in nature, plasma flows centrifugally outward from the anode to cathode along the current sheath boundary throughout the acceleration. The radial force term and centrifugal flow would lead to plasma pileup and stagnation at the cathode surface which gradually reducing the annular region between the electrodes. The use of 6 cathode rods in our Mather type plasma focus device was meant to help in preventing such stagnation and plasma pileup. Along the acceleration down the tube, the current sheath scooping up almost all the gas particles it encounters. The behaviour of the magnetic piston and the plasma it drives resembles the snowplow effect in an electromagnetic shock tube. The evolution of current sheath structure often impact the final compression dynamics and hence the neutron production (Gratton et al., 1977; Milanese & Pouzo, 1985).

Kwek et al. (Kwek et al., 1990) using Schilerean photography observed that the current sheath structure acts as a strong ionizing shock wave, driven by the magnetic piston, propagating into the ambient gas and ionizing it. At low pressure operation however, thickening of the current sheath structure due to the effect of specific heat ratio can result in weaker plasma compression. On the other hand, at high pressure and slow driving speed can result in leaky piston and ineffective compression. Evidence of the current sheath as strong ionizing shock structures was also reported by BilBao et al. (Bilbao et al., 1985). Typical current sheath speed during the axial phase is about 1.7 - 13 cm/μs (Krompholz et al., 1981) with average thickness of about 3 cm (Bhuyan et al., 2003).

Practically not all the discharge current flows in the current sheath, some current stays behind the vicinity of the backwall insulator. The phenomenon observed experimentally is known as “current shedding” effect. Usually, an average of 70 % of the total discharge current flows in the current sheath in the axial acceleration phase (Tou, 1995). It was also shown in another report that an average of 68.5 % of the total discharge current took part in the compression phase where the rest was regarded as leakage current (Mathuthu et al., 1996).

Towards the end of this phase, a decrease in the thickness of the current sheath from few centimetres to a few millimetres can be observed (Kwek et al., 1990). This indicates a decrease in the swept mass along the snowplow action due to the effect of mass loss. The escape of swept mass is believed to be the consequences of pressure gradient in the parabolic current sheath structure (Chow et al., 1972).

2.2.3 Radial Phase

The radial phase starts when the axisymmetric and slanted current sheath reached to the end of the anode. The total duration of the radial phase is much shorter than the axial acceleration phase. In this phase, one end of the current sheath that is attached to the anode will begin to implode radially inwards slide across the face of the anode by the $(J \times B_{\theta})_r$ force. The other end which has been sliding along the cathode continue in its motion axially, sweeping along with it the greater portion of the accumulated mass in axial direction. A schematic representation of the dynamics of the radial phase with discharge voltage is delineated in Figure 2.5.

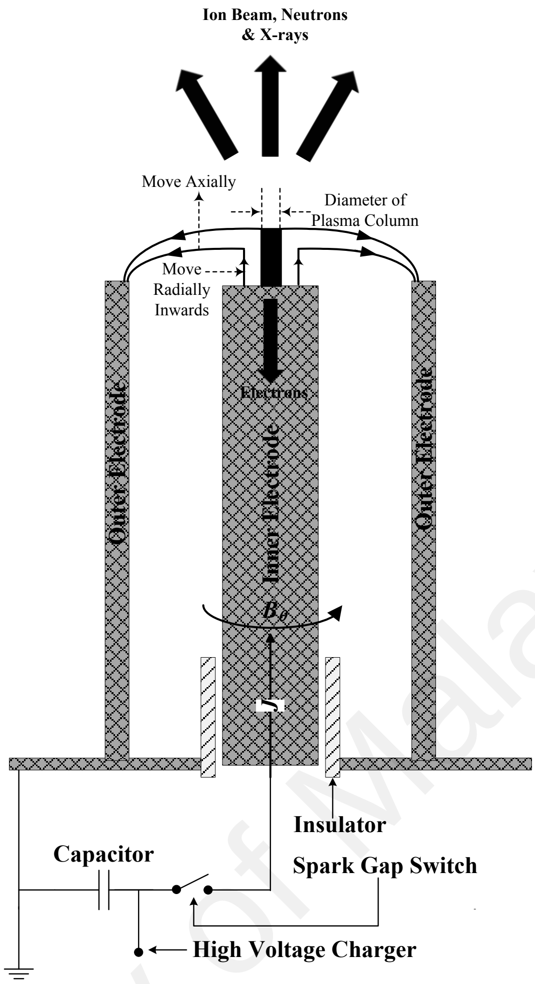

Figure 2.5: Dynamics of radial phase during plasma focus development

During the radial implosion of the current sheath, neutral gas is continuously snow-plowed, accelerated and heated by the shock wave. The radial implosion of the current sheath has a typical value of 10 – 50 cm/μs (Bernard et al., 1977; Borowiecki et al., 2006; Moreno et al., 2003). At the end of the radial compression, the non-cylindrical funnel-shaped current sheath is compressed and confined to form a very dense plasma column.

At the instant when the plasma column has pinched to a minimum radius, there is sudden increase of plasma impedance which leads to a sharp rise of voltage spike in the discharge voltage signal and a 'dip' in the discharge current signal as shown in Figure 2.6. This is the characteristic features of a good focusing discharge.

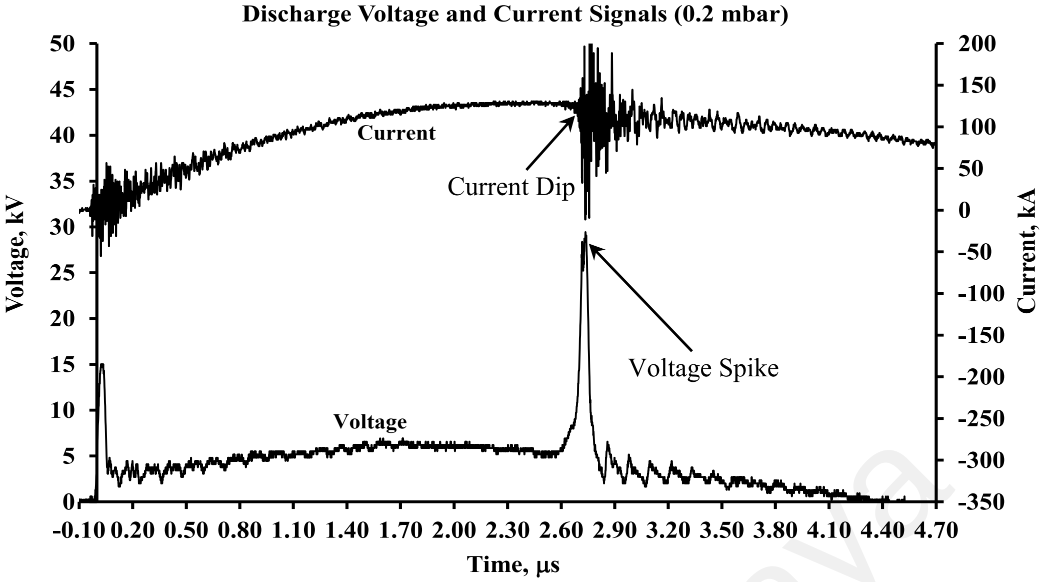

Figure 2.6: Typical discharge voltage and current signal for a good focusing discharge

There is a short duration when the plasma column has reached to a minimum radius before it is disrupted by the set in of instabilities. The pinched plasma emits intense burst of soft X-ray and neutrons when deuterium is used as the working gas. As a result of rapid change of impedance upon plasma pinch, a strong localized electric field is induced in the plasma column. This transient electric field plays the role in accelerating the energetic ion beams (deuterons) along the pinch axis in the downstream direction. Along the interaction with ambient deuterium, such deuterons may produce more neutrons in the downstream direction via beam-target fusion reactions. At the same time, fast electron beams are also produced but accelerated in the opposite direction. Consequently, strong hard X-ray burst is also produced by the electron beam bombardment to the anode surface.

Substantial efforts and accumulated research (Borowiecki et al., 2006; Jalufka & Lee, 1972; Moreno et al., 2003; Pouzo et al., 2005; Sadowski et al., 1984; Tarifeño et al., 2011) were taken to investigate the dynamics of radial phase for plasma focus device ranging from small to large energy yet the dynamics is however complicated where on the basis of experimental data it can be subdivided into four sub-phases, namely compression phase, quiescent phase, unstable phase and decay phase. A typical dynamics of radial phase obtained using Cordin model 511 image converter camera (ICC) is presented in Figure 2.7 (Castillo et al., 1997). The images have been synchronized with respect to the *dI/dt* signal.

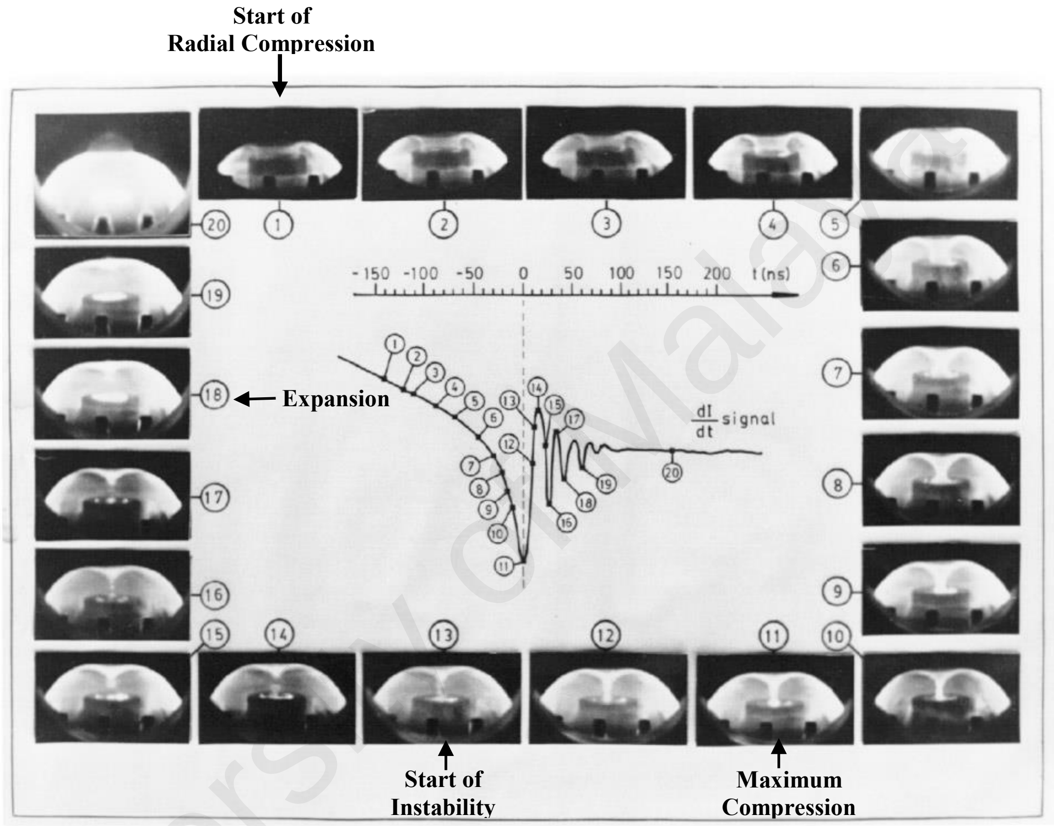

Figure 2.7: Chronology of plasma dynamics in radial phase

2.3 Modelling the Dynamical Behaviour of Plasma Focus Discharge

The plasma focus discharge can be approximated in a circuit model where the plasma is expressed in terms of time varying resistance and inductance. The equivalent circuit is shown in Figure 2.8, and it is in the form of a LCR circuit.

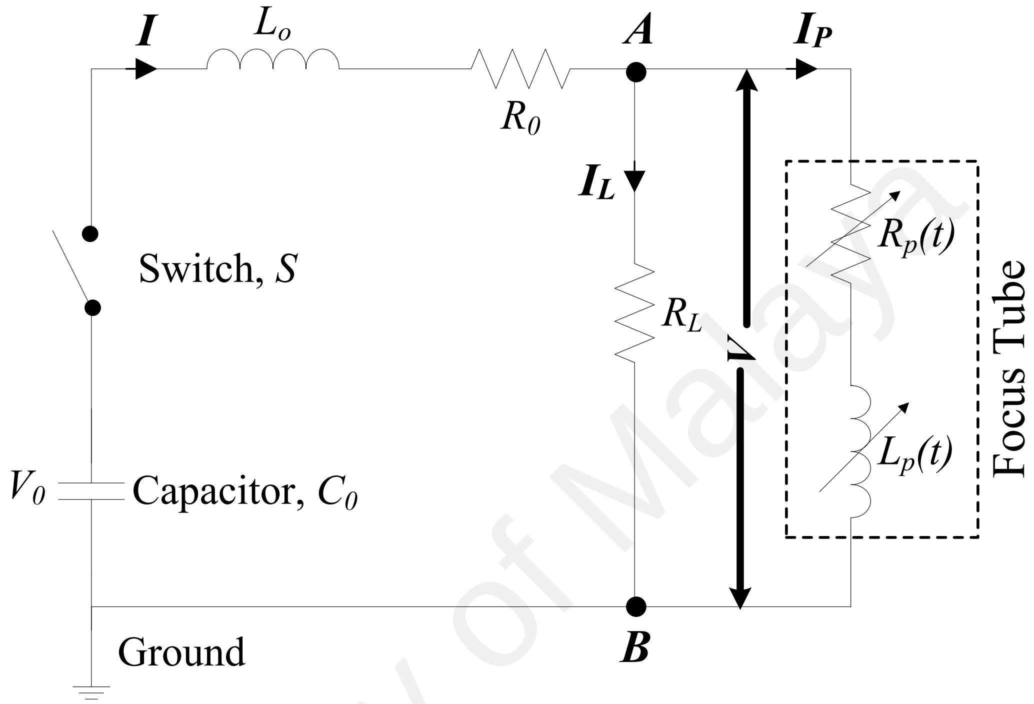

Figure 2.8: Equivalent circuit of the plasma focus discharge in a typical plasma focus device

In this electrical circuit, symbols C_0, R_0, and L_0 represent the capacitance of the capacitor bank, equivalent total series resistance and equivalent total series inductance, respectively. The value of R_0 and L_0 according to the experimental setup contributed by the capacitors, transmission line, switches and circuit connection, and they are taken to be a constant. The plasma is represented by resistance, $R_p(t)$ and inductance, $L_p(t)$.

In a plasma focus discharge, only a fraction of the total discharge current is flowed into the plasma which is represented as I_p $(\sim f_c I)$ where f_c is the current shedding factor and I is the total discharge current. Balance of the current that does not take parts in the accelerated plasma sheath is referring as leakage current, I_L. Here, R_L represents the leakage resistance in the focus tube which is correlated to the current leakage along the insulator surface.

Upon closing of the switch *S,* the capacitor is discharged through the circuit where the voltage V_0 will be distributed to all the circuit components including the plasma. By applying Kirchhoff's law, the circuit equation of the plasma focus circuit can be expressed as:

$$\frac{1}{C_0}\int_0^t Idt - V_0 + R_0 I + \frac{d}{dt}(L_0 I) + R_p I_p + \frac{d}{dt}(L_p I_p) = 0 \quad \textbf{(2.1)}$$

Therefore, the focus tube potential difference, *V* which is the potential difference across the point *A* and *B* in the circuit can be read as:

$$V = V_0 - \frac{1}{C_0}\int_0^t Idt - R_0 I - \frac{d}{dt}(L_0 I) = R_p I_p + \frac{d}{dt}(L_p I_p) \quad \textbf{(2.2)}$$

Thus, the total power input into the focus tube (Behbahani & Aghamir, 2011) can be written as:

$$P_{total} = I_p V = I_p L_p \frac{dI_p}{dt} + I_p^2 (R_p + \frac{dL_p}{dt}) \quad \textbf{(2.3)}$$

Therefore, the total energy transferred into the focus tube can be obtained by integrating Equation 2.3.

Total energy into plasma focus tube,

$$E_{total} = \int P_{total} dt$$

$$= \int I_p L_p \frac{dI_p}{dt} dt + I_p^2 (R_p + \frac{dL_p}{dt}) dt$$

$$= \int I_p L_p \frac{dI_p}{dt} dt + \int I_p^2 \frac{dL_p}{dt} dt + \int I_p^2 R_p dt \quad \textbf{(2.4)}$$

There are three ways that the energy is delivered into focus tube which can be represented by each term in Equation 2.4. The first, second and third term in the equation is corresponded to inductive energy, work done by magnetic piston and joule heating, respectively (Bing et al., 2000). It is important to note that not all the energy will be transferred to the plasma where some of the energy is stored inductively in the focus tube inductance (Wong, 1978). Fraction of the total energy that is stored inductively in the focus tube comes from the magnetic energy stored in the focus tube inductance. The magnetic energy stored in the focus tube inductance is given as:

$$E_I = \frac{1}{2} L_p I_p^2 \quad \textbf{(2.5)}$$

This showed that the magnetic energy is dependent on the total inductance of the focus tube and current flowing into the plasma. It is interesting to note that this energy is not dissipative in nature but may act as energy source for the plasma pinch during current drop (Bing et al., 2000).

By excluding the power stored inductively in the focus tube, the power transferred to the plasma can be written as:

$$P_{Plasma} = P_{total} - \frac{d}{dt}(\frac{1}{2} L_p I_p^2) = I_p^2 (R_p + \frac{1}{2} \frac{dL_p}{dt}) \quad \textbf{(2.6)}$$

The first term on the right hand side is the joule's heating due to plasma resistance and current flow into the plasma. The plasma resistance R_p is given by:

$$R_p = \frac{l_p}{\pi r_p^2 \sigma} \quad \textbf{(2.7)}$$

where l_p, r_p, σ are the final compressed plasma column length, plasma column radius and the plasma electrical conductivity, respectively (Behbahani & Aghamir, 2011). The term of $\frac{1}{2}dL_p/dt$ is the 'dynamic resistance' of the plasma.

Integration of Equation 2.6, gives the net energy transferred to the plasma (Behbahani & Aghamir, 2011):

$$E_{Plasma} = \int_0^t I_p^2 (R_p + \frac{1}{2}\frac{dL_p}{dt})dt \quad \textbf{(2.8)}$$

which is dependent on plasma resistance *(R_p)* and dynamic resistance *($\frac{1}{2}dL_p/dt$)*. The second term in the Equation 2.8 turn out to be half of the work done by the magnetic piston. Thus, the other half of the piston work is used to increase the tube inductance by pushing the current sheath along the electrode and stored as inductive energy in the focus tube. Energy transferred into plasma is the source of kinetic energy, internal energy, radiation energy, ionization and excitation in the plasma column (Bing et al., 2000).

The current dip and voltage spike in the discharge current and voltage signal is an evidence of energy transferred into plasma. However, the transfer of energy to the plasma depends on the static inductance of the plasma focus device. Plasma focus can then be categorized as type 1 with static inductance < 100 nH and type 2 with static inductance > 100 nH for modeling purpose. It has been reported that anomalous resistance played a major role in type 2 plasma focus device (Lee et al., 2011).

2.4 Current Sheath Dynamics on Focus Performance

The dynamics and structure of current sheath during the acceleration phase plays an important role in the focusing dynamics and associated plasma phenomena. Many works have been done to investigate the effect of current sheath dynamics on plasma compression and radiation emission (Bienkowska et al., 2005; Borowiecki et al., 2006; Gupta et al., 2000; Kwek et al., 1990; Rawat et al., 1994; Zhang et al., 2005). One of the essential factor that affected the focusing quality is the speed of the current sheath. Various experimental observation made from low to high energy plasma focus device showed that peak axial current sheath speed between 6 – 10 cm/μs is good for plasma pinch (Serban & Lee, 1998). Auluck explained that the reason of plasma focus operate in narrow range of velocities is related to gas properties such as electric breakdown strength, specific ionization and dissociation energy (Auluck, 2014).

The lowest speed limit is related to the poor coupling of the magnetic piston with the driven plasma as the effect of low magnetic Reynold number, R_m (Lee et al., 2013). While the higher speed limit is due to high magnetic Reynold number that cause a significant separation between the magnetic piston with the driven plasma. From the point of view of strong shock wave theory, too high current sheath speed will cause the driven current sheath layer to be too thick until effectively separate the shock front from the magnetic piston (Gross, 1967). This may result in current sheath layer that had collapsed radially, whilst the magnetic piston is still in the axial phase. In this condition, usually weaker focusing discharge is obtained due to such a force-field flow field separation.

Operation of plasma focus at high current sheath speed is benign for good focusing action as higher temperature of the pinched plasma can be achieved (Serban & Lee, 1998). High temperature plasma produces high radiation emissions. However, it is a challenge to obtain intense focus at higher speed beyond a certain limit. Some major challenges are the development of Rayleigh-Taylor instabilities, increase of plasma-anode interactions especially the ions or the increase of mean free path which causing the shock wave to become diffusive and hence decrease the driving efficiency of the current sheath.

There are several ways to drive the current sheath at high speed. One way is by increasing the charging voltage. Increase in the charging voltage thus discharge energy will increase the Lorentz force that drive the current sheath and thus increase the speed of the current sheath. Often the maximum voltage applied is limited the rating of the capacitor, which is set to prevent over-voltage causing insulation problem.

Other way is to modify the electrode geometry by using tapered anode where the anode has a section of gradually slimmed diameter until the anode tip. In this way, higher Lorentz force will be experienced by the current sheath that is in contact with the anode surface since the magnetic field is inversely proportional to the radial distance from the anode axis ($B \sim 1/r$). The correlation between the current sheath speed V with radial distance r and operating pressure can be represented as $V \sim (1/r)\, P^{-1/2}$. More detail of the tappered anode operation can refer to previous work (Aghamir & Behbahani, 2011).

On the other hand, the speed is increased in reducing gas pressure. However, reducing the operating pressure beyond certain limit may defer the optimum operation regime. The optimum current sheath speed is determined based on a practice where the conversion of the electrical capacitor energy to inductive magnetic energy must be maximized in order for the plasma focus device to be in optimize performance. This is often done experimentally to ensure the current sheath arrives at the open end of the anode at the maximum discharge current.

CHAPTER 3: LITERATURE REVIEW ON PLASMA FOCUS RADIATION EMISSION & RELATED PHENOMENA

3.1 Pulsed Plasma Radiation Source

Plasma focus community has made a rapid progress in the research of plasma focus as plasma radiation source. It is popular among other pulse plasma devices because it is capable of compressing most gas type and produces abundant amount of different radiations including fast neutrons (Bures et al., 2012; Burns et al., 1988; Conrads, 1990), X-rays (Bostick & Prior, 1972; Herziger et al., 1978; Kato & Be, 1986; Zakaullah et al., 2000), energetic ions (Hirano et al., 1989; Lim et al., 2013; Sadowski et al., 1985) and electrons (Harries et al., 1978b; Neog & Mohanty, 2007; Schneider et al., 1985). The very short pulse duration in the regime of nanoseconds make it suitable for used in pulsed radiation physics, chemistry, biology such as pulsed activation analysis (Rapezzi et al., 2004; Tartari et al., 2002), X-ray lithography (Bogolyubov et al., 1998; Kalaiselvi et al., 2013; Kato et al., 1988; Tan et al., 2006), short lived radioisotope production (Angeli et al., 2005; Roshan, Springham, et al., 2010; Shirani et al., 2013; Sumini et al., 2006; Talaei et al., 2010) and radiobiology (Gribkov & Orlova, 2004).

Radiation source based on plasma focus device is considered ecologically friendly and radiation-safe device because it is not a radiation source beside the short windows of discharge and radiation emission. Many works have been done to study the mechanism involved in the production of radiation as well as the parameters that influence the radiation yield. However, there are still a number of key questions to be answered by plasma physicist which are crucial in develop the plasma focus as commercially viable pulse plasma radiation source. A brief review of the literature is presented here with the aims to scheme through the various explanation obtained based on experimental observation or theoretical prediction on the radiation emission mechanisms. Particular attention is given to possible mechanisms responsible for the neutron and ion beam emissions.

3.1.1 Ion Beam

Plasma focus is typically discharged at energy of a few tens of kilovolts, but the resulted ion beam emitted in the forward direction possess energy of several keV to MeV (Sadowski et al., 2000). Ion beam emitted in the backward direction has also been reported (Roshan et al., 2009). This has thus formed an important subject of study for the research and development as well as technological applications.

It has been reported that the ion beam energy spectra follow a power law of $\frac{dN_i}{dE} \propto E_{bi}^{-x}$, where E_{bi} is the ion beam energy, N is the ion number and x ranges between 2 to 5 (Sánchez & Feugeas, 1997; Stygar et al., 1982). However, the production of ion beam are mostly still unambiguously demonstrated mainly due to the challenge in measuring this transient emission with sufficiently high resolution over a wide range of energy.

Ion beam was observed to be emitted from different micro sources in the pinch region (Malinowski et al., 2009; Sadowski et al., 1985; Skladnik et al., 2005; Yousefi et al., 2007) with anisotropic nature in the ion beam angular distribution (El-Aragi, 2010; Mohanty et al., 2005). Bhuyan et al. explained that the anisotropy of ion beam emission was due to ion Larmor radius effects (Bhuyan et al., 2006).

In 1988, Sadowki et al. reported a comparison on ion beam emission for plasma focus of energy capacity ranging from 3.6 – 200 kJ (Sadowski et al., 1988). He found that the angular distributions of fast (> 50 keV) deuterons demonstrate a highly anisotropic character and a characteristic drop in the emission at angles between 40 and 80 degrees.

High energy deuterons were observed to be emitted in a narrow (with divergence < 8^o) bunches as evidenced from the space-resolved ion pinhole pictures. He concluded that macroscopic characteristics of the ion emission from plasma focus device of different energy can be preserved but the microscopic features such as fine-spatial and time structures cannot be similar due to stochastic phenomena in plasma focus discharge.

Using solid state nuclear track detector (CR-39), Bhuyan et al. (Bhuyan et al., 2010) measured the ion tracks formed from ion beam of energy from few tens of keV to hundreds of keV are having average crater diameter of 4.35 μm and density of 10^{10} tracks/m^2. His other works (Bhuyan et al., 2011) found that the size of the ion tracks shifted to higher diameter at increasing angular position.

Behbahani et al. investigated the correlation of ion beam emission with operating pressure (Behbahani & Aghamir, 2012). Two range of pressure: 0.2 – 0.8 mbar and 0.8 - 1.5 mbar was examined. Higher ion beam intensity with longer duration of emission was obtained at low pressure range of 0.2 – 0.8 mbar. The increase in ion beam intensity is correlated to the intensified instability due to the effect of anomalous resistance. Anomalous resistance was the factor where considerable current dip and multi dips measured in the discharge current signal and its effect correlate to the ion beam and hard X-ray emissions (Behbahani & Aghamir, 2011).

In recent years, Lee & Saw (Lee & Saw, 2012) reported for the first time the modelling of the ion beam properties using Lee model code. The Lee model code was modified by incorporated the plasma diode mechanism for the ion beam acceleration as proposed by Gribkov et al. (Gribkov et al., 2007) to characterize the beam at the exit of the pinch. The modelling starts from the basis of ion beam fluence equation which is the number of ions per m^2 and compared the computed results with experiments using deuterium filling. Deuteron beam fluence of 2.4 -7.8 x 10^{20} ionsm^{-2} was computed for plasma focus with energy from 0.4 – 486 kJ showing almost independency of the fluence with the storage energy.

A year later, he extended the works on ion beam modelling to include various gases (Lee & Saw, 2013) with aim to provide a benchmark on the selection of gases for material application such as damage studies. Numerical results showed that the ion beam number, fluence, flux and current decreases from the lightest to heaviest gas except for Argon where the correlation breaks. Argon was found to be a compromise gas delivering a higher value of ion beam fluence and flux over a broad pressure range. As the radiative cooling and collapse effects became severe, the energy fluence, energy flux, power flow and damage factors was also computed to be higher. Studies of nitrogen ion beam properties (Akel et al., 2014) and interaction of the deuteron beam with graphite target (Akel et al., 2014) based on Lee model were also reported. A numerical study (Akel et al., 2017) reported later shown that ion current densities in the order of 10^7 Am^{-2} was obtained for plasma focus operated in nitrogen filling with maximum power flow density of 10^{14} Wm^{-2}.

The special hybrid features of the plasma focus device due to its energetic ion beam deposition and instantaneous annealing effect has become a subject of current interest for its development as economic pulse ion beam source for applications in surface properties modification (Agarwala et al., 1997; Ayash et al., 2016; Bhuyan et al., 2007; Kelly et al., 1996; Pimenov et al., 2002), ion implantation (Feugeas et al., 1988; Gribkov et al., 2003; Habibi & Laktarashi, 2016; Sadiq et al., 2006; Sánchez & Feugeas, 1997), thin film deposition (Ghareshabani & Sobhanian, 2016; Gupta et al., 2004; Rawat et al., 2003), semiconductor doping (Srivastava et al., 1996), synthesis of nanoparticles (Zhang et al.,

2006) and simulator for the test of first wall material of nuclear fusion facilities (Chernyshova et al., 2016). Phase transformation from amorphous to crystalline phase using argon ion beam irradiation on hydrogenated amorphous silicon film has been demonstrated (Ngoi et al., 2012). Single pulse irradiation was found to be more effective in enhancing the crystallinity of the film whereas increasing number of irradiations resulted in lower crystallinity and contamination of impurities by anode material.

3.1.2 Electron Beam

Energetic electron beam emission from the plasma focus has been reviewed as efficient candidate for the rapidly growing technological fields such as biophysics (Tartari et al., 2004), electron beam lithography (Lee et al., 1997)， pulse laser pumping (Sauerbrey et al., 1987) and sterilization (Kotov & Sokovnin, 2000). Yet, only a few efforts were made to study the pulse electron beam emission from a broad energy range of plasma focus particularly lies to the difficulty in the direct measurement of the emission.

The difficulties lies to the fact that the magnetic field from the electron beam source is sometime too strong to trap the very low energy electrons left only the fraction of higher energies electrons which may suffer from the interaction with the filling gas, plasma medium or the anode. Yet, the very high energy electrons are of very high tendency to interact among themselves. In other words, this has masked or reduced the detection efficiency for the electron beam measurement. Moreover, the extraction of the electron beam was laborious as the coupling of the diagnostic tool to oscilloscope was difficult due to the high voltage connection at the breech of the focus tube.

In earlier studies, Yamamoto et al. measured energy spectrum of the electron beam in the range of 0.1 to 1 MeV from a 6 kJ plasma focus device (Yamamoto et al., 1982). Maximum population of electron beam was observed to distribute from 150 to 200 keV with maximum current of several kA corresponded approximately one percent of the total discharge current was detected. He also correlated the electron beam emission with ion beam and found that both emissions occurred simultaneously.

An extensive studies on electron beam emission has been made by Patran et al. (Patran et al., 2005) using magnetic electron analyzer and Rogowski coil. Most of the electron beam emitted was below energy of 200 keV. It was reported for the first time that a well collimated electron beam giving rise to low medium energy X-ray emission due to low off-axis anode bombardment whereas poorly collimated electron beam due to poor compression dynamics was shown to generate more medium energy X-ray emission from the anode rim.

Neog & Mohanty (Neog & Mohanty, 2007) observed the electron beam was emitted corresponded to different pinch phases with average electron beam current of 13.5 kA obtained at optimum pressure of 0.3 torr. Electron beam energies from 10 keV to more than 200 keV has been detected with most probable electron beam lies within energy range of 80 -110 keV. At charging voltage of 22 kV operated at 0.6 mbar argon, energy spectrum of the electron beam using an indirect method shown that most of the electron emissions were in the energy range of 125 – 375 keV and negligible for energy beyond 375 keV (Neda et al., 2017). In a few other reports, the energy spectrum of electron beam was found to follow a power law of $\frac{dN}{dE} \propto E_{be}^{-x}$, where E_{be} is the electron beam energy with the value of x in between 2 – 4 (Bernstein et al., 1969; Johnson, 1974; Stygar et al., 1982).

For application purpose, Zhang et al. (Zhang et al., 2007) has investigated the electron beam emission from neon, argon, hydrogen and helium to find an optimum condition for plasma focus application in thin film deposition using electron beam source. Hydrogen gas was found to be the best candidate as it produces the highest electron beam charge (22.7 ± 2.7 mC) and higher energy electron beam (from 50 to 200 keV). Neon is examined to be the next choice as it produces next highest electron beam charge (10.8 ± 1.2 mC) with electron energy of 30 – 70 keV.

3.1.3 Neutrons

Many progresses have been marked in plasma focus device since five decades ago, yet it still continue to attract attention particularly for its high neutron yield in the application as intense pulse neutron sources when operated in deuterium medium (Ahmad et al., 2006; Bernard et al., 1977). The transient nature of the plasma focus become an advantage when compare to the conventional radioactive neutron source such as americium-beryllium (Am-Be) or Californium-252 (^{252}Cf). These continuous isotopic neutron source even though has the merit of having relatively constant flux but the main disadvantage lies to the handling issue due to special care is needed to store the radiation source with bulky shielding at all times.

In 1965, Mather the pioneer of the "Mather type" plasma focus has obtained experimentally neutron yield of more than 10^{10} neutrons per shot from 18 kJ device using pure deuterium filling (Mather, 1965). He found that higher neutron yield of 3.3 x 10^{11} neutrons per burst was obtained for deuterium-tritium admixture with an increase by a factor of 80 in comparison to average yield of 4 x 10^9 neutrons per burst for pure deuterium filling (Mather, 1966).

Maximum neutron emission of up to 10^{11} neutron per shot has been measured (Szydlowski et al., 2001) from the world largest plasma focus facility (PF 1000) operated at 500 kJ while neutron emissions from sub-kilojoule device in the order of 10^6 has been reported (Milanese et al., 2003; Rishi et al., 2009; Silva et al., 2003). Enhancement of neutron yield up to 3 times has been reported for plasma focus device operated at high voltage and fast rise time compared to low voltage but equal energy (Decker et al., 1980). Improvement of the current delivering efficiency and thus neutron yield with the use of fast high impedance capacitor bank was also reported by Decker et al. (Decker et al., 1983).

Substantial efforts on the neutron measurement from various plasma focus device all over the world in a wide range of energies and operating condition has led to several experimental observed scaling law of neutron yield to scale with various input parameters such as the storage energy of the capacitor bank and the discharge current. In earlier studies, the empirical scaling law of $Y_n \; \alpha \; E_0^2$ (Bernard et al., 1998) and $Y_n \; \alpha \; I^{3.2}$ (Krompholz et al., 1981) was established where Y_n is the neutron yield, E_0 is the storage energy in kJ and I is the discharge current in kA. However, it is well known that only a fraction of the total discharge current flows through the pinch region. Thus, a scaling of neutron yield with pinch current should be more appropriate. Oppenlander et al. (Oppenlander et al., 1977) and Lee & Saw (Lee & Saw, 2008) has established the neutron scaling law based on the pinch current as $Y_n \alpha \; I_{pinch}^4$ and $Y_n \; \alpha \, I_{pinch}^{4.7}$, respectively.

It has been summarized from the basis of experimental works from various research groups in the world and found that most of the neutron optimized plasma focus device showed same limited peak axial sheath velocity of 10 cm/μs and speed parameter of about 89 kAcm^{-1}torr$^{-1/2}$ which varies at standard deviation of less than 10 % (Lee & Serban, 1996). Speed parameter was found to be the determining factor for optimum neutron production in either Mather or Filippov type plasma focus (Zhang et al., 2006).

Lerner et al. (Lerner et al., 2012) had recently proposed a scheme for neutron production using Proton-Boron 11 instead of deuterium filling. Enhancement of almost three times is expected with neutron yield up to ~ 4 x 10^{11} neutrons per shot. Verma et al. (Verma et al., 2013) on the other hand had demonstrated an increase in the neutron yield from a fast miniature plasma focus device of 200 J as a table top system operated in repetitive mode. Neutron yield of (1.4 ± 0.6) x 10^6 n/sec under 1 Hz operation was enhanced to one order of magnitude higher (~10^7) at higher repetition rate of 10 Hz with pure deuterium filling. Higher and better reproducibility in neutron emission per shot was obtained with repetitive mode over single shot mode operation.

Other than the experimental studies, substantial efforts were also taken to model the neutron yield. One of the earliest modelling effort was done by Potter (Potter, 1971) using two-fluid MHD model. The neutron yield calculated based on the thermonuclear mechanism showed a qualitative agreement with the experimental measured D-D neutron yield. However, the model did not explain the discrepancy of the neutron yield anisotropy measured in most plasma focus discharges. Other models including Von Karman approximations (Gonzalez et al., 2009) and fully kinetic simulation (Schmidt et al., 2012) were used to estimate the neutron yield.

Lee has developed a Lee model code (Lee, 2013) based on beam-target mechanism to compute the neutron yield by fitting the computed current waveform against measured current waveform. Using Lee model code, Saw & Lee (Saw & Lee, 2011) has also reported the possibility of scaling up the plasma focus at just 3 MJ to produce D-D neutron yield of 10^{13} per shot in PF-1000 facility with the use of less damped capacitor bank compared to operate at 19 MJ with conventional capacitor bank. She also showed that the neutron yield can be increased up to 10^{15} neutrons/shot using deuterium-tritium filling.

The current interest in developing the plasma focus as a unique neutron sources stems from some potentially interesting applications such as half-life measurement (Bar & Porath, 1975; Pheng et al., 1989), calibration of dark matters detectors (Beg et al., 2002), treatment of transplanted human liver using boron neutron capture therapy (BNCT) (Benzi et al., 2004), testing of prospective fusion reactor wall materials (Zucker et al., 1977), detection of gold in ingots (Verri et al., 2000) and for short pulse-applications (Bennett et al., 2017).

3.1.4 Soft and Hard X-Ray

Much efforts and endeavors has been done in the past for the studies of neutron emission with minor attention being paid to the X-ray emissions. Yet, X-rays emission in the soft and hard X-ray region from the hot and dense plasma has then lead to more intensive studies on the X-ray emanated from the plasma focus (Beckner et al., 1969; Bostick & Prior, 1972; Choi et al., 1989; Harries et al., 1978a; Van, 1971; Van et al., 1970; Zakaullah et al., 2000) in view of its potential application as a high brightness source for X-ray lithography (Kato & Be, 1986), micromachining (Gribkov et al., 2003) and radiography (Castillo et al., 2001; Raspa et al., 2008; Raspa et al., 2004).

Inside the hot and dense plasma, the electrons, ions and neutral particles were mutually collides with each other that will lead to conversion of the kinetic energy to emissions of electromagnetic radiation in a wide range of spectrum that is dependent on the temperature of the plasma. There is a wide consensus that the electromagnetic radiation in the X-ray region from plasma focus can be categorized into two component, i.e.: Soft X-ray and hard X-ray. The soft X-ray emission can be ascribed as due to three types of processes, namely Bremsstrahlung (free-free transition), recombination (free-bound transition) and line radiation (bound-bound transition) (Neff et al., 1989; Stratton, 1965).

On the other hand, hard X-rays emission which is detectable outside of the vacuum chamber was ascribed as due to the bombardment of non-thermal high energy electron beam to the metallic anode surface (Neog et al., 2008). Newman et al. (Newman & Petrosian, 1975) proposed that the origin of hard X-ray emission was due to the interaction of electron beam with anode target. Works by Tartari et al. (Tartari et al., 2004) suggested that the origin of the X-ray emission composed of both relativistic electron beam and electrode component of energy about 30- 45 keV.

Most of the reported hard X-ray was measured to have average energy of about 100 keV (Moreno et al., 2006; Patran et al., 2005; Raspa et al., 2004). It has been reported that when hard X-ray yield is increased, the neutron yield also increased accordingly but the effect is reversed for soft X-ray (Serban & Lee, 1997). Tremendous efforts were made to study the plasma focus X-rays which the characteristic of the emission was found to be dependent on the nature of the filling gas (Favre et al., 1992; Liu et al., 1998), pressure (Etaati et al., 2010), input energy (Farahani et al., 2011; Roomi et al., 2011), anode tip material (Habibi et al., 2010) and electrode geometry (Habibi et al., 2010; Mohammadi et al., 2009).

Serban et al. (Serban & Lee, 1997) observed that higher soft X-ray emission can be obtained at higher current sheath speed. At peak axial speed up to 15 cm/μs, soft X-ray has been enhanced by 120 %. He proposed a scaling law for soft X-ray production as

$Y_{sx}\ \alpha\ I_{\max}^{2}V_{axial}^{4}$, where Y_{sx} is the soft X-ray yield, I_{max} is the maximum discharge current and V_{axial} is the peak axial current speed.

On the other hand, Barbaglia et al. observed that the hard X-ray emission is strongly dependent on the voltage drop in the forming pinch (Barbaglia et al., 2009). The voltage drop has a threshold value which is corresponded to the minimum energy for electron beam in exceeding the runaway Dreicer condition (Dreicer, 1959). Current sheath symmetry during the rundown phase also played an important role in hard X-ray production (Amrollahi et al., 2009). Higher hard X-ray yield was obtained with a formation of symmetric current sheath.

Zakaullah et al. (Zakaullah et al., 2001) observed from X-ray pinhole image found that the X-ray emitting region has a complicated structure which is situated in the vicinity and above the anode surface that was extended up to 25 mm away from the anode tip. Sometime the spot-like structures or “hot spots” superimposed with the X-ray image obtained with different absorption filter can be observed and become dominant in heavier gases of $Z \geq 18$ (Bayley et al., 1991; Beg et al., 2000; Bostick & Prior, 1972; Ng et al., 1998; Yanagidaira et al., 1996).

In most recent study, the enhancement of the total hard X-ray yield by the effects of pre-ionization created using different shunt resistors was reported (Piriaei et al., 2017). Pre-ionization was found to reduce the impurities created due to sputtering of electrons on the insulator sleeve and anode tip while produce a faster moving and more uniform current sheath. Hence, a more stabilized pinched plasma can be formed which is conducive for X-ray emission.

In spite of many experiments on the studies of high intensity X-ray have been reported, yet the exact mechanism corresponded to the emission are still a disputable issue. Moreover, the quest of cost effective and efficient X-ray source had thus continuously motivated the researchers for more experimental works in optimizing the plasma focus as X-ray source for practical applications.

3.2 Correlation Studies of Radiation Emissions and Discharge Parameters

Extensive experimental works and theoretical efforts has been undertaken to study various emission from the plasma focus by many research groups. However, a satisfactory explanation on the emission mechanism and their inter-correlation with discharge dynamics still not available. Such investigations still remain as interesting topic of research which are important for the development of the plasma focus as plasma based radiation sources.

In 1985, Yamamoto et al. (Yamamoto et al., 1985) performed a simultaneous measurement between neutrons, X-rays, ion and electron beam and correlates with pinching dynamics observed using interferometry method in streak and framing mode. He found that $m = 0$ instability has no effect on neutron production and suggested the acceleration of charged particle beam that lead to neutron production was due to abrupt rise of the plasma resistivity rather than the rapid change in the plasma inductance. Other researchers showed that neutron production decreases with the presence of $m = 0$ instability (Yousefi et al., 2006). The growth of $m = 0$ instability is observed to occur more likely at lower pressure.

Zakaullah et al. (Zakaullah et al., 1996) have reported the neutron emission profile has *FWHM* of almost twice compared to X-ray emission (40 - 50 ns). Different production mechanism was speculated for these two radiation emission. His later work found that X-ray emission became dominant at lower pressure where the emission is mainly $Cu\text{-}K_\alpha$ line radiation (Zakaullah et al., 1998). However, neutron yield was observed to decrease towards lower pressure.

Heo & Park (Heo & Park, 2002) investigated the correlation between ion beam and X-ray emission in argon filling at low pressure. Higher ion beam emission was observed when X-ray emission increased. Similar observation was reported by Zakaullah et al. (Zakaullah et al., 1998). He observed that at low pressure, the soft X-ray is mostly originated from the anode surface.

Szydlowski et al. (Szydlowski et al., 2004) have reported observation of two neutron pulses emitted from PF 1000 facility with total neutron yield of 10^{10} - 10^{11} neutrons/shot. The second pulse was observed to be more intense than the first one and the author was able to identify the thermal and non-thermal mechanism of neutron production. Similar works was reported by Scholz et al. (Scholz et al., 2004) where the first neutron pulse was found to be corresponded to thermal neutrons and second pulse is attributed to beam-target neutrons.

Kubes et al. (Kubes et al., 2006) also observed X-ray and neutron emission from PF 1000 were emitted in two pulses. The first pulse in X-ray signal is usually dominated by soft X-rays and corresponded to maximum compression of plasma column while hard X-ray is dominated by second pulse. Three to ten times more neutrons is observed to be emitted during the second pulse. Using magnetic spectrometer and automated counting system, Springham et al. (Springham et al., 2000) concluded that low energy deuterons (predominatly 30 - 60 keV) are the major contributors to the neutron production.

Neog et al. (Neog et al., 2008) carried out a simultaneous time resolved measurement on X-rays, ion and electron beam emission. Soft X-rays with total duration up to 300 ns were observed to be emitted corresponding to different pinch stages, which was analogous with the electron beam emission. Soft X-ray emission was observed to dominate in subsequent compression whereas hard X-ray only produced at maximum pinch stage when the electron beam has sufficient energy to generate hard X-ray upon interaction with anode surface. Estimated effective hard X-ray photon energy (~110 keV) was obtained to be consistent with electron beam energy distribution. Time correlation analysis showed that ion beam and electron beam were both accelerated by the same local accelerating field.

Recently, Roshan et al. (Roshan et al., 2010) reported plasma focus operated in high pressure regime is favourable for neutron production while low pressure regime is for ion beam generation. The pinch image showed that at low pressure regime, the discharge occurred at the open end of the anode due to bombardment of high energy electrons (and ions) of about 500 keV on the anode. At high pressure regime, a compressed and elongated plasma column was formed on the anode surface followed by intense neutron emission. Deuteron energy in the range of 40 – 50 keV was found to be correlated with the optimum neutron yield.

Rafique et al. (Rafique et al., 2010) investigated the correlation of radial compression dynamics with neutron and X-rays emission from a 3.2 kJ Mather type plasma focus device. His work revealed that the neutron yield and hard X-ray emission for discharge with multiple voltage spikes is less compared to single voltage spike but vice-versa for the soft X-rays emission. The author also pointed out that a fast implosion speed of the current sheath with a geometrical profile that does not favour a good confinement of the plasma column may result in low neutron output.

Aghamir & Behbahani (Aghamir & Behbahani, 2011) have shown enhancement in ions and X-ray emission at higher axial current sheath velocity using step anode as a result of increase in plasma temperature and intensified effect of anomalous resistivity. However, he pointed out that the choice of step region is very important that it must be long enough to increase the current sheath velocity but short enough to prevent separation between the shock front and magnetic piston.

Etaati et al. studied (Etaati et al., 2011) the angular distribution of argon ion beam and X-rays using an array of 5 Faraday cups and TLD-100 dosimeters, respectively. Angular distribution of ions is found to be highly anisotropic and confined within $\pm 11^{o}$ whereas X-ray emission has bimodal distribution which peaked at about $\pm 15^{o}$. The author explained this behaviour is either due to self-absorption effect of soft X-ray in the dense plasma or the growth of $m = 0$ instability which results in more intense hard X-ray emission at the central anode axis.

3.3 Instabilities in the Pinched Plasma (*R-T*, *m=0*, *m=1*, Micro-Instabilities)

The formation of hot and dense plasma in plasma focus by electromagnetic acceleration and compression mechanism is both its beauty and drawback. The confinement time of the pinched plasma is restricted from hundreds of nanoseconds to tens of nanoseconds where the lifetime scale linearly with anode radius (Lee & Serban,

1996) as a consequences of evolution of various types of instabilities and turbulence that hindered the plasma confinement.

In plasma physics research, plasma instabilities has been the subject of most of the technical literature and many types of instabilities have been identified in various plasma system. Generally, plasma instabilities can be divided into two categories that is Macroscopic (MagnetoHydroDynamic-MHD instabilities) and Microscopic (Kinetic).

It has been reported by Rafique et al. (Rafique et al., 2010) that the plasma column suffered from various types of instabilities such as Rayleigh-Taylor instability, sausage (m=0) and kink (m =1) instability which leads to the disruption of the pinched column. He obtained higher neutron and hard X-ray emission when there is presence of $m = 0$ instability in a focusing discharge. Rawat et al. also observed sausage and kink instabilities formed in the plasma column (Rawat et al., 2004) using CCD based pinhole imaging technique. Castillo et al. (Castillo et al., 2002) observed a fine structure of 'hot spot' presence in the plasma column as a consequence associated with the manifestation of $m = 0$ instability.

During the plasma compression, there is diffusion of magnetic and electric field into the plasma column due to increase of plasma resistivity and thus induced a localized electric field in the pinched plasma that is responsible for the ions and electrons acceleration (Peter, 1974). Furthermore, the rapid change in the magnetic field at each of the constricted area of plasma column also induces a strong axial electric field ($E_z \equiv dB_\theta / dt$) which accelerate the ions and electrons up to very high energies of hundreds of keV (Beckner et al., 1969; Haruki et al., 2006; Neff et al., 1980).

Mather et al. (Mather et al., 1969) demonstrated that the application of external axial magnetic field leads to spatial stability to the pinched plasma but caused considerable reduction in X-ray emission. Similar observation also reported by Mohanty et al. (Mohanty et al., 1997). Rawat et al. (Rawat et al., 1994) imaged the structure of current sheath under the influence of axial magnetic field using shadowgraphic technique. He observed a hump formed in the current sheath structure during radial collapse phase. He inferred that this may be the cause of less effective pinching and lower neutron yield.

Apart from the macroinstabilities, the existence of microinstabilities and turbulence in the pinching dynamics was also observed in plasma focus experiment. The nonthermal radiation in the microwave range, acceleration of charged particles to high energy and presence of anomalous resistivity in the pinched plasma are an indication of the manifestation of micro-instabilities and turbulence in the plasma focus discharge (Bernard et al., 1977).

Evidence of microwave signals in the frequency range from 2.6 GHz to 18 GHz has been reported (Schönbach et al., 1977). Bernard et al. (Bernard et al., 1975) commented that the super thermal scattering during the pinch phase and excitation of the ionizing wave is correlated to micro-instabilities. The micro- instabilities are evolved from the intense electric current and plasma interaction (Bernard et al., 1979). Various types of beam-plasma interaction due to electron beam drifts through the pinched plasma has resulted micro-instabilities such as Weibel instabilities (Lee & Lampe, 1973).

Even though, the inevitably growth of instability might be a threat to confinement period but it is on the other hand a source of intense multi-radiation products. Thus, completely stable plasma may not necessarily be the best condition whereby it becomes more important to learn to live with instabilities rather than to avoid them completely.

3.4 Neutrons Production Mechanism

Various models have been proposed to explain the mechanism involved in neutron production, yet a satisfactory explanation is often lacking in explaining the complexity of the phenomenon. Principally, the mechanisms responsible in neutron production can be categorized as thermonuclear and non-thermonuclear.

The early experiments on neutron measurement often point to the thought of thermonuclear origin (Mather, 1965). The fusion neutron was considered to be produced by thermal collisions between deuterons in the pinched plasma that resulted isotropic neutron emission with characteristic energy of 2.45 MeV. However, abundance of experimental results on the observed neutron energy greater than 2.45 MeV and highly anisotropic nature of neutron emission suggested the existence of other mechanisms (Bernstein & Hai, 1970b; Lee et al., 1971; Springham et al., 2002). The presence of anisotropy in the neutron emission could also be interpreted as there could not be any single proposed model (Lee et al., 1972).

Castilo Mejia et al. (Castillo et al., 1997) deduced the anisotropy to be the coexistence of thermal and non-thermal mechanisms. The angular distribution of neutrons emissions measured by employing CR-39 nuclear track detectors (Castillo et al., 2002) suggested that 70 % of the total neutron production was found to be contributed by thermonuclear component with 30 % from the non-thermonuclear origin.

In 1972, Lee et al. (Lee et al., 1972) tried to explain the anisotropy in the neutron yield using moving thermal plasma model (Hübner et al., 1978) which was of thermonuclear origin. In this model, the plasma centre of mass is expected to move in the forward direction which caused anisotropy to the neutron emission. However, he showed that the required centre of mass velocity to produce anisotropy of 1.48 is 440 cm/μs seems to be unrealistic as the measured velocity through optical observation is not more than 50 cm/μs.

It was later reported by Moo et al. (Moo et al., 1991) that the anisotropy of the measured neutron yield was reasonably interpreted with beam-target model. In beam target model which is in the category of non-thermal mechanism, a beam of deuterons accelerated in the downstream direction were considered to interact with the ambient plasma that produced D-D fusion neutrons. His work showed that the total neutron yield was dominated by beam-target mechanism and more than 85 % of neutrons were produced by the deuteron beam-plasma interaction in the region of 20 – 60 mm above anode surface.

Further evidence of beam target mechanism in neutron production was observed by Yousefi et al. (Yousefi et al., 2006). He speculated that the neutron energy along the axial direction of more than 2.45 MeV was due to additional energy transferred from energetic ion beam produced in the forward direction. Beam target effect is postulated to enhance at lower pressure which could produce more unidirectional neutron emission.

The role of $m = 0$ instability on the neutron generation was investigated by means of numerical modelling (Vikhrev et al., 1993). He showed that the onset of the $m = 0$ instability to the plasma column is the source of intensive neutron emission. Based on a review of many theoretical and experimental investigations, they summarized that the neutron emission does not simply contributed by thermal and beam-target mechanism rather the neutron emission is shown to be correlated to the ion energy distribution (Vikhrev & Korolev, 2007)

Castillo et al. reported the evidence of thermonuclear and non-thermonuclear mechanism coexisted in the neutron productions (Castillo et al., 2000). Even in Filippov type plasma focus (Abdollahzadeh & Sadat, 2010) thermonuclear and non-thermonuclear mechanism were also observed. However, thermonuclear mechanism was observed to play the dominant role for the neutron production in Filippov type plasma focus.

Yap et al. (Yap et al., 2005) experimentally resolved the neutron emission was comprised of thermonuclear and non-thermonuclear reaction. She had observed two neutron emitting periods for discharge in pure deuterium and deuterium doped with argon mixture. In both discharges, second period was found to be highly anisotropy. Klir et al. (Klir et al., 2011) also reported two distinct neutron pulses from a PF 1000 facility. A fraction of 5 % from the total neutron yield was estimated to be thermonuclear origin. In spite of the neutron production mechanism has not being fully understood, yet it has been observed experimentally and widely accepted that the beam target is the predominant mechanism of neutron production from deuteron beam of 30 – 100 keV (Springham et al., 2000; Tiseanu et al., 1994).

3.5 Ion Beam Production Mechanism

Investigation on energetic ion beam emission is of vital importance that could provide us the useful information on the underlying physics regarding to their acceleration mechanism as well as developing the plasma focus as an efficient ion beam source. Despite significant efforts (Bernstein & Hai, 1970a; Castillo et al., 1997; Conrads et al., 1972; Gullickson & Sahlin, 1978; Haines, 1983; Springham et al., 2005) at various front either theoretical or experimentally has been taken but till date neither of the proposed models is in satisfactory agreement to explain the phenomena of formation and acceleration of ion beam. There are few models have been proposed to explain the ion acceleration mechanism which some of the important models are discussed here.

Some numerical works based on the crossed electric and magnetic field acceleration model to account for the ion trajectories in the pinched plasma has been reported by Bernstein and co-workers (Bernstein, 1970a, 1970b; Bernstein & Comisar, 1972). In this model, they assumed an axisymmetric radially varying current density where the azimuthal magnetic field and axial electric field vary as a function of the radial coordinate and ions move only in the axial and radial plane. Another important assumption made in his calculation is that the ion-ion collisions was assumed to be negligible in the acceleration phase. Significant numbers of deuteron shown to accelerate up to axial energies of 600 keV. The calculated ion trajectories could be accounted for the higher neutron yield and observed anisotropy due to beam-target neutron production.

In 1973, Imshennik et al. (Imshennik et al., 1973) attempted to relate the experimentally observed instability to the acceleration of ions based on magnetohydrodynamic (MHD) theory. He postulated that the constriction of plasma column could induced strong localized electric field by the evolution of $m = 0$ instability. The computed value of the potential difference that attained hundred thousands of electron volts by the induced electric field was consistent with the measured ions energy with the assumption of ions being accelerated at the boundary of the plasma column where the potential difference is the highest.

In the same year, Peter & Hohl (Peter & Hohl, 1973) modified the model developed by Bernstein (Bernstein, 1970a) to include axial electric field at the centre axis of plasma column. His numerical calculation for ion trajectories in three-dimensional space showed that the model is more realistic and effective in terms of energy transfer for all ions within a Larmor radius which is in accordance with experimental results. He later presented an extension by incorporating the factor of anomalous enhancement of resistivity caused by a micro instability (Peter, 1974). The model demonstrated the accelerated deuterons with large radial velocities but was insufficient to explain the acceleration of high energy ions. Anomalous resistivity was necessary to account for the ion-acoustic turbulence and Buneman two-stream turbulence.

Kondoh et al. using the crossed field acceleration model (Kondoh & Hirano, 1978) demonstrated the appearance of betatron-like acceleration process with negligible drift velocity in the collapse phase. This strong free-streaming acceleration process due to decreasing current density was shown to be the most efficient way of transferring energy to the ions resulted in high, axial velocity of ions during the expansion phase.

Zambreanu & Doloc (Zambreanu & Doloc, 1992) had proposed an empirical plasma model to describe the kinematic and dynamic of the ion trajectories. Ions were shown to gain a very small energy in the range of 10 - 20 keV in the collapse phase while gyrate with small drift along the anode axis. A strong acceleration process was observed during the expansion phase and evolution of $m = 0$ instability which produced high energy ions. Expansion of the plasma column was suggested as an important role for the acceleration process.

Lee et al. (Lee et al., 1971) suggested a converging ion model to account for the observed neutron energy and anisotropy. He compared the experimental measured neutron emission with the results predicted by the model and a fair agreement was obtained. In this model, he assumed a uniform ion density that converged into a neutron producing region which moving away from the anode surface. Centre of mass deuteron energies of 80 keV was required to give the measured total neutron yield of 1 x 10^{10} in converging ion model which is in good agreement with the measured average value of 53 keV.

Later, Tanimoto & Koyama proposed a possible mechanism that accelerated ions up to very high energy of the order of MeV based on resistive-ion acceleration model (Tanimoto & Koyama, 1982). He demonstrated that the induced electric field by rapidly changing inductance which is inductive in nature only provide weak acceleration to the ions. On the other hand, stronger axial electric field induced due to enhancement of resistivity by self-magnetic field can qualitatively explain the emission of high energy ions up to MeV. He shown that the ion acceleration by resistive electric field is 16 times more dominant than the inductive one.

Kondoh (Kondoh, 1984) has instead proposed a hybrid ion acceleration model based on rapid expansion of plasma column and anomalous resistance. In this model, ion acceleration up to MeV was possible with a short acceleration time of less than or near 1 ns and short acceleration length of about 1 mm. His simulation results showed that rapid expansion of plasma column was important for high energy production. In the experimental point of view, Yamada et al. (Yamada et al., 1985) suggested plasma diode mechanism is responsible for the production of higher energy deuteron up to 3 MeV. He had confirmed experimentally a structure of plasma diode formed just above the anode surface through ion pinhole images on Kodak CN 85 film. The efficiency of producing high energy ion beam of more than 330 keV was found to be less than 1 %.

Other ion acceleration models such as gyro-reflection acceleration model (Deutsch & Kies, 1988a) and gyrating particle model (Jaeger & Herold, 1987) were also proposed. It is suggested that gyro-reflection acceleration play the dominant role for neutron production in high current and high performance plasma focus device such as SPEED 2. This model was extended from the idea of free ion motion in dynamically induced electric field and supplementary field due to current sheath acceleration. There is experimental evidence showed that gyrating particle model is of better fusion efficiency compared to acceleration of ions due to instability.

CHAPTER 4: RESEARCH METHODOLOGY

4.0 Introduction

A Mather type plasma focus has been configured based on UNU/ICTP PFF machine (Lee et al., 1988) with objectives of producing plasma focus at low pressure and enhanced ion beam emission. This is achieved by scaling the length of the electrodes with the desired filling pressure using the selected electrical parameters. Deuterium was used for the entire experiments to produce deuterium pinched plasma. The plasma focus device consists of focus tube driven by a low inductance 30 μF Maxwell capacitor, charged to a voltage of 13.5 kV, which gives the maximum energy of 2.7 kJ. Upon discharge at 13.5 kV, the capacitor is capable of delivering a peak current up to 180 kA. The basic idea for the operation of this device is to utilize the high electric current to heat and compressed the prefilled gas that in turns creates a dense but short-lived fusion plasma. Basically, the plasma focus device consists of the other subsystems:

- Driver (high voltage charge, capacitor and high voltage transmission cable)
- Load (Focus tube, vacuum chamber)
- Switching system (Spark gap switch)
- Triggering electronics
- Evacuation system (Rotary pump, turbo molecular pump and valves)
- Dumping Switch
- Data Acquisition system (Digital storage oscilloscopes, computer and software package, screen room)
- Plasma diagnostics

4.1 Experimental Setup

4.1.1 Experimental Layout

The schematics of plasma focus device from different viewing directions are shown in Figure 4.1. Some of the major subsystems are also indicated in the figure.

a) Side View 1

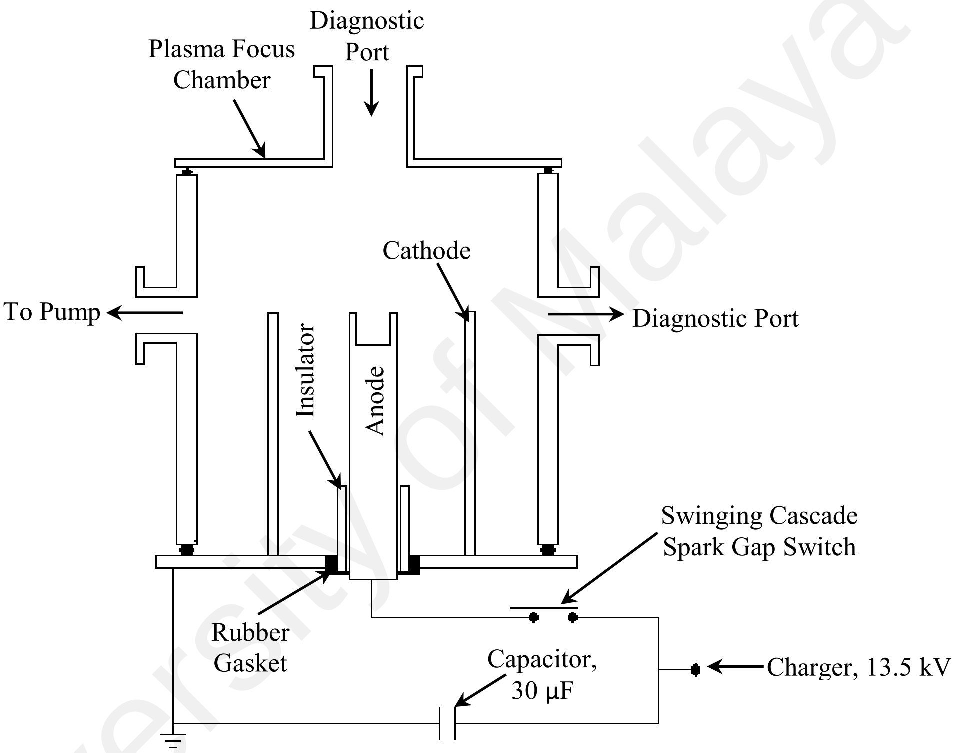

Figure 4.1: Schematic diagram of the Plasma Focus Device a) Side view 1, b) Side view 2, c) Top view

b) Side View 2

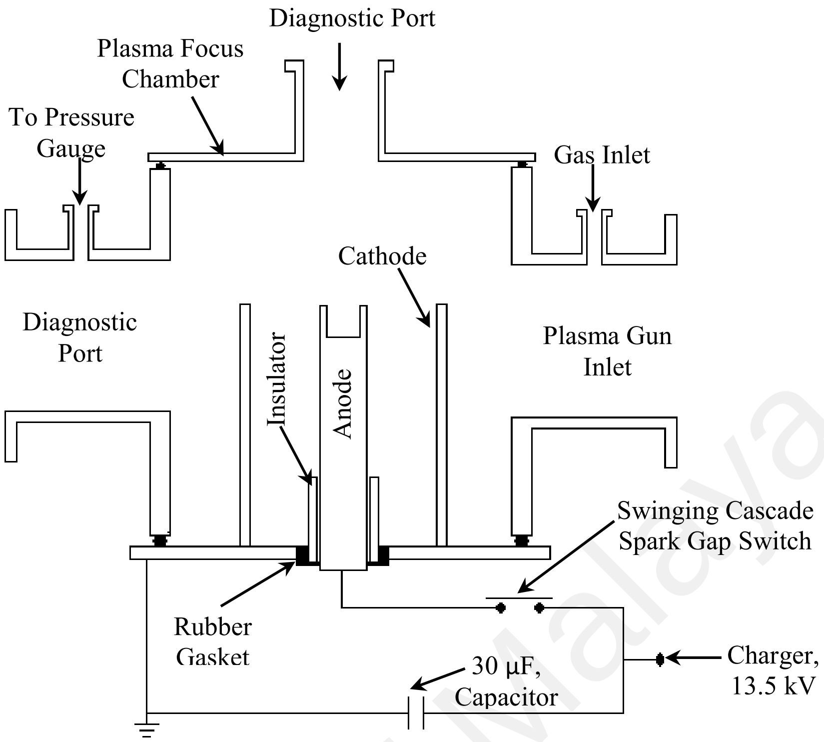

c) Top View

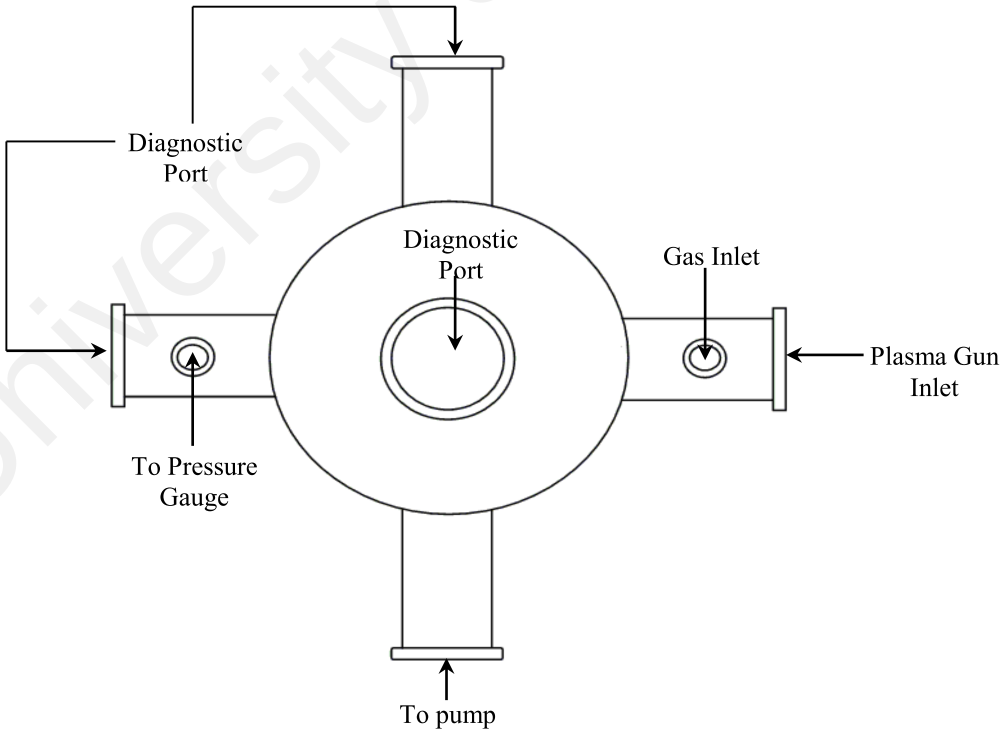

Figure 4.1: Continued.

The plasma focus tube forming part of the discharge load is immersed in a cylindrical chromed mild steel vacuum chamber of diameter 15 cm and 30 cm height. Several ports were welded onto the vacuum chamber for the diagnostic and evacuation purpose. The chamber is pumped to the base pressure of 10^{-3} mbar by means of high vacuum rotary vane pumps and flushes with the operating gas before experiments. The gas pressure inside the chamber is monitored by both Pirani gauge and Capsule-type dial gauge. The experimental layout for the plasma focus device with the sub systems can be summarized in a block diagram as illustrated in Figure 4.2.

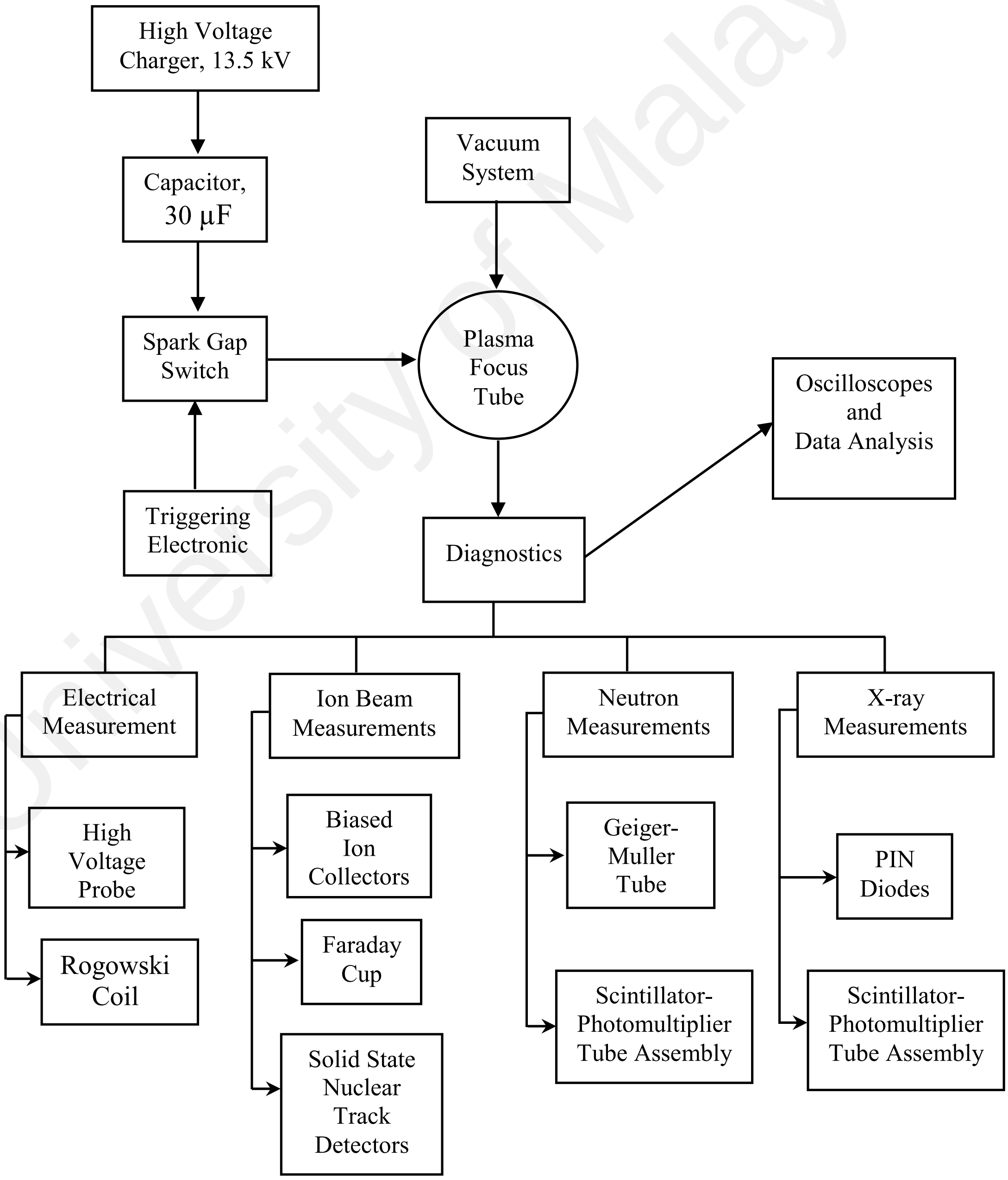

Figure 4.2: Block diagram of the experimental layout

To obtain a high current discharge in a plasma focus device, the total inductance of the system must be kept low while capacitance and charging voltage must be high. This is apparent from the relation based on the LCR discharge circuit given below as:

$$I_0 = V_0 \left(\frac{fC}{L} \right)^{1/2} \quad \textbf{(4.1)}$$

where I_0 is the peak discharge current, V_0 is the peak charging voltage, C is the total capacitance, f is the reversal ratio and L is the total inductance. However, increase the charging voltage to above the threshold of the capacitor breakdown voltage could lead to insulation problem in the circuit while the use of high capacitance but low inductance capacitor or more capacitors will increase the operation cost and synchronization difficulties. Thus, with the above mentioned constraint, a single low inductance oil filled (Maxwell) capacitor rated at capacitance of 30 μF and breakdown voltage of 15 kV with internal inductance of about 27 nH is used to power up the plasma focus device. The capacitor is charged up to 13.5 kV via a high voltage charger, which gives a maximum energy of 2.7 kJ upon discharged.

The energy is transferred from capacitor into the focus tube by means of spark gap switch. Despite there are various type of high current switches available but spark gap switch (Mankowski & Kristiansen, 2000) is preferable due to its reliable and consistent performance over a wide range of voltages, cost effective, fast response with low jitter and maintenance free even after few hundred of shots. In this work, a simple parallel plate spark gap in a swinging cascade design (Smith et al., 1986) capable of switching 280 kA with jitter within 50 ns has been used as a switch to transmit high current pulse from the capacitor. The ratio of the gap is set at 3:2 (4.5 mm: 3 mm) which is suitable for the operating voltage (13 - 15 kV) in the plasma focus device.

Another important part of the experimental setup is the triggering system. It is required to generate a pulse with very sharp rise and fall times in order to trigger the spark gap switch for best switching performance. The schematic diagram of the triggering system including spark gap switch and focus tube is depicted in Figure 4.3. As a safety precaution to the experimenter, a dumping switch is employed in conjunction with the triggering system such as to dump the charge from the capacitor in case of failure or improper discharge.

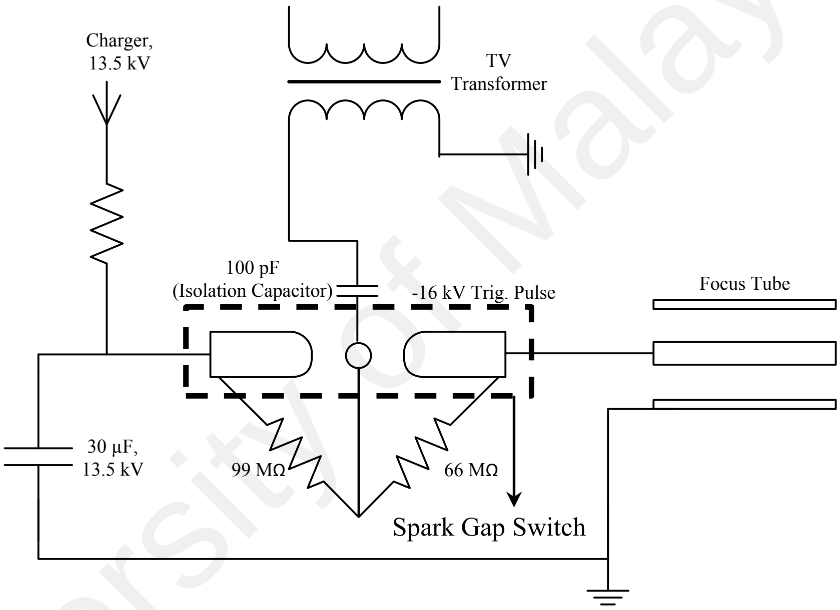

Figure 4.3: Schematic diagram of arrangement for the driver, load and triggering system

4.1.2 Data Acquisition and Experiments

For the data acquisition, all the time resolved signals obtained from various diagnostic tools are recorded by digital oscilloscopes. For the purpose of time correlation measurement, all the signals has been obtained simultaneously. Thus, there are few oscilloscopes need to be occupied at one time and all the oscilloscope signals were properly synchronized for time correlation purpose.

For the purpose of recording the transient phenomena that occur in a plasma focus discharge, digital oscilloscope include 8 channels Yokogawa model DL 7480 of 2 GHz sampling rate with 500 MHz bandwidth, 4 channels Yokogawa model 6104 of 5 GHz sampling rate with 1 GHz bandwidth and 4 channels Tektronix model DPD 4034 of 2.5 GHz sampling rate with 350 MHz bandwidth have been used. With this data acquisition system, the time resolution that can be achieved is better than 1 ns. All the signals obtained with oscilloscope was process and analyzed using Microsoft Excel software and OriginPro 8.0.

The high rate of change of current during a focusing discharge generates high electromagnetic noise which in turns could reduce the signal-to-noise ratio in the measured electrical signal. Thus, all the data acquisition system such as oscilloscope and Geiger-Muller counters has been shielded against this electromagnetic noise. This is done by putting all the acquisition system in a screened room (Faraday cage). This room is earthed through a copper strip of low inductance and connected to the main earth. All the electrical signals are then transmitted to the screen room via noise shielded coaxial cables.

4.1.3 Plasma Focus Tube

The plasma focus tube is a set of coaxial electrodes assembly consists of six equally spaced outer electrodes (cathode) arranged concentrically around an inner electrode (anode) with diameter of 6.4 cm as shown in Figure 4.4. The design is of the Mather-type plasma focus.

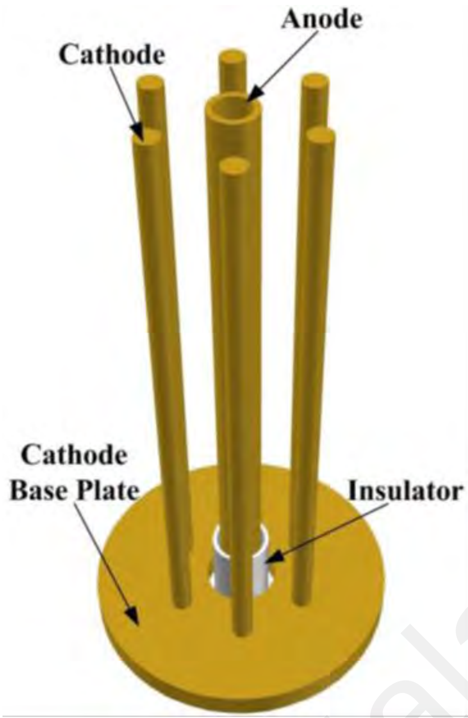

Figure 4.4: Schematic diagram of the plasma focus tube

Both electrodes are made out of solid copper rods with 22 cm in length but the anode has been engraved to 4 cm deep at the truncated end. This is to reduce the contamination caused by the ablation of electron beam on the anode surface (Ngoi et al., 2012) and also the copper line radiation (Zakaullah et al., 2001). The diameter of the rod used for anode and cathode is 19 mm and 9.5 mm, respectively. The anode is electrically insulated from the cathode behind the back wall with the use of Mylar and Perspex sheets together with a silicon rubber gasket which holds one end of the insulator at the centre. A piece of copper base plate has the design of circular knife edge surrounding the glass insulator is used to mount the cathodes.

The glass insulator used in this work is made of cylindrical Pyrex glass of 50 mm long with outer diameter of 26 mm and 2 mm thick. Due to low pressure operation, a set of delayed triggered plasma gun is in-cooperated in the system. The plasma gun is made of six pairs of microwave cable (RG405U) surrounding around the cathode circumference in order to enhance the initial breakdown of the current sheath at the surface of glass insulator. The performance of the plasma gun has been investigated separately in other device with ICCD camera. Geometrical parameters for the plasma focus tube is given in Table 4.1.

Table 4.1: Geometrical parameters of Plasma Focus Tube

Parts	Length (mm)	Diameter (mm)	Material
Anode rod	220	19	Copper
Cathode rod	220	9.5	Copper
Insulator Sleeve	50	22 (*I.D*)	Borosilicate glass (Pyrex glass)
Plasma Focus Chamber	300	150	Chromed mild steel

4.1.4 Vacuum System

The experiments required the focus tube to be filled with deuterium for pressure of 0.1 mbar to 1.0 mbar. Thus, the vacuum system has been improved as this is relatively stringent compared to conventional operating pressure of several mbars. The focus tube is operated in low pressure of less than 1.0 mbar by a rotary pump. The system is always filled and kept at a low pressure when not in operation. Evacuation up to base pressure of 10^{-3} mbar can be achieved after half hours of pumping. We believe this is sufficient to get rid of most of the impurities in the chamber before the first discharge is performed.

On the other hand, a drift tube was installed at the end on direction on top of the focus chamber for ion beam measurement. The drift tube is differentially pumped and separated from the focus chamber by a gating valve. The pressure inside the drift tube is evacuated to below 10^{-4} mbar with the aid of turbo molecular pump. This is so as to reduce the perturbation of the ambient gas to the ions trajectory. The pressure in the drift tube is read out by an Edwards CP25EK Penning Gauge Head.

4.2 Discharge Current Measurement

4.2.1 Rogowski Coil

Measurement of the discharge current has always being one of the fundamental diagnostic in the plasma focus device and serves as the indicator of gross performance of the focusing plasma. Thus, a diagnostic having fast response to the transient discharge while not create any perturbation to the plasma is required. One of such passive diagnostics which is specially designed to measure the pulsed discharge current is Rogowski coil named after Walter Rogowski. It is essentially a multi-turn solenoid wound on an insulated wire which is bent into the shape of a torus.

The reason for choosing Rogowski coil over other types of current transformer is that it can be made open-ended and flexible, hence conveniently measure a fast time varying current based on the principle of Faraday's law of electromagnetic induction. Furthermore, the sensitivity of Rogowski coil is independent of its position as long as it is topologically equivalent to a torus enclosed around a live conductor (Leonard, 1965). The coil is insulated in a plastic piping hose and placed at the backwall of the plasma focus device surrounding the inner electrode. The Rogowski coil is terminated with a low inductance resistor with $r \sim 0.1$ ohm to function as current transformer as shown in Figure 4.5. In this way, the potential difference induced across the resistor r is proportional to the discharge current going through the coil. Without the termination, it is only measure the rate of change of the discharge current dI/dt.

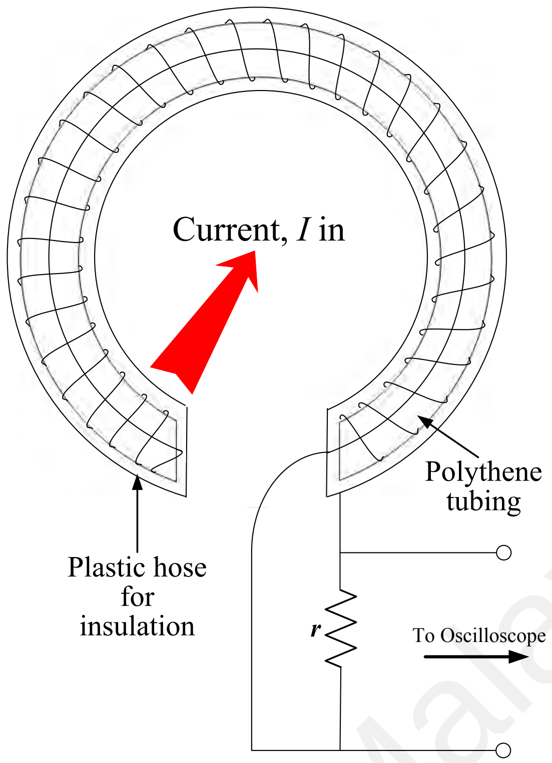

Figure 4.5: Schematic design of Rogowski coil

The way of Rogowski coil work as current transformer can be interpreted from the equivalent circuit illustrated in the Figure 4.6.

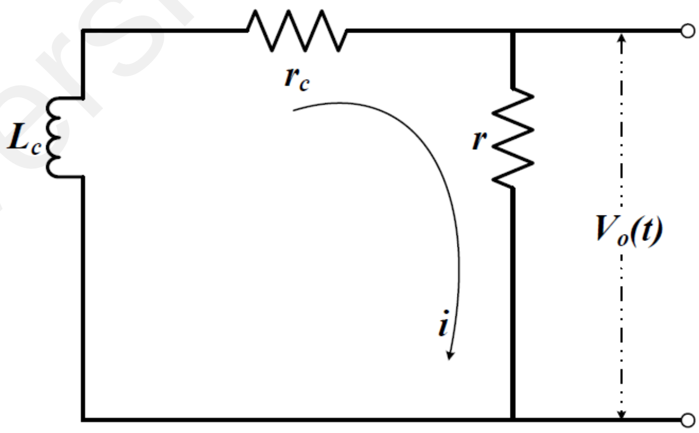

Figure 4.6: Equivalent circuit of Rogowski coil as current transformer

The purpose of using very low inductance resistor with very small resistance is to fulfill the condition of $\omega L_c >> (r_c + r)$, where ω represent the frequency of the varying discharge current, L_c is the inductance of the coil and r_c is the resistance of the coil.

Such criterion is needed to ensure that the diagnostic tool is at sufficient high resolution to measure a fast time varying current. The equivalent circuit equation can be written as:

$$\frac{d\phi}{dt} = L_c \frac{di}{dt} + i(r_c + r) = k\frac{dI}{dt} \qquad \textbf{(4.2)}$$

where ϕ is the magnetic flux, i is the induced current in the coil, k is a constant and I is the discharge current flowing through the coil.

When $L_c \frac{di}{dt} >> i(r_c+r)$, then from Equation 4.2 one can obtain $i = k\frac{I}{L_c}$ since

$$L_c \frac{di}{dt} = k\frac{dI}{dt} \qquad \textbf{(4.3)}$$

Thus, the output voltage across the terminal is also proportional to discharge current, I going through the coil which can be expressed as:

$$V = ir = (k\frac{I}{L_c})r$$

$$= \frac{kr}{L_c} x\ I$$

$$= KI \qquad \textbf{(4.4)}$$

where K is the calibrating constant of the Rogowski coil. The procedure to obtain the constant K will be discussed in following section.

4.2.2 Calibration of Rogowski Coil

In order to measure the absolute value of the discharge current, the Rogowski coil has been calibrated by using an in-situ method. The calibration is done by discharge the plasma focus at high pressure of 25 mbar in deuterium filling. The measured discharge current resembled an underdamped LCR discharge waveform. By considering the conservation of charges flowing in and out from capacitor, the first peak current I_0 can be expressed in following equation below (Lee, 1969):

$$I_0 = \frac{\pi C_0 V_o (1+f)}{T} \qquad \textbf{(4.5)}$$

where C_0 = capacitance of capacitor

V_0 = initial charging voltage

f = reversal ratio of the current peak

T = Period of current discharge

The value of f and T can be obtained from discharge current waveform. Practically, it is advised to take the average value of the reversal ratio from several consecutive current peaks. For instance,

$$f = \frac{1}{4}\left(\frac{V_5}{V_4} + \frac{V_4}{V_3} + \frac{V_3}{V_2} + \frac{V_2}{V_1}\right) \qquad \textbf{(4.6)}$$

where V_1, V_2, V_3 and so on are the first and consecutive peak value on the measured current waveform.

Similarly, period time T also determined by averaging over several cycles. Once the value of the first current peak, V_1 and peak discharge current, I_0 is obtained, the calibration constant of the coil can be determined and express as:

$$K = \frac{I_0}{V_1} \text{ A/volts} \qquad \textbf{(4.7)}$$

A typical short circuit signal of deuterium discharge at 25 mbar is given in Figure 4.7.

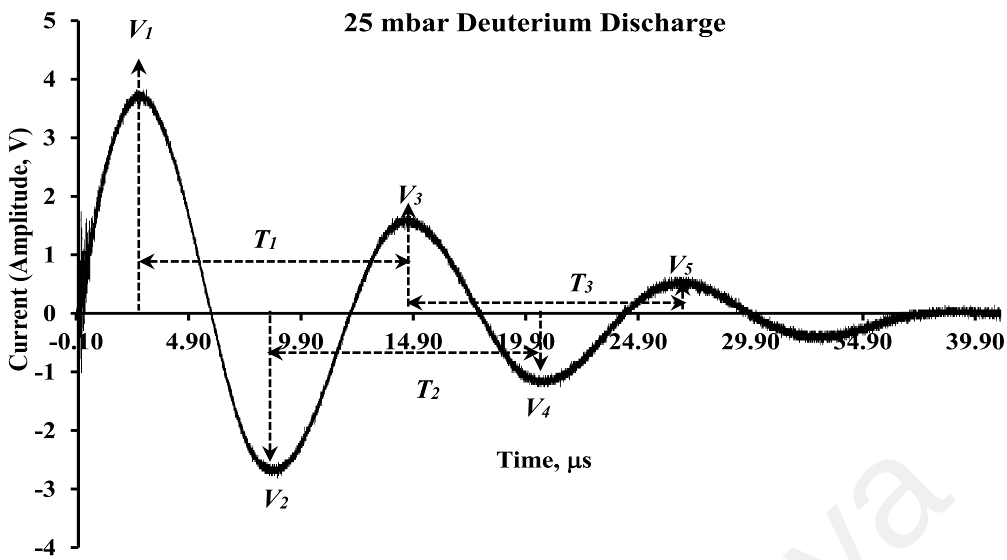

Figure 4.7: Typical short circuit signal (25 mbar deuterium discharge)

The calibration constant for the Rogowski coil used in present experiment has been determined to be about K = 48 kA/V for signal attenuated by a 10 times attenuator. The value has been calculated by averaging over 5 short-circuited discharges. It is worthwhile to mention that the measured discharge current with Rogowski coil provides not only the plasma dynamics but can also yield other important information such as electrodynamics and thermodynamic properties in the various phases of the pinching dynamics when fitted the measured current waveform against computed current waveform using Lee model code.

4.3 High Voltage Probe for Transient Voltage Measurement

The technical challenge in the measurement of transient voltage across the plasma focus device is due to the requirement of fast response diagnostic probe. Various types of high voltage probe has been developed for such purpose (Leonard, 1965). In this work, the transient voltage across the focus tube and plasma during the whole discharge process is monitored with a homemade resistive high voltage probe working based on the principle of voltage divider as shown in Figure 4.8.

Resistive high voltage probe was chosen due to its simplicity in design, low fabrication cost and fast response to discharge voltage with frequency in the order of 80 kHz. It is made up of ten 510 Ω/1W resistors connected in series shunted by a 51 Ω resistor at one end of the chain. The chain of resistors is enclosed in a copper tube of 20 mm diameter shielded by PVC pipe. The amplitude of the discharge voltage is measured across the 51 Ω shunting resistor which is further attenuated by a 10 times attenuator with the characteristic impedance of 50 Ω before transmit the signal from coaxial cable to the oscilloscope. A frequency response of better than 15 ns with rise time of approximately 2 ns has been achieved in our homemade high voltage probe.

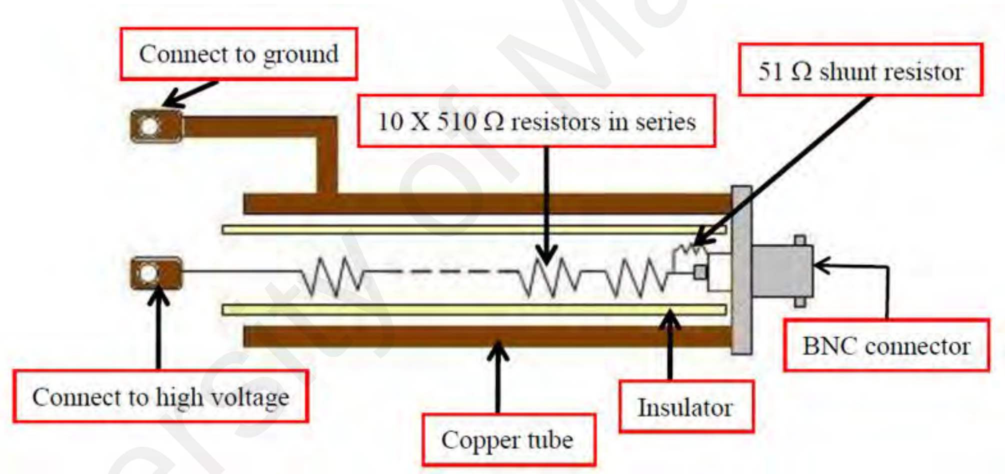

Figure 4.8: Schematic diagram of high voltage probe

4.4 Ion Beam Measurement

Several diagnostic techniques are developed for the measurement of ion beam characteristic with sufficiently high resolution over a wide energy range. However, there is no one simple design that can fulfil the measurement of the all the characteristics of ion beam emission such as time profile, beam energy, beam fluence, beam flux, etc. Biased ion collector, Faraday cup, magnetic analyser, nuclear track detectors and Thomson spectrometer are commonly used for this purpose. Each of this diagnostic has its own constraint and advantages. For example, biased ion collector and Faraday cup can be used to provide time history of the ion beam emission but not possible to exclusively determine the ion energy spectra. For nuclear track detectors, the etching process is time consuming and the threshold energy for ion beam detection need to be overcome. On the other hand, magnetic energy analyzer and Thomson spectrometer can resolve higher ion beam energy but cannot provide time history of the ion beam emission. Furthermore, the construction of such diagnostic and its operation is highly complicated.

4.4.1 Biased Ion Collector

Biased ion collectors were used for the time of flight ion beam measurement. Such detector is simple in construction and cost-effective having sufficient time resolution for ion beam detection over a wide energy range from several keV to hundreds of keV. The ion collector is essentially made from a piece of copper disk as the charge collector and negatively biased to certain potential, which is then called as biased ion collector as shown in Figure 4.9.

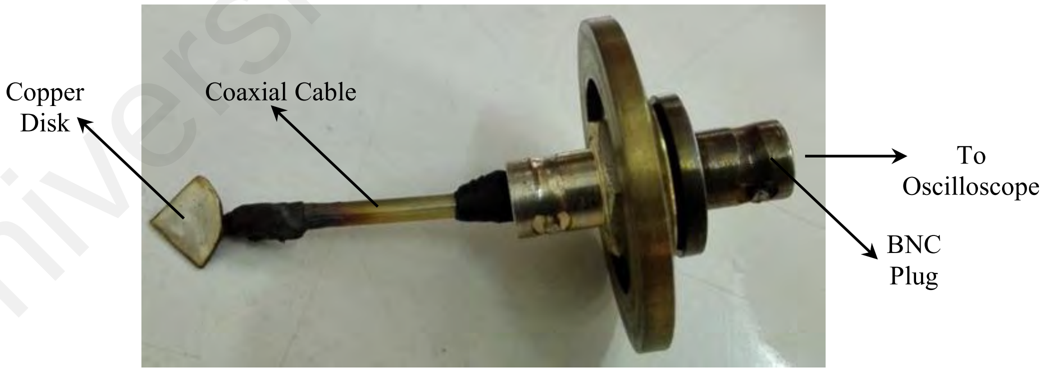

Figure 4.9: Picture of the biased ion collector

The output of the biased ion collector is fed to an oscilloscope via coaxial cable connected to a biasing circuit to record the ion beam signal. The purpose of the biasing circuit is to provide the negative biasing potential to the biased ion collector. This is to screen out the electrons accompanying the incoming ion beam and secondary electron emission due to photoelectric effects having equivalent energy of the potential or lower so that these electrons do not contribute to ion beam signal. A schematic of the biasing circuit is given in Figure 4.10.

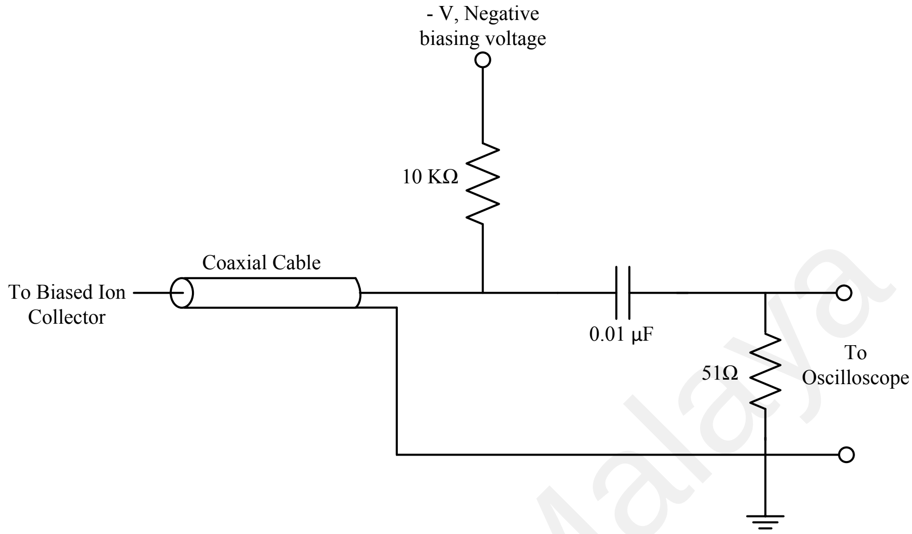

Figure 4.10: Biasing circuit for biased ion collector

The working principle of the biased ion collector is very simple. Upon pick up of charged particle on the detector which is negatively biased, a current will be induced in the circuit and a corresponding voltage generated across the resistor 51 Ω in the biasing circuit is registered as a pulse on the oscilloscope. The voltage is proportional to the flux of the registered ion beam. In this work, two biased ion collectors have been employed for the time of flight measurement to detect the axial ion beam emitted from plasma focus discharge. It is worth to mention that at least two biased ion collectors are suggested to give a time resolved signals for the estimation of the kinetic energy of ion beam.

All the biased ion collectors are installed inside a differentially pumped drift tube along the end on direction of the anode. The pressure inside the drift tube is kept below 10^{-4} mbar with the aid of turbo molecular pump. The drift tube is attached to the top plate of the plasma focus chamber separated by an aperture and gating valve. The purpose of the aperture is to reduce the contamination by the strong shock wave during ion beam detection. It also reduces the equalization of pressure upon open up of high vacuum valve due to pressure difference between the plasma focus chamber and drift tube. The biased ion collectors are arranged in such a way that the subsequent detector does not block the previous detector. The first and second biased ion collector is located at 30.5 cm and 57 cm from the anode tip. All the biased ion collectors are negatively biased to 15 V by DC power supply units.

The first biased ion collector is made from an octant of 2 cm diameter copper disc while second biased ion collector is made of quadrant of a 2 cm diameter copper disc. The area of biased ion collectors from nearest to farthest is 3.93 x 10^{-5} m^2 and 7.85 x 10^{-5} m^2. Schematic arrangement of the biased ion collectors in the differentially pumped drift tube is demonstrated in Figure 4.11.

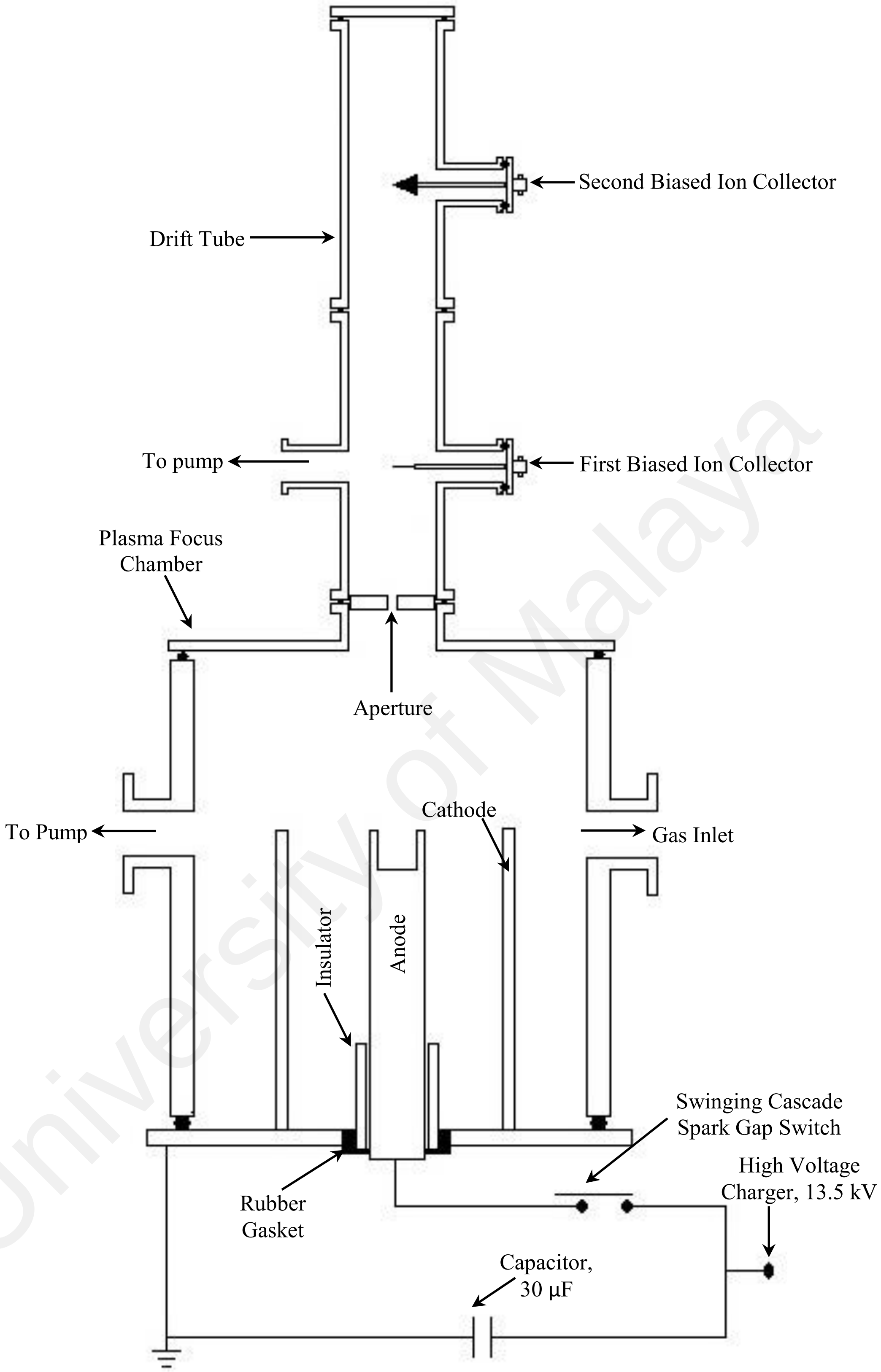

Figure 4.11: Schematic arrangement of the biased ion collectors

4.4.2 Faraday Cup

In the present work, a Faraday cup was employed for the determination of ion beam fluence and number of ions per shot. Nevertheless, it also used for the energy measurement of the ion beam emission. Faraday cup is another type of simple and inexpensive charge collector which generally consists of a small aperture and a plain metal plate. Faraday cup was chosen due to its fast response for charged particle detection but it do have some demerits such as low signal to noise ratio and the secondary electron emission from the collector surface due to impinging charge particles. The Faraday cup fabricated for ion beam measurement was made of a copper disk as the charge collector, which is used in unbiased mode. A flat circular copper disk of diameter 1 cm diameter is used and enclosed by a metallic cylinder tube as shown in Figure 4.12. Diameter of the copper disk is limited by the inner diameter of the cylinder tube. A small extraction hole was made on the cylinder tube with diameter of 1 cm in front of the disk that allows registration of the axial ion beam. Similarly the output of the Faraday cup was fed into the oscilloscope through coaxial cable without the biasing circuit.

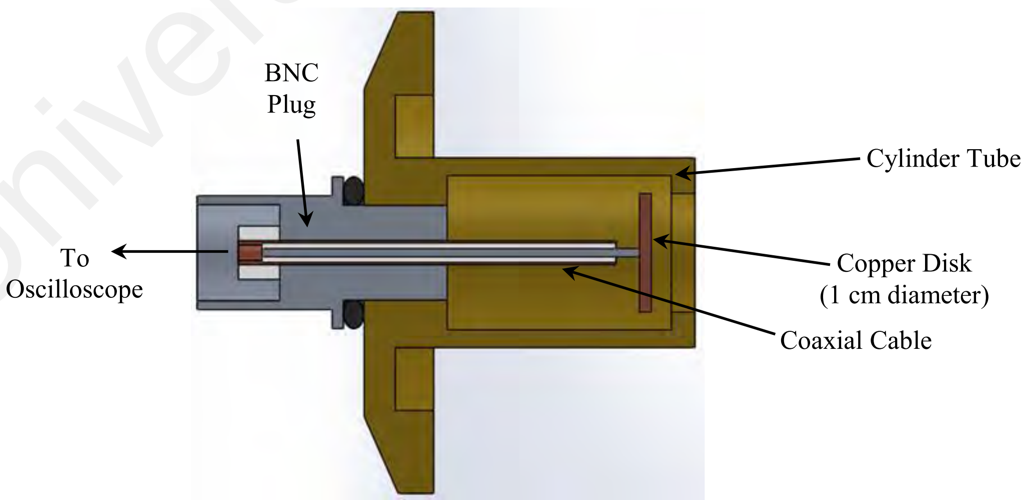

Figure 4.12: Diagram of Faraday cup

The working principle of the Faraday cup is same as the biased ion collector where it also can register ion beam energy from a threshold value of few keV to hundreds of keV. A voltage pulse will be registered on the oscilloscope when a beam of charged particles incident on the grounded metal plate. The difference between Faraday cup and biased ion collector as described in previous section lies on the design of Faraday cup being relatively destructive to ion beam trajectory. In other words, only one Faraday cup can be mounted at the end of the drift tube thus limit the arrangement for multiple detectors time of flight measurement.

The Faraday cup was installed on top of the drift tube at the end on direction as shown in Figure 4.13. The pressure inside the drift tube was kept below 10^{-4} mbar by using a turbo molecular pump backed by rotary vacuum pump. The drift tube is separated from the plasma focus chamber with a gating valve and an aperture of 2 mm diameter. Distance of the Faraday cup from the anode tip is about 40 cm.

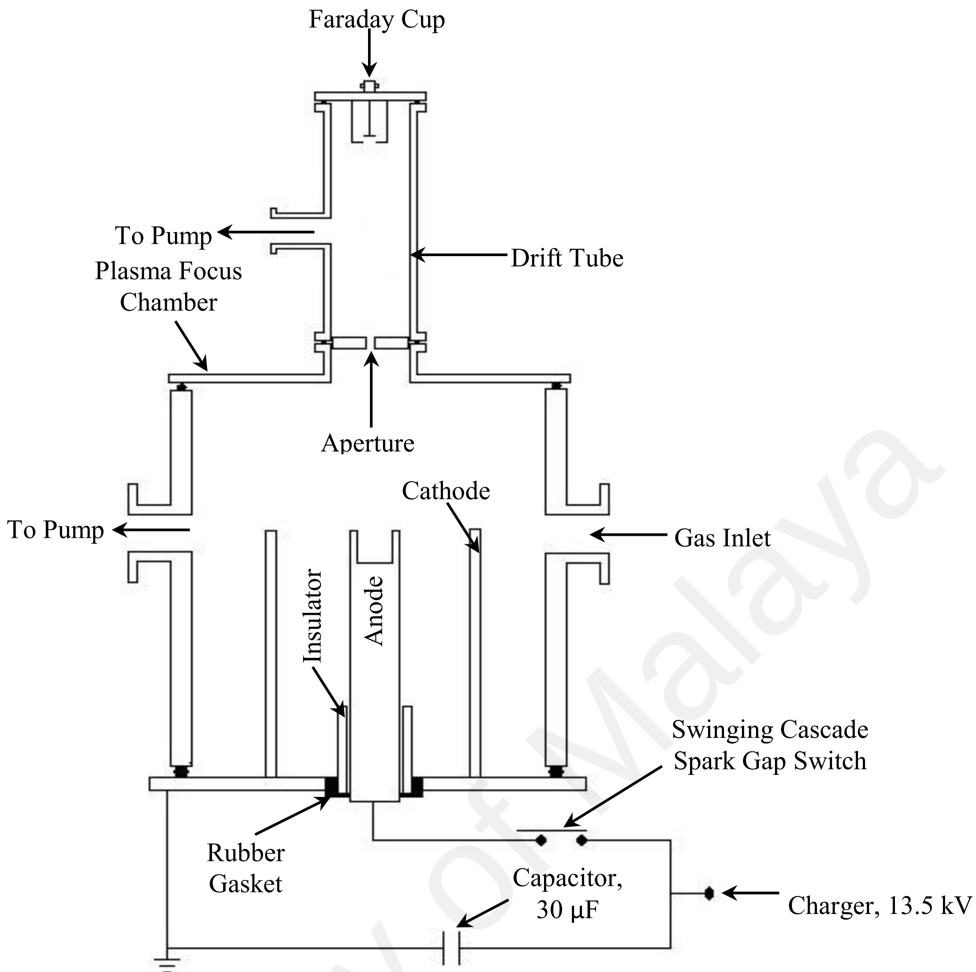

Figure 4.13: Schematic arrangement of Faraday Cup for ion beam measurement

4.4.3 Solid State Nuclear Track Detectors (SSNTD)

Solid state nuclear track detectors (SSNTDs) such as LR115, PM-355, PM-600 and CR-39 (Malinowski et al., 2005; Skladnik et al., 2001; Skladnik et al., 2005; Szydłowski et al., 1999) has been widely used for ion beam detection particularly due to its advantage of being relatively insensitive to electromagnetic radiation. However, time resolved information of the emission is usually not available with such detectors. This diagnostic technique belongs to the group of static or passive detector which gives permanent record of the incident ion beam where information of the incident ion beam is typically analyzed by counting unsaturated tracks using optical scanning. Thus, an extra care must be taken to avoid the detector being overexposed to ion beam irradiation or over etched.

In our work, CR-39 nuclear track detector was used to register the ion beam emitted from the focusing discharge. CR-39 is a clear, transparent, rigid plastic with a density of 1.3 g/cm^3, chemical formula $C_{12}H_{18}O_7$ and is made out from the material of polyallyl diglycol carbonate (Gaillard et al., 2007). CR-39 detector was chosen due to its relative advantage of high sensitivity and ability to detect single ions of very wide energy range (100 keV to few MeV) whereas low sensitivity towards electrons and electromagnetic radiation.

A) Principle of ion track formation

When a charged particles is incident on the detector, the transfer of their energy to the stopping medium damage the bulk material leaving etchable tracks. However, this latent damage trails are not able to visualize with unaided eye. Therefore, the exposed detector has to be specially treated with a suitable chemical reagent that attack preferentially the material around the damage trails to form a cylindrical or a cone-shaped hole tracks. Such technique to amplify the damages and produces an observable tracks to be conveniently visualized under an optical microscope is called as etching. For an optical microscope examination, the track size must be of the order of or greater than an optical wavelength. Usually, a track diameter typically of 1 – 2 μm is sufficient.

Fleischer et al. (Fleischer et al., 1965) proposed in 1965, a mechanism for track formation in solids. They suggested that for a heavily ionizing particle travelling through a polymer, the tracks are formed due to breaking of the polymeric bonds in the plastic. The electrons are removed from their initial position in the bulk material (electron defect), leaving a narrow cylinder which is densely filled with excess of positive ions in its wake. These ions strongly repel one another which drive them into interstitial positions surrounding a now depleted core region. Such narrow regions of atomic defects (lattice vacancies, interstitial, etc.) or broken molecular chains is known as latent damage trails.

The transformation of latent damage trails to a visible track is determined by the simultaneous action of two etching process, named as material etching rate, V_M and track etching rate, V_T. Both the etching rate is defined in the unit of micrometer per hour. The damaged material around the track is etched more rapidly than the undamaged material since the track region being more chemical reactive. In other words, the undamaged bulk material is removed with a slower rate than the damaged region. The material etching rate and track etching rate strongly depends on the types of track detectors, concentration of etching solution and the temperature of solution. In addition to that, track etching rate also depends on the energy loss of the ion.

The geometry of the ion tracks formed is dependent on the incident angle of the particle on the detector (Durrani & Bull, 1985). For the case of normally incident particle, the track geometry is illustrated in Figure 4.14. During the etching process, the undamaged material is etched equally in all directions on the plastic surface at the rate of V_M, whereas the damage trail is etched at the rate of V_T. Thus, after an etching time t, the undamaged surface has been removed by an amount $V_M x\ t$ whereas the damaged region was removed by an amount of $V_T x\ t$. Because of these two simultaneous action but at different etching rates, a conical hole etch track is resulted in the surface at the position of particle impacts (Figure 4.14).

The length of the track is then given by:

$$L = (V_T - V_M)\ t \quad \textbf{(4.8)}$$

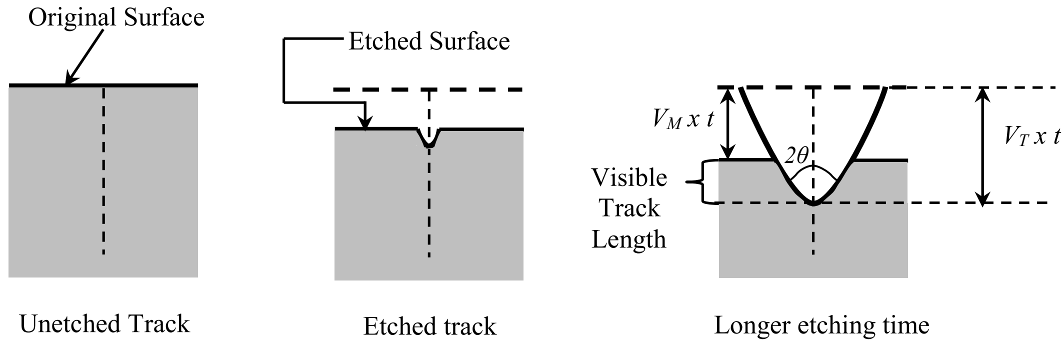

Figure 4.14: Schematic presentation of track etching geometry for normally incident particle

There is a critical angle to be considered for an obliquely incident particle as illustrated in Figure 4.15. For all the incident angle less than the critical angle, θ_c, there will be no observable track even after etching. This happens because of the smaller track etching rate V_T for the component perpendicular to the detector surface than the material etch rate V_M for the incident angle less than critical angle. The critical angle is found by taking the condition of $(V_T x\ t)sin\theta_c = V_M x\ t$ and given as:

$$\theta_c = sin^{-1} (V_M/V_T) \quad \textbf{(4.9)}$$

where V_M is material etch rate and V_T is track etch rate.

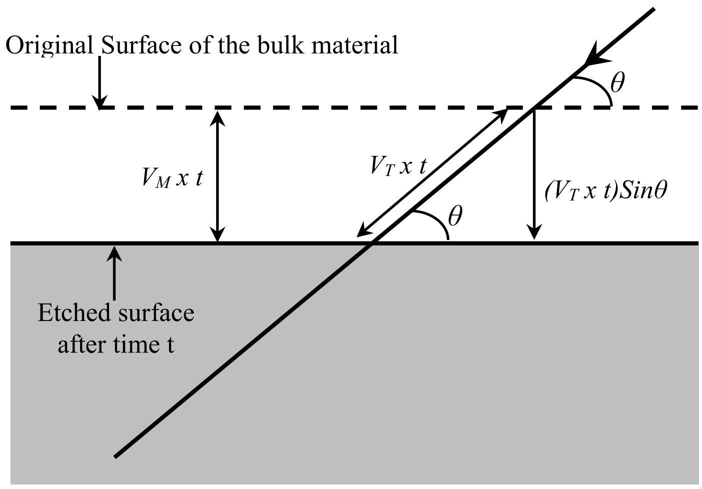

Figure 4.15: Schematic presentation for the phenomenon of critical angle (When component of the track etch rate $(V_T\ x\ t)\ Sin\ \theta = V_M\ x\ t$, the angle θ is called the 'critical angle' which denoted as θ_c)

Nevertheless, the depth and size of the ion track is also dependent on the nuclear atomic number *Z*, particle energy, nuclear charge and nuclear mass (Gaillard et al., 2007). For a given nuclear atomic number *Z*, higher particle energy results in a greater penetration depths. For a given particle energy, the penetration depths increases with a decrease in atomic number *Z*. For particle of same nuclear charge, increase in mass results in larger track diameter. In other words, heavier isotopes will leave a larger tracks.

B) Etching procedure

In this work, all the exposed CR-39 to ion beam irradiation was etched with aqueous solution of 6 *N* (moldm^{-3}) NaOH and maintained at temperature of 60 ^{o}C with a temperature stabilized water bath. The etched detectors were cleaned in an ultrasonic bath using deionized water for 30 minutes. There are few precaution steps need to be taken in handling the plastic track detector, CR-39. The detector should all the time handle with the use of gloves because accidently touches a detector with bare hand could sometimes leave a permanent mark on its surface. These marks are difficult to be removed which in turns obscure the viewing of the tracks. It is advised to use fresh etchant for each etching especially after a prolonged used of the etchant for a long hour. This is because the built up of high concentration of the etch product after previous etching could degrade the etching efficiency. After the etching process is done, the detectors are necessary to be washed in an ultrasonic bath using fresh deionized water for the removal of the etchant molecules from the inside of the etched track.

4.4.4 Angular Distribution Measurement

The characterization of ion beam angular distribution from the focus region was carried out with the use of solid state nuclear track detectors, CR-39. CR-39 detector of dimension 1 cm x 1 cm and 1 mm thick was employed. A set of CR-39 nuclear track detectors were fixed to a semicircular holder inside the chamber at four angular positions of 0^o (end on), 30^o, 60^o and 90^o (side on) relative to the anode axis. All the detectors were housed inside a small cylindrical brass container with an opening for ion beam entrance and placed at same radial distance of 5.7 cm from the anode tip. These arrangements could help to justify the area due to ion beam bombardment without saturated the ion tracks and also protecting the detectors from contamination by plasma jet. A shutter made of aluminium strip of 0.6 mm thick was used to isolate the detectors from the ion beam irradiation during the conditioning shots.

The imaging of the ion tracks formed on CR-39 detector at each angular position was done using optical microscope interface with computer. Thus, counting and measurement of the ion tracks such as diameter, area and circumference were done using the interface program (Motic image). The optical microscope is equipped with five objective lens of different magnification power of X40, X100, X400, X500, X1000. Counting of the number of ion tracks formed at different angular position provides a quantitative measurement of the ion beam angular distribution as well as ion beam anisotropy. A schematic of the experimental setup for angular distribution measurement of ion beam emission is depicted in Figure 4.16.

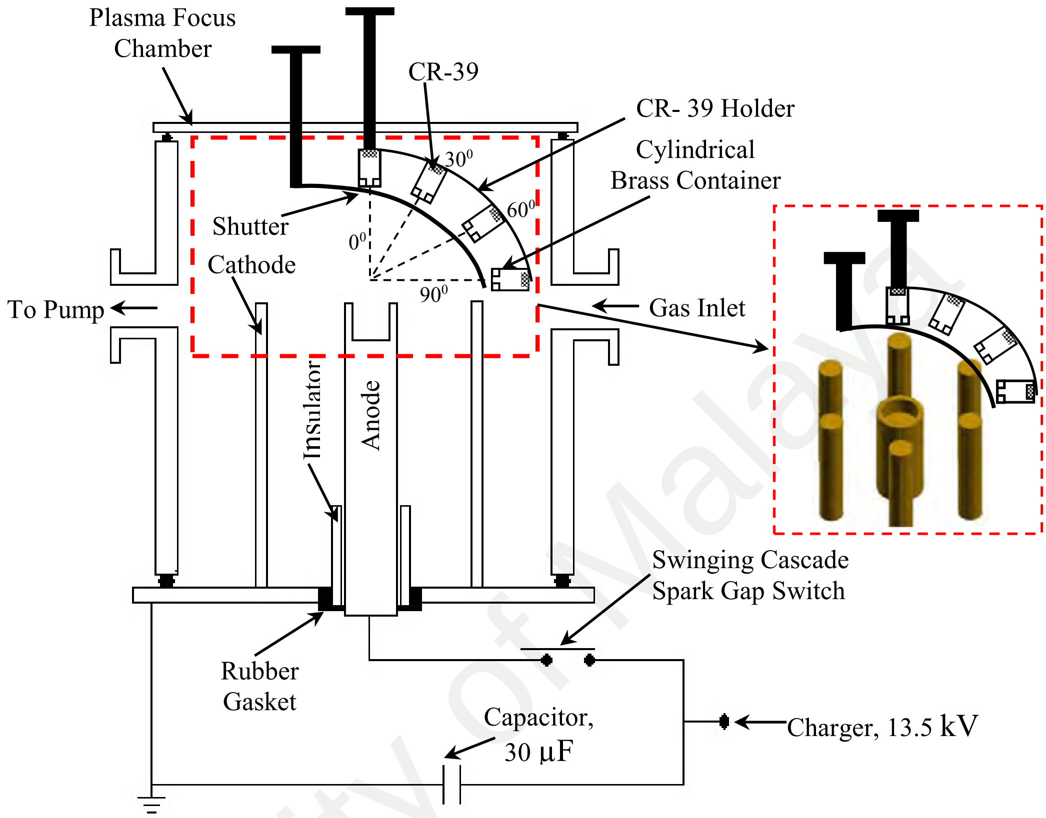

Figure 4.16: Experimental setup for measuring ion beam angular distribution

4.5 Neutron Measurement

4.5.1 Time Integrated Neutron Yield (Principle of Neutron Measurement)

The pulsed neutron emission from the focusing discharge is usually measured using metal foil activation technique to determine the number of neutrons per burst. Measurement of neutrons emission was done outside the chamber since the neutrons can penetrate relatively freely through the chamber and reached to the detector located outside. The fast neutrons emitted from the pinched plasma are first to be slowing down (thermalized) by a paraffin block before being allowed to activate the metal foil. This thermalization process is necessary as to increase the activation cross-section of the neutrons. The activated foil is then decay by emitting radioactive particles which the induced activity can be measured by a suitable counting system. The emitted radioactive particles are linearly proportional to the number of neutrons activate with the foil, thus providing an integrated neutron yield.

Usually, indium or silver foil is conveniently used in neutron yield measurement (Kubes et al., 2006; Michel et al., 1974; Yap et al., 2005). Selection of the activation foil is based on the consideration of desired energy response, magnitude of neutron emission, irradiation time and half-life of the nuclides. In this work, the neutron yield was measured using indium foil activation technique. For the case of indium foil, natural indium consists 95.8 % of ^{115}In and 4.2 % of ^{113}In. The thermal neutron activation cross section for ^{115}In is higher than ^{113}In which is 202 barns and 57 barns, respectively. Thus, we will only consider the dominant activities due to the decay of ^{115}In. The activated indium decays and producing beta particles in two schemes, one of which has 14 seconds half-life and the other has a 54 minutes half-life given as below:

$^{115}\text{In} + n \rightarrow {}^{116}\text{In} \rightarrow {}^{116}\text{Sn} + \beta^-$ (W_{β^-} = 3.29 MeV; $T_{1/2}$ = 14 seconds)

$^{115}\text{In} + n \rightarrow {}^{116m}\text{In} \rightarrow {}^{116}\text{Sn} + \beta^-$ (W_{β^-} = 1 MeV; $T_{1/2}$ = 54 minutes)

The beta activities of the decay scheme are detected using a thin wall Geiger Muller tube and counted by a scalar counter. Due to shorter half-life, it is thus more convenient to work with the 14 seconds decay scheme. Our time integrated neutron yield detection system consisted of a Victoreen 1B85 thin wall Geiger Muller tube wrapped with indium foil of 0.5 mm thick and connected to a scalar counter of model Labtech BICRON analyzer. The GM tube wrapped with indium foil is housed in a 4 cm thick hydrogenous paraffin hollow cylinder of 10 cm height for neutron thermalization.

The counting period of the Geiger Muller tube was set to 96 seconds immediately after each focusing discharge. In this time interval, the contribution to the total count by 54 minutes decay scheme is less significant as the activity of ^{116m}In is almost constant due to its long half-life. The time interval between two consecutive discharges was set to 5 minutes to allow the activity of the foil induced by neutron activation decay down to background level. Background radiation level was monitored for each discharge and take into account in the time integrated neutron measurement.

Two set of such neutron detection system was used and has been normalized to determine the relative neutron yield emission. These detectors are positioned, one along the end on direction from the anode tip and the other is at side on direction. Since the scalar counter is sensitive to the electrical noise produced during a discharge, thus it is located inside a remote screen room to avoid operation malfunction. Experimental setup for the time integrated neutron measurements is shown in Figure 4.17.

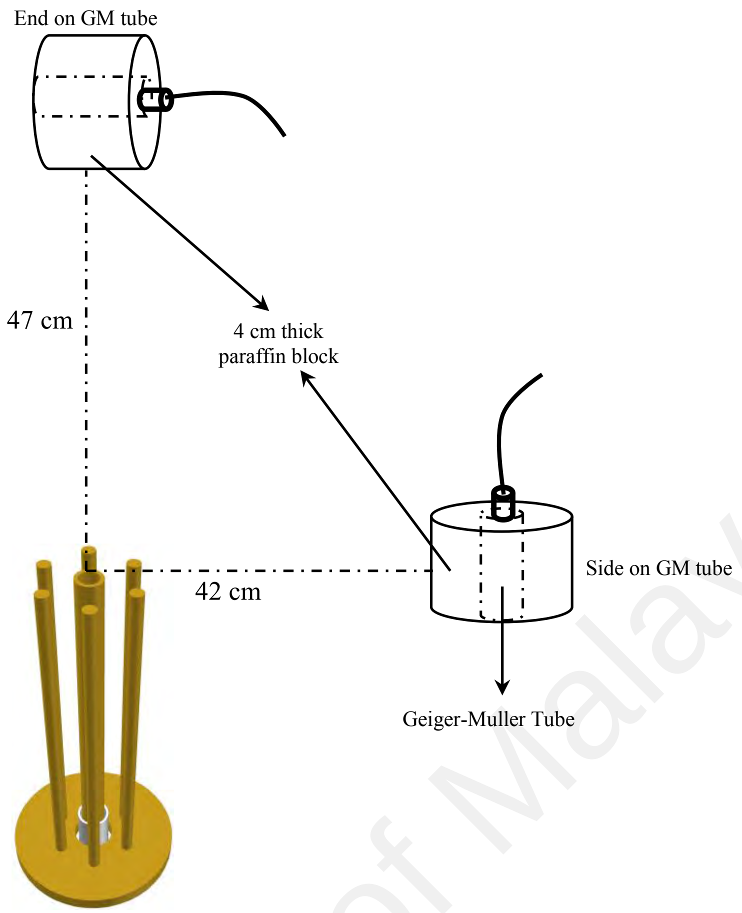

Figure 4.17: Schematic of the GM tubes arrangement for time integrated neutron measurement

4.5.2 Time Resolved Neutron Emission

The time resolved neutron measurement was used to determine the energy of the neutron emission by time of flight method. This measurement when correlated with other diagnostics can use to investigate the temporal evolution of the transient plasma. An assembly of plastic scintillator and fast photomultiplier tube was employed for this purpose. When neutrons falling upon a suitably activated scintillation material, light pulses will be produced which may be detected with photomultiplier tube (PMT).

There are crystal and plastic type scintillation material. NaI is one type of the crystal scintillation material which produces greater light output (about three times more) at a given energy than plastic scintillator and able to resolve lower-energy photons from the photomultiplier tube noise. However, when good time resolution is required, plastic scintillator offers a better choice.

In our work, a 5 cm diameter, 10 cm long cylinder of NE102A fast plastic scintillator having decay time constant of 2.4 ns is employed (Verma et al., 2008). This type of scintillator is suitable for the low and high energy neutron measurement. Bailey (Bailey, 1963) showed that the scintillation light is proportional to the photon energy as low as 3 keV. Usually, the plastic scintillator is coupled to the photomultiplier tube with a layer of silicon vacuum grease or high viscosity silicon grease such as Dow Corning DC-200 in between for a proper optical coupling. The scintillation light output is then detected by the photomultiplier tube.

However, our neutron diagnostic does not directly optical bonded to the photomultiplier tube. Instead, the light output from the scintillator is transmitted to the photomultiplier tube which is stored in a remote screen cage using fiber optic of several meters long. Such arrangement is superb to shield the sensitive photomultiplier tube from the plasma focus discharge while at the same time able to position the scintillator at a distance as close possible from the plasma focus device without being influenced by electrical noise. In addition, the fiber optic that is replacing the coaxial cable for the signal transmission has the special feature of shielding towards pick up of electrical noise during a focusing discharge.

It must be pointed out that the light output of the NE102A has a peak emission in the blue-violet region of ~ 423 nm. Thus, a special fluorescent fiber is necessary to couple this light output before transmitted to the normal commercial plastic optical fiber and photomultiplier tube in order to reduce the optical loss. We had chosen a dye-shifter green fluorescent fiber which has absorption spectral of 300 nm to 477 nm and emission spectral between 470 nm and 511 nm with maximum sensitivity for the emission at 493 nm.

Two fluorescent fibers each of 0.5 mm diameter and 1 m long are carefully wrapped around the plastic scintillator and evenly spaced without overlapping of one another. To ensure a good optical coupling between the florescent fibers and plastic scintillator, a little Dow Corning DC-200 silicon grease is applied at the scintillator surface. The plastic scintillator is then wrapped with a piece of aluminium foil to reduce the loss of scintillation light. Finally, the four ends of the two fluorescent fibers are channel out from the aluminium foil and polished into mirror finish. These four ends are fit into a low loss opto-coupling connector which joined to normal plastic optical fiber of 1 mm diameter and 9 m long. The light output is then guided to the photomultiplier tube located in a remote screen cage with absorption loss of well below 0.3 dB/m for wavelength between 470 nm and 511 nm. The optical signal detected by the photomultiplier tube is converted into electrical signal which represents the time dependence of the neutron emission.

The choice of the photomultiplier is dependent on the experimental requirements. The side window Hamamatsu photomultiplier tube of model no. R928 is selected for its fast responds and highest efficiency for detection of optical wavelength from 477 nm to 511 nm which matched with the emission spectral of the fluorescence fiber used here. This photomultiplier tube is made of high sensitivity multi-alkali photocathode and UV glass window with an electron transit time of 22 ns. The photomultiplier tube is powered by a voltage divider networks at -800 V. A schematic diagram of the scintillator-photomultiplier tube assemble is depicted in Figure 4.18.

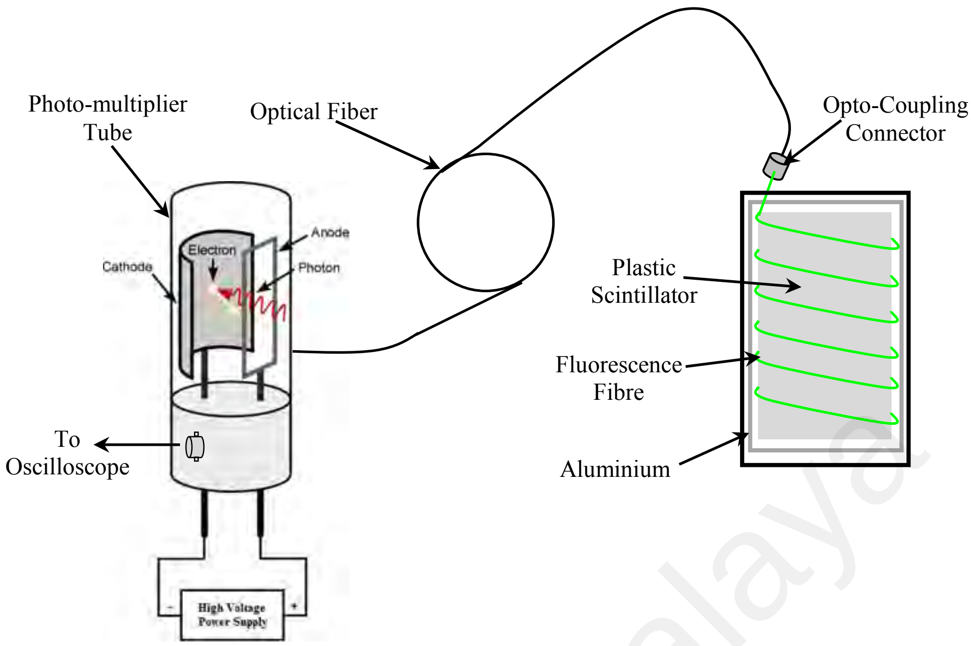

Figure 4.18: Component of a set of scintillator-photomultiplier tube assembly

For the time resolved neutron measurement, 5 sets of scintillator-photomultiplier tube assemble were employed. Three detectors labelled as D1, D2 and D3 was positioned at a distance of 87 cm, 97 cm and 149 cm from the anode tip in the end on direction, respectively. End on detectors were placed in line with the axis of the focus tube but each of the detector, was displaced slightly offset the axis so as not to obstruct each other. The other two detectors labeled as D4 and D5 were placed at same distance of 104 cm from the anode tip in the side on direction, respectively.

Detector D2 and D4 was enclosed in a cylindrical lead casing to eliminate or cut off interference due to hard x-rays. The cylindrical lead casing is about 3.5 cm thick, 15 cm diameter, 15 cm height and 20 kg weigh. It is custom made to just fit the plastic scintillator. The output from the green fluorescent fiber is channeled out through the opening on the cover of the lead casing at an angle of 45^{o}. A schematic diagram of the experimental arrangement for time of flight neutron measurement is depicted in Figure 4.19.

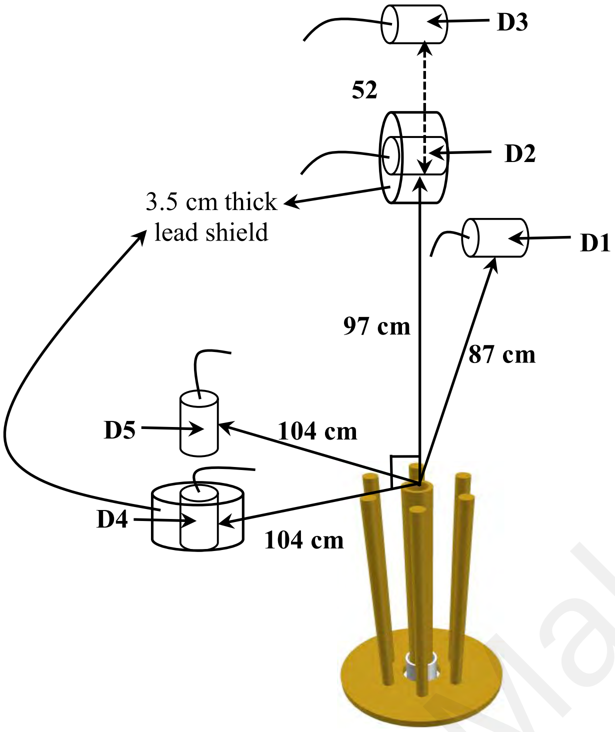

Figure 4.19: Experimental arrangement of the Scintillators for neutron measurement

From the time resolved signal, the time for the neutron to travel over a known distance can be measured. Thus, the velocities of the neutrons and hence the neutron energy can be determined from the kinetic energy formula. In order to determine the neutron time of flight, the electron transit time in the photomultiplier tube and the difference in the transit time in the transmission cable must be taken into account.

4.6 X-Ray Measurement

4.6.1 Time Resolved Soft X-Ray (BPX 65)

Studies of soft X-ray emission from pinched plasma serves as powerful means for acquiring various important parameters on the hot and dense plasma. Time resolved soft X-ray measurement provides not only temporal evolution of the soft X-ray emission but also the overall picture regarding the plasma dynamics when correlated with other diagnostic techniques. Moreover, the mechanism by which the soft X-rays are emitted may also be inferred as well as deducing the electron temperature of the transient plasma.

In plasma focus discharge, it is crucial to have a special designed experimental technique and instrument for the diagnosis of the pulsed radiations emitted naturally from the plasma. The choice of a detector for time resolved soft X-ray measurements depends on the information required and would also need to have enough resolution to follow the rapid changes of the plasma event. In this work, BPX 65 Silicon PIN diodes are used to provide time resolved information on the soft X-ray emitted from the pinched plasma.

The BPX-65 PIN diode is a detector normally used for the photon emission in the visible range. BPX-65 is a photodiode with sensitivity in the visible range, one need to remove the glass layer for X-ray measurement. It is preferred due to its simple installation, fast response and high sensitivity for the measurement of pulsed radiation between 1 – 30 keV (L., 1971). The PIN diode is similar to PN junction diode with an extra light doped intrinsic silicon layer between a p-type and n-type semiconductor region, which are typically heavily doped. The n-type region is called as “dead layer”, which is maintained at ground potential and used as the entrance window of the diode. As a photo-detector, each diode is reversed biased where the p-type layer is maintained at negative potential with respect to n-type layer. The diode is contained inside a T0-18 casing with the glass window being removed for the purpose of soft X-ray detection.

The typical parameters of the BPX 65 PIN used are given below:

- ✓ Effective detection area ~ 1 mm^2
- ✓ Intrinsic Si wafer thickness (estimated) ~ 10 μm
- ✓ Dead layer thickness (estimated) ~ 0.5 μm
- ✓ Rise time (typical) ~ 0.5 ns

The diode used is suitable to detect soft X-ray for the wavelength in the region of 0.3–10 Å. The sensitivity curve of BPX 65 diode for wavelength below 20 Å is presented in Figure 4.20.

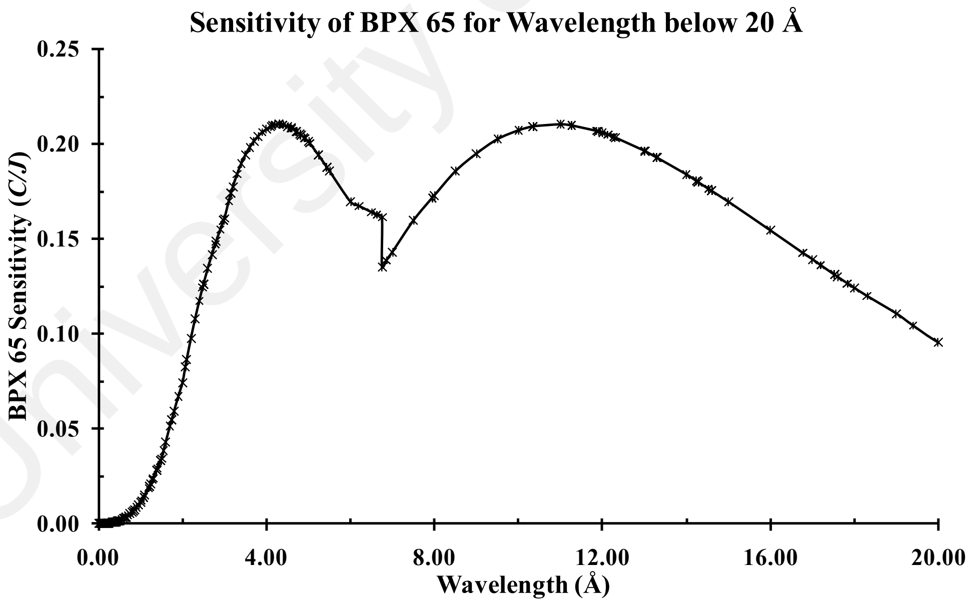

Figure 4.20: Sensitivity of BPX 65 PIN diode in X-ray region below 20 Å

Each diode consists of two connecting terminal of opposite polarity where it is connected to a biasing circuit and reverse biased at 45 V by two 22.5 V dry cells connected in series. Biasing voltage of - 45 V is chosen since the breakdown voltage of BPX-65 PIN diode is 50 V. A setup of the PIN diode with biasing circuit is illustrated in Figure 4.21.

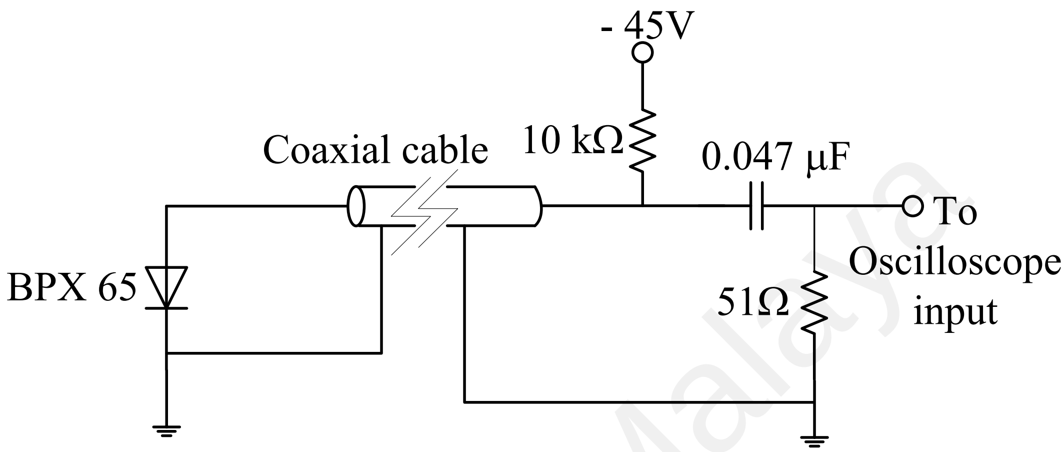

Figure 4.21: Circuit diagram of PIN diode with biasing circuit

The working principle of PIN diode is straightforward. Under reversed bias, the diode does not conduct. However, when the diode absorbs a soft X-ray photon of energy equal or more to form an electron-hole pair in the intrinsic layer, one or more electron hole pairs will be created resulting in charge flow in the biasing circuit. For the case of silicon at room temperature, average energy needed to form an electron-hole pair is 3.55 eV (Siegbahn, 1965). Therefore, for every joule of X-ray energy absorbed in the intrinsic layer will results in charge flow of about 0.282 coulombs of charge. For time resolved soft X-ray measurement, an array five windowless BPX 65 PIN diodes is used to monitor the soft X-rays temporal and spectral profile. Each of the diodes is filtered with different thickness of absorption foil. Details of this soft X-ray diagnostic will be given in following section.

4.6.2 Electron Temperature Measurement (Filter Ratio Method)

The electron temperature of deuterium plasma focus can be determined using foil absorption technique or filter ratio method (Jahoda et al., 1960; Robouch & Rager, 1973). This technique is widely used to determine the electron temperature in laboratory plasmas assuming Bremsstrahlung (free-free) as the dominant radiation process. The analysis is done by examined the ratio of soft X-ray intensities through two different absorption filters. However, the main difficulty in measuring the plasma electron temperature was due to the selection of appropriate filter that can provide a measuring window to discriminate line radiation from the impurities or anode surface.

Theoretically, the ratio of the soft X-ray intensities $E(\lambda)$ integrated over the transmission spectra through two detectors having different absorption filters is a function of electron temperature. The ratio R_T is given by:

$$R_T = \frac{\int E(\lambda) e^{-\sum_a \mu_a x_a - \sum_b \mu_b x_b} d\lambda}{\int E(\lambda) e^{-\sum_a \mu_a x_a} d\lambda} \quad \textbf{(4.10)}$$

For Bremsstrahlung (free-free) radiation, the:

$$E(\lambda) = 1.88 \text{ x } 10^{-29} \frac{n_e n_i Z_i^2}{\lambda^2 T_e^{1/2}} g_{ff} e^{\frac{-12398.4}{\lambda T_e}} \quad \textbf{(4.11)}$$

While for recombination (free-bound) radiation,

$$E(\lambda) = 1.38 \text{ x } 10^{-30} \frac{n_e n_i Z_{i+1}^4}{\lambda^2 T_e^{3/2}} g_{bf} \sum_n \frac{\chi_{i,n}^2 \xi_n}{n} e^{\frac{\chi_{i,n} - \frac{12398.4}{\lambda}}{T_e}} \quad \textbf{(4.12)}$$

where:

T_e is the electron temperature in eV

λ is the wavelength in Å

n_e is the electron density in cm^{-3}

n_i is the ion density in cm^{-3}

$\chi_{i,n}$ is the ionization potential of the n-th state of the i-th species

ξ_n is the number of vacancies in n-th state

$Z_{i,i+1}$ is the effective charge of the ion

$x_{a,b}$ is the thickness of *a* and *b* foils, respectively in cm

$\mu_{a,b}$ is the mass absorption coefficients of *a* and *b* foils, respectively

g_{bf} is the Gaunt factor for free-bound transition

g_{ff} is the Gaunt factor for free-free transition

n is the electronic state

The mass absorption coefficients (μ) are a function of photon energy and depend on the type of absorption filter which can be found at NIST database (Hubbell & Seltzer, 1996). In plasma focus operated with deuterium filling, most of the characteristic soft X-ray emission is free-free radiation. Thus, the term $E(\lambda)$ in Equation 4.10 is given by the expression in Equation 4.11 when determine the electron temperature of deuterium plasma.

For the electron temperature measurement, an array of five windowless BPX 65 PIN diodes was employed. The five diodes are glued on five good fit holes on a circular brass flange of diameter 7 cm and thickness 5 mm with one of the diodes situated at the centre of the flange. The schematic arrangement of the 5-channel PIN diode array is illustrated in Figure 4.22. Each diode is labeled as X1 through X5 with X2 at the middle.

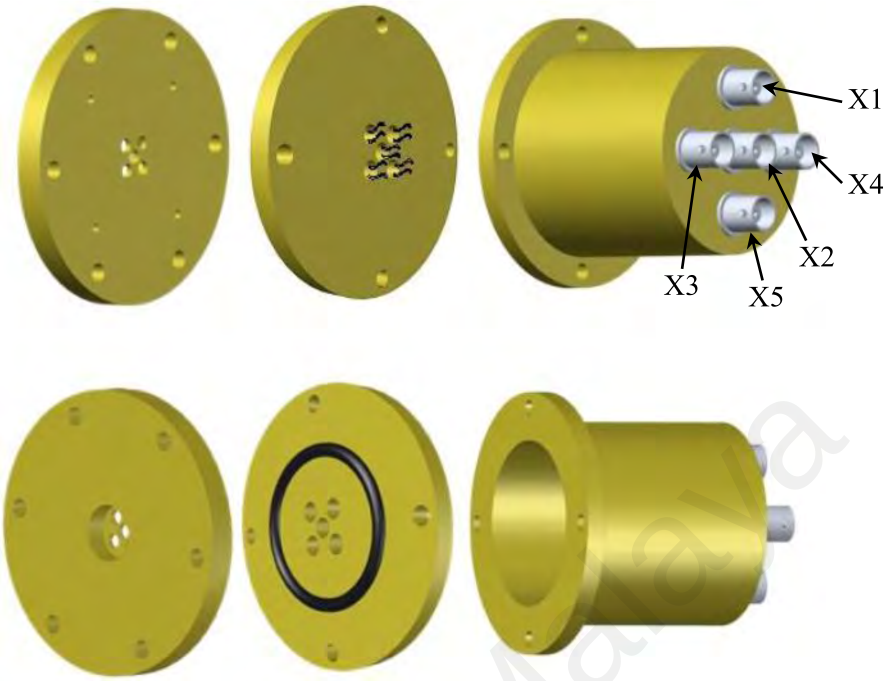

Figure 4.22: Design of five channels PIN diode array

Each diode is made vacuum tight by mounting the circular brass plate onto a cylindrical brass casing with an O-ring. This is required to reduce the attenuation of X radiation through the ambient gas from reaching the diode. It is then adapted to the view port of the plasma chamber coupled with an O-ring at a radial distance of 15 cm from the anode axis. The experimental arrangement of the multi-channel PIN diodes is displayed in Figure 4.23.

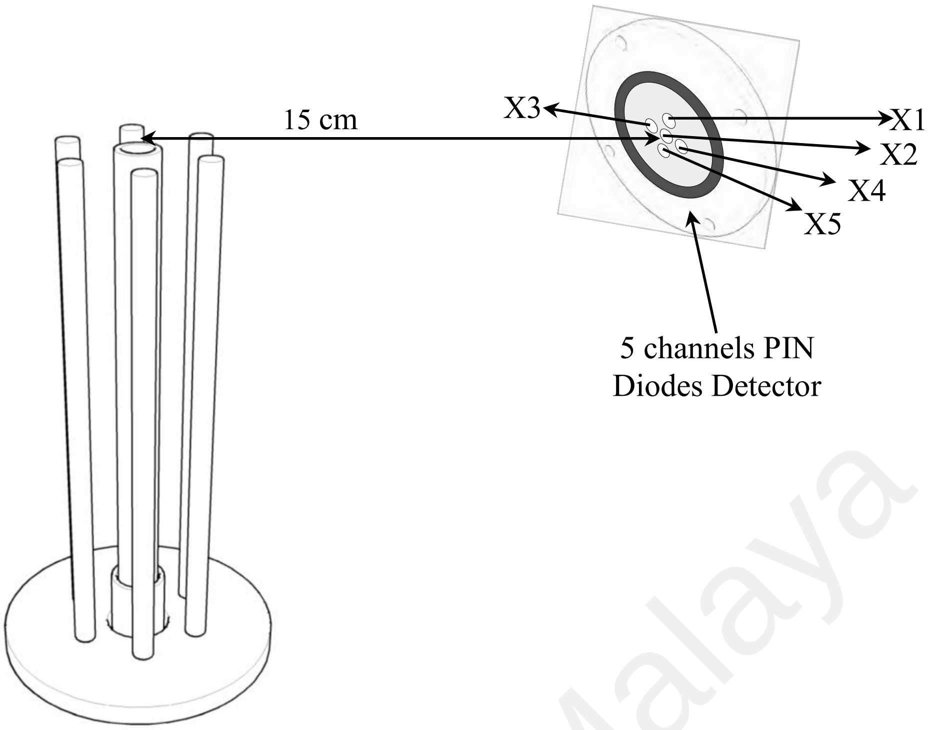

Figure 4.23: Schematic arrangement of the multi-channel PIN diodes

All the PIN diodes have been cross-calibrated before it is ready to be used for measuring the electron temperature. This is to take into account the detectors sensitivity and geometrical differences due to different position. For that, same foil thickness, 23 µm aluminized Mylar are used on all PIN diode detectors.

In the present work, Aluminium foil of different thickness is used as an absorption foil. Below is the description for combination of foil thickness used at different channel.

Channel 1 - 23 µm aluminized mylar

Channel 2 - 23 µm aluminized mylar + 20 µm aluminium foil

Channel 3 - 23 µm aluminized mylar + 40 µm aluminium foil

Channel 4 - 23 µm aluminized mylar + 80 µm aluminium foil

Channel 5 - 23 µm aluminized mylar + 120 µm aluminium foil

The sensitivity of the PIN diode can be estimated from the two thickness model (Corallo et al., 1980) given as:

$$S(\lambda) = 0.282 e^{-\mu(\lambda)\cdot x_1}(1 - e^{-\mu(\lambda)\cdot x_2}) \text{ A/W} \quad \textbf{(4.13)}$$

where

$\mu(\lambda)$ is the X-ray mass-absorption coefficient of silicon in cm^2/g

x_1 is the mass thickness of the entrance windows in g/cm^2

x_2 is the effective depletion region of the intrinsic layer in g/cm^2

The first exponential term represents the transmission of X-rays through the entrance window (n-type layer) of PIN diode and the second term in the bracket represents the absorption coefficient of the intrinsic layer. The resultant sensitivity of each detector filtered with different foil thickness can also be estimated from the expression given in Equation 4.13 by multiply it with a term of $e^{-\mu\cdot x}$ where μ is the absorption coefficient of the filter material and x is the thickness of the filter. The overall sensitivities of each PIN diodes coupled to different aluminium foil thickness are depicted in Figure 4.24.

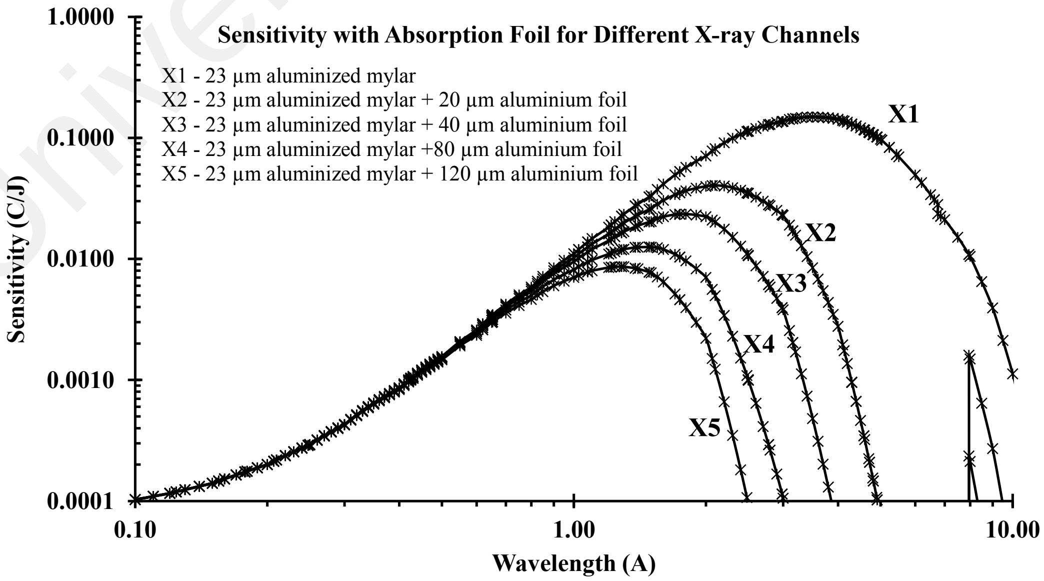

Figure 4.24: Sensitivity of BPX 65 PIN diodes with foil absorption folded in

In each of the channel, a 23 μm thick aluminized Mylar is used in conjunction with the aluminium foil. It is actually a piece of Mylar sheet coated with aluminium. Aluminium coating is employed for the purpose of filter off the visible light and ultraviolet radiation that are emitted together with X-ray as illustrated in the sensitivity curve shown in Figure 4.24. This in turns helps to reduce the impurity emitted along with the soft X-ray from the pinched plasma.

Our choice of absorption filters showed that the PIN diodes is suitable to detect photons wavelength in the range of 0.1 – 10 Å, which corresponds to the soft X-ray region. Furthermore, X5 and X4 showed maximum sensitivity for detection of X-ray with wavelength around 1.39 Å and 1.54 Å which is the copper K_β and copper K_α line radiation, respectively. This implies that this combination of foil absorption thickness can also be used to detect copper line radiation other than continuum radiation of soft X-rays.

The intensities ratio curve for aluminium filter of different thickness corresponding to a different electron temperature has been computed and shown in Figure 4.25. This is done by first calculating the ratio for a pair of foil filters at different electron temperature. This process is repeated for a different pair of filters with the thickness of one absorption filter progressively increased while the other remains unchanged in all pairs of the filters. The experimental observed soft X-ray intensities ratio is then compared with these absorption curves to estimate the electron temperature of the deuterium plasma.

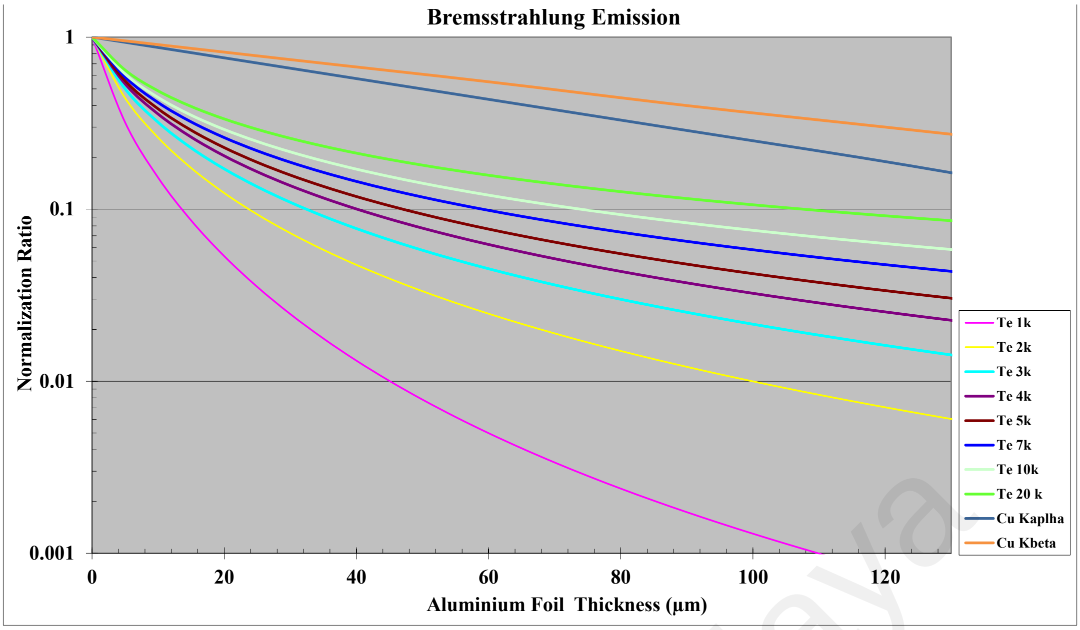

Figure 4.25: Calculated intensities ratio transmitted through aluminium foil for deuterium plasma of different temperature

4.6.3 Time Resolved Hard X-Ray Measurement

The principle of detecting hard X-rays from the focusing discharge is similar to the one described earlier for the detection of time resolved neutron emission. In the light of this fact, the temporal evolution of hard X-ray emission was also studied using the scintillator-photomultiplier tube assembly similar to the one used for neutron measurement. The difference is that the scintillator-photomultiplier tube assembly was exposed directly to the plasma focus device without enclosed in the cylindrical lead casing.

The detection of the hard X-ray emission was done outside discharge chamber which simplified the measurement in the standpoint of diagnostic. The time resolved hard X-ray signals when correlated with discharge voltage, discharge current, ion beam, and soft X-ray signal is very useful to provide a better understanding of the plasma focus dynamics as well as the mechanisms of the ion beam emission. Integration of the hard X-ray signal over the duration of emission can be used to infer the qualitative information on the overall yield and its correlation with ion beam emission.

Three sets of scintillator-photomultiplier tube assembly were used for time resolved hard X-ray measurement labeled as D1, D3 and D5. Two detectors, D1 and D3 was positioned along the end on direction at a distance of 87 cm and 149 cm from the anode tip, respectively whereas the other detector D5 was placed at a distance of 104 cm from the anode tip in the side on direction. A schematic arrangement of the experimental setup for hard X-ray measurement is shown in Figure 4.26.

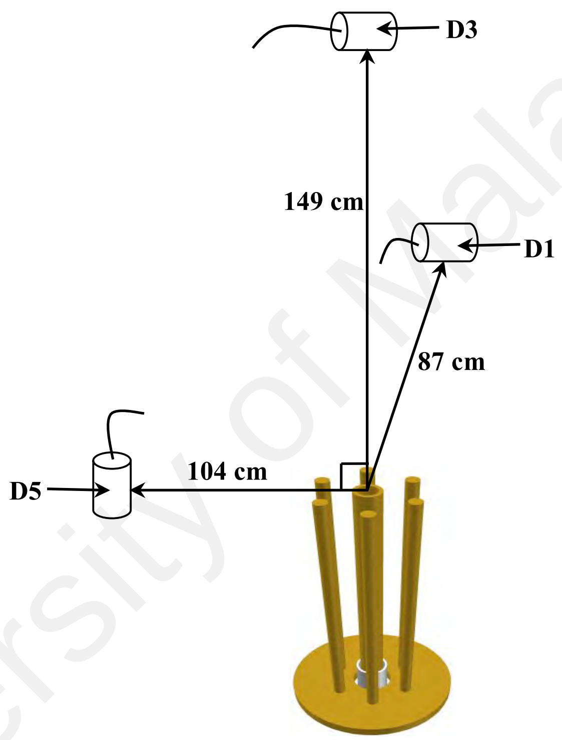

Figure 4.26: Experimental arrangement of the Scintillators for hard X-ray measurement

CHAPTER 5: EXPERIMENTAL RESULTS & DISCUSSIONS

5.0 Introduction

In this chapter, the results of the experimental investigation performed on the 2.7 kJ plasma focus device with various diagnostic techniques described in previous chapter are presented. Pure deuterium gas was used throughout the experiments and charging voltage was fixed at 13.5 kV. Fresh gas was filled for each shot to minimize the effect due to impurities. The main objective of the project is centered on optimizing the plasma focus for radiation emission (ions, neutrons and X-rays) emitted from the focusing discharge. The correlation of the radiation emission and discharge parameters is investigated. The experiments were carried out at different operating pressure in the low pressure regime of less than 1 mbar rather than the conventional operating pressure range of 3 – 6 mbar for deuterium filling. Optimization in low pressure regime is implemented in long electrode configuration so that the discharge current is maximum during plasma pinch. The purpose of varying the pressures is to find a suitable operating condition in beam optimized mode for the plasma focus device to operate as reliable ion beam source for manifold applications. Interesting results and phenomena have been observed and discussed for the operation of the plasma focus device shifted in low pressure regime. The presentation of the results is mainly divided into few parts.

The first part of the chapter presented the results of qualitative and quantitative information obtained from the discharge current and voltage measurement. In the second part, experimental results on ion beam measurement using various diagnostics are presented, discussed and compared. Neutron and hard X-ray emission will be discussed in next part. In the last part of the chapter, correlations of the radiation emission with discharge parameter are also discussed.

5.1 Gross Dynamics of Plasma Focus Discharge from Current & Voltage Measurement

The basic and yet essential diagnostic in most of the pulse plasma discharge experiments is nevertheless, current and voltage measurements. Due to the characteristic of the discharge current being very fast and in the range of hundreds of kA, a suitable diagnostic for the current measurement have to be used such as Rogowski coil. On the other hand, the transient voltage across the focus tube was measured by high voltage probe. Discharge current and voltage signal from the focusing discharge has been very useful as benchmark of the overall performance of the plasma focus device and able to provide basic study of the dynamical evolution of the plasma during the pinch. Relative intensity of a plasma pinch can be gauged in terms of voltage spike and current dip from the recorded discharge voltage and current signal.

Unique feature of a focusing discharge is the observation of a sharp rise of voltage spike in the discharge voltage signal and distinct dip in the discharge current signal. A shot with very sharp rise of voltage spike and the associated significant current dip is an indication of strong focusing action and good focusing discharge. In this project, focusing discharge was obtained in the pressure range of 0.01 to 1.0 mbar. At the charging voltage of 13.5 kV and capacitance of 30 μF, the quarter cycles of ~ 2.76 μs was measured in the discharge current. Two types of focusing discharge was observed, i.e. first–type of discharge with single voltage spike and second type of discharge with multiple voltage spikes.

At operating pressure near to 1 mbar, focusing discharge with single voltage spike is more likely to be obtained. These discharges are grouped in a first type of focusing discharge where the single voltage spike is corresponded to one main compression of the plasma during the focus event and it is characterized by a single and sharp rise of voltage spike. Rise time of the voltage spike is found to vary from 25 to 70 ns in the pressure range of 0.1 – 1.0 mbar. When the operating pressure is reduced towards 0.1 mbar, focusing discharge with more than one voltage spikes is more likely to be obtained. These discharges are grouped in second type as distinguished by two or more voltage spikes in the discharge voltage signal which corresponded to a sequence of pinching other than the main compression.

Performance of the plasma focus discharge is closely related to the dynamics of the evolution of the plasma which is dependent on the Lorentz force induced by the discharge current. The motion and dynamics of the plasma can be explained by the speed parameter,

$$S = \frac{(I/a)}{\sqrt{\rho}}$$

where I is the maximum discharge current, a is the anode radius and ρ is the density of the filling gas. The lower the operating pressure, the higher is the value of S and thus the faster is the current sheath speed. Therefore, current sheath reaches the end of axial phase in shorter time at lower pressure. The experimental results obtained at 0.1 – 1.0 mbar (Figure 5.1a – 5.1g) showed the evidence of plasma focus occurs at earlier time at lower pressure.

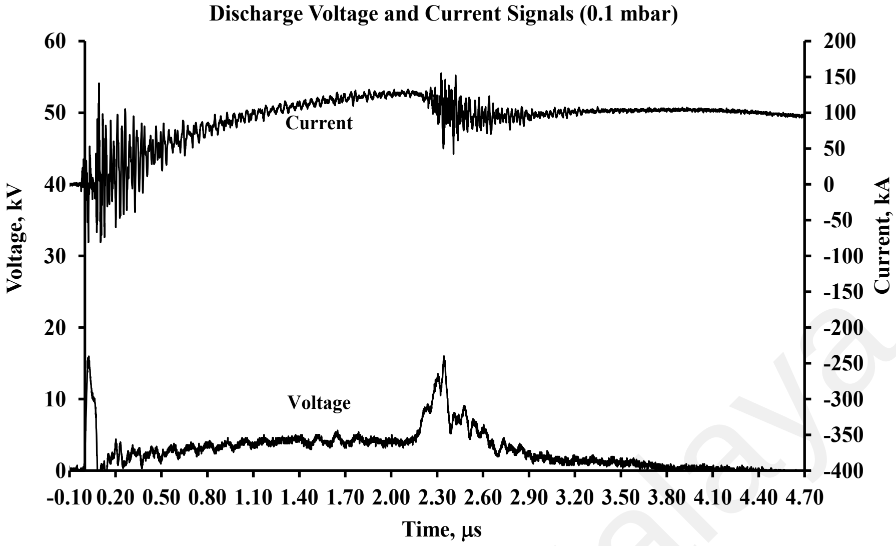

Figure 5.1(a): Typical discharge voltage and current signal at 0.1 mbar deuterium discharge

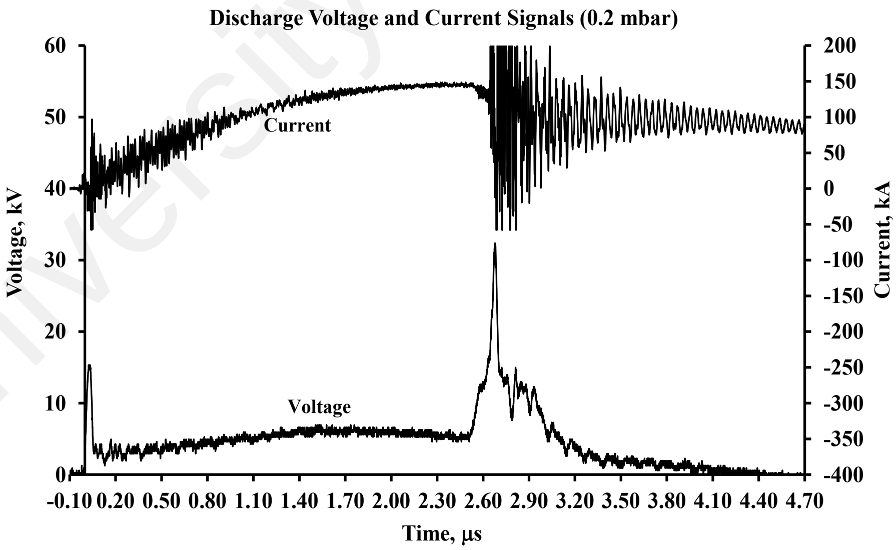

Figure 5.1(b): Typical discharge voltage and current signal at 0.2 mbar deuterium discharge

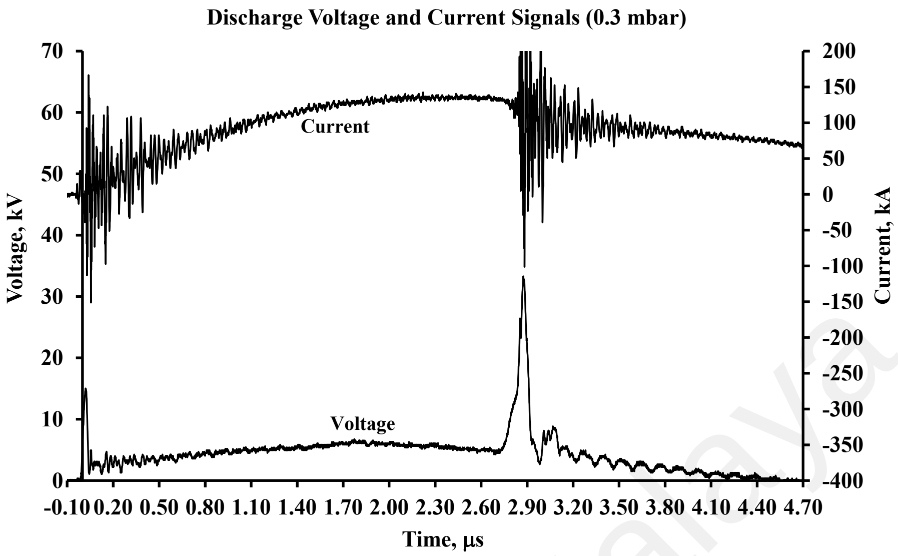

Figure 5.1(c): Typical discharge voltage and current signal at 0.3 mbar deuterium discharge

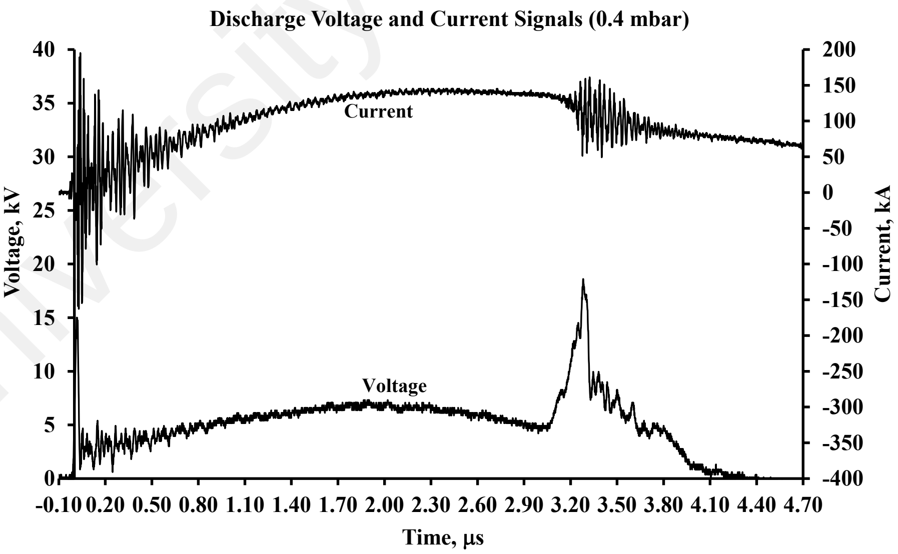

Figure 5.1(d): Typical discharge voltage and current signal at 0.4 mbar deuterium discharge

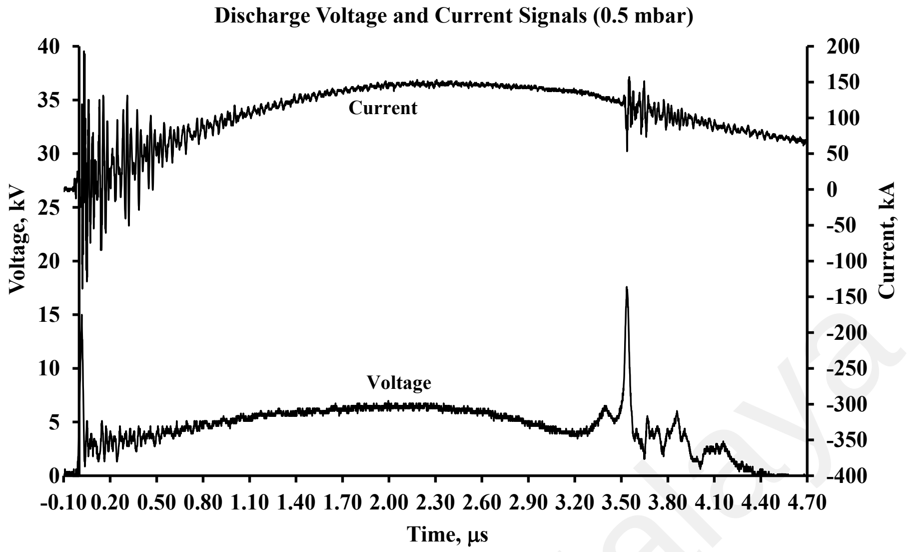

Figure 5.1(e): Typical discharge voltage and current signal at 0.5 mbar deuterium discharge

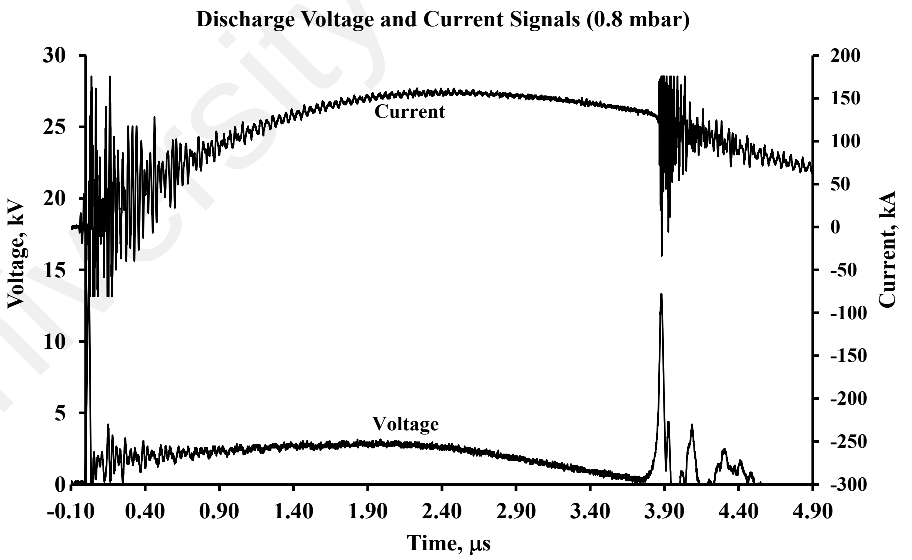

Figure 5.1(f): Typical discharge voltage and current signal at 0.8 mbar deuterium discharge

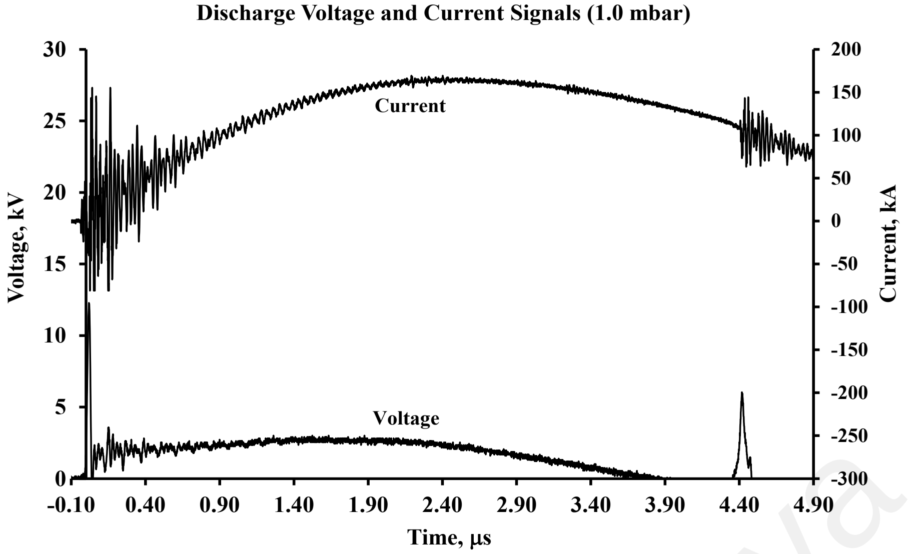

Figure 5.1(g): Typical discharge voltage and current signal at 1.0 mbar deuterium discharge

It is noticed that at pressure in the range of 0.1 – 1.0 mbar, more than 80 % of the discharge is in second type (multiple spikes) except at 1.0 mbar as presented in the histogram in Figure 5.2. Overall results indicates that focusing discharge with multiple voltage spikes is more readily to occur at operating pressure of less than 0.8 mbar. The origin of this multiple voltage spikes in the focusing discharge is suggested to be correlated with micro instability and turbulences occurred in the plasma pinching. Even though the lower the operating pressure, the more likely is the occurrence of multiple voltage spikes but the amplitude of voltage spike is on the other hand increasing suggested a more severe plasma pinch had occurred at lower pressure.

Strong focusing discharge can be obtained in a pressure range of 0.1 to 0.3 mbar. Discharge in this pressure range showed consistent focusing discharge with high amplitude of voltage spike. At this narrow pressure range, the frequency of occurrence for single voltage spike discharge is almost the same which lies within 11 to 12 %. Hard X-ray emission and intense ion beam emission is usually obtained at this pressures range.

Overall experiments showed that discharge with single voltage spike is rather seldom being obtained for operation in low operating pressure.

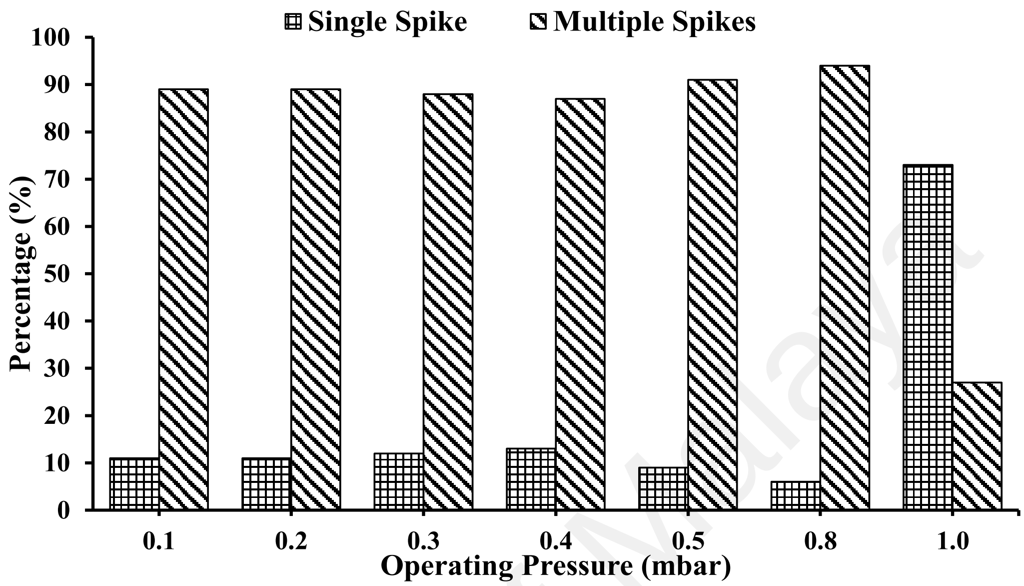

Figure 5.2: Frequency of single and multiple voltage spikes for deuterium discharge at respective operating pressure

A summary has been made by recording the amplitude of voltage spike for all the shots at different operating pressure. Figure 5.3 showed the summary of amplitude of voltage spike for the pressure in the range of 0.1 to 1.0 mbar. Each data point on the graph has been averaged over 15 shots. It is noticed that the amplitude of voltage spike increases at lower pressure and peaks at 0.2 mbar. This implies that the focusing discharge at this pressure is the strongest with average amplitude of voltage spike measured to be 32 ± 3 kV. Small standard variation in the amplitude of voltage spike indicates a consistent and reproducible strong focusing discharge. Maximum amplitude of voltage spike of 41 kV has been obtained at 0.2 mbar.

At pressure beyond 1.0 mbar, no significant focusing discharge was registered as the result of poor current sheath formation. Thus, the focusing action is weak and resulted in small amplitude of voltage spike. It is worthwhile to mention that at lower pressure, focusing discharge occurs at earlier time and closer to the peak of discharge current. At 0.2 mbar, the focus occurs at few tens of nanoseconds before the discharge current reached maximum as indicated in Figure 5.1(*b)*.

This was observed as a favourable condition for a good focusing discharge where the discharge current is still increasing while the plasma is being compressed. Therefore, this could explain the reason of highest average amplitude of the voltage spike obtained at this pressure. Generally, it was observed that the higher is the amplitude of voltage spike, the higher is the radiation burst. Also, discharge with single spike is usually accompanied by higher radiation emission compared to multiple spikes.

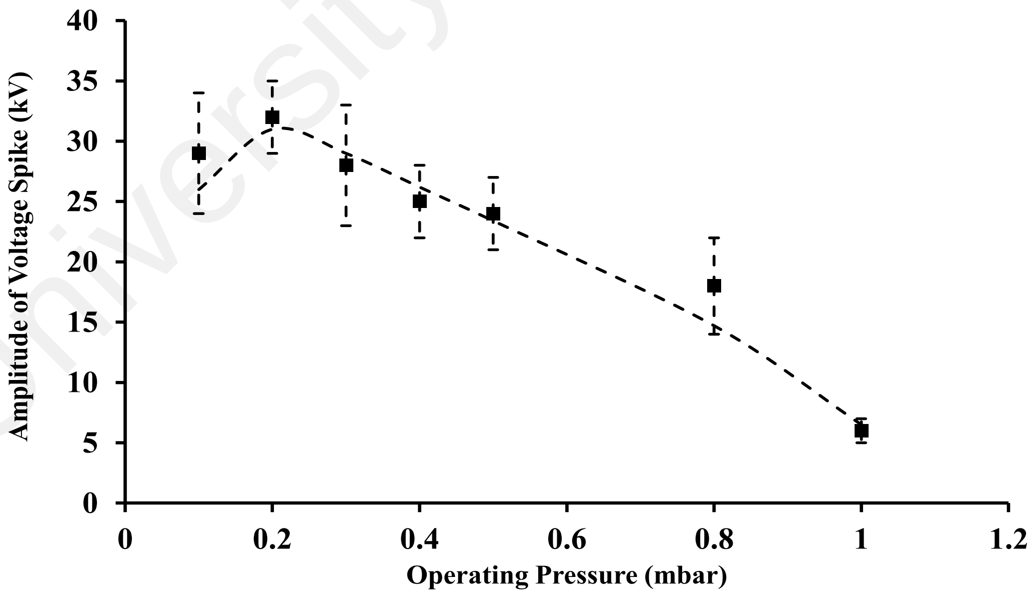

Figure 5.3: Average amplitude of voltage spike for pressure of 0.1 – 1.0 mbar

5.1.1 Focusing Time & Axial Speed

Focusing time is generally defined as the time taken from the beginning of the breakdown phase '*A*' until the maximum compression of the plasma to form a plasma column of minimum radius '*B*' (Figure 5.4).

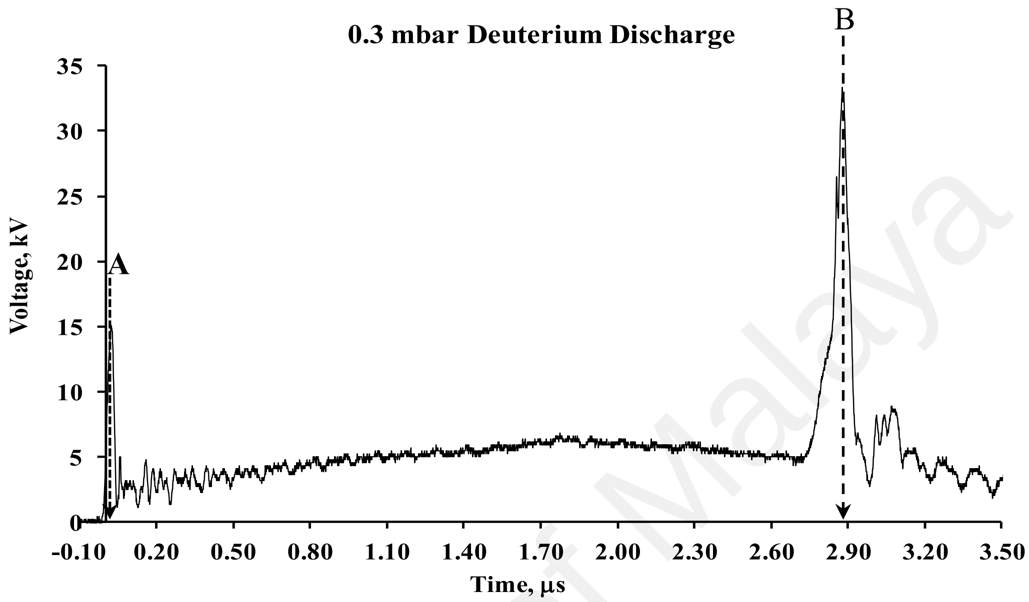

Figure 5.4: Focusing time can be determined from the time interval between point '*A*' to point '*B*' from the discharge voltage signal

Variation of focusing time with different operating pressure is presented in Figure 5.5. Each data point on the graph is the average of 15 shots. A proportional correlation can be observed between the focusing time and operating pressure. This is because for a fixed anode length and charging voltage, the mass load of the plasma in motion is proportional to the operating pressure. Therefore, higher pressure results in higher inertia to the plasma motion and longer time is needed for the focus to occur. At 0.2 mbar, the focusing time is about 2.67 ± 0.11 μs which occurs near to the moment of maximum discharge current.

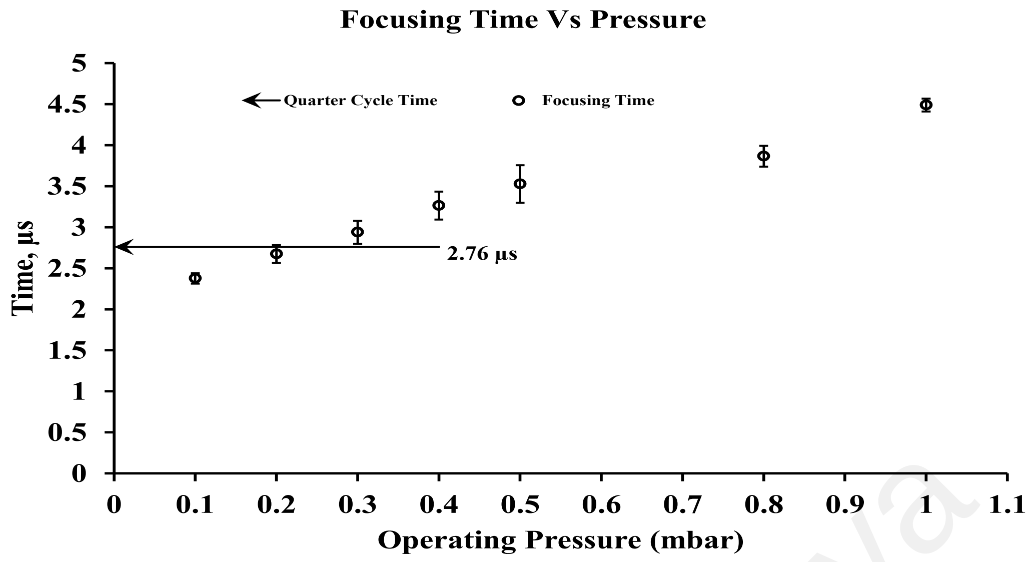

Figure 5.5: Average focusing time of deuterium discharge at different operating pressure

The average speed of the plasma in the axial phase is determined from the ratio of anode length to focusing time. Average axial speed of the current sheath as a function of operating pressure is illustrated in Figure 5.6.

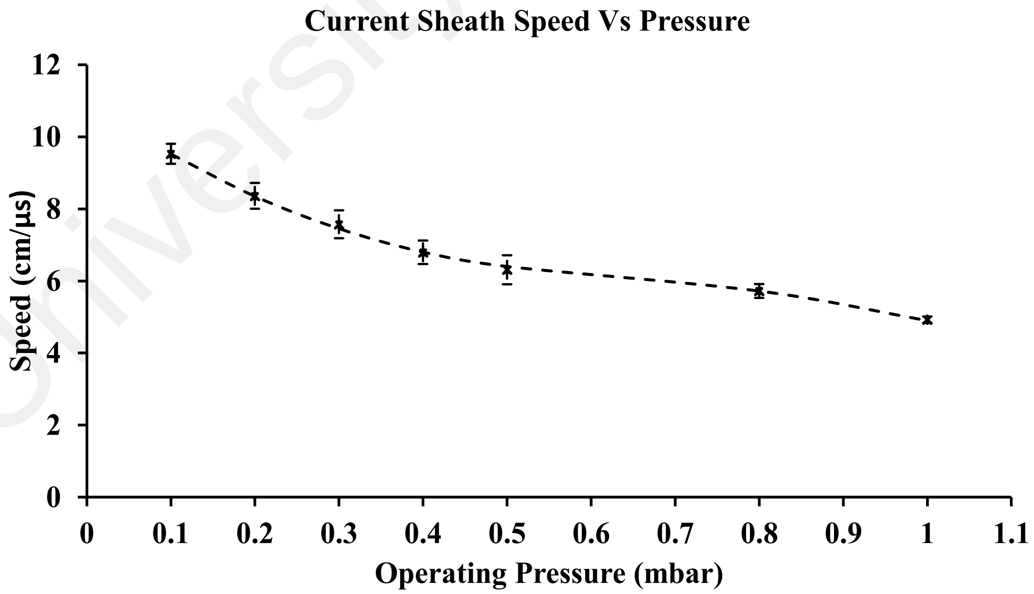

Figure 5.6: Axial speed of current sheath as a function of operating pressure. Each data point has been averaged to 15 shots

When the speed of the current sheath is plot against the square root of pressure, almost a linear pattern can be observed except there might be an underestimation for the speed at 0.1 and 1.0 mbar as illustrated in Figure 5.7. The axial speed of the current sheath is observed to vary reciprocally with the square root of the pressure (Zhang et al., 2006). The underestimation of scattering of the data around the linear line is suggested to be caused by the device effects such as current shedding and mass shedding effect (Bhuyan et al., 2003). Such effects are found to play a crucial role in discharge process and hence the plasma dynamics (Al-Hawat, 2004). Since the presentation of the data is deduced from the recorded discharge voltage signal alone, thus the results is sufficient to show a fair agreement between the correlation of speed and square root of pressure.

At 0.2 mbar, average current sheath speed has been determined to be 8.4 cm/μs. In fact, a strong focusing discharge has been obtained in the pressure range of 0.1 – 0.3 mbar driven at average peak axial current sheath speed of 7.6 – 9.5 cm/μs. At this pressure range also, reproducible and good radiation output is consistently observed. Focusing discharge at this pressure range showed that the peak axial speed of close to 10 cm/μs is a favourable speed for good focusing discharge. Operation of the plasma focus device at very high peak axial speed has been reported to improve radiation output as long as within the limit of force-field-flow-field separation where a good coupling between the magnetic piston and plasma layer can still be hold (Serban & Lee, 1998).

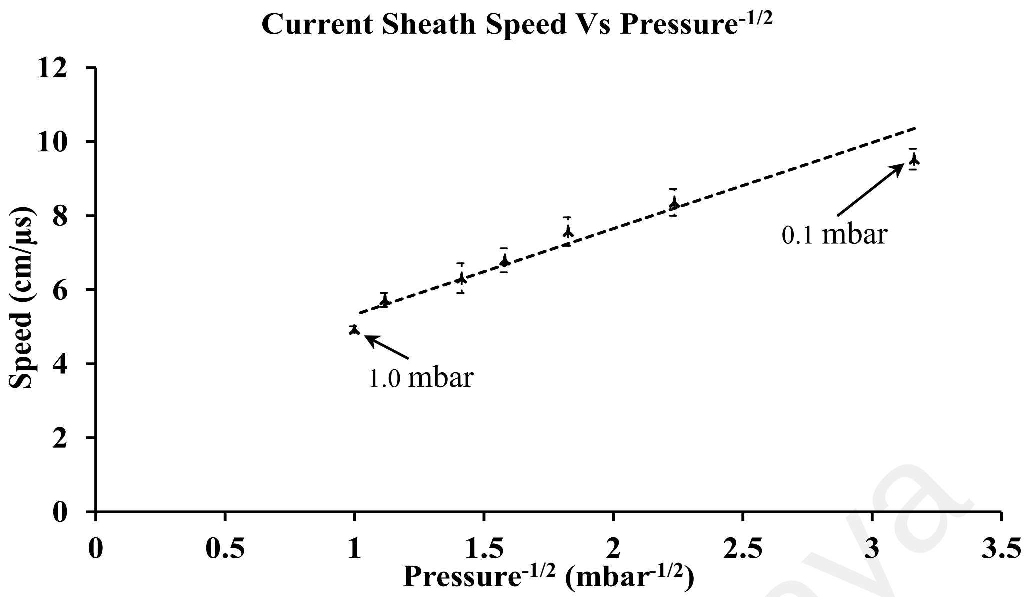

Figure 5.7: Axial speed of current sheath as a function of reciprocal of the square root of the pressure. Each data point has been averaged to 15 shots

5.1.2 Energy & Power into Plasma Focus Tube

The electrical power and energy transferred into the plasma focus tube have been estimated from the current and voltage signal of the focusing discharge. The power P was calculated from the current I and voltage V signal where ($P = I.V$) while the energy was determined from the integration of the calculated power waveform. Not all the power and energy transferred into the plasma focus tube will be absorbed by the plasma as partly will be stored inductively in the focus tube or remains in the energy bank.

Figure 5.8 shown a typical temporal evolution of the power and energy transferred into the plasma focus tube at 0.2 mbar taken from a set of the current and voltage signals. The sharp spike in the power curve corresponded to the power transferred into the focus tube during radial compression phase. In this set of analysis, the maximum power transferred into the focus tube was determined to be 3.1 GW. In the operating pressure of 0.1 to 1.0 mbar, the maximum power transferred to the focus tube varies from 0.6 GW to 4 GW.

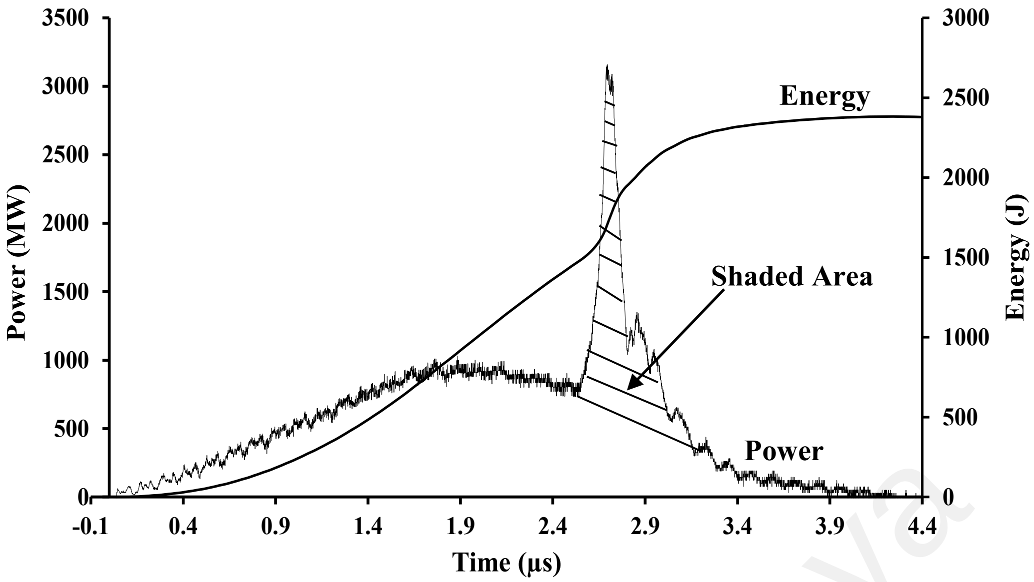

Figure 5.8: Temporal evolution of power and energy transferred into the plasma focus tube at 0.2 mbar

Figure 5.9 showed the average maximum input power at different operating pressure. Each data point on the graph has been averaged over 10 shots. Averagely, highest power of 2.8 GW transferred into the focus tube has been obtained at 0.2 mbar. It has been observed that at lower operating pressure, the maximum power transferred to the pinched plasma increases indicating stronger plasma pinch at low operating pressure.

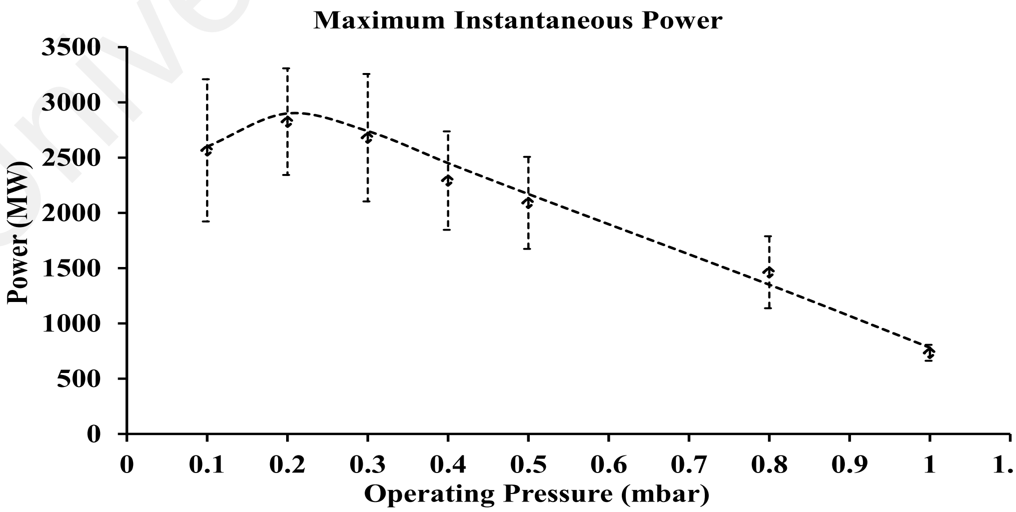

Figure 5.9: Maximum power transferred into focus tube (average over 10 shots)

The amount of energy transferred into the pinched plasma reflects the efficiency of the plasma focus discharge. This energy was estimated from the integration of the shaded area in Figure 5.8. For the input energy of 2.7 kJ (13.5 kV, 30 μF) as stored in the driver, the amount of energy estimated corresponded to an efficiency of 2 – 9 %. Lowest efficiency was obtained at 1.0 mbar where the focusing discharge becomes weaker whereas highest efficiency was obtained at 0.2 mbar. Higher ion beam energy has been measured for the shots with higher efficiency.

The amount of energy as a function of operating pressure is illustrated in Figure 5.10. Each data point has been average over 10 shots. The energy transferred into the pinched plasma was determined to spread over a large range between 60 J to 290 J due to shot-to-shot variation. Overall, highest energy was obtained at 0.2 mbar. Highest efficiency with maximum energy transferred at 0.2 mbar could be ascribed as the effect of plasma pinched at the time few tens of nanoseconds before the discharge current reaches its maximum. It is speculated that this is a favourable condition for an effective plasma pinch where the driver is still able to transfer energy to the plasma during the compression phase.

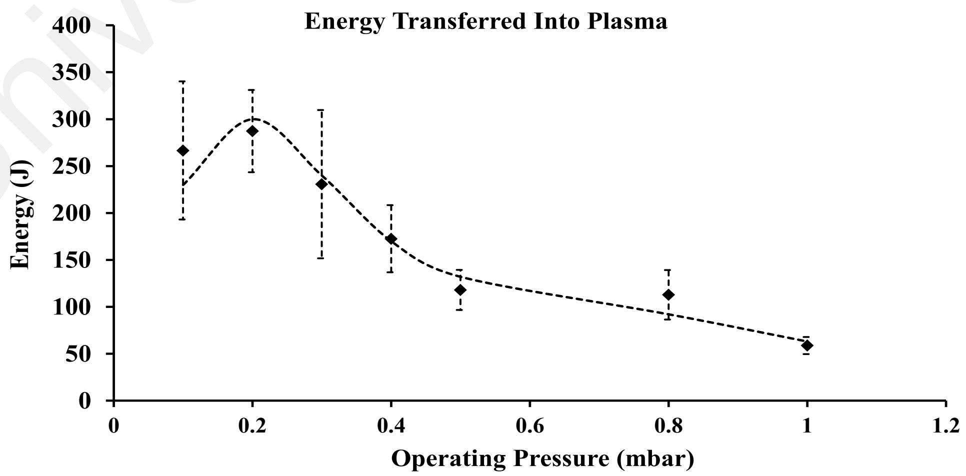

Figure 5.10: Amount of energy transferred into pinched plasma at different operating pressure

5.1.3 Characteristic of Current Dip in Discharge Current

During the compression phase, while discharge voltage surge the current measured across the focus tube drops significantly. Correlation of the current drop measured in terms of the length of current dip with respect to pressure was analyzed and depicted in Figure 5.11. Each data point on the graph was averaged over 10 shots. Noticed that the current drop is sensitive to the operating pressure. The current drops increases towards lower pressure until a maximum at 0.2 mbar and decreases at further lower pressure.

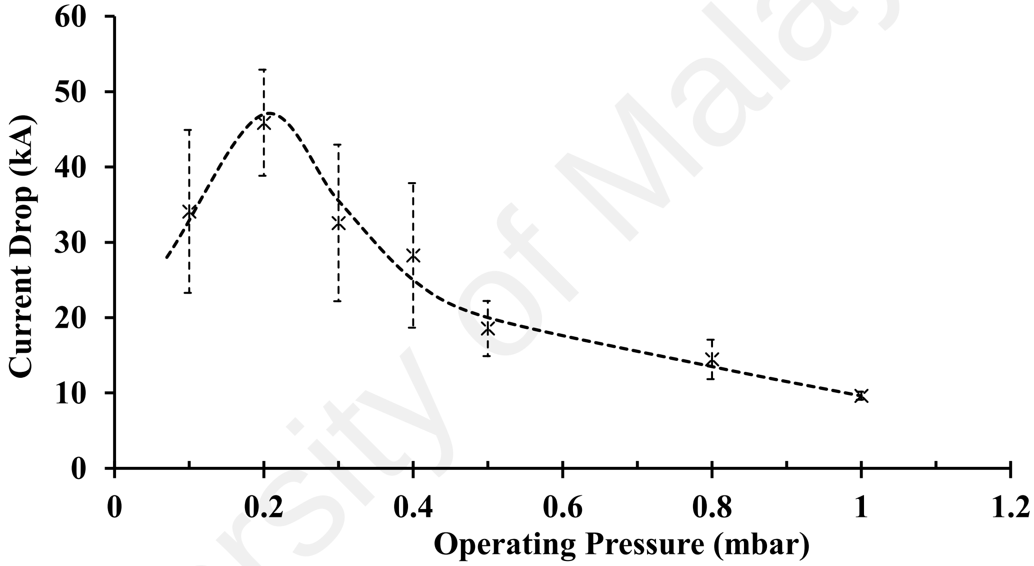

Figure 5.11: Average current drop as a function of pressure

By lowering the pressure, the current drop can last up to few hundreds of nanoseconds. A plot of the duration of current drop versus pressure average over 10 shots is illustrated in Figure 5.12. It is clearly observed that duration of current drop increasing at lower pressure. Longer durations of current drops at low pressure were also correlated to the multiple dips in the current signal and multiple voltage spikes. It is worthwhile to mention that when the current drop is significant, the intensity and energy of the ion beam emission observed was high.

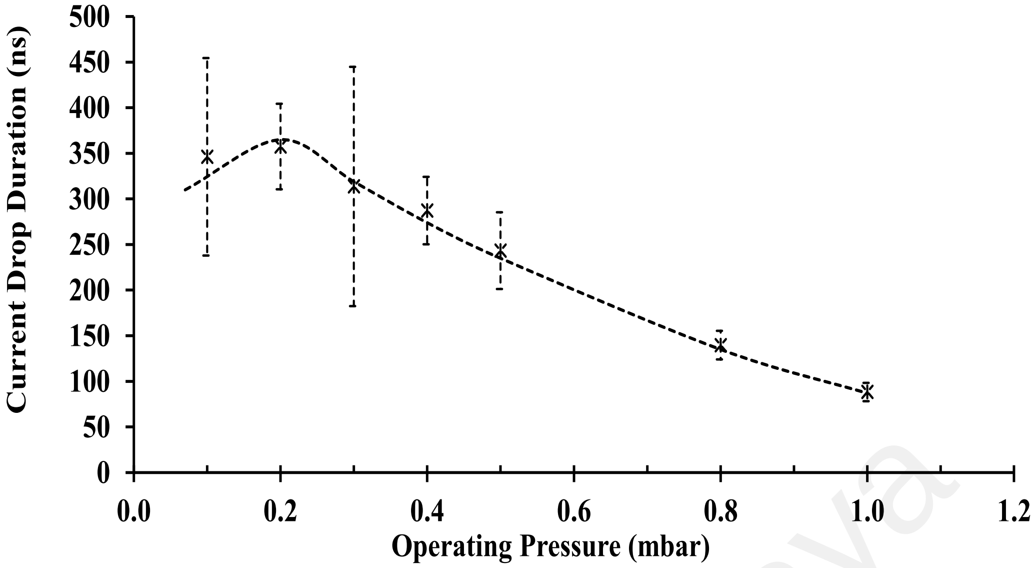

Figure 5.12: Average duration of current drop versus pressure

5.1.4 Anomalous Resistance Modelled using Lee Model

Anomalous Resistance (**AR**) ascribed to the growth of various types of instabilities and micro turbulence play an important role in the pinched plasma. The presence of anomalous resistance is modelled into the current trace fitting analysis using two versions of Lee model code (Lee, 2013), one with the parameter anomalous resistance effect and the other without.

The Lee code models the plasma focus dynamics. It couples the equivalent discharge circuit with plasma focus dynamics, thermodynamics and radiation, enabling a realistic simulation of all gross properties of the pinched plasma. The dynamics of plasma focus discharge is modelled in the code using snow-plow model for the axial phase, slug model with thermodynamics for the radial phase and radiation-couple compression for the pinch phase. All the phases are rigorously circuit-coupled so as to be energy-, charge-, mass- and momentum-consistent. The effect of transit times of small disturbances and plasma self-absorption was incorporated in the code.

Measurement of the discharge current has always being one of the fundamental diagnostic in the plasma focus device and serves as the indicator of gross performance of the pinched plasma. Therefore, the fitting of the measured current waveform through numerical approach using Lee model code could provide a lot of valuable insights of the pinched plasma.

Information that is quickly available from the numerical experiments includes the dynamic, electrodynamics and thermodynamic properties in the various phases of the plasma focus. The code also outputs some radiation properties of the pinch phase including radiation yields in various gases, fast ion beam (FIB) and fast plasma stream (FPS) properties and neutron yields when operated in deuterium or deuterium-tritium mixtures.

The fitting was carried out by input the experimentally measured total current waveform, the capacitor bank parameters, the focus tube parameters and the operational parameters to the Lee model code. Four model parameters, the mass swept-up factor f_m, plasma current factor, f_c for the axial phase, then factors f_{mr} and f_{cr} for the radial phase are adjusted sequentially to give a matching current waveform. Firstly, the axial phase model parameters are adjusted until the computed rising slope of the current waveform and peak current are in reasonable fit with the measured current waveform. This is follow by fits the current dip up to the end of the radial phase by adjusting factors of radial phase. A current trace at 0.2 mbar was chosen and numerically fitted.

The following bank, tube and operating parameters was used.

Bank Parameters: L_o = 117 nH, C_o = 30 μF, r_o = 24 mΩ

Tube Parameters: a = 0.95 cm, b = 3.2 cm, Z_o = 22 cm

Operation Parameters: V_o=13.5 kV, P_o=0.15 torr, MW=4, A=1, $At\text{-}Mol$=2

From this fit, the model parameters are found and tabulated in the Table 5.1 below:

Table 5.1: Model parameters obtained from the fitting at 0.2 mbar

f_m	f_c	f_{mr}	f_{cr}
0.54	0.7	0.9	0.7

A computed current trace fitted to the measured current trace without introducing the anomalous resistance is presented in Figure 5.13. The computed current dip cannot fit the measured current dip suggested that some additional process taken in the 'extended dip' in the measured current trace.

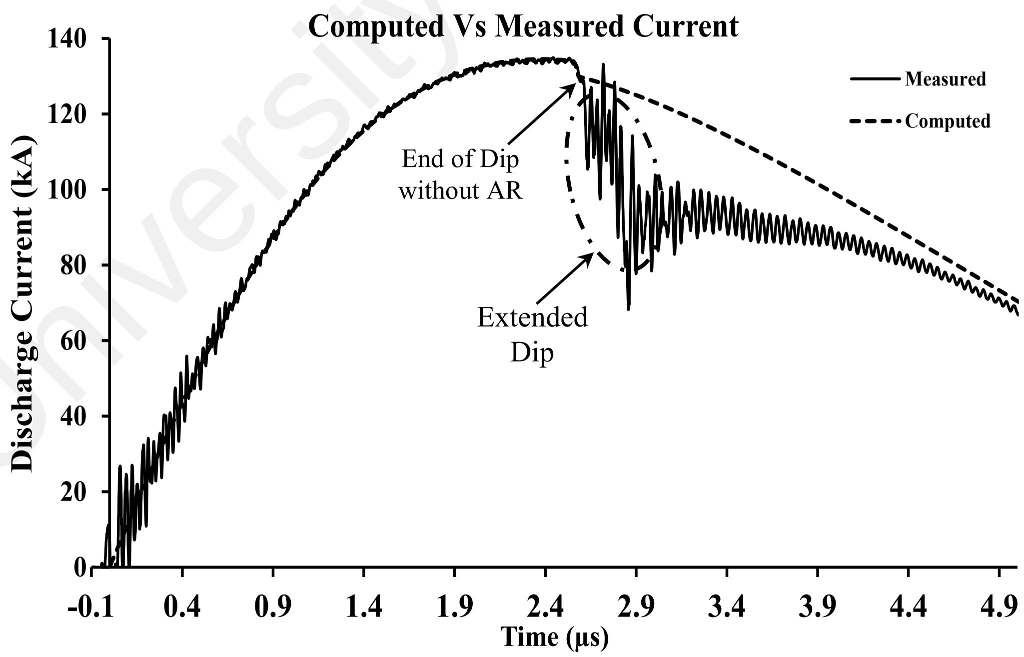

Figure 5.13: Computed and measured current trace at deuterium discharge of 0.2 mbar without anomalous resistivity effect

Second fitting process using the 6 phase Lee model code (Lee et al., 2011). In this version of the model, additional term of anomalous resistance attributed to the different type of instabilities and micro turbulence that occur during and after the pinch phase was incorporated. The anomalous resistance has been introduced as:

$$R = R_0 \, [exp(-t/t_2) - exp(-t/t_1)] \tag{5.1}$$

where R_0 is a constant in the order of 1 Ω, t_1 is the characteristic rise time of the anomalous resistance, and t_2 is the characteristic fall time.

Additional parameter called end fraction was also introduced in the model which terminates the anomalous resistance that appeared as a current dip. In Figure 5.13, there seems to have three dips on the measured current trace. Thus, the fitting was carried out using three anomalous resistance labelled as dip 1, 2, and 3 (Table 5.2).

Table 5.2: Anomalous resistances used for the fitting

Current Dip with Anomalous Resistance (AR)	R_0 (Ω)	t_1 (ns)	t_2 (ns)	Endfraction
Dip 1	0.6	20	100	1.0
Dip 2	0.3	20	150	0.7
Dip 3	0.8	30	170	0.8

Comparison of the computed and measured current trace from the same discharge is shown in Figure 5.14. Good match was seen between the computed and measured current trace.

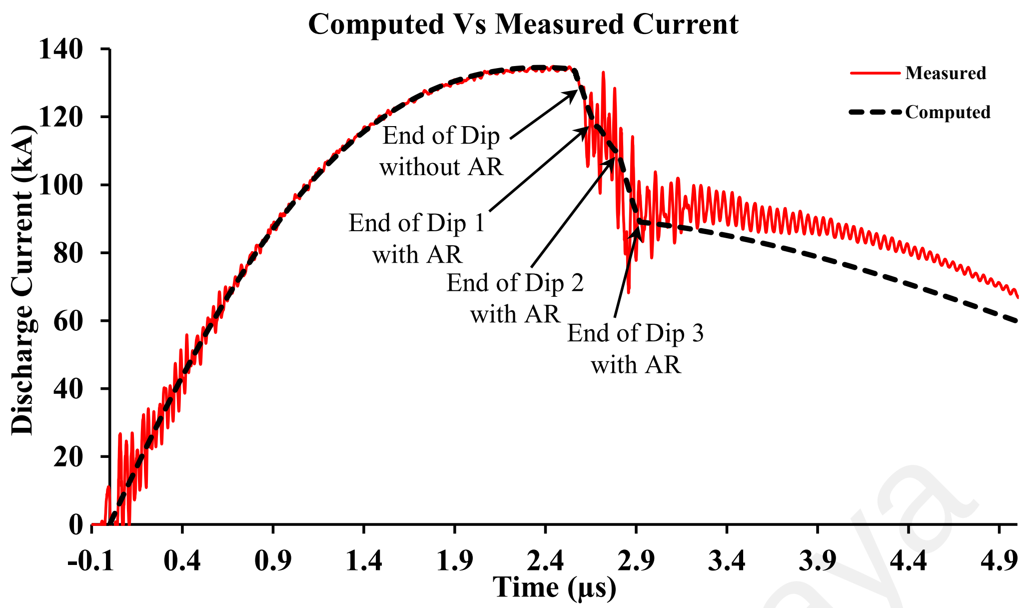

Figure 5.14: Computed and measured current trace with anomalous resistivity effect

Anomalous resistance plays a prominent role and believed to have consumed energy that can lead to a considerable drop in the current dip. Since it has been shown that at lower pressure, the length of current dip is increased which implies that the effect of anomalous resistance and hence the instabilities is intensified.

The growth of these instabilities enhanced at lower pressure can be explained in the following manner. As the plasma column is gradually compressed to a minimum size, the reduction of the column radius leads to an increase in magnetic pressure where magnetic pressure is inversely proportional to the square of plasma column radius. At increasing magnetic pressure, number of ions in the pinch cross section will decrease due to the outflow of the ions from the plasma column. Reduction of the number of ions may drive different kind of plasma instabilities which gets intensified at lower operating pressure since the probability of occurrence of the instabilities is inversely proportional to the number of ions in the plasma column (Scholz et al., 2004).

Following this, lower operating pressure may correspond to lower number of ions in the pinched plasma and leads to the effect of enhanced instabilities. As a result, anomalous resistance is appeared to be higher at lower pressure as indicated by longer current dip in the current signal.

5.1.5 Current Drop and Focused Energy

The current drop during focusing discharge is attributed to the consumption of energy by the pinched plasma. Thus, longer dip in the discharge current suggested more energy is transferred into the pinched plasma. To clarify this, correlation of energy transferred to the pinched plasma (focused energy) to the current drop was analyzed and presented in Figure 5.15. It is clearly noticed that with increase in the current drop, the energy consumed by the pinched plasma also increases. The correlation between focused energy and current drop is quite linear and does depend on operating pressure. Maximum focused energy of ~290 J and current drop of ~46 kA was obtained at 0.2 mbar where the focusing discharge at this pressure occurred at moment near to the maximum discharge current. At pressure below 0.2 mbar, the focusing discharge occurs too early before the discharge current has reached to its maximum and thus weaker focusing discharge was obtained that resulted in decrease in the current drop and thus less energy transferred to the pinched plasma.

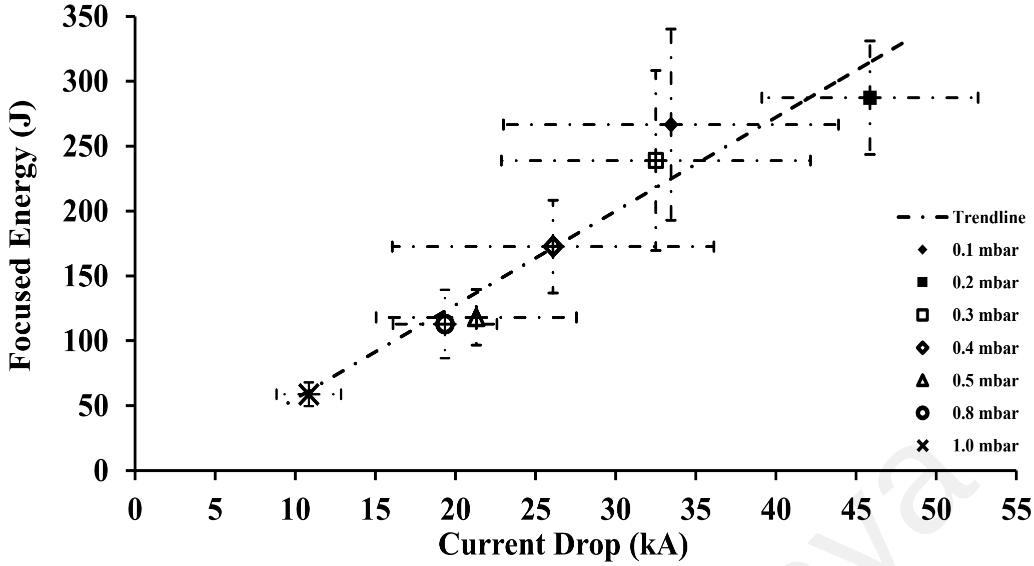

Figure 5.15: Correlation of focused energy with respect to current drop at respective pressure

5.2 Ion Beam Measurement

In this section, the various experimental observations from Faraday cup, biased ion collector and solid state nuclear track detector for ion beam diagnostics are presented and compared. A series of systematic experiments has been carried out to have comprehensive characterization of the ion beams emission in terms of energy, ion beam fluence (ions/m^2), number of ions, intensity (signal amplitude) and ion tracks size at the operating pressure in the range of 0.1 – 0.8 mbar in static gas filling. Significant and reproducible ion beam emission has been obtained at pressure of 0.1 – 0.5 mbar. For discharges of 0.8 mbar above, ion beam emission becomes insignificantly low due to weak focusing discharge. The motivation behind this works is to optimize the plasma focus device operated in beam optimized mode at low operating pressure for a practical used as the pulsed deuteron beam source for the studies of beam-target neutron generation. It is also intended to have more advance and better understanding of the mechanism and variety of physical phenomena taking place in the ions production.

5.2.1 Faraday Cup

Faraday cup was commonly used for ion beam measurement due to its advantage of able to register ions energy from a threshold of few keV to few MeV with sufficient temporal resolution. Ion beam emission from the focusing discharge was first measured with Faraday cup. Ion beam signal measured with Faraday cup at different operating pressures are presented in Figure 5.16. The ion beam signal measured with Faraday cup showed a multiple peaks structure. The amplitude of the ion beam signal is observed to increase at lower pressure and occurred at earlier time. It is clearly observed that there is at least two peaks can be identified in the Faraday cup signal where the first peak occurred at the moment near to the voltage spike. No peaks were observed before the voltage spike indicated that the registration of the ion beam signal is originated from the focusing discharge.

The first peak is believed to be the pick-up of strong photon emission (X-rays or ultraviolet radiation) during the focus formation since the detector can respond to photon by photoelectric effect (Kelly et al., 1998; Mohanty et al., 2005). Therefore, for each of the focusing discharge only the second or later peaks in the Faraday cup signals is considered as the registration of ion beam emission. Profiles of the ion beam signal measured with Faraday cup at each pressure were seen to exhibit similar features.

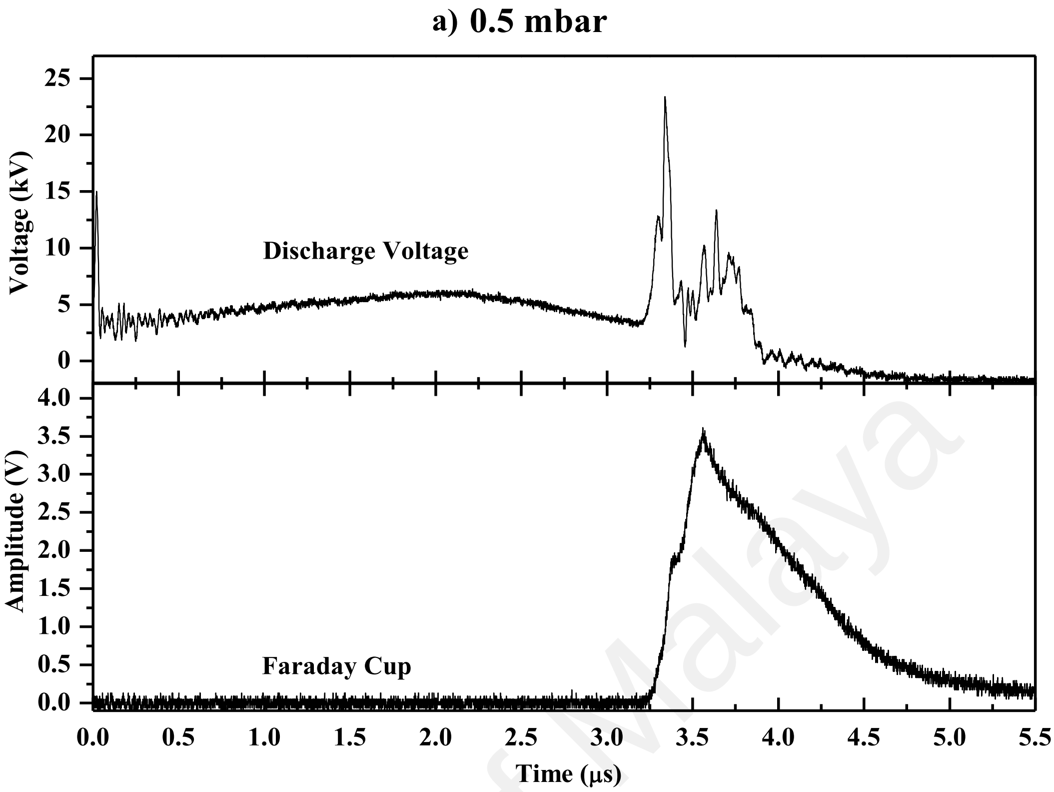

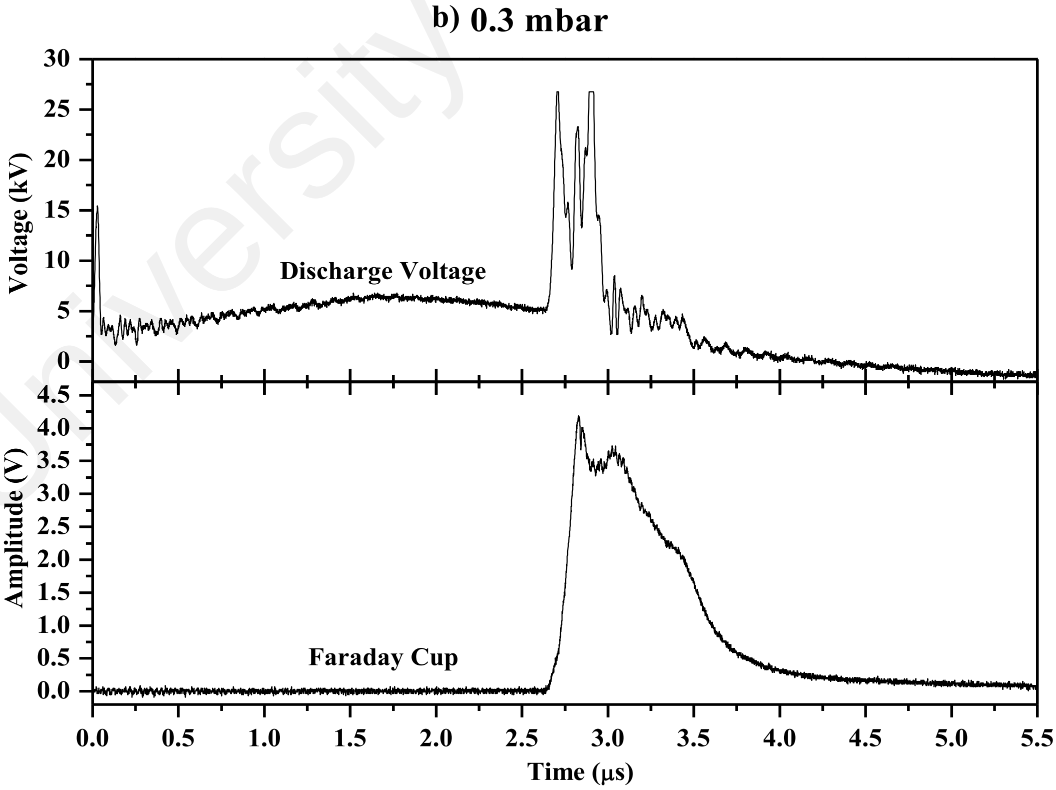

Figure 5.16: Faraday cup signal with discharge voltage signal at pressure of a) 0.5, b) 0.3 and c) 0.1 mbar

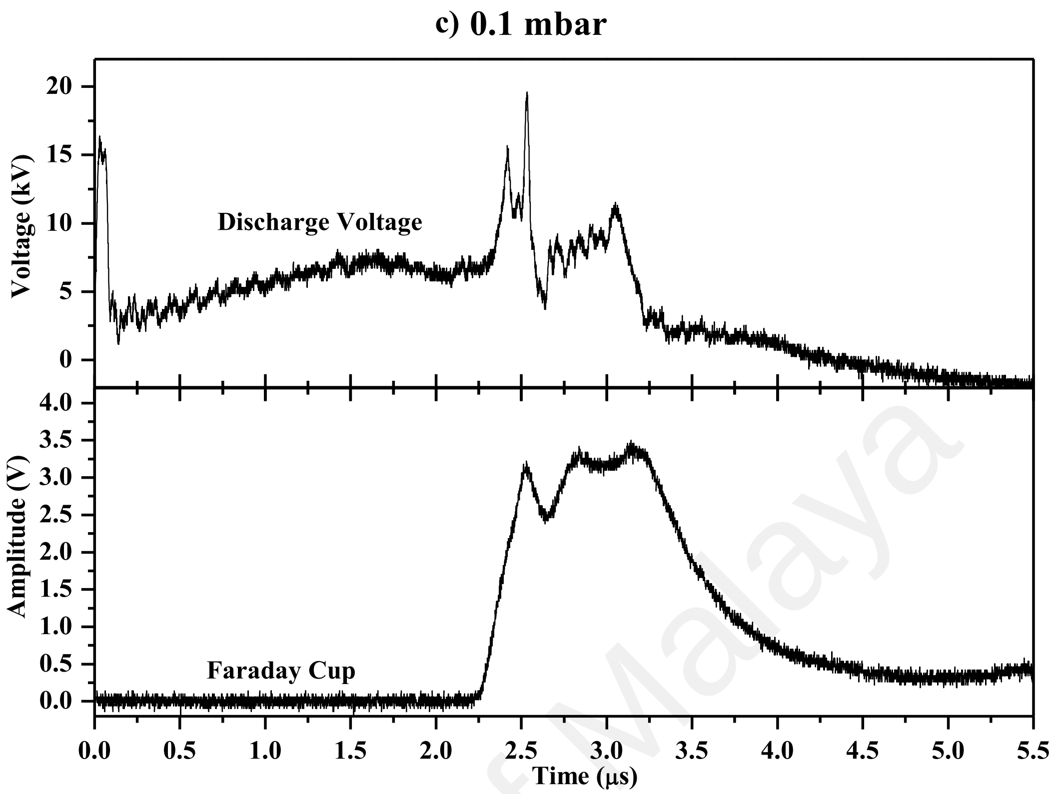

Figure 5.16: Continued

The ion beam velocity, energy, intensity, ion beam fluence and ions number have been determined from the Faraday cup signal. The ion beam velocity was estimated using the time of flight technique (TOF) by taking the ratio of the distance from the anode tip to Faraday cup over ion beam flight time. Typical ion beam signal at 0.2 mbar registered with Faraday cup together with the discharge voltage signal is demonstrated in Figure 5.17.

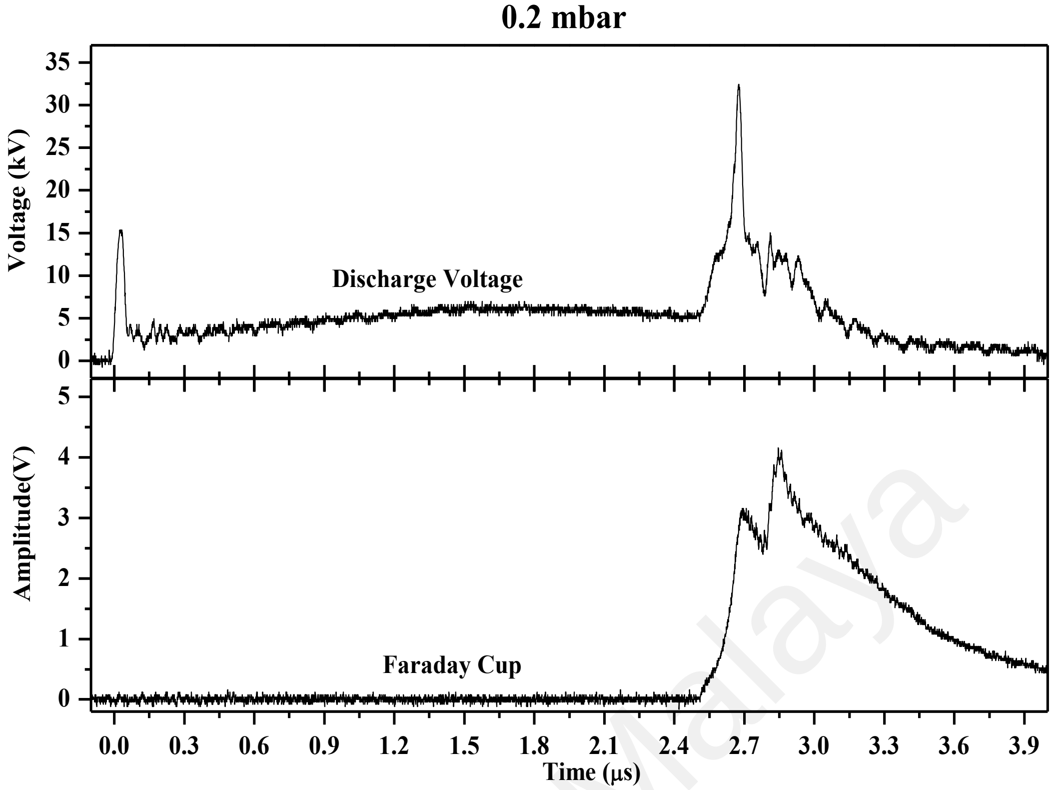

Figure 5.17: Time-of-flight ion beam measurement using Faraday cup at 0.2 mbar

The flight time of ion beam was determined by taking the time difference between the peak of voltage spike to the second peak in the Faraday cup signal as illustrated in Figure 5.18 with 1 μs window of the same discharge. Using the time of flight method, the ion beam energy at this shot is estimated to be about 58 keV. Average ion beam energy at 0.2 mbar is determined as ~ (52 ± 7) keV.

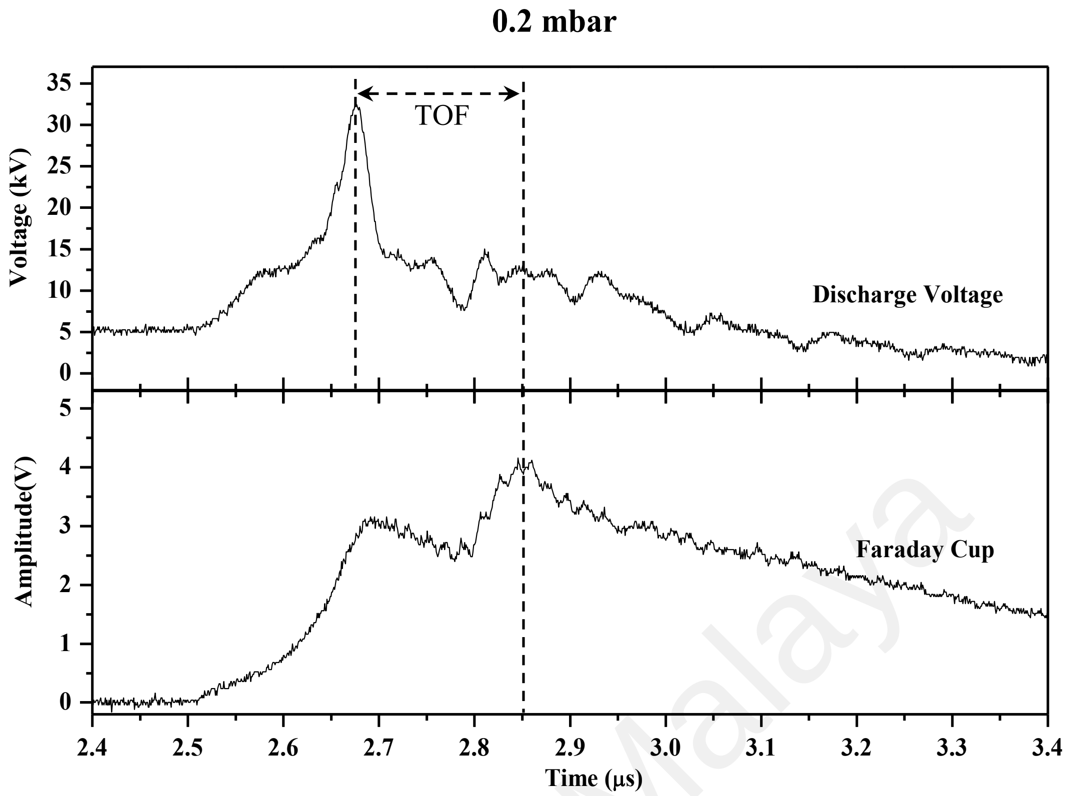

Figure 5.18: Same discharge with time window of 1 μs to show the ion beam flight time

Attempt was made to find the average ion beam energy determined from the Faraday cup signal at all pressures that produces significant ion beam emission. In each series of discharge, the first 5 shots were excluded from calculation which considered as conditioning shots. Ion beam energy determined from the average of 5 shots for all operating pressures were summarized in Figure 5.19. The calculation was done based on the ion peak of highest intensity in the Faraday cup signal. Noted that, the ion beam energy increases at lower pressure until a maximum was obtained at 0.2 mbar. Further decrease in the operating pressures lead to drop in the ion beam energy. This is believed to be due to poorer formation of current sheath that deteriorates the focusing discharge. Ion beam energy was not shown at 1.0 mbar because the intensity of the signal was very weak and would not be resolved clearly in this diagnostic technique. In the pressure of 0.1 – 0.8 mbar, ion beam energy of 7 – 200 keV has been obtained.

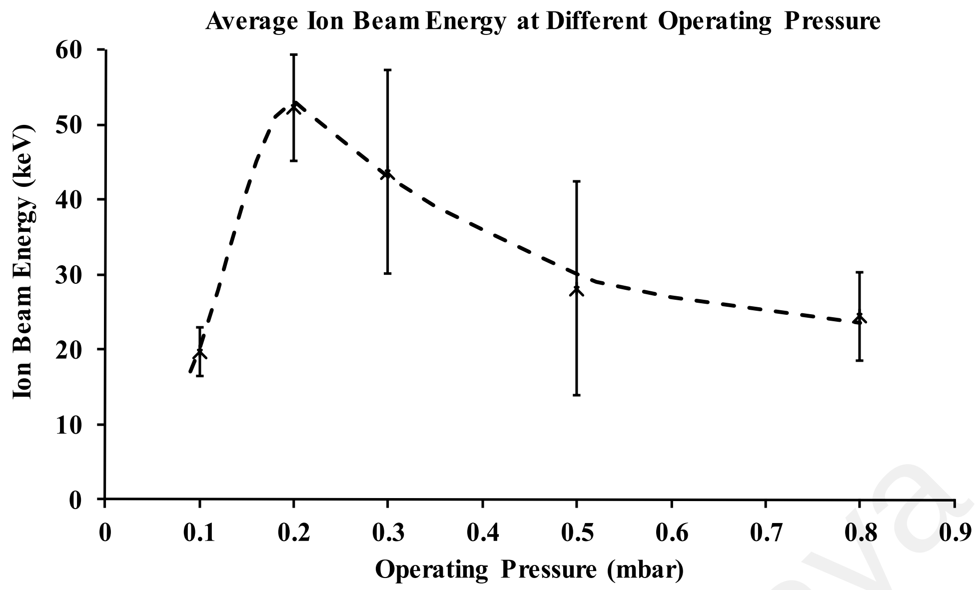

Figure 5.19: Average ion beam energy determined from Faraday cup signal

Despite the demerits of low signal to noise ratio and the effect of secondary electron emission, Faraday cup do offer a relative advantage for the ion beam fluence and ions number measurement. Faraday cup was chosen in view of its larger detecting surface area that could collect all the incoming charged particles directed to its collector. By integrating the Faraday cup signal with respect to time and excluded the part of signal contributed by photon emission, total charges collected can be found and hence one can determine the total number of ions collected by consider the amount of charge of one deuteron ion. The total number of ions emitted per shot at the end on direction was determined. The average number of total ions per shot is presented in Figure 5.20. Each data point on the graph was average over 5 shots. It is clearly shown that the total number of ions is highly dependent on operating pressure. In this pressure range, the average number of ions emission is at the same order and lies in the range of (1.47 – 3.87) x 10^{11} ions per shot. The highest number of ions was obtained at 0.2 mbar with average number of ions estimated as ~ (3.87±0.21) x10^{11} ions per shot.

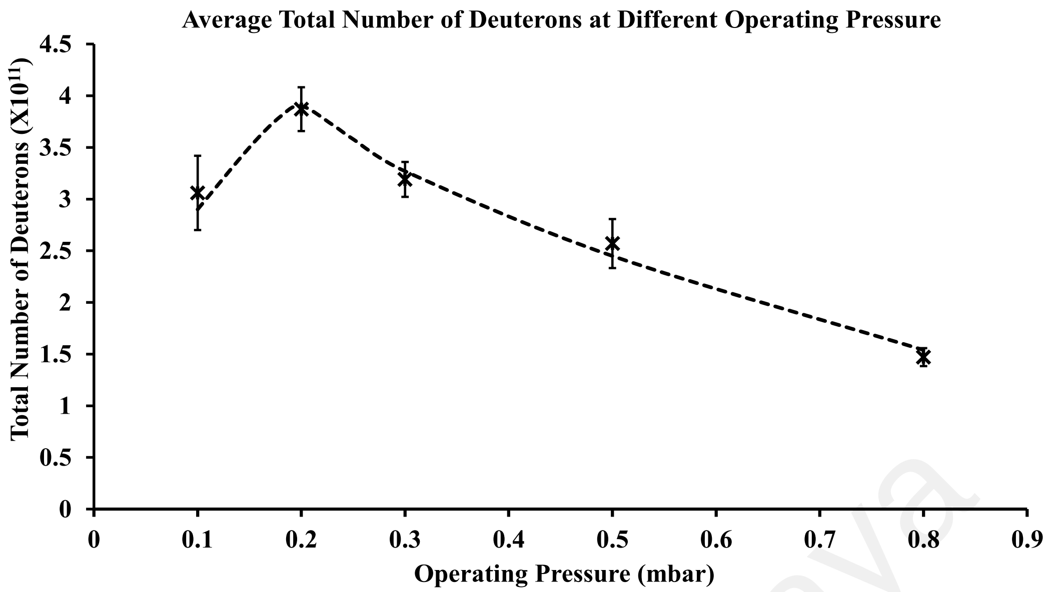

Figure 5.20: Average total number of ions per shot at different pressure

Ion beam fluence was calculated by dividing the total number of ions to the detector area of the Faraday cup. The ion beam fluences as a function of pressure is displayed in Figure 5.21. Each data point on the graph has been average over 5 shots. Average ion beam fluences in the order of 10^{15} ions/m^2 was estimated for all the pressure examined with highest fluence also obtained at 0.2 mbar.

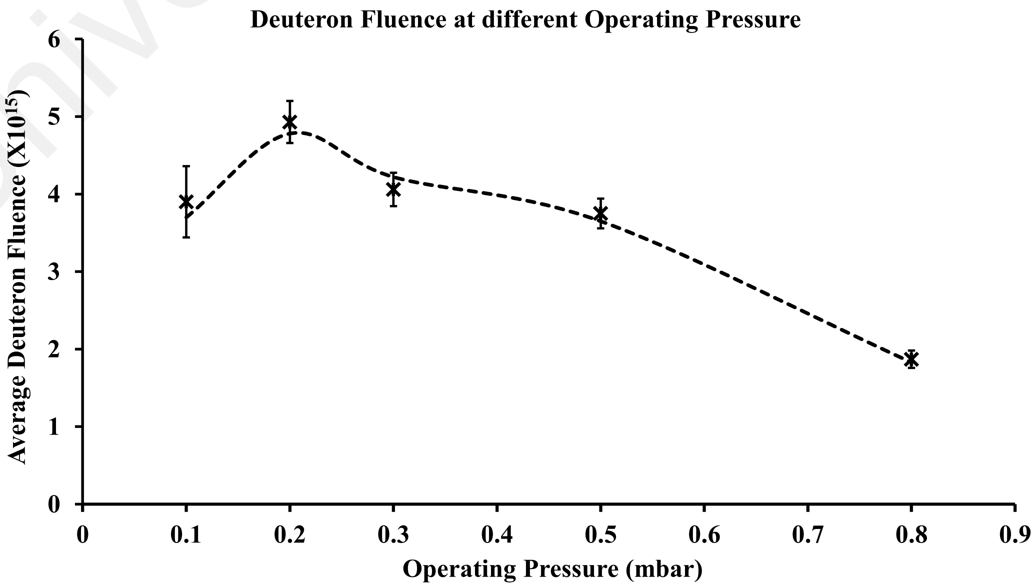

Figure 5.21: Average ion beam fluences per shot at different pressure

The ion beam intensity (signal amplitude) was also examined based on the highest peak of the Faraday cup signal and plotted as a function of pressure as shown in Figure 5.22 with each data point averaged over 5 shots. At decreasing pressure, the intensity of ion beam emission is increased until a maximum at 0.2 mbar. Overall results of Faraday cup measurement showed a consistent result for the ion beam energy, ion beam fluences, ions number and ion beam intensity as a function of pressure.

The analysis shown that Faraday cup can be employed to determine ion beam energy upon very careful analysis. However in case of multiple voltage spikes, it is hard to correlate the voltage spikes to the ion beam signals and the estimation resulted uncertainty in the ion beam energy calculated with the time of flight technique. The use of two or more biased ion collectors for time of flight have been employed subsequently and presented in following sections.

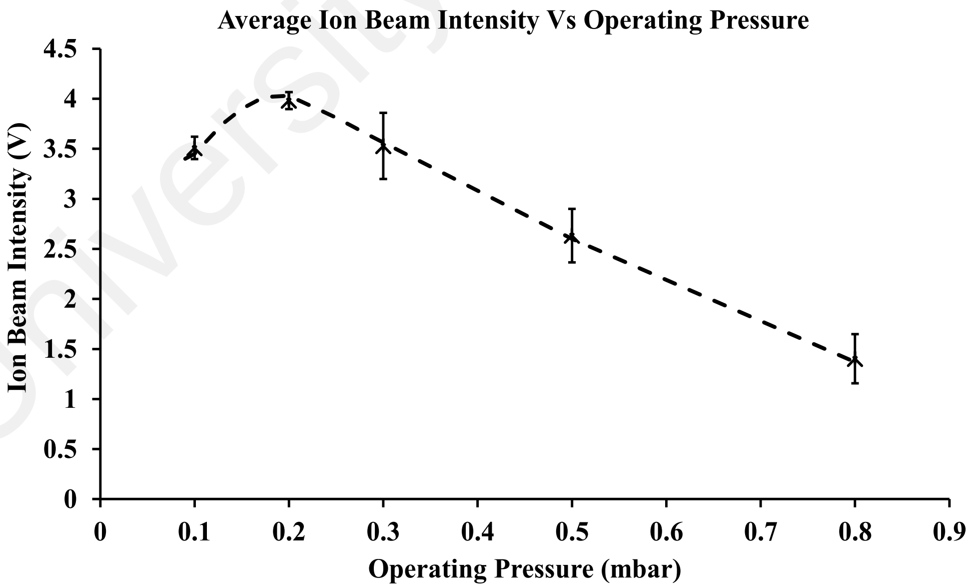

Figure 5.22: Average ion beam intensity per shot at different pressure

5.2.2 Biased Ion Collector

In this part of ion beam measurement, two ion collectors made of copper metals biased at negative potential were employed. Ion beam energy was determined from the time resolved ion beam signal registered by the two biased ion collectors using time-of-flight method. The purpose of the applying negative potential is to screen out the pickup of secondary electron emission and also co-moving electrons within the ion beam. Typical discharge voltage and ion beam signals registered by two biased ion collectors is depicted in Figure 5.23.

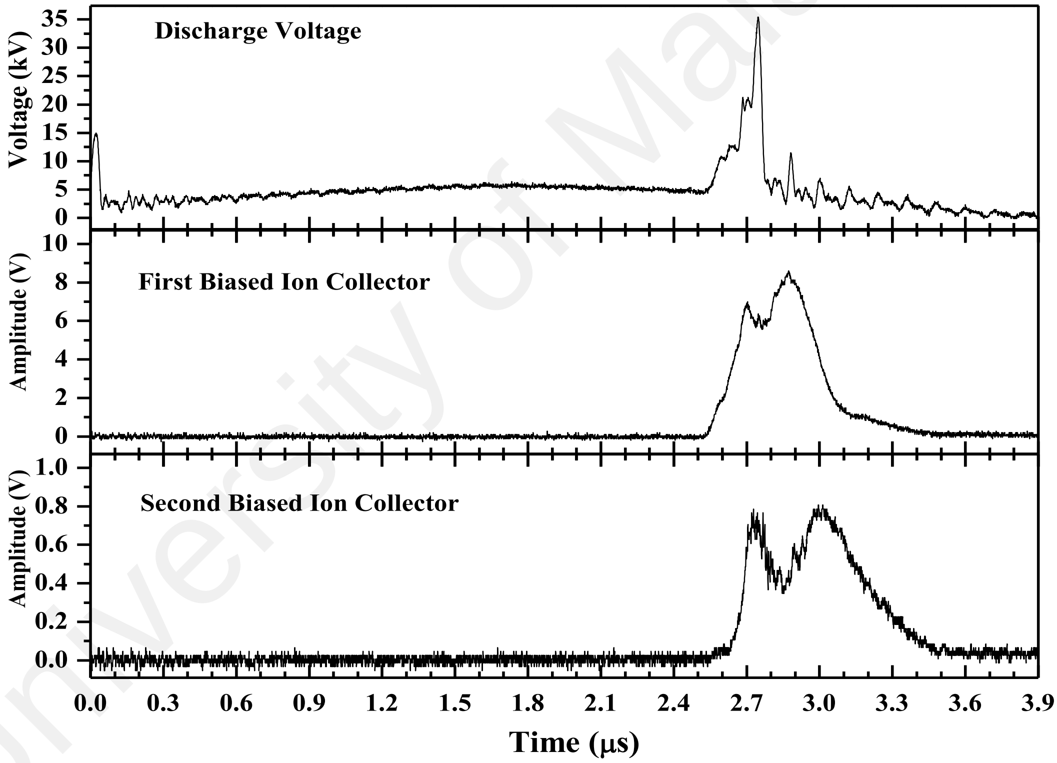

Figure 5.23: Typical discharge voltage and biased ion collectors signals at 0.2 mbar

The waveforms of the ion beam signal registered by biased ion collector compared to that measured with Faraday cup are clearer. It is noticed that two peaks were often identified in both biased ion collectors. In fact, it has been observed that most of the focusing discharge producing ion beam signals with these multi peak structures and in some cases there are more than two peaks can be seen. No ion beam signal was registered before the focusing discharge which is consistent to the observation using Faraday cup.

To have better view on the time of flight measurement, same discharge is enlarged with time window of 1 μs as illustrated in Figure 5.24. There is always observed a peak registered simultaneously in both biased ion collector and occurs at the same time or near by the voltage spike. This region has been highlighted in the graph, believed to be due to photon emission. The ion beam emission is first pick up by the first biased ion collector as a pulse depicted as peak 2 and registered after some delay of time at second biased ion collector depicted as peak 2' due to longer distance travelled by the ion beam. The pulse registered at second biased ion collector also exhibited a broader pulse shape compared to the pulse in first biased ion collector. Time of flight of the ion beam can be deduced from the time interval of peak 2 to peak 2'. It is determined to be 120 ns in shot shown in Figure 5.24. Thus, ion beam energy is determined to be 53 keV.

From this time of flight, one can correlate back the starting time of the ion beam emission. This can be done by determining the ion beam's flight time from anode tip to first biased ion collector. In this shot, the starting time of the ion beam emission is deduced to occur at 2.734 μs instead of 2.75 μs (peak of voltage spike). Following this observation, the calculation based on the time difference between the peak of voltage spike to the peak of ion beam signal to determine the ion beam energy has shown to have more uncertainty.

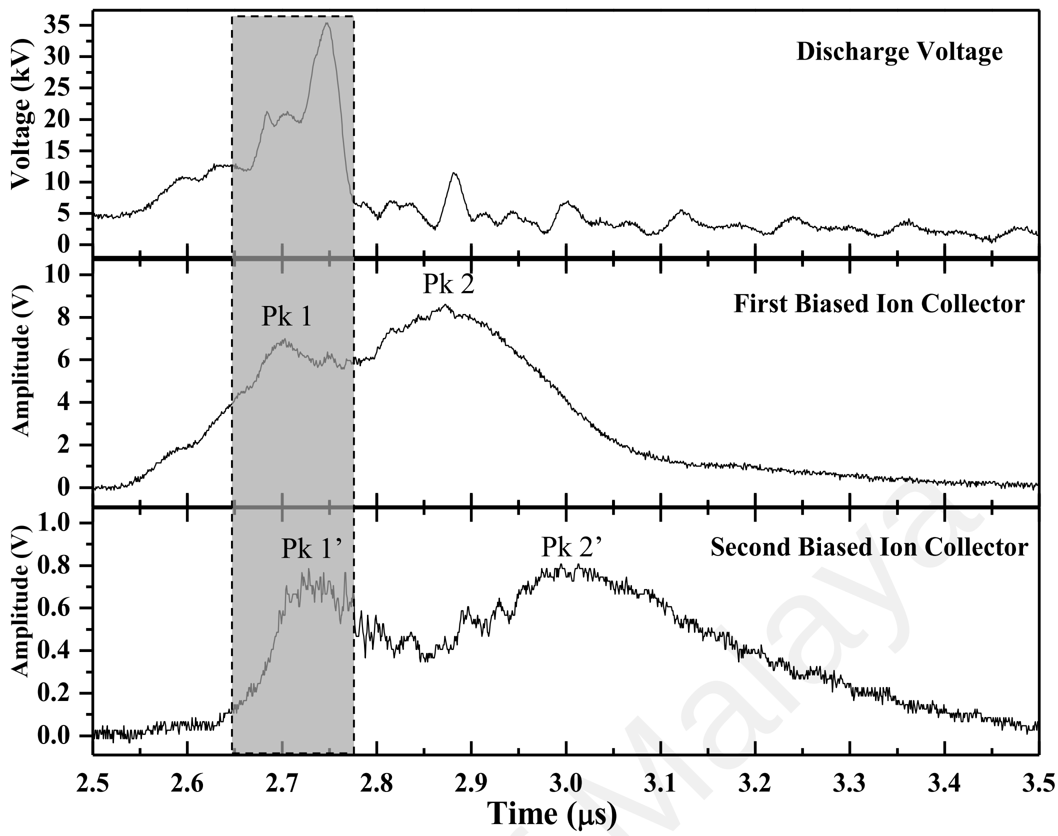

Figure 5.24: Discharge voltage and ion beam signals with 1 μs time window of the same discharge

The analysis of ion beam energy at each operating pressure was done and the time of flight is determined from the highest ions peak in each ion beam signal. Thus, the energy determined is referred to a group of ions of highest intensity. Correlation of the average ion beam energy as a function of pressure is depicted in Figure 5.25. Each data point is averaged over five shots. Average ion beam energy calculated in the pressure range of 0.1 – 0.8 mbar varied from 21 – 53 keV. Ion beam energy was not shown at 1.0 mbar because of weaker focus action that results in less ion beam emission which is hardly resolvable.

At pressure below 0.8 mbar, ion beam energy is noted to increase as pressure decrease until a maximum obtained at 0.2 mbar. Further lowering of the pressure below 0.2 mbar leads to a decrease of ion beam energy. The increase of ion beam energy is consistent with the strength of focusing discharge. At 0.2 mbar, average ion beam energy is determined to be (53 ± 13) keV. It is worth to notice that the average ion beam energy calculated in this diagnostic is in agreement with the Faraday Cup measurement. Ion beam measured in this diagnostic techniques has been determined to have energy in the range of 18 – 350 keV for the pressure range of 0.1 – 0.8 mbar.

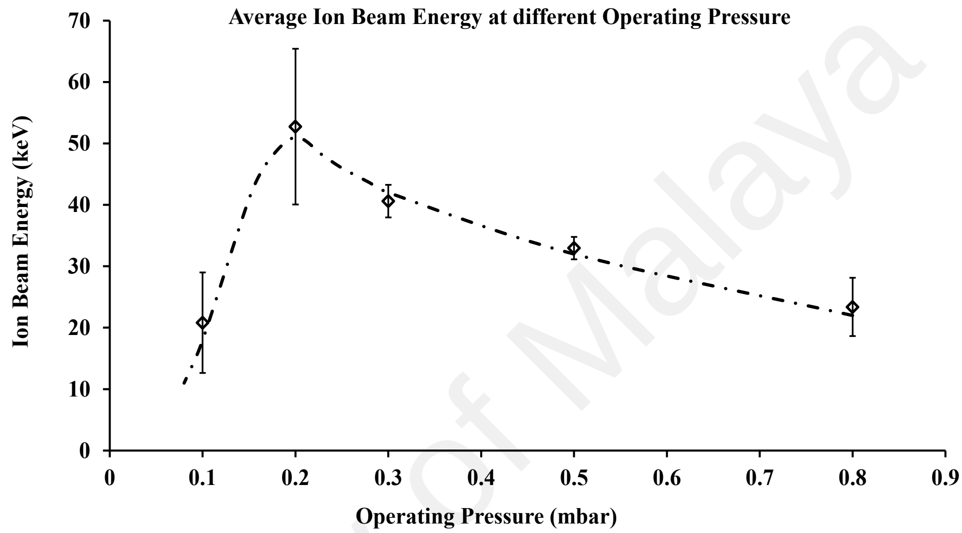

Figure 5.25: Average ion beam energy as a function of pressure

Even though it is not quite accurate to consider the ion emitting region from the anode tip but it is sufficient as a rough estimation where the error in the ion beam time of flight is within 5 % if the ion emission region is at 1 cm above the anode tip. Moreover, with two biased ion collectors the ion beam signals are better resolved where the components of high and low energy ions can be identified for the case of multi ion peaks. Upon careful analysis, these components of ions can be examined and identified separately in both biased ion collectors.

Another time of flight ion beam signals is shown in Figure 5.26 where three peaks can be identified and labelled as peak 1, 2 and 3. Peak 1 in both detectors is seen to rise in accordance with the voltage spike and hence the highlighted region is considered corresponded to the photon-emission period. Peak 2 and 3 registered by the biased ion collectors were resolved and found to correspond to ion beam of different kinetic energy. Peak 2 and 3 were determined to have kinetic energy of 106 keV and 24 keV, respectively. The intensity of ion beam for peak 2 is less compared to the peak 3 suggested that component of ions with higher energy has less number than the lower energy component. Though the shot-to-shot variation, component of ions with lower energy is observed to be more in comparison to high energy ions.

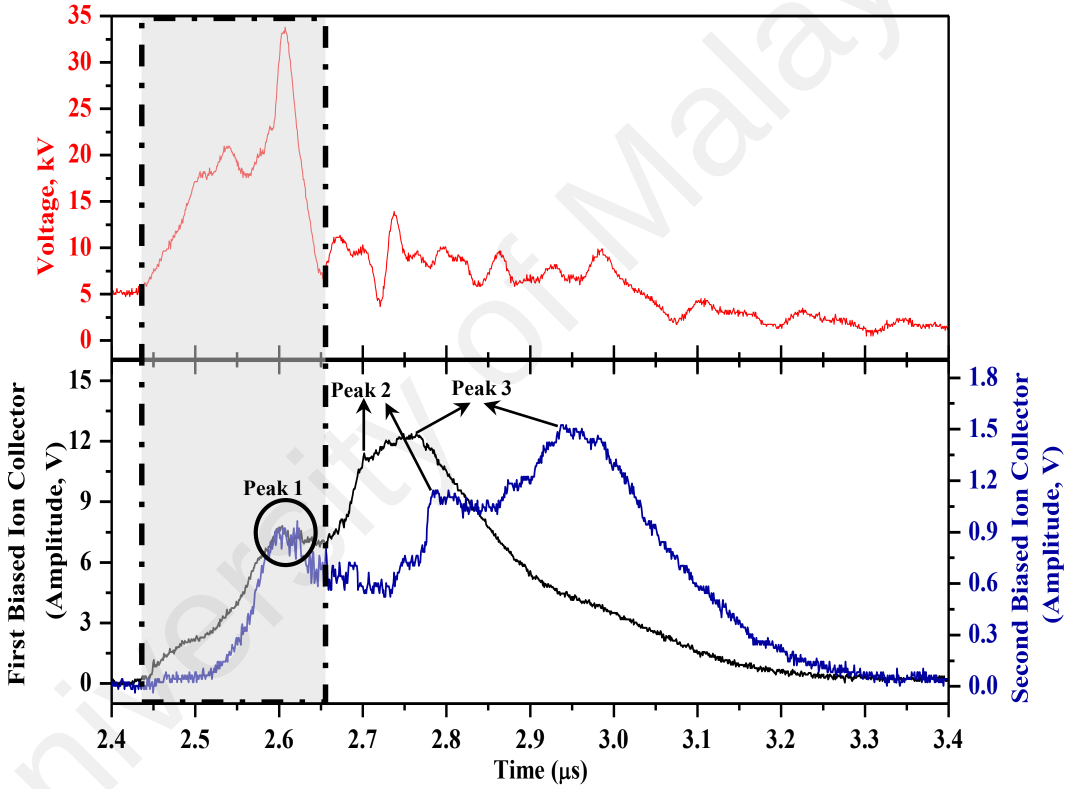

Figure 5.26: Discharge voltage and ion beams signal at 0.2 mbar

Since the discharge above shown only single voltage spike which corresponded to one plasma compression, thus it is speculated that the low energy and high energy component of the ions were emitted at different compression phase during a focus event. During the radial compression of the plasma, sudden increase in plasma impedance is resulted at the maximum compression and when micro-instabilities set in. The enhanced localized electric field accelerated the ions from the plasma column. Therefore, two instants of ion beam may be corresponded to the maximum compression and the onset of instabilities.

The correlation of ion beam intensity (signal amplitude) as a function of pressure is also studied and summarized in Figure 5.27. Since the data is plotted based on the highest ion peak in the ion beam signal, thus the results is a representation of ion beam emission with highest intensity. The graph shows that as pressure decreased, more ions were emitted. Highest ion beam intensity has been obtained at 0.2 mbar. This trend is similar to the correlation of ion beam energy, ion beam fluences and number of ions per shot with operating pressure. From the overall results, it can be concluded that the characteristic of ion beam emission is greatly dependent on the operating pressure and the focusing discharge. At present electrode configuration, 0.2 mbar was tested to be the most favourable pressure for ion beam production in terms of highest ion beam energy and significant ion beam fluences with good reproducibility.

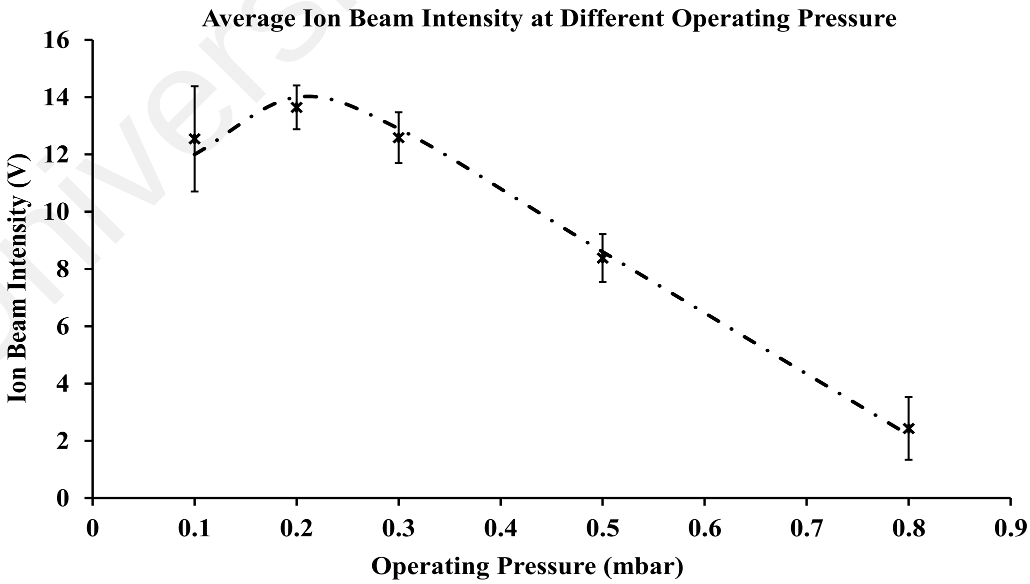

Figure 5.27: Ion beam intensity as a function of pressure average over 5 shots

In addition to ion beam, the biased ion collector also registered the plasma jet at time of later than 15 μs after initial breakdown. The plasma jet contained the impurities from the anode material ejected due to bombardment of energetic electron beam. Detail of the plasma jet and their effect on hydrogenated amorphous silicon thin film has been reported in our previous work (Ngoi et al., 2012). Evidence for the presence of plasma jet emission from a focusing discharge is shown in Figure 5.28 at a compressed time scale. The plasma jet is observed with time of flight of about 31 μs. The ion beam signal shown was measured by directly exposed the biased ion collector to the source without any use of aperture and therefore it can be seen there is pickup of impurities before the focusing event. The intensity of plasma jet emission is always less than the ion beam and in this case the velocity of the plasma jet has been deduced to be about 0.87 cm/μs using the same time of flight technique. Almost similar value of the plasma jet velocity was measured in our previous work with velocity of 1.2 cm/μs in argon discharge (Ngoi et al., 2012).

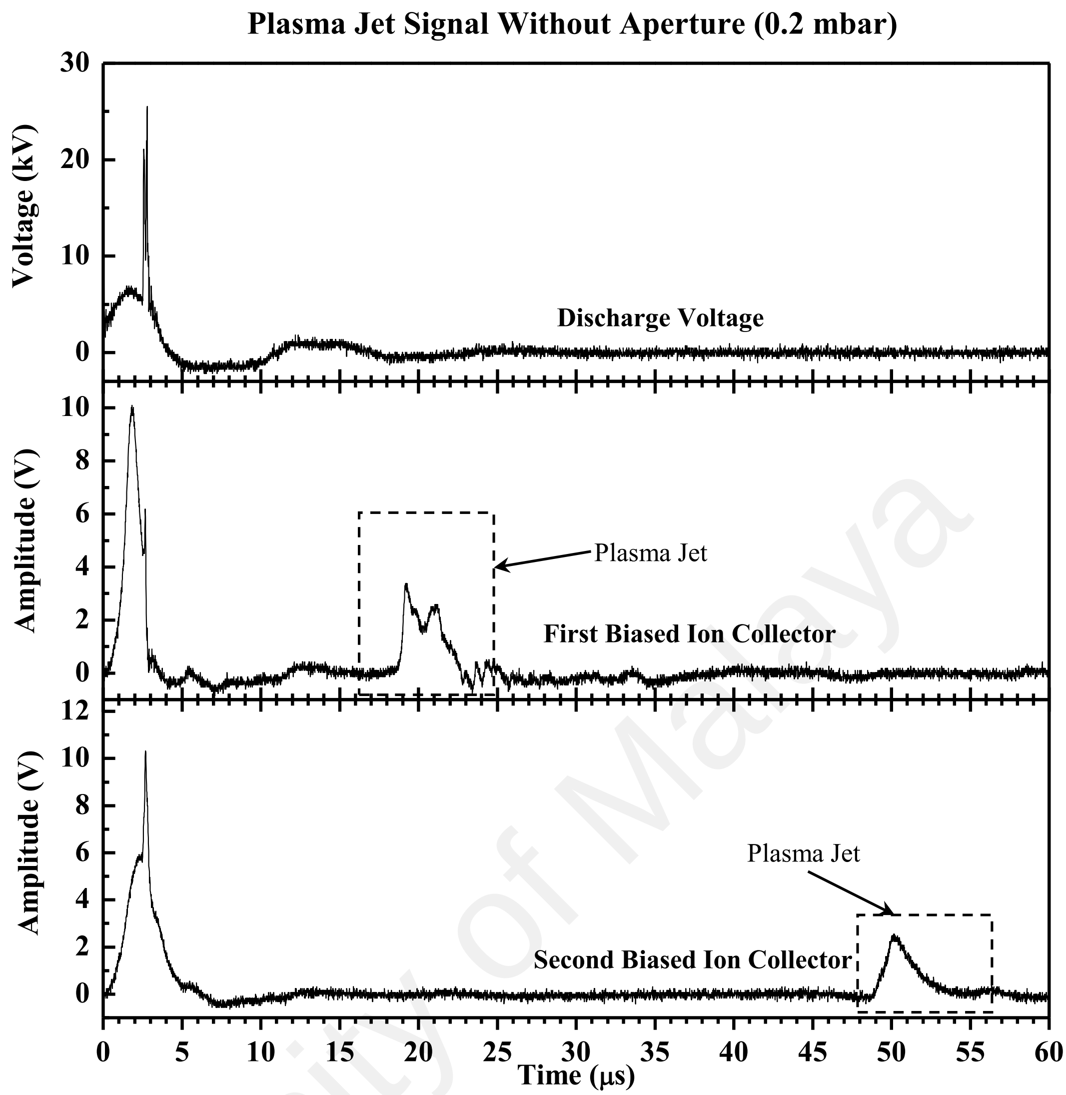

Figure 5.28: Evidence of plasma jet signal at 0.2 mbar focusing discharge

In the current experiment, bombardment of plasma jet on the biased ion collector are reduced significantly by using a 2 mm aperture. The aperture was located before the biased ion collector. Figure 5.29 shown the measured signal with the aperture. The pickup of the plasma jet signal was observed in the ion beam signal registered by first biased ion collector and not observable at the second biased ion collector.

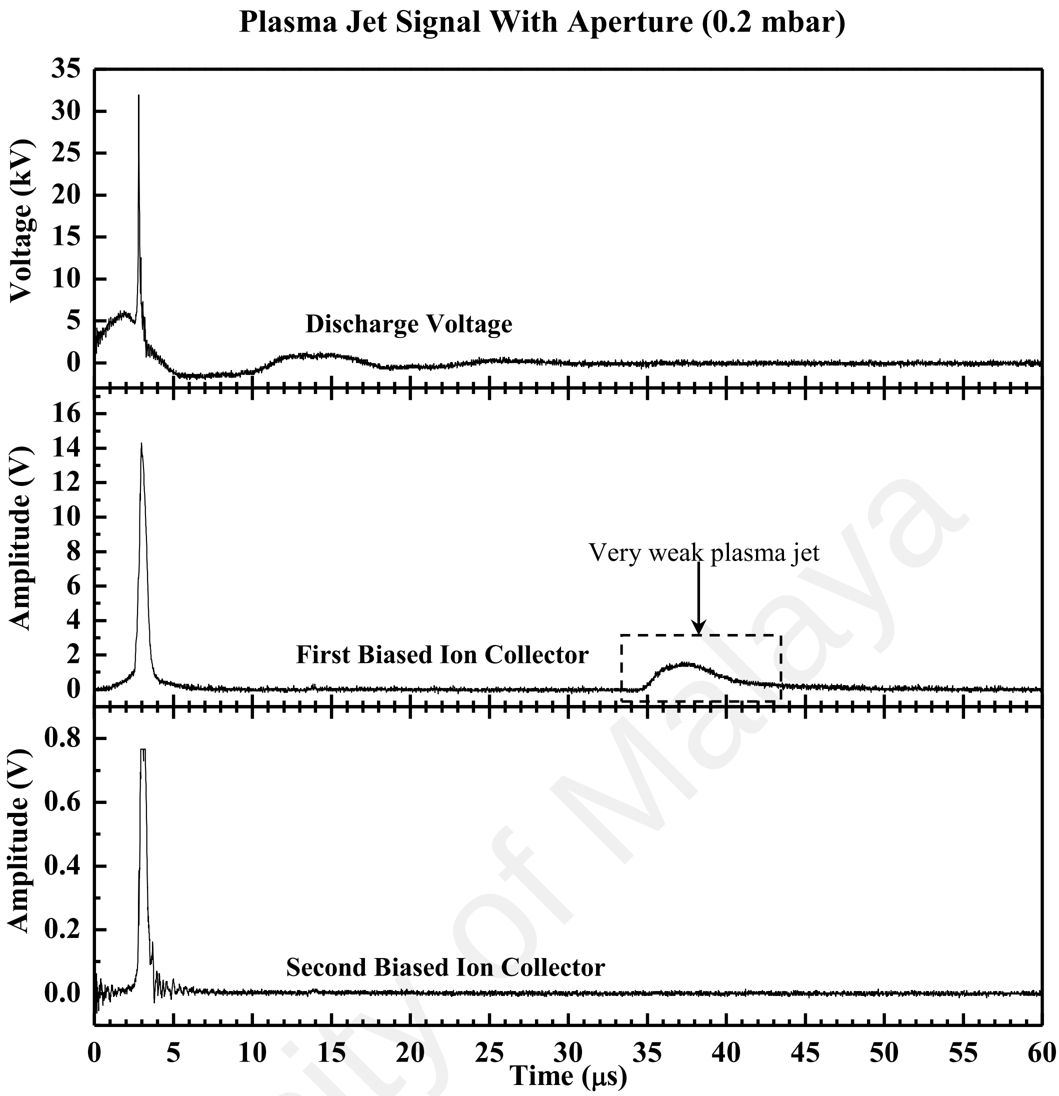

Figure 5.29: Attenuation of plasma jet signal after the aperture at 0.2 mbar

5.2.3 Solid State Nuclear Track Detectors

Time integrated measurement of the ion beam emission has been investigated with solid state nuclear track detectors, CR-39. This diagnostic provided a supplement for a more comprehensive study of the ion beam emission in conjunction with previous diagnostic technique. However, the accuracy of the analysis is dependent on the saturation limit of the detector which is greatly dependent on the size of the ion tracks (influence by etching time and ion energy) and ion beam fluences (Gaillard et al., 2007). For ion tracks size of 3 μm above, the saturation limit is 10^{11} particles/m^2. In this work, effect of etching time on the exposed detector and angular distribution measurement of ion beam emission has been performed. Information of the size and density of ion tracks has been determined from the CR-39 detector.

We had examined in previous experiment that consistent ion beam emission was obtained at pressure of 0.2 mbar, hence the experiment with CR-39 discussed here is for 0.2 mbar only. For all the fresh exposed CR-39 detector, the ion tracks formed were not visible even under microscope view. Therefore, all the detectors exposed have to be etched with the standard solution for several hours to enlarge the tracks size formed. Procedure for the etching of the detector was described in better detail in chapter 4. In all the experiments, a few conditioning shots were run before exposed the detector to ion beam emission. A metal strip was used as a shutter to isolate the detector from the conditioning shots. In this way, we can control the detector to expose to only selected discharge.

5.2.3.1 Effect of etching time

Experiment was first carried out to investigate the effect of etching time on the exposed detector. The purpose is to obtain a suitable etching time for the analysis of ion tracks. Size of the ion tracks on the CR-39 at etching time of 2 – 8 hours with time interval of 1 hour has been studied. In this study, an aperture of 1 mm diameter was used and located before the CR-39 detector. The distance from the anode tip to detector is 69 cm. An exemplary picture of the CR-39 detector irradiated to single focusing discharge and etched at different time is presented Figure 5.30.

From the comparison of images below, the ion tracks were denser at longer etching hours. At too short etching time such as 2 hours, no visible ion tracks can be identified in the optical microscope image. It is seen that the size of the ion tracks increases at longer etching time. In these etching time, crater diameter ranged from 1.0 µm – 5.0 µm has been measured. Average crater diameter of the ion tracks were determined to be 1.3, 1.5, 1.7, 1.9, 2.0 and 2.4 µm for etching time of 3, 4, 5, 6, 7 and 8 hours, respectively. Average size of the ion tracks were determined by taking average over more than 10 ion tracks at three different areas.

In this study, etching duration of 5 – 7 hours was found to be suitable to measure the formed ion tracks. Average crater diameter of the ion tracks were varied with a slight difference only in these range of etching duration. At least 5 hours of etching duration is suggested to induce most of the ion tracks to be visible for quantitative analysis. Noticed that at etching time of 6 hours, a clear contour of the ion tracks can be identified with average crater diameter of 1.9 µm. With further increase in the etching hour to 7 hours, the average size of the ion tracks were increase slightly only to 2.0 µm. Thus, an etching time of 6 hours was preferred which is sufficient to give a better resolution of the ion tracks to be viewed under optical microscope. It is interesting to note that after 8 hours etching, the density of the ion tracks were seems to be decreases as some of the smaller ion tracks size has been over etched and diminished.

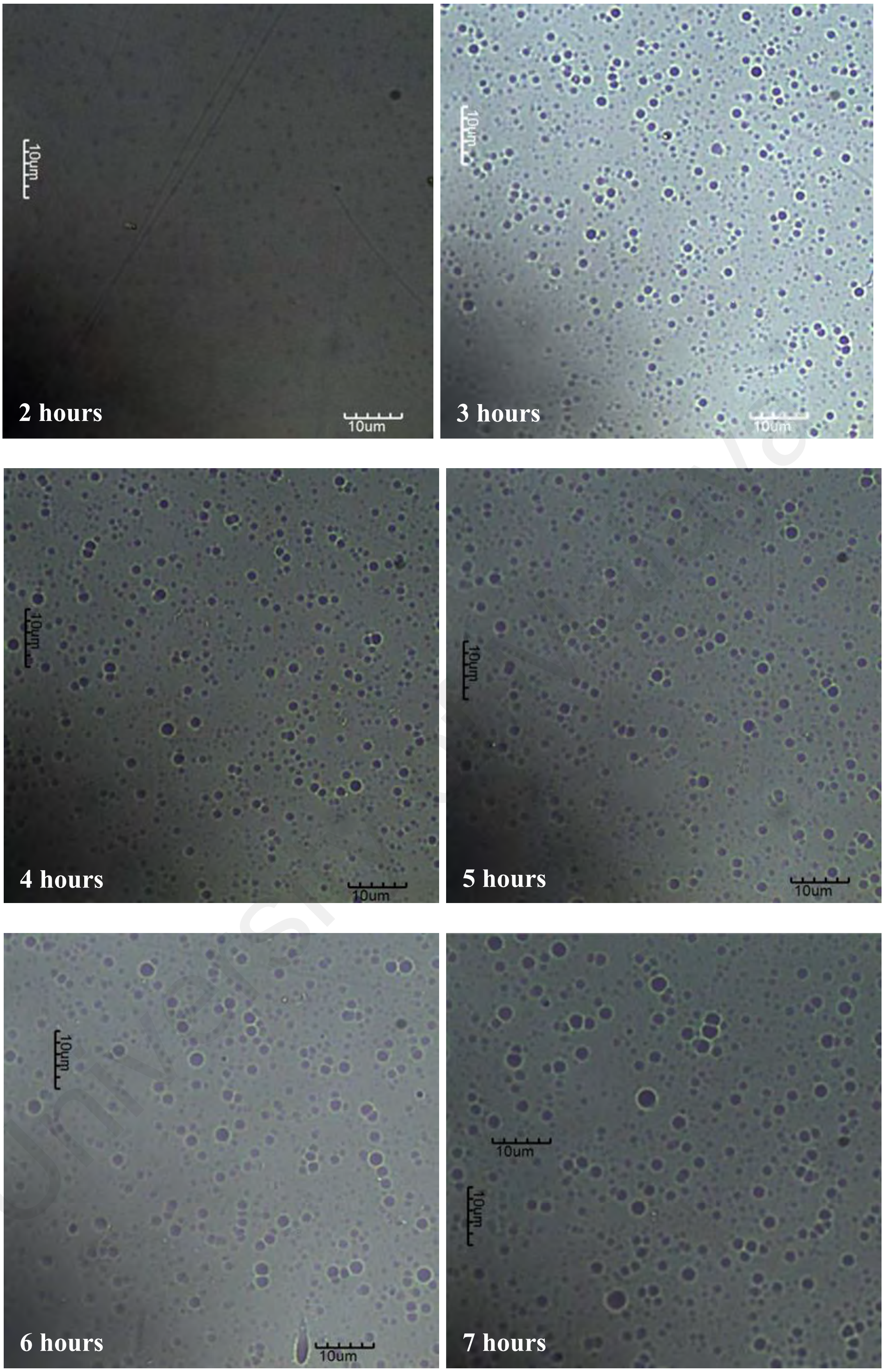

Figure 5.30: Optical microscope image of CR-39 at 2, 3, 4, 5, 6, 7 and 8 hours etching time under 1000X magnification power

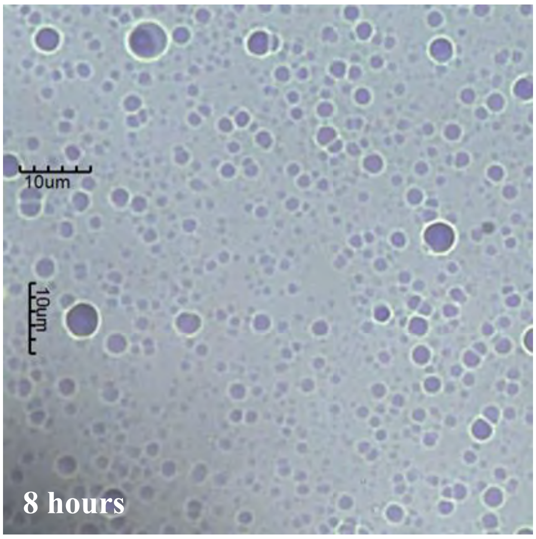

Figure 5.30: Continued

Overall results found that either too short or too long duration of etching is not good for the etched tracks. At too short etching time such as 2 hours may not be sufficient for the ion tracks to be visible even under optical microscope or the induced tracks were still too small or diffusive to be measured. Furthermore, most of the ion tracks formed was of crater diameter less than 1 μm which is below the resolution of optical microscope. On the other hand, at longer etching hours the smaller tracks becomes bigger and more apparent. However, too long etching time may cause the tracks size become too big or too shallow to be identified and might be overlapped with other ion tracks thus resulted in difficulties for the measurement. This showed that an over etched detector could lead to loss of some information and should be prevented. The density of the ion tracks at 8 hours etching time was determined to be 9.8 x 10^{10} ions/m^2.

5.2.3.2 Population studies of ion tracks

The correlation of ion tracks density with crater diameter from the ion tracks registered on CR-39 detector was analyzed. Analysis was done on a CR-39 detector positioned at 54 cm from the anode tip and exposed to a single shot etched for 5 hours as shown in Figure 5.31.

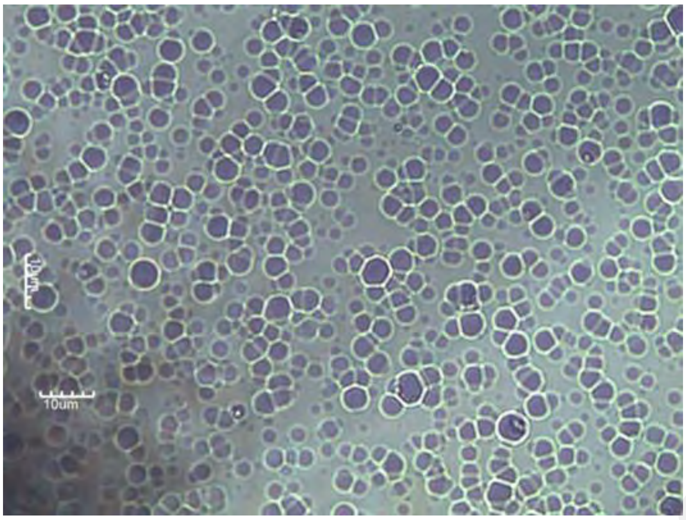

Figure 5.31: Optical microscope image of CR-39 irradiated for single ion beam emission at 0.2 mbar with magnification power of 1000X

Calculation of the ion tracks density and measurement of the crater diameter has been manually done by counting the tracks formed one by one. The measurement and calculation was based on two areas chosen on the image of the size 50 μm X 50 μm and the results is averaged. The crater diameter of the ion tracks formed lies from 1 – 5 μm. Total density of the ion tracks was measured to be 6.3 x 10^{10} ions/m^2. Density of ion tracks with crater diameter less than 3 μm is 3.9 x10^{10} ions/m^2 after averaging over 10 areas. For crater diameter of larger than 3 μm, the density is lesser and measured to be 2.4 x10^{10} ions/m^2. This is in agreement with the ion beam measurement using biased ion collectors where numbers of high energy ions (larger crater diameter) is less than small energy ions.

In addition to that, the population of the ion tracks has been categorized according to crater diameter and shown in the histogram in Figure 5.32. It is noticed that about 76 % of the total population of ion tracks lies between 2 – 4 μm. Moreover, the ion tracks formed in this category of size is more apparent as the contour of the crater formed is easier to be identified. For the ion tracks having size of crater diameter less than 2 μm, it is believed that these categories of tracks were induced by group of protons or deuterons of lower energy. Thus, this group of ions registered a relatively shallower crater that the contour of the craters became diffuse. This in turns causes difficulties for the crater diameter to be measured precisely by means of an optical microscope. Even though the exposed CR-39 sample only etched for 5 hours but this fact does not influence the quantitative information on the ion tracks density and crater diameter considerably. Interpretation of the ion beam energy in terms of crater diameter is sufficient in this case to investigate the correlation of ion tracks density with ion beam energy where the size of the ion tracks is dependent on the ion beam energy under same etching duration.

At the same etching duration, the higher the energy of the particle the larger is the crater diameter induced by the charged particle. From the analysis, it can be concluded that the population of the ions are mostly emitted in the mid energy range. The distribution of the ion tracks population was observed similar to the shape of Maxwell distribution.

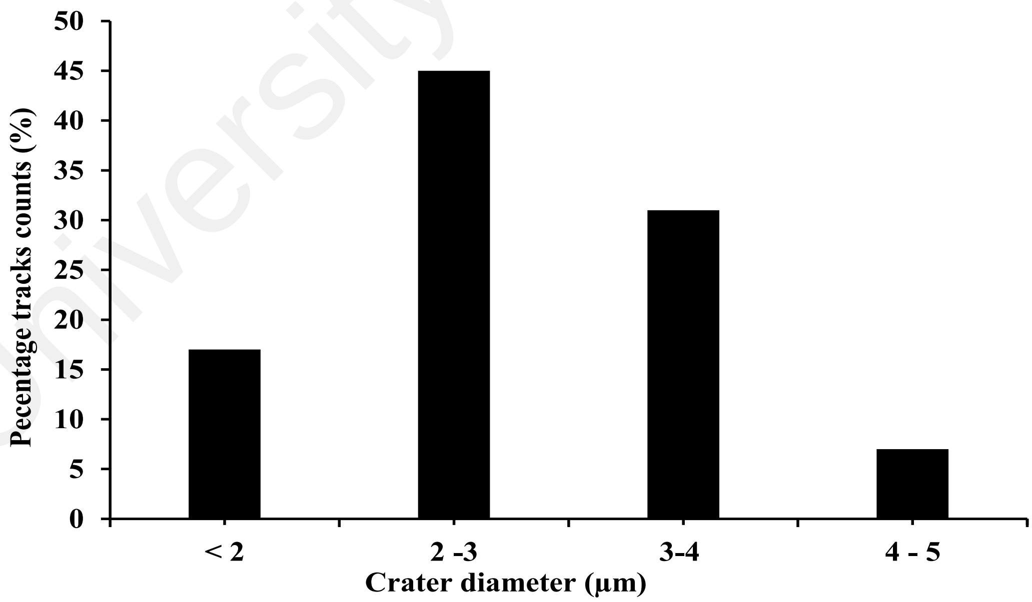

Figure 5.32: Percentage of tracks counts as a function of crater diameter

5.2.3.3 Angular distribution of ion beam emission

The angular distribution of the ion beam emission from the pinch column was carried out with CR-39 detectors positioned at different angular position and equal distance from the anode tip. Four angular position at 0^o (anode axis), 30^o, 60^o, and 90^o were examined where the detectors were fixed upon a special quarter-circular support. The purpose is to find the centre position of the ion beam emission which will be useful for the studies of beam target activation.

Figure 5.33 displayed all the etched CR-39 detectors at each angular position which was exposed simultaneously to a single focusing discharge and etched for 5 hours. It can be clearly seen that the total number of ion tracks registered at each angular position showed distinct characteristic with high anisotropy. The density of the ion tracks was apparently observed to be decreased at higher angular position. The ion tracks registered at the end on direction was shown to be saturated which implied that the density of ions is more than 10^{11} ions/m^2. Even at angular position of 30^o, there is still significant ion tracks registered which the density of the ion tracks is at the limit of saturation. Only at angular position of 60^o, there is significant drop of the ion beam emission.

Interesting results was observed where at increasing angular position, the density of the ion tracks were seen to be decreased but the size of the ion tracks were on the other hand getting larger. This was more obvious as can be seen for ion tracks registered at 90^o where very little ions were emitted along this position. The size of the ion tracks registered at this position also the largest compared to other angular position. Measurement of the ion tracks size at each angular position has been made by average the size measured for more than 100 ion tracks except at angular position of 90^o. Average crater diameter of the ion tracks at 0^o, 30^o, 60^o and 90^o was measured to be 1.7 ± 0.3 μm, 1.9 ± 0.3 μm, $2.3 \pm$

0.4 µm and 3.7 ± 1.0 µm, respectively. Due to the saturated ion tracks along the end on direction, the anisotropic factor of ion beam emission was not able to be determined.

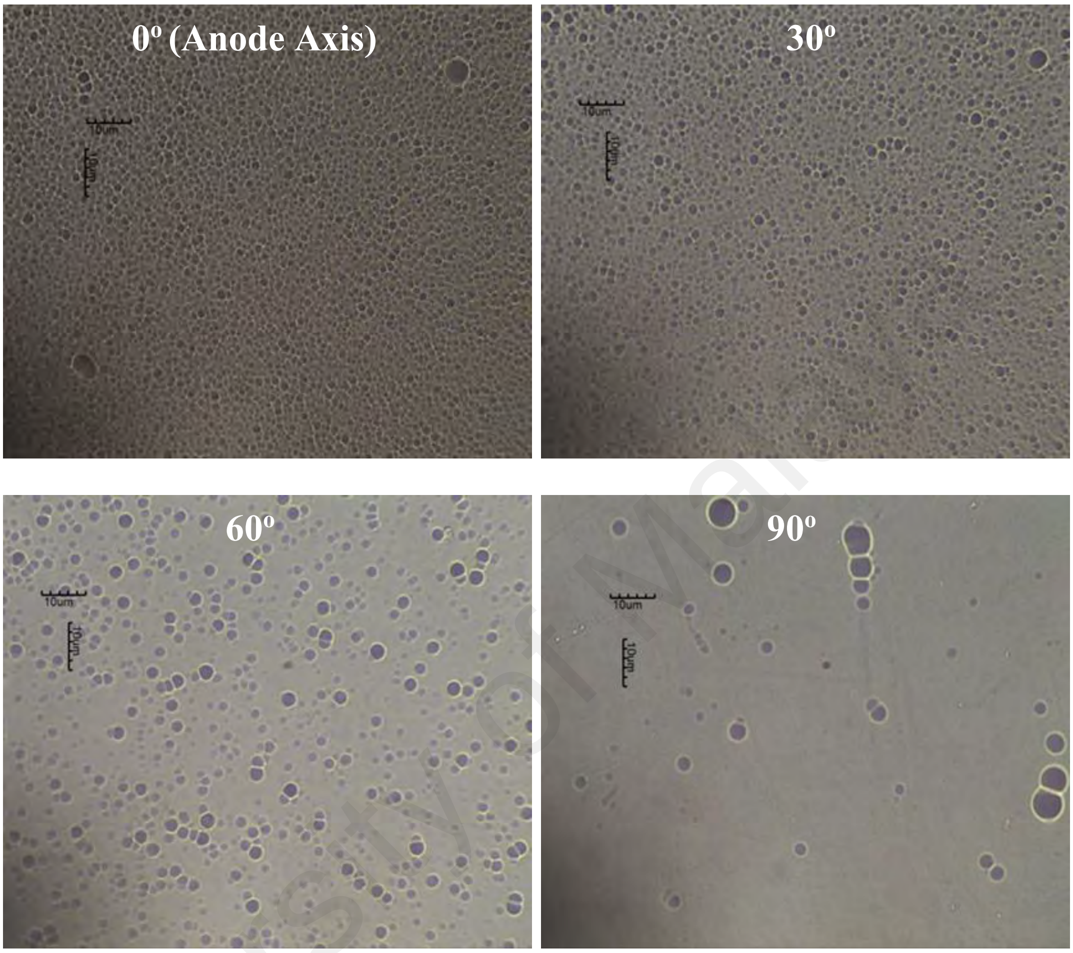

Figure 5.33: Optical microscope images (1000X) of CR-39 nuclear track detectors at all angular position exposed to 0.2 mbar deuterium discharge after 5 hours etching

5.2.4 Lee Model Results (Comparison between Experiments & Theoretical Results)

This section presented the numerical results of ion beam emission using modified Lee model code. Several works for the study of ion beams emitted from plasma focus using the modified Lee model code has been reported elsewhere (Akel et al., 2014; Lee & Saw, 2012, 2013). Details on the principle of computation of ion beam properties using Lee model code for different type of working gas has been extensively discussed by Lee et al (Lee & Saw, 2013). Ion beam properties from the measured results and numerical calculation was compared and studied. Three operating pressure at 0.1, 0.2 and 0.5 mbar were examined. The numerical procedure was carried out with following plasma focus parameters:

Bank Parameters:	L_o = 119 nH, C_o = 30 μF, r_o = 21 mΩ
Tube Parameters:	a = 0.95 cm, b = 3.2 cm, Z_o = 22 cm
Operation Parameters:	V_o=13.5 kV, P_o= variable, *MW*=4, *A*=1, *At-Mol*=2

The numerical experiment was first carried out by input the parameters tabulated above using 5 phase Lee model code and fitted against the experimentally measured current waveform. At each operating pressure, the properties of ion beam energy, ion beam fluences and number of ions were computed from 5 shots and averaged. Firstly, the axial phase model parameters in the Lee model code was adjusted followed by adjusting the radial phase model parameters until the computed rising slope of the current waveform and peak current are matched with the measured current waveform. Typical fitted current waveform was shown in Figure 5.34. Good match was observed between the measured and computed current waveform up to the end of the computed current dip as shown by the arrow. Fitting was stopped after fit the dip up to the end of the radial phase as shown by the arrow. There is "extended" dip observed in the measured current waveform in which the code does not emulate. However, the fit is reasonable for the important regions of the topping profile, the top profile and the current dip.

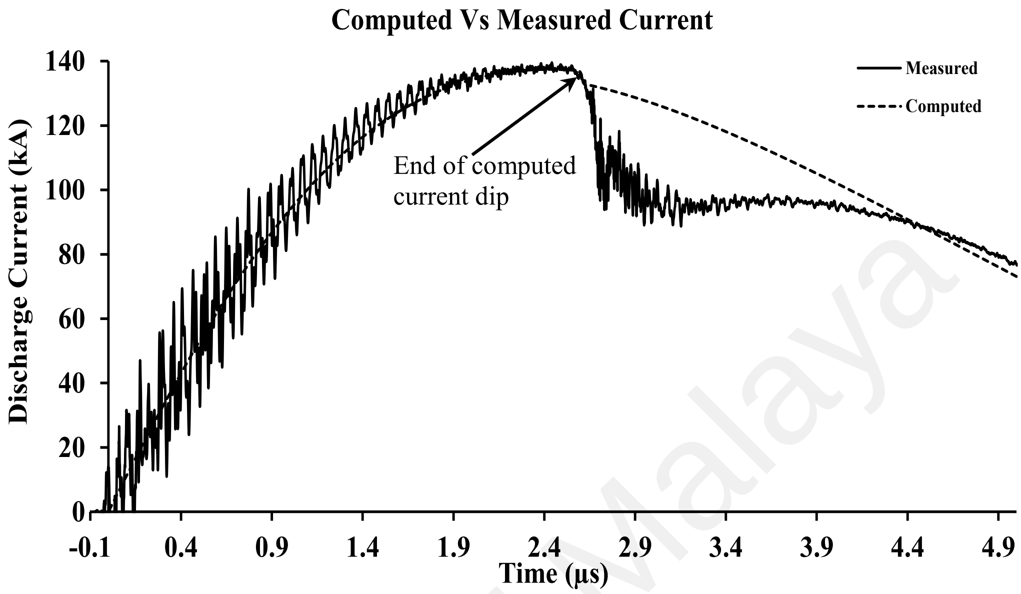

Figure 5.34: Measured and computed current waveform at 0.2 mbar

Comparison of the measured and numerically calculated ion beam energy was compared as depicted in Figure 5.35. The trend of ion beam energy versus pressure curve for experiment and numerical results are the same. Highest ion beam energy was obtained both experimentally and numerically at 0.2 mbar. Computed ion beam energy was determined to be higher than the measured value. The computed value is closest to the measured value at 0.2 mbar with a factor less than 1.5.

The discrepancy of the measured results compared to the computed value could be due to the adopted mechanism of ion beam acceleration in the Lee model. In the numerical computation of ion beam energy using Lee model, plasma diode mechanism was adopted (Gribkov et al., 2007). The ion beam is modelled to be accelerated by the diode action in the plasma column. Therefore, our experimental results suggested that there may be more than one mechanism taking place for the ion beam acceleration from the plasma column.

Closest matching between the measured and numerical results at 0.2 mbar implies that plasma diode may be the predominant acceleration mechanism at this pressure.

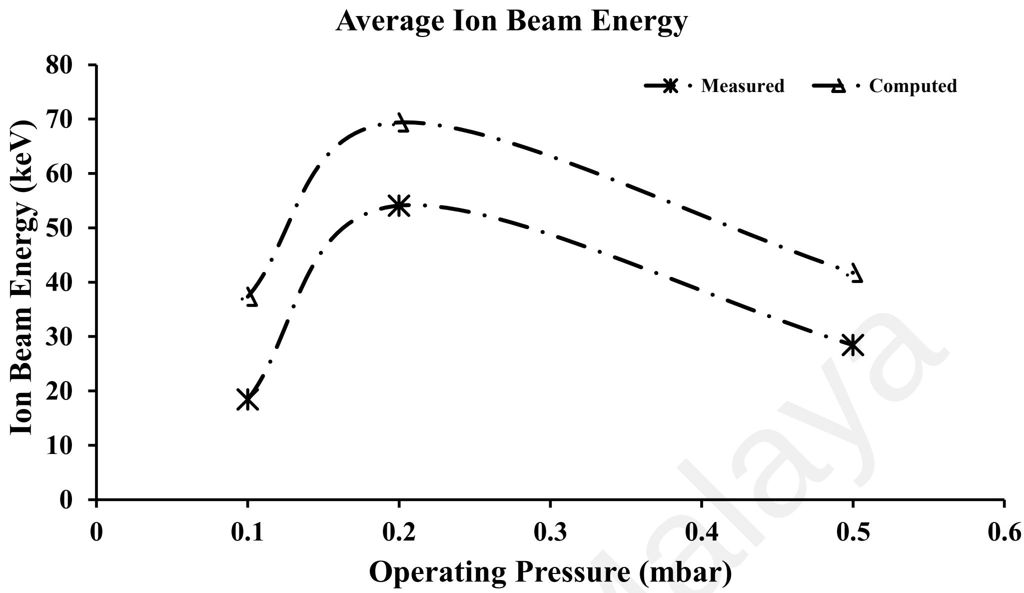

Figure 5.35: Comparison of experiment and numerical calculated ion beam energy

The ion beam fluence and number of ions were also computed using the modified Lee model code. The code characterized the ion beam by the number of ions per unit cross-section which is termed as ion beam fluence attribute to the fact of ion beam exits the plasma column as a narrow beam (having the same cross-section as the plasma column). Thus, ion beam fluence equation was first developed and incorporated in the Lee model code to compute the ion beam fluence and other properties including number of ions per shot.

The ion beam fluence equation is dependent on the working gas where the deuteron beam fluence equation used in Lee model code (Lee & Saw, 2013) is expressed as following:

$$\text{Deuteron Beam Fluence (ions/m}^2\text{)} = 8.5 \text{ X } 10^8\, \mathrm{I}_{Pinch}^2 Z_p \text{ X} \left[\frac{In(b/r_p)}{\pi r_p^2 U^{1/2}} \right] \quad \textbf{(5.2)}$$

where I_{pinch} is the pinch current value taken at the start of the pinch; Z_p is the length of the pinch; b is the radius of outer electrode of the focus tube; r_p is the plasma column radius; and U is the diode voltage that providing the accelerating voltage to the ion beam.

However, the computation of the ion beam properties using Lee model code does not include the Magnetic Reynold Number MNR effects (Lee et al., 2013). This effect is known to play an important role on the plasma dynamics especially at low current sheath speed. In other words, this effect become dominant at higher pressure when the current sheath speed became too low resulting in diffused current sheath structures and poorer pinching dynamics. This is detrimental for a good plasma compression and hence deteriorates the ion beam production.

The effect of Magnetic Reynold Number is evident from the comparison of the measured and numerically computed results for the ion beam fluence and number of ions as a function of pressure as shown in Figure 5.36 and 5.37, respectively. The role of Magnetic Reynold Number is shown to become significant at pressure beyond 0.2 mbar where the current sheath might be getting diffuse resulted a poorer electromagnetic drive mechanism causes a drop in the measured ion beam output. This analysis shows that the plasma dynamics and ion beam acceleration mechanism is rather complex where no single mechanism is sufficient to explain for the ion beam production and thus more studies are required to understand the plasma focus ion beam.

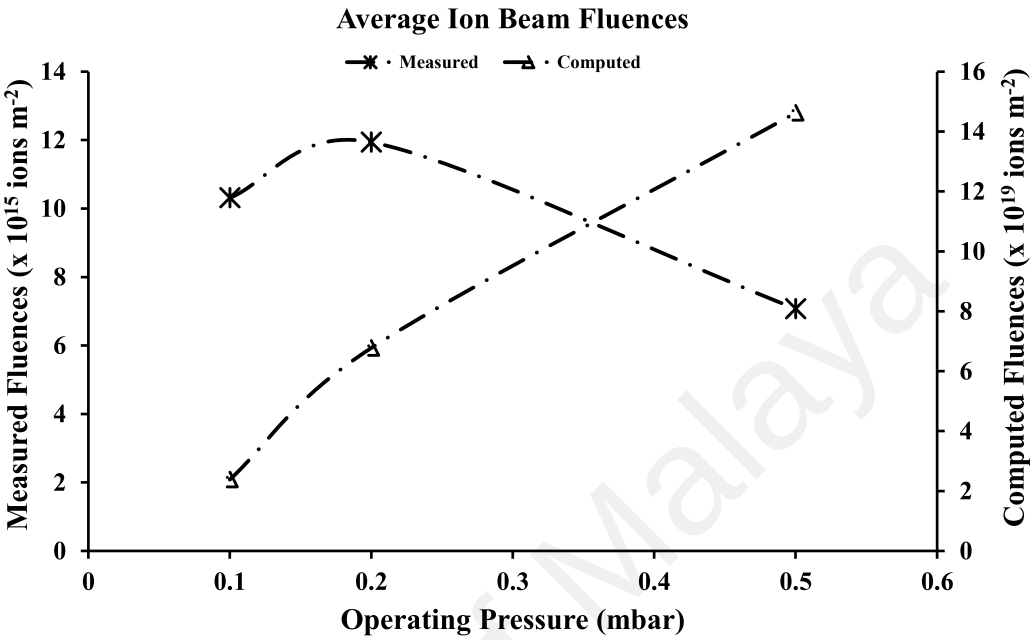

Figure 5.36: Measured and computed ion beam fluences as a function of pressure

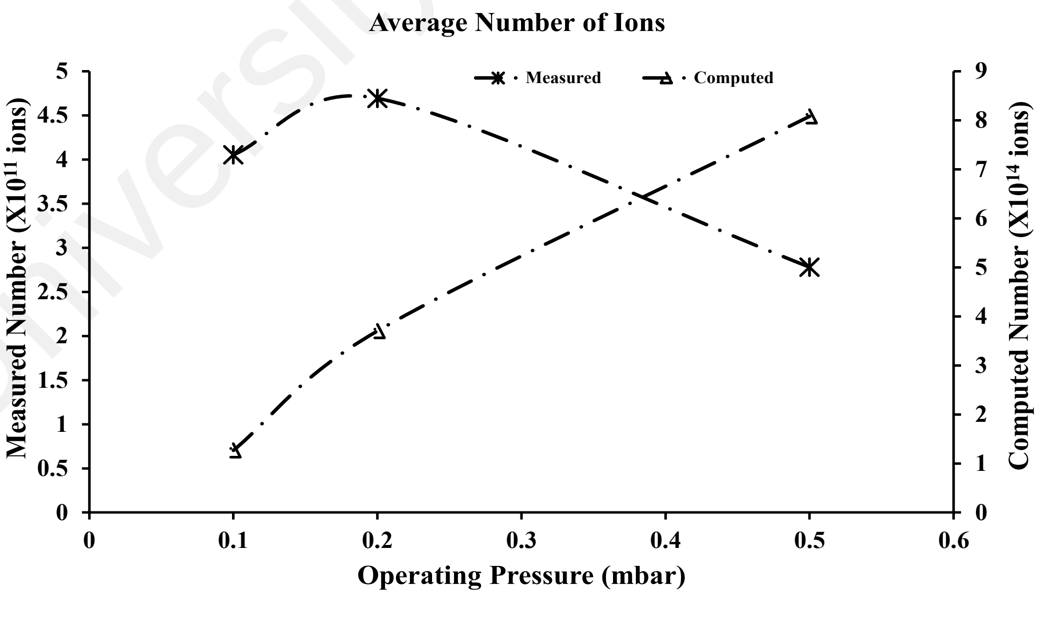

Figure 5.37: Measured and computed number of ions as a function of pressure

5.3 Time Integrated Neutron Measurement

Many works have been reported that the neutron productions from all plasma focus devices are strongly dependent on operating pressure and input energy of the plasma focus. Our plasma focus device has been modified to operate in low pressure that is optimized for ion beam emission. Thus, with deuterium filling at low pressure operation, the neutron yield is expected to be low. Neutron yield in terms of number of neutron counts per burst as recorded using GM tubes by nuclear activation foil method has been carried out. Measurement of neutron yield was carried at pressure of 0.1 - 0.5 mbar.

A series of 20 shots have been fired at each operating pressure where a fresh gas was filled after every discharge. Two GM tubes located at equal distance from the anode tip with one at the end on direction and the other at the side on direction. Both detectors have been cross calibrated and normalized. The calibration constant of each detector in its present geometry is about ~ 10^5 neutrons per count. Thus, if the neutron yield is in the order of 10^5 or less then the yield might be too low for the measurement to be made in current diagnostic tool. After a series of discharge at the examined pressure range, maximum neutron yield is found to be in the order of 10^6 per shot. Table 5.3 displayed the average neutron yield measured in end on and side on direction.

Table 5.3: Average Neutron Yield at different pressure

P(mbar)	Neutron Yield (X10^6)	
	End on	**Side on**
0.2	1	1
0.3	1	0.8
0.5	0.9	0.8

Maximum neutron yield was obtained at the pressure of 0.2 mbar and the yield was seen to drop with the increase of pressure. This is in accordance to the fact that stronger focusing discharge can be obtained at pressure of 0.2 mbar which may produce more neutrons emission. However, the neutron yield obtained was very low due to operation of the plasma focus device in low pressure regime. This could be due to the fact that at low pressure operation, the magnetic field in the pinch is insufficient to gyrate the high energy deuterons within the pinched plasma (Roshan et al., 2010). Moreover, these deuterons were having a larger mean free path which could run away from the pinched plasma to interact with other deuterons at less density. Both conditions are hence resulted in a lower neutron yield production.

The structure of the current sheath at low pressure operation might be asymmetrical and distorted during radial collapse phase which might deteriorate the neutrons production (Deutsch & Kies, 1988b). Such distortion arose from the collisions of runaway ions with the constricted plasma column that may result in lower neutron output. Due to too low neutron yield, no quantitative measurement on the anisotropy of neutron emission can be made. In this pressure range, there are several shots with no emission of neutrons probably due to the yield is less than the detection threshold of the GM tube. Generally, a shot with high neutron yield is followed by high ion beam and radiation emission.

5.4 Time Resolved Neutron Measurement

Five sets of scintillator-photomultiplier tube detectors were used for this purpose and the description of the experimental setup has been given in Chapter 4. Experiment has been carried out by varying the filling pressure of deuterium gas in the range of 0.1 – 0.5 mbar at the interval of 0.1 mbar. A total number of about 600 shots have been fired in this series of experiment. All the recorded signals have been time corrected and synchronized so that the comparison can be made.

Throughout the whole series of experiment, there is no significant neutron signal registered. This could be due to the possibility of low neutron yield at low pressure regime or the limitation attributed to the detection sensitivity of detector assembly. However, there is some shots showed possible registration of the neutron signal for the sets of scintillator-photomultiplier tube assembly without lead casing. Typical neutron and hard X-ray signals at 400 ns time window of waveform is illustrated in Figure 5.38.

There are two pulses can be observed in all detectors without lead shield. The first pulse is the hard X-ray signal that often overshot as such pulse was not seen in detector D2 and D4 (detector with lead shield) otherwise the peak of this pulse is a good indicator of the pinch time of $t = 0$. Subsequent pulses are due to neutrons with energy of 2.45 MeV from D-D reaction. The first neutron pulse was registered at D3 at the time of 2.71 μs. The time of flight of this neutron pulse is about 68 ns to the detector at 148 cm. Thus, the origin time $t = 0$ is estimated as 2.64 μs, which is within the duration of the hard X-ray pulse. Therefore, this confirmed the second pulse was corresponded to neutrons emission.

It is also noted that the intensity of hard X-ray correlated to the neutron emission, the high intensity hard X-ray is accompanied by the neutron signal. Higher the hard X-ray signal, higher pulse of neutrons signal observed.

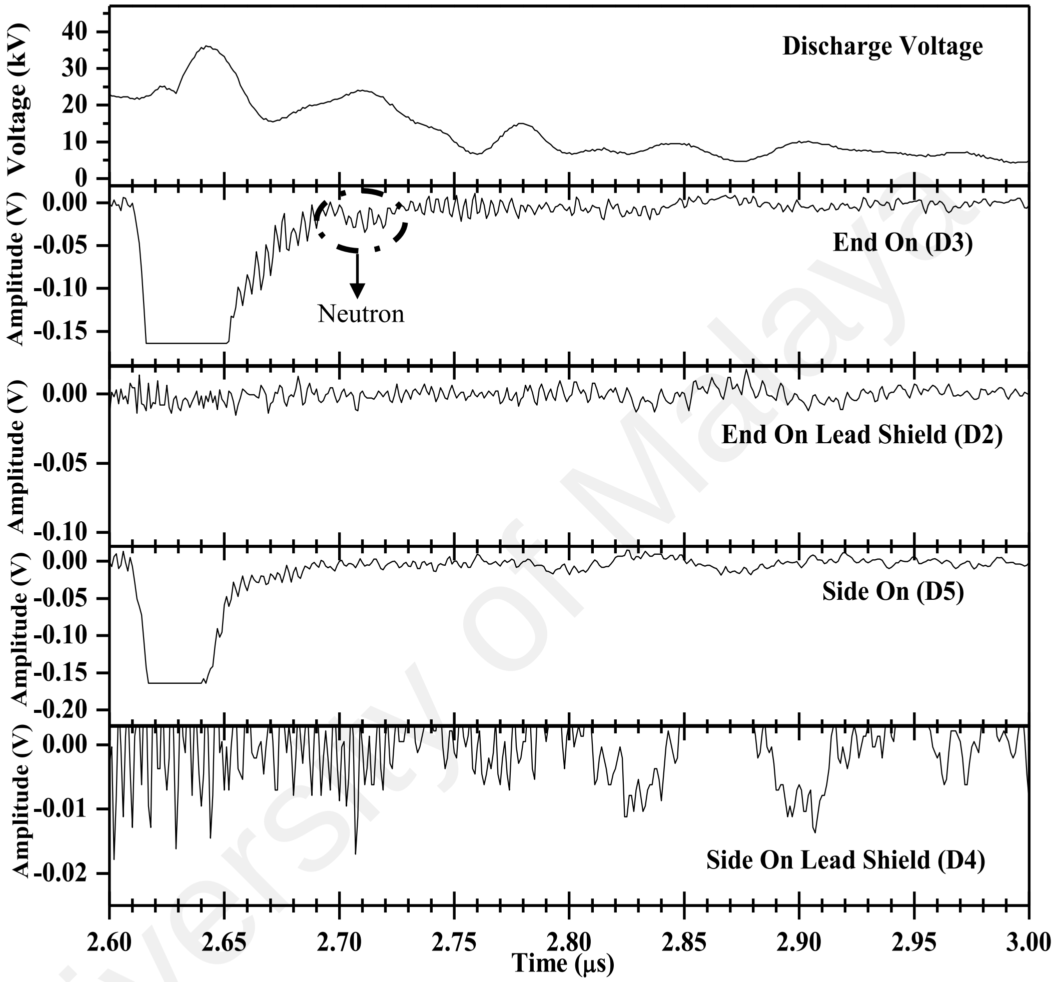

Figure 5.38: Time resolved scintillator-photomultiplier detectors and discharge voltage signal at 0.2 mbar

Figure 5.39 shown another set of scintillator-photomultiplier signals at 0.1 mbar. The first pulse was very broad and registered by all the detectors without lead shield, at time near to the voltage spike. Second pulse of very small amplitude were observed at D3 and D5. TOF for the second pulses, taken as neutrons as measured by D3 and D5 were determined as 59 ns and 42 ns, respectively. The neutron energy in end on direction was

3.31 MeV while for side on direction was 3.17 MeV. The origin time of the neutron pulse is deduced as 2.35 μs which was coincided with the hard X-ray pulse.

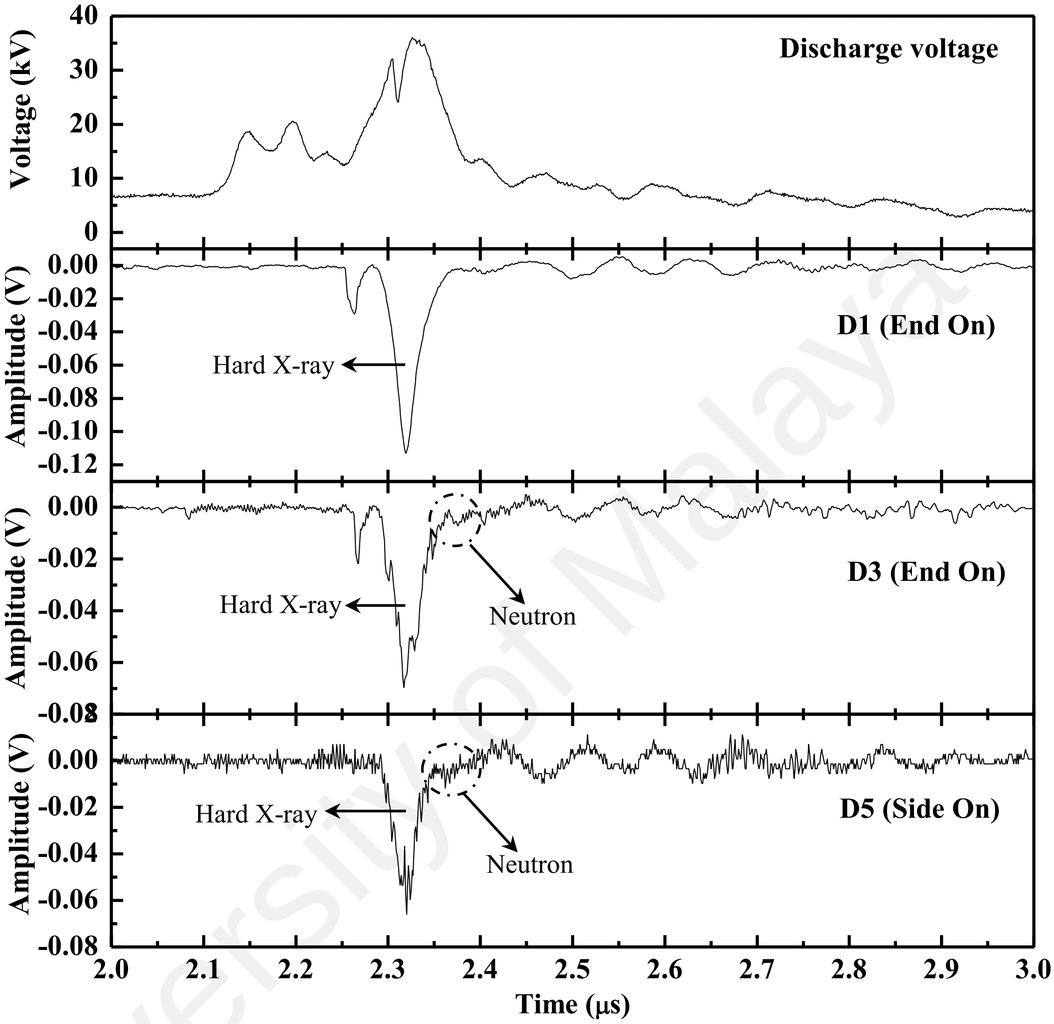

Figure 5.39: Time resolved scintillator-photomultiplier detectors and discharge voltage signal at 0.1 mbar

5.5 Time Resolved Hard X-Ray Measurement

At low pressure operation, hard X-ray emission is more likely to be obtained compared to neutron emission. Analyses of the hard X-ray emission registered for discharge in the range of 0.1 – 0.5 mbar has been summarized. Hard X-ray pulses were observed only in less than half of the discharge and found to be pressure dependent. The statistics of the frequency of hard X-ray signals at each operating pressure is presented in a histogram as shown in Figure 5.40.

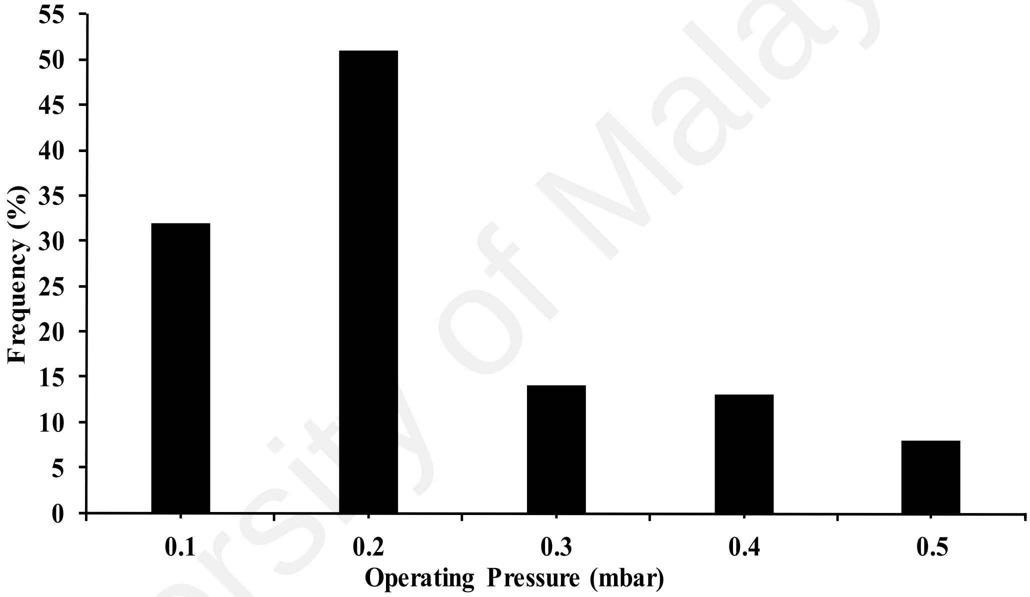

Figure 5.40: Percentage frequency of discharge producing hard X-ray for pressure of 0.1 – 0.5 mbar

About 50 % of the discharge at 0.2 mbar was observed to produce hard X-rays. Lowest frequency of hard X-ray production was obtained at 0.5 mbar. Pressure of 0.2 mbar was also found to generate most hard X-rays emission. The statistic also showed that it is more likely to get hard X-ray emission at low operating pressure of 0.1 – 0.2 mbar. Typical hard X-rays signals measured in the end on direction at 0.2 mbar is depicted in Figure 5.41. There is a slight difference in the width of the hard X-ray signal evident the broadening due to distance of flight. For discharge with single voltage spike, only single hard X-ray pulse was observed. Focusing discharge with multiple voltage spikes produced either single or sometimes multiple hard X-ray pulse which corresponded in time to the voltage spikes.

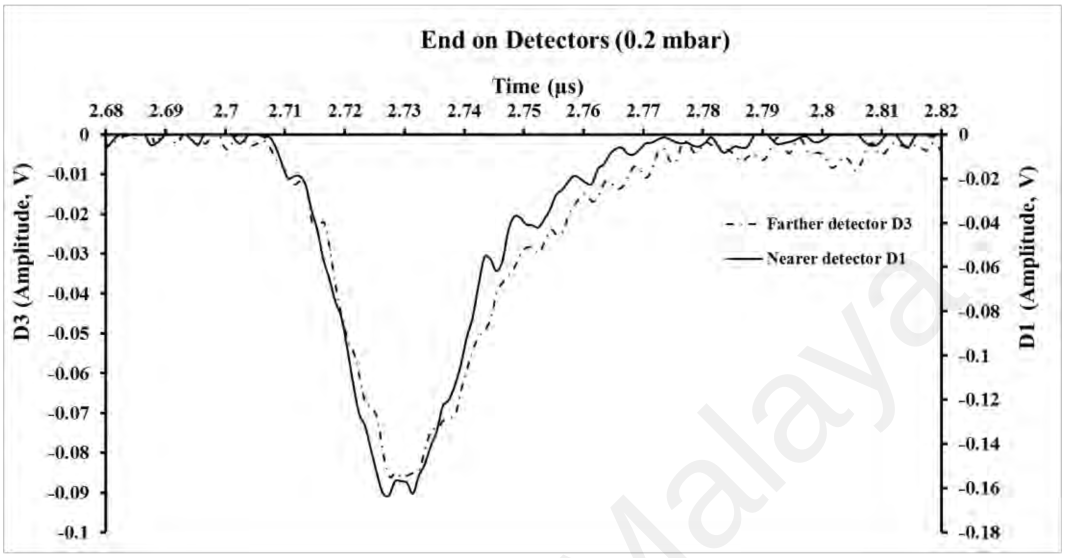

Figure 5.41: Typical hard X-ray signals measured at end on direction at 0.2 mbar

5.5.1 Hard X-Ray Emission from Discharge with Single Voltage Spike

In the focusing discharge with single voltage spike, a very significant hard X-ray pulse was registered. The intensity of hard X-ray emission is found dependent on the pressure and the strength of the focusing discharge. The hard X-ray pulses always seen with high voltage spike of strong focusing discharge (Figure 5.42). Longer duration of hard X-ray emission was also obtained at stronger focusing discharge. The rise time of the hard X-ray signals was found in the range of 10 – 16 ns with average FWHM of 18 ± 4 ns.

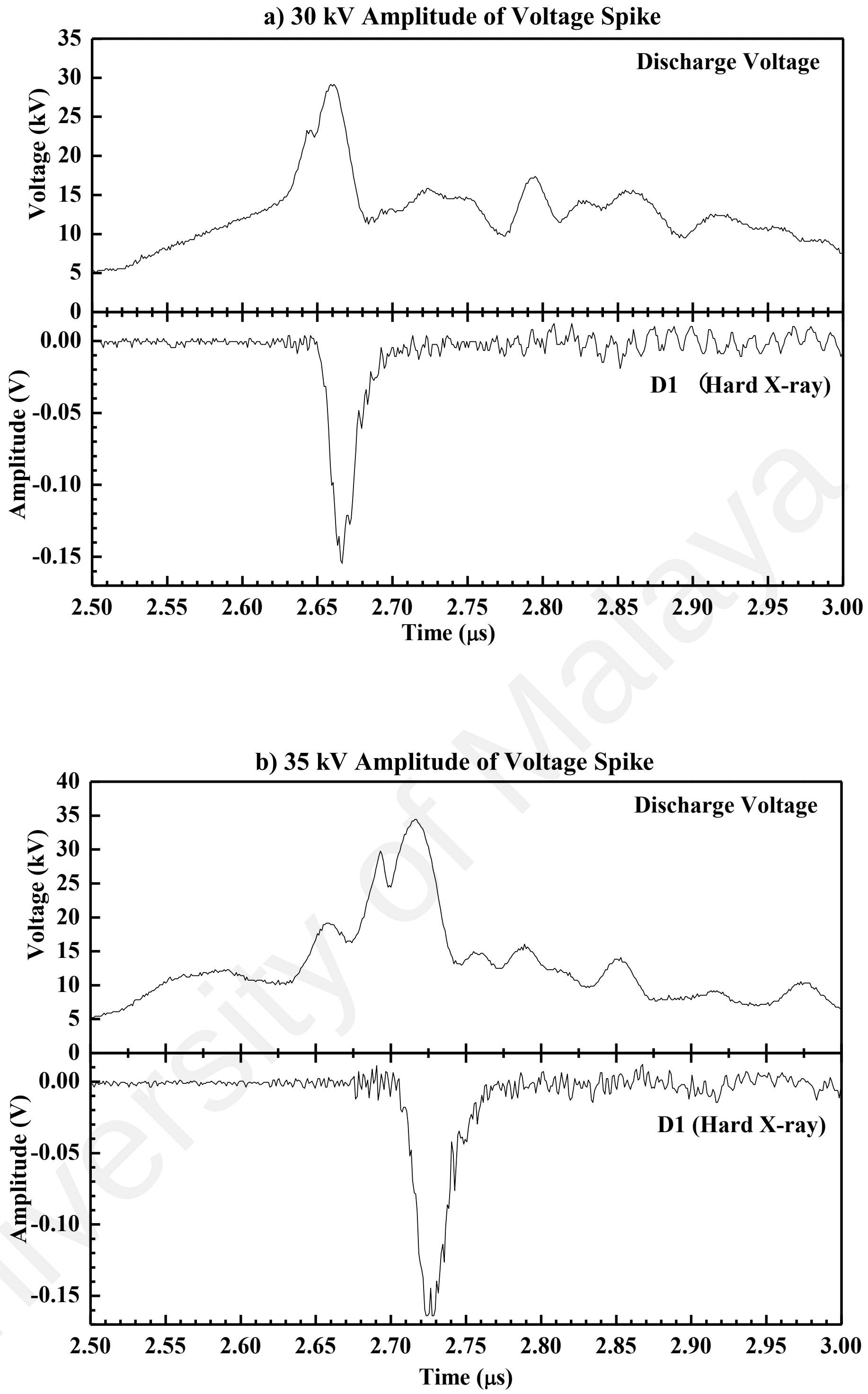

Figure 5.42: Hard X-ray signal at 0.2 mbar deuterium discharge measured by nearest end on scintillator detector. (a) Voltage spike of 30 kV, (b) Voltage spike of 35 kV

5.5.2 Hard X-Ray Emission from Discharge with Multiple Voltage Spikes

In the discharges when multiple voltage spikes were observed, about 80 % showed only single hard X-ray pulse. This hard X-ray pulse corresponded to the highest voltage spike among the multiple peaks. Those discharges where two or more hard X-ray pulses observed were usually obtained at pressure range of 0.2 – 0.4 mbar. This could be ascribed to the condition of the plasma pinch in these pressure regime, that energetic electron beam emitted at multiple voltage spikes were able to generate the hard X-ray by anode bombardment.

For the case of two or more hard X-ray pulses, the first hard X-ray pulse is always seen to be more intense than the later pulses. One of the typical signals are shown in Figure 5.43. Usually the second hard X-ray emission is detected around 60 – 140 ns after the first hard X-ray emission. As seen in this signals, even though second pinch might be stronger with higher voltage spike but the intensity of second hard X-ray was weaker than the first hard X-ray pulse. This could be due to second plasma compression or breaking up of plasma column into hot spots at the time where the discharge current was lower. This resulted in less energy transferred into the plasma and hence produces relatively weaker particle beams.

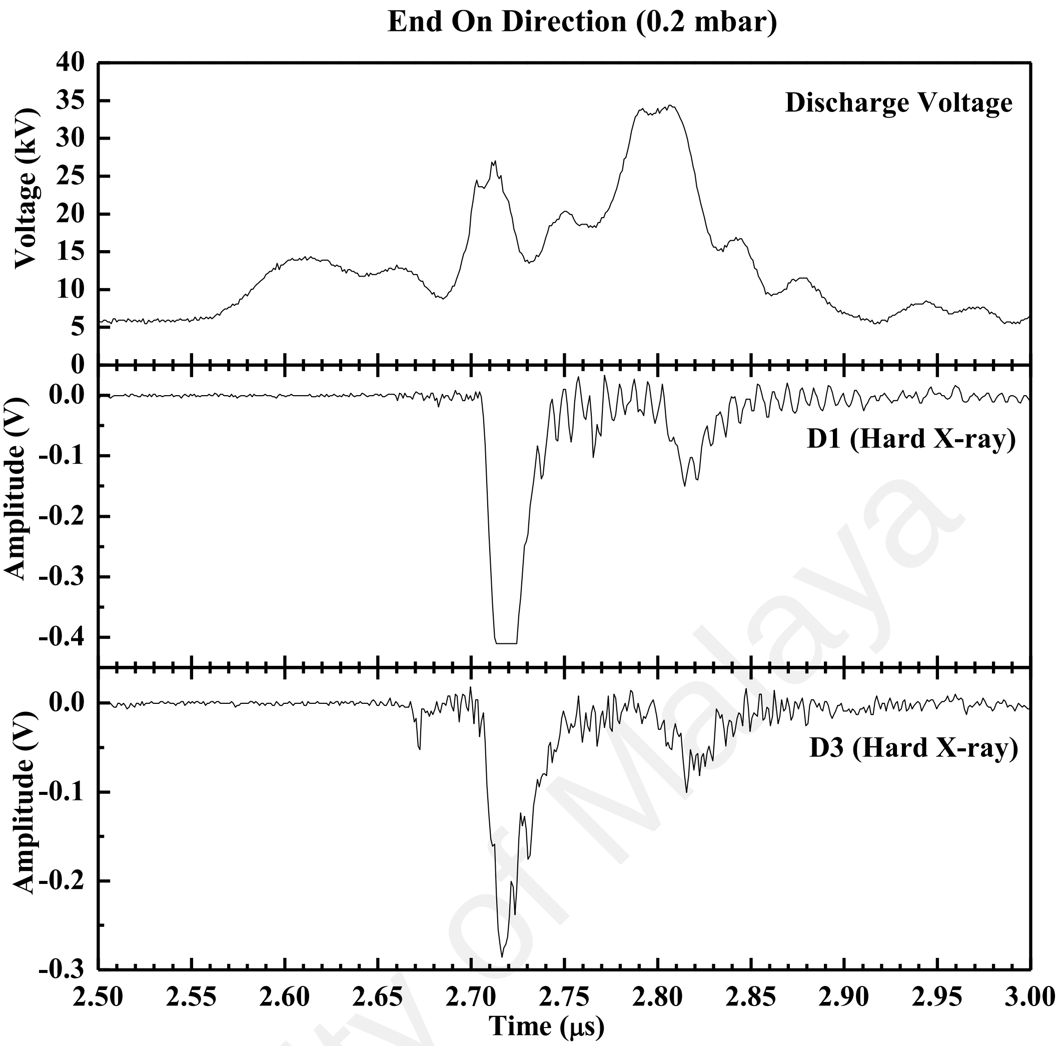

Figure 5.43: Two hard X-ray pulses in the multiple compression discharge at 0.2 mbar

In the discharge where two peaks were identified in the voltage and the hard X-ray signals (Figure 5.44), the first peak correlated to the maximum plasma compression to the minimum radius and the second peak due to the set in of $m = 0$ instability. The second peak was relatively higher in amplitude than the first. Time interval of ~ 29 ns was determined from D5 between the two hard X-ray peaks which could be corresponded to the duration of pinch. However, signals of two hard X-ray peaks like this were seldom obtained. This could be due to the fast rise time of the first hard X-ray pulse and short pinch lifetime where the two hard X-ray peaks could have been seen as merged signal.

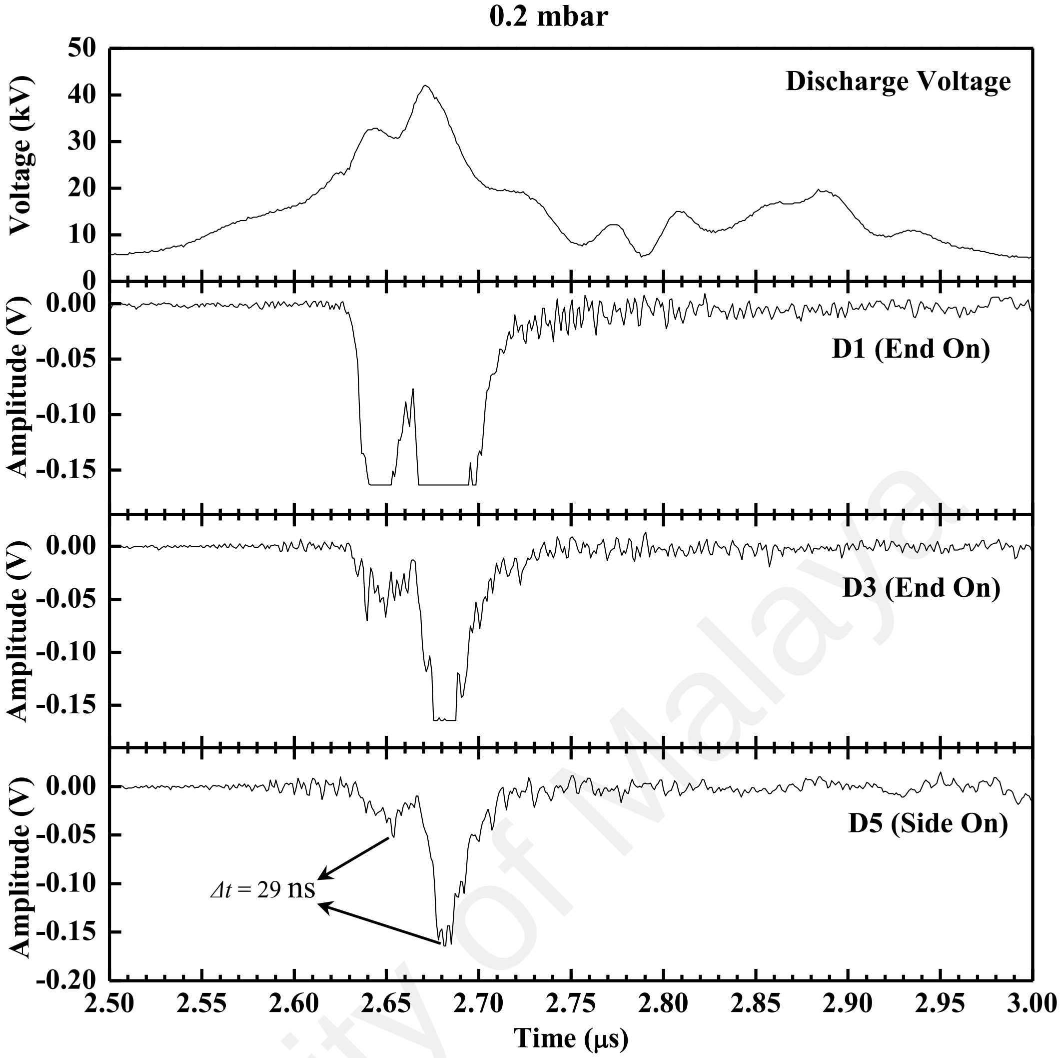

Figure 5.44: Hard X-ray emission from different compression phases

The trend of hard X-ray emission versus pressures is shown in Figure 5.45. The plots showed the intensity of hard X-ray measured by the detector at end on direction (D1) and side on direction (D5). The pattern of hard X-ray intensity versus pressure curve is the same for both end on and side on detector. Similar trend was also observed for the farthest end on detector (D3) which the data does not shown here. This showed that highest hard X-ray emission was obtained at 0.2 mbar.

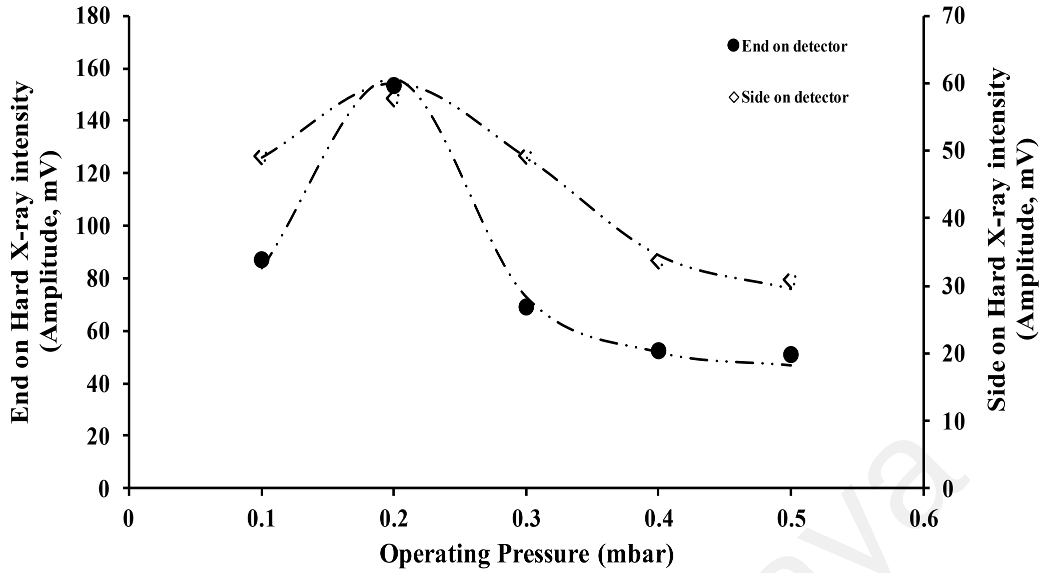

Figure 5.45: Hard X-ray intensity measured from end on and side on detector at different operating pressure

5.6 Soft X-Ray Measurement with BPX 65

Time resolved soft X-ray emission was measured using an array of 5 channels BPX-65 PIN diode detectors. A typical time evolution of soft X-ray signals recorded simultaneously with discharge voltage is shown in Figure 5.46 for deuterium discharge at pressure of 0.2 mbar.

The shot shown was corresponded to discharge with single voltage spike. There are 3 soft X-ray pulses can be seen in whole emission period marked as '*A*', '*B*' and '*C*'. The first soft X-ray pulse marked '*A*' was overlapped with the duration of the voltage spike which was corresponding to the main focusing period and last for 122 ns. The duration of the first soft X-ray emission period was found to be consistent with the duration of the first voltage spike which varies at a broad range of 40 – 122 ns. Usually, the duration of the first soft X-ray emission period last longer for discharge with single voltage spike as compared to multiple voltage spikes. At higher pressure beyond 0.2 mbar, the pulse width of the first soft X-ray emission observed increased. This implies that high pressure discharge is more favourable for soft X-ray emission.

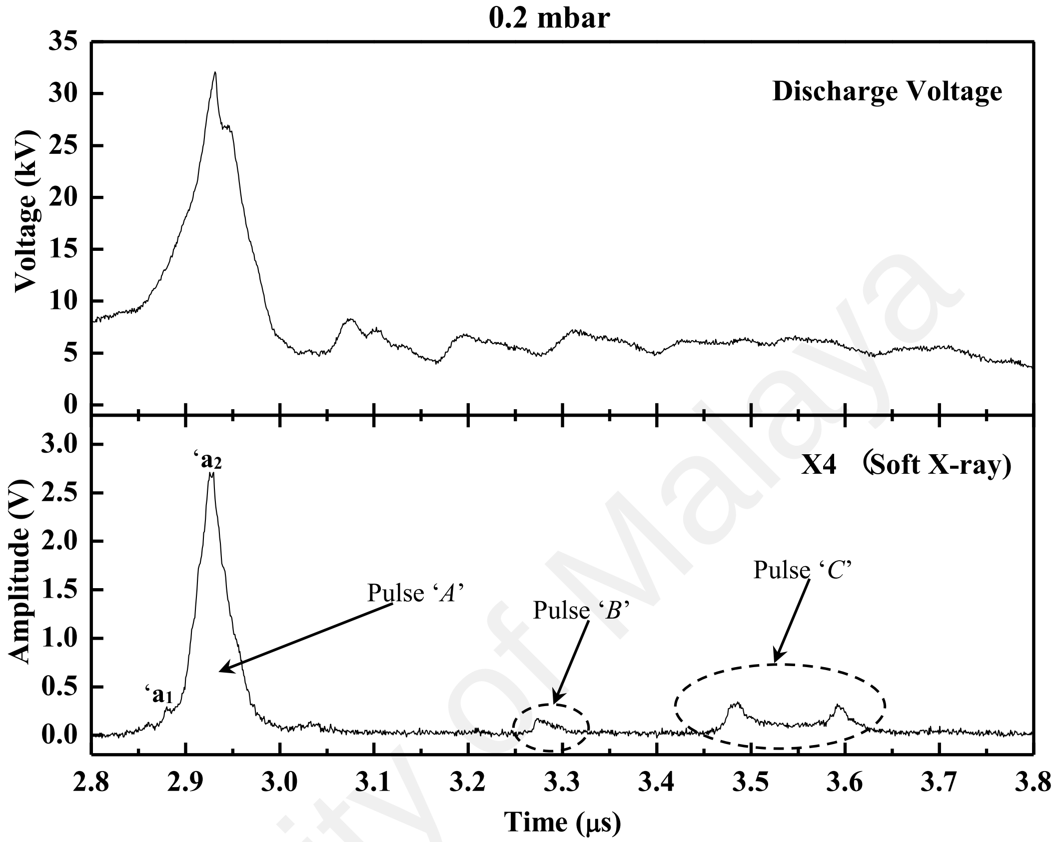

Figure 5.46: Discharge voltage and soft X-ray signal at 0.2 mbar deuterium discharge

Usually, three peaks were seen in the first soft X-ray pulse which is associated with different pinch phases, i.e. first plasma compression to the minimum radius, onset of instability and plasma disruption. However, in some of the strong focusing discharge the first soft X-ray pulse was broad and the peaks were not clear. One of the typical signal is shown in Figure 5.46. The first soft X-ray pulse '*A*' has two peaks marked as 'a_1' and 'a_2'. The peak marked 'a_1' is corresponded to the time of maximum compression to the minimum radius, i.e. $t = 0$. It has a very sharp rise time about 4 ns (typically 2 - 6 ns) is estimated in this signal. Peak 'a_2' is associated with the quiescent phase and is correspond to the onset of the $m = 0$ instability. The peak 'a_2' has a long rise time of 17 ns (typically 2 -17 ns) with FWHM of 30 ns (typically 12 - 30 ns). The time interval between peak 'a_1'

and 'a_2' can be used to estimate the lifetime of the pinched plasma which was determined to be 45 ns in this shot. The peak corresponded to the unstable and decay phase was not clear in this shot which might be embedded within the two peaks.

At the instant of approximately 385 ns (typically 60 ns - 390 ns) after the first compression, second X-ray pulse marked '*B*' with lower intensity, having rise time of 4 ns and FWHM of 30 ns was recorded may be due to the breaking up of remnant plasma filaments. The third soft X-ray emission period (third pulse marked '*C*') was detected at *t*= 575 ns (typically 170 - 575 ns) after the first compression. This is ascribed to the vaporized copper jet emitted from the inside or the edge of the anode due to electron beam-anode target bombardment. A rather longer lasting and broad pulse for duration of 190 ns (typically 90 - 310 ns) was observed. In some of the shots, this emission period extended to more than 300 ns. For the case of discharge with multiple voltage spikes, several soft X-ray pulses were also observed and corresponded to the voltage spikes.

Meanwhile, further quantitative analysis was carried out to investigate the dependence of soft X-ray yield with axial current sheath speed. This is presented in Figure 5.47. In this analysis, only the emission from the first soft X-ray emission period is considered. Soft X-ray yield was obtained by integrating the time resolved soft X-ray signal recorded by one of the filtered PIN diodes (X5). A gross picture can be seen that at increasing current sheath speed, soft X-ray yield also increases. This can be interpreted as increase in current sheath speed due to lower operating pressure had led to higher temperature of the pinched plasma and hence enhances the radiation yield. Enhancement in soft X-ray yield at higher current sheath speed with the used of stepped anode has also been reported (Serban & Lee, 1997).

Noted that the soft X-ray yield at 0.1 mbar is the highest compared to 0.2 mbar despite the focusing discharge is weaker at 0.1 mbar. This could be interpreted as the effect of current sheath speed on soft X-ray emission may be more dominant than the strength of focusing discharge provided the force field flow field separation between the driving magnetic piston and shock front is not significant. It is important to prevent the development of force-field flow field separation at the end of the axial phase which could lead to poor plasma pinch and hence deteriorates the radiation emission (Serban & Lee, 1998). Overall results shown that the soft X-ray yield is dependent on the current sheath speed as well as operating pressure.

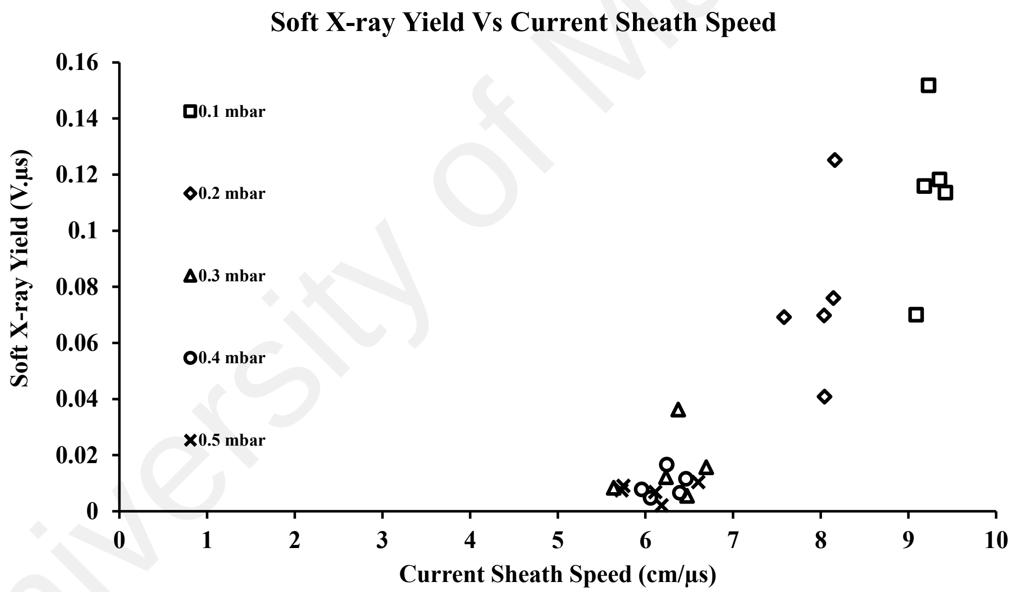

Figure 5.47: Soft X-ray yield as a function of current sheath speed

5.6.1 Electron Temperature Measurement

In the electron temperature measurement, an array of 5 channels windowless BPX-65 PIN diode detectors were employed. Each of the channels was filtered with aluminium foil of different thickness following the Ross filter technique to estimate the temperature of the deuterium plasma. Details of the method for electron temperature measurement have been described in subsection 4.2.5.2.

Here, we assuming the soft X-ray emission was dominated by the Bremsstrahlung process. In some cases, the soft X-ray emission from plasma focus discharge could be dominated by the copper k-alpha line radiation when a solid anode is used as reported by Zakaullah et al. (Zakaullah et al., 2001). However, in our case the anode has been engraved to 4 cm deep to reduce the effect of electron beam bombardment on the anode surface that could enhance the copper line emission by bound-bound transition.

Before the experiment on electron temperature measurement, all the five PIN diodes have been cross-calibrated and signals have been normalized. In the cross-calibration process, all the diodes were masked with same filter of 23 μm thick aluminized mylar and simultaneously exposed to a single discharge for about 20 shots were obtained. A typical time resolved soft X-ray signal for all the Pin diode detectors labelled as X1, X2, X3, X4 and X5 at 0.2 mbar deuterium discharge are depicted in Figure 5.48.

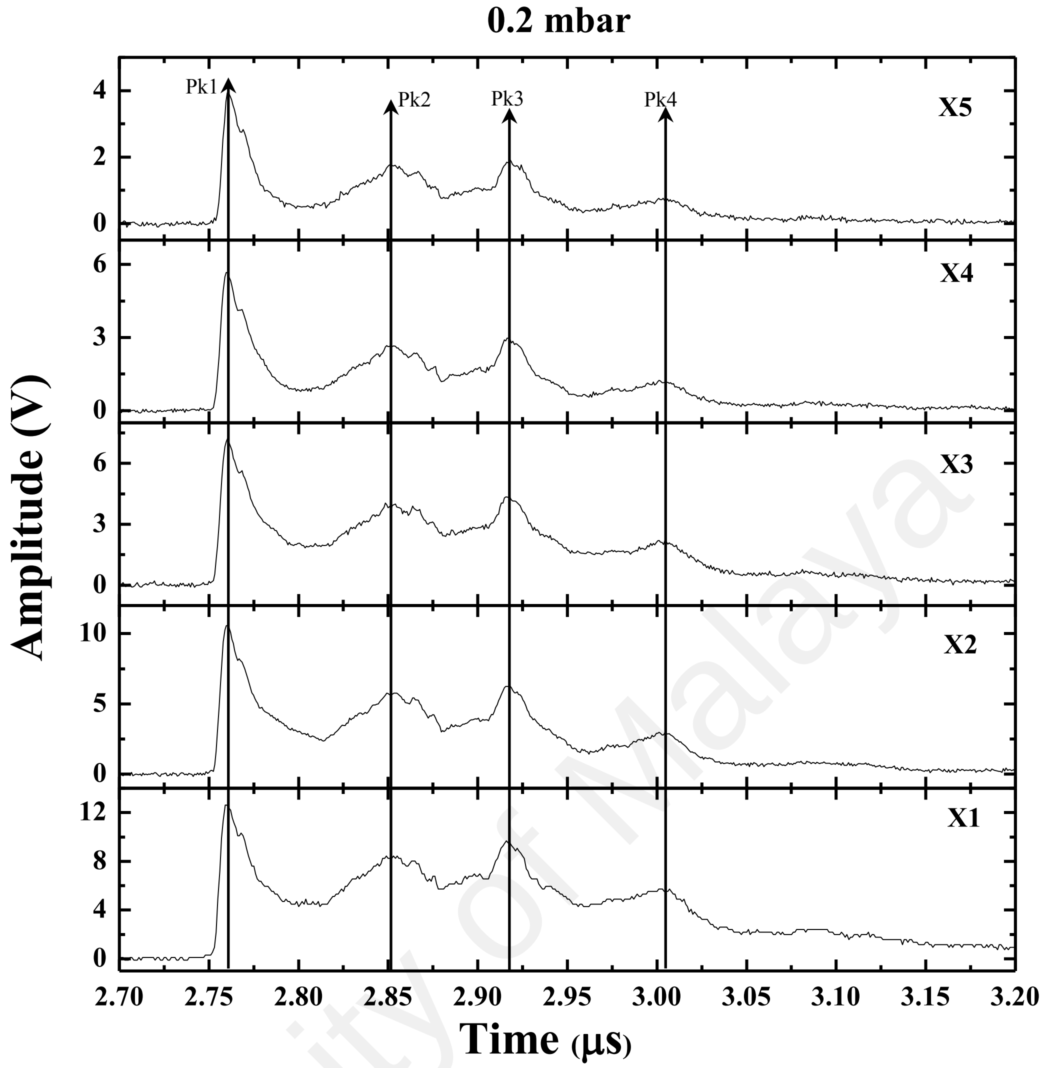

Figure 5.48: Time resolved soft X-ray signal at 0.2 mbar

As seen in each of the recorded soft X-ray signals, several X-ray emission periods can be discerned in a focusing discharge. A few distinct peaks in the soft X-ray signal can be identified in all the PIN diode detectors. Four of these peaks were selected for ratio calculation and plotted against aluminium foil thickness as presented in Figure 5.49. It is noticed that the whole of the soft X-ray emission period was strongly dominated by copper line radiation. Peak 1 and 2 in the soft X-ray signals were observed to be closed to the copper K_β of 8.904 keV while peak 3 and 4 lies closed to the copper K_α of 8.040 keV, suggesting the soft X-ray emission were still dominated by copper radiation.

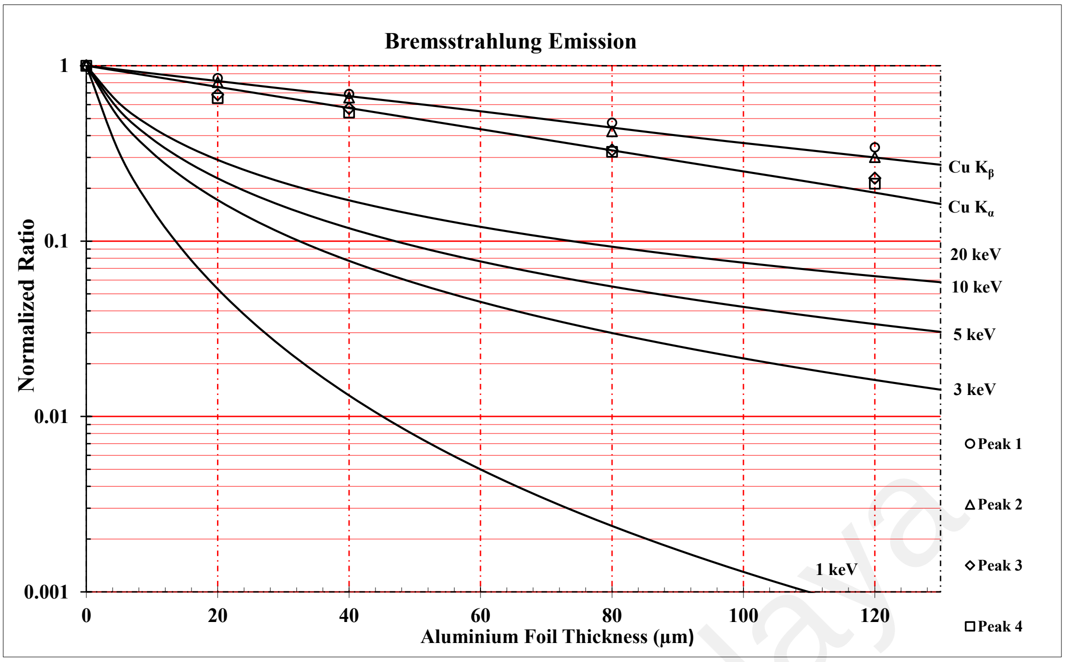

Figure 5.49: Comparison of experimental intensities ratio curves with calculated aluminium absorption curves for deuterium plasma at 0.2 mbar

In fact, for most of the discharge where the bulk of the whole soft X-ray emission including the first soft X-ray emission period was strongly dominated by copper line emission. Usually, determination of electron temperature was taken based on the soft X-ray intensity ratio of the highest peak in first soft X-ray emission period. However, the dominant copper line emission has caused the difficulties in the determination of electron temperature as can be inferred in Figure 5.50. Each experimental point was averaged over 13 discharges at 0.2 mbar and was taken from the highest peak in first soft X-ray emission period. This peak was found to lie close to the absorption curve for copper K_α line radiation indicates the soft X-ray emission was dominated by copper X-rays. This suggested the existence of strong electron beam activities bombarded at the copper anode leading to the significant emission of copper line radiation.

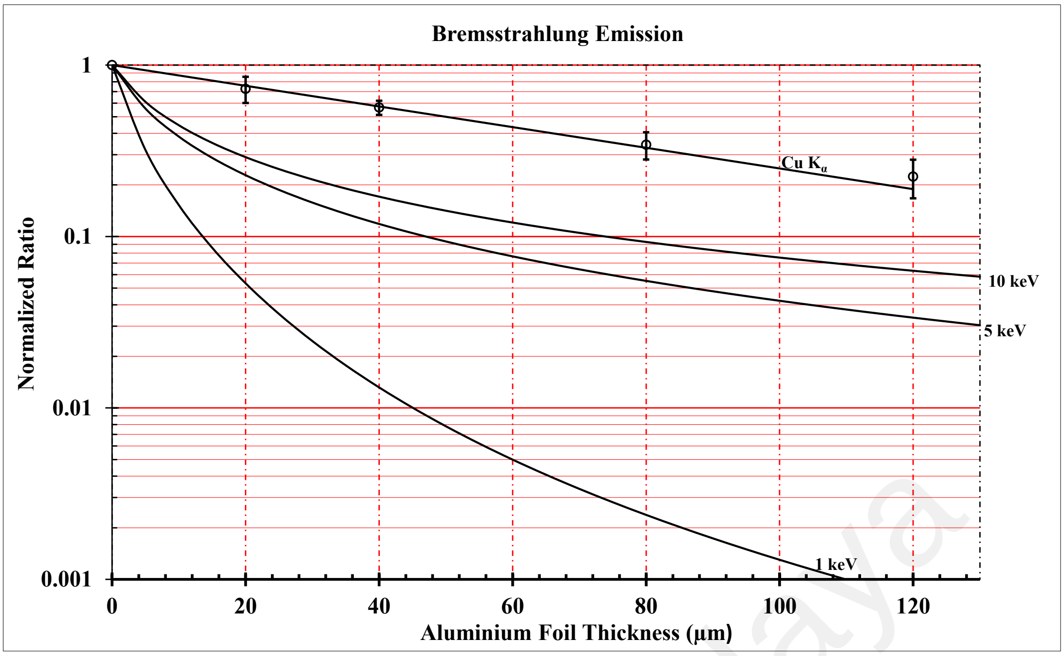

Figure 5.50: Comparison of experimental intensities ratio curves with calculated aluminium absorption curves for deuterium plasma at 0.2 mbar. Each data point has been average over 13 shots

In some of the discharges when weaker focusing discharge was obtained the contribution from the copper X-ray emission was less, the soft X-ray emission from deuterium plasma was used to determine the electron temperature of the plasma. A set of the typical time resolved soft X-ray signals is shown in Figure 5.51, where the ratio of X-ray signal detected by different channels is used to determine the electron temperature.

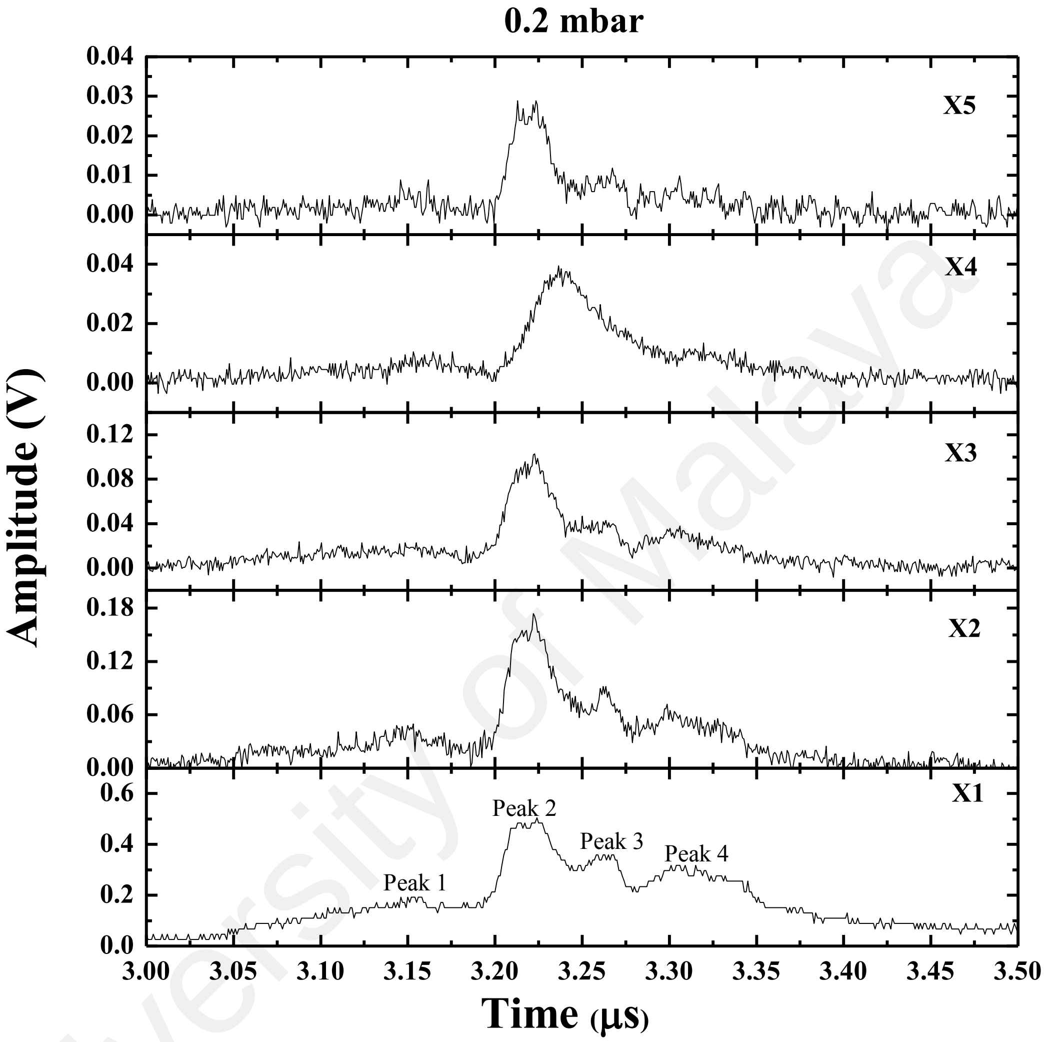

Figure 5.51: Time resolved soft X-ray signal from weaker focusing discharge at 0.2 mbar

The intensities ratio of the corresponding soft X-ray peaks was plotted against aluminium foil thickness in Figure 5.52. It is measured that the electron temperature peak 1, peak 3 & peak 4 in the soft X-ray signals are in the range of 3 – 5 keV. At this type of weak focusing discharge, the X-ray emission is not dominated by the copper line radiation as inferred from the ratio curve. No conclusive comment can be given to peak 2 as the intensities ratio fluctuates between 5 – 20 keV temperature curves.

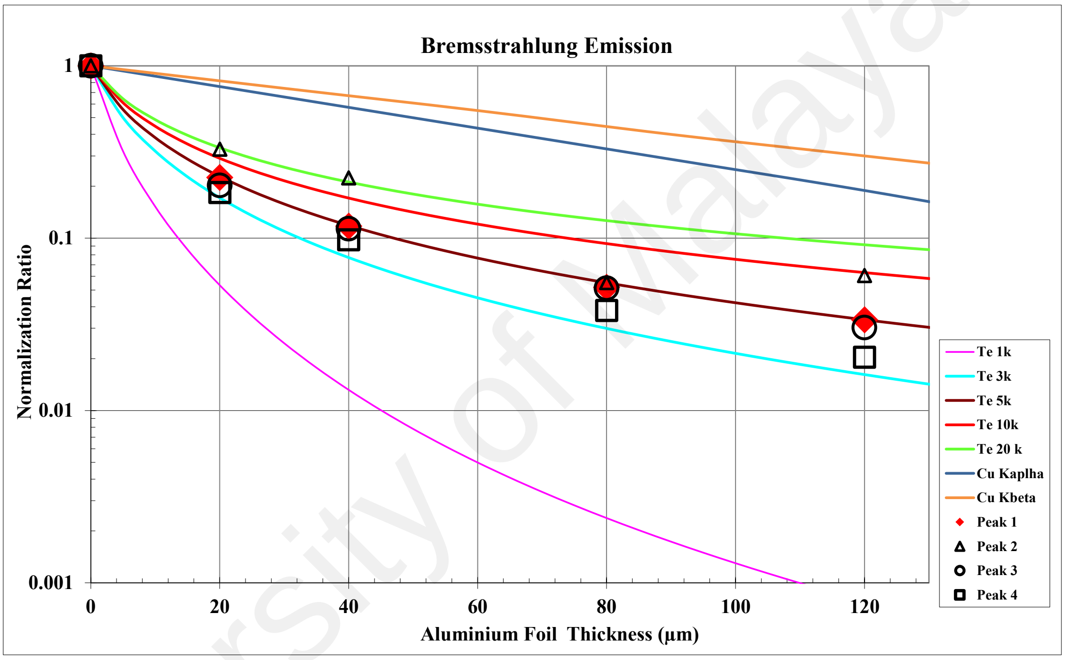

Figure 5.52: Comparison of experimental intensities ratio curves with calculated aluminium absorption curves for deuterium plasma at 0.2 mbar

5.7 Time Correlation of Voltage, Ion Beam, Soft and Hard X-ray Signal

A series of time resolved signals of ion beam, soft X-ray, hard X-ray and discharge voltage were measured simultaneously and analyzed. These time resolved studies are very useful to investigate the mechanism of charge particle acceleration. The soft X-ray signals were recorded with BPX 65 pin diode filtered by 23 μm Aluminized Mylar.

Figure 5.53 illustrated the temporal evolution of soft X-ray, hard X-ray, ion beam with the corresponding discharge voltage signal. The figure is presented in a 600 ns time window. Three peaks marked '*a*', '*b*' and '*c*' are seen in first soft X-ray burst and are corresponded to the peak of voltage spike. Peak '*a*' is attributed to the X-ray emission from the pinched plasma at maximum compression. This peak is considered to be the moment of maximum compression where the plasma column is at minimum radius. Peak '*b*' is larger than peak '*a*' which is associated with the onset of $m = 0$ instabilities. The duration of pinch life time (quiescent phase) can be determined from the time interval of peak '*a*' to peak '*b*' corresponded to 22 ns in this case. Peak '*c*' may be correlated to the X-ray emission from the unstable phase. Second soft X-ray burst after 81 ns later from peak '*a*' was speculated to be contributed from the turbulent plasma which occurred due to the disruption of the plasma column into the cloud of plasma as no indication of second compression in the voltage signal. At about 160 ns after the first soft X-ray peak (peak '*a*'), a lower intensity and longer lasting soft X-ray emission was observed which was due to emission by electrode material evaporated from the anode.

On the other hand, multiple peaks structure were also observed in biased ion collector signals, where at least 4 peaks were identified. The first peak in both biased ion collector signals was of low intensity and occurred at the same instant with soft X-ray, hard X-ray and voltage spikes. Hence, this peak was due to the photon emissions. Peak 2, peak 3 &

peak 4 showed time difference between first and second biased ion collector. The ion beam energies were determined as 127 keV (peak 2), 38 keV (peak 3) & 31 keV (peak 4), respectively. The origin time of ion peak 2, 3 & 4 when the ions emission started were 2.75, 2.73 and 2.79 μs, respectively. Ion peak of highest intensity was emitted at the time of maximum compression. Later ion beam was to have higher energy emitted at the moment corresponding to the development of $m=0$ instability. At the instant of the growth of instabilities, a higher localized electric field was generated as indicated by higher amplitude of voltage spike. The high electric field accelerated the ions to the high energy.

The start time of peak 4 calculated as 2.79 μs, where there is no indication of plasma compression in the voltage signal therefore the peak 4 is believed to be emission after the disruption of the plasma column. The ion beam signals resolved indicated that the ion beams were generated by different mechanism. The ion beam intensity generated during the pinch was higher compared to the ion beam emitted after the pinch (during plasma disruption).

Together with the emission of ion beam in the forward directions, electron beams were emitted in the backward direction. The electron beam hitting the anode produced hard X-ray. From the time of hard X-ray signal, it is found that the electron beam was emitted during the pinch. It has been observed that the ion beam (in peak 2 and 3) was emitted at the time coincided with the hard X-ray signal, therefore confirm that the ion beam and the electron beam were due to a same localized high electric field. The ion beam detected at peak 4 was emitted after pinch and less energetic. The corresponding electron beam did not result in hard X-ray emission.

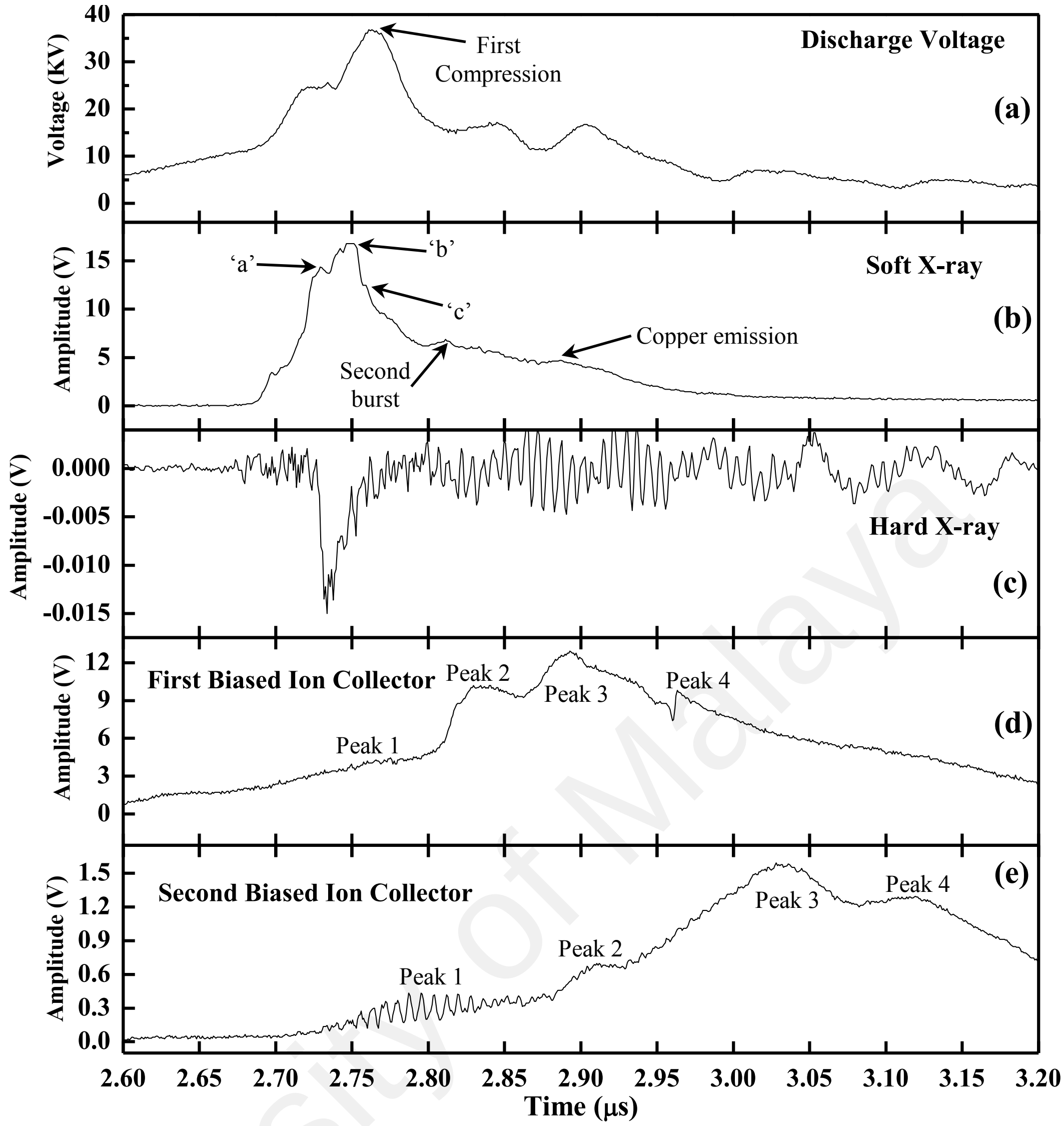

Figure 5.53: Time resolved ion, soft X-ray, hard X-ray with corresponding voltage signal at 0.3 mbar. From top to bottom traces are (a) discharge voltage signal, (b) soft X-ray recorded by PIN diode, (c) hard X-ray signal recorded by scintillator-photomultiplier tube detector, (d) & (e) time of flight ion beam signals recorded by biased ion collector

Another set of signals consisting the time resolved ion beam, soft and hard X-ray together with the discharge voltage signals are shown in Figure 5.54. The voltage spikes indicated several pinches. The few soft X-ray pulses were also correlated to the voltage spikes. In the first pulse of the soft X-ray signal three peaks have been identified to be associated to the first plasma compression, onset of instabilities and disruption of plasma column. Thus, the peak *1a* in the soft X-ray signal was corresponded to the instant of *t=0* which the plasma pinched to minimum radius. The electron beam was emitted during the pinch and after the pinch, where a hard X-ray peak was also observed after the maximum compression. Peak *1b* of the soft X-ray signal indicated the onset of instabilities. Duration of pinch was estimated to be about 20 ns from the maximum compression to the disruption due to instabilities.

A second soft X-ray pulse was registered at 2.83 μs, which was 100 ns after the pinch and associated with a second pinch. This soft X-ray emission was less compared to the first emission. There are another two X-ray pulses correlate to the third and fourth voltage spikes. If the two voltage spikes registered due to another two plasma compression, the signals showed that the plasma was more turbulent, the soft X-ray was more while no ion beams and hard X-ray were registered.

The three ion peaks are labelled as pk 1, 2 & 3, each has the energy of 94, 30 & 17 keV, respectively. Ion peak 1 & 2 was found to be emitted during the first pinch and peak 3 was emitted at second pinch. During the first pinch, higher ion beam energy was found correlated to emission at the onset of instabilities while the lower energy component was emitted at the maximum compression of the pinch. The ion beam emission during the maximum compression of the pinch was found to have higher intensity.

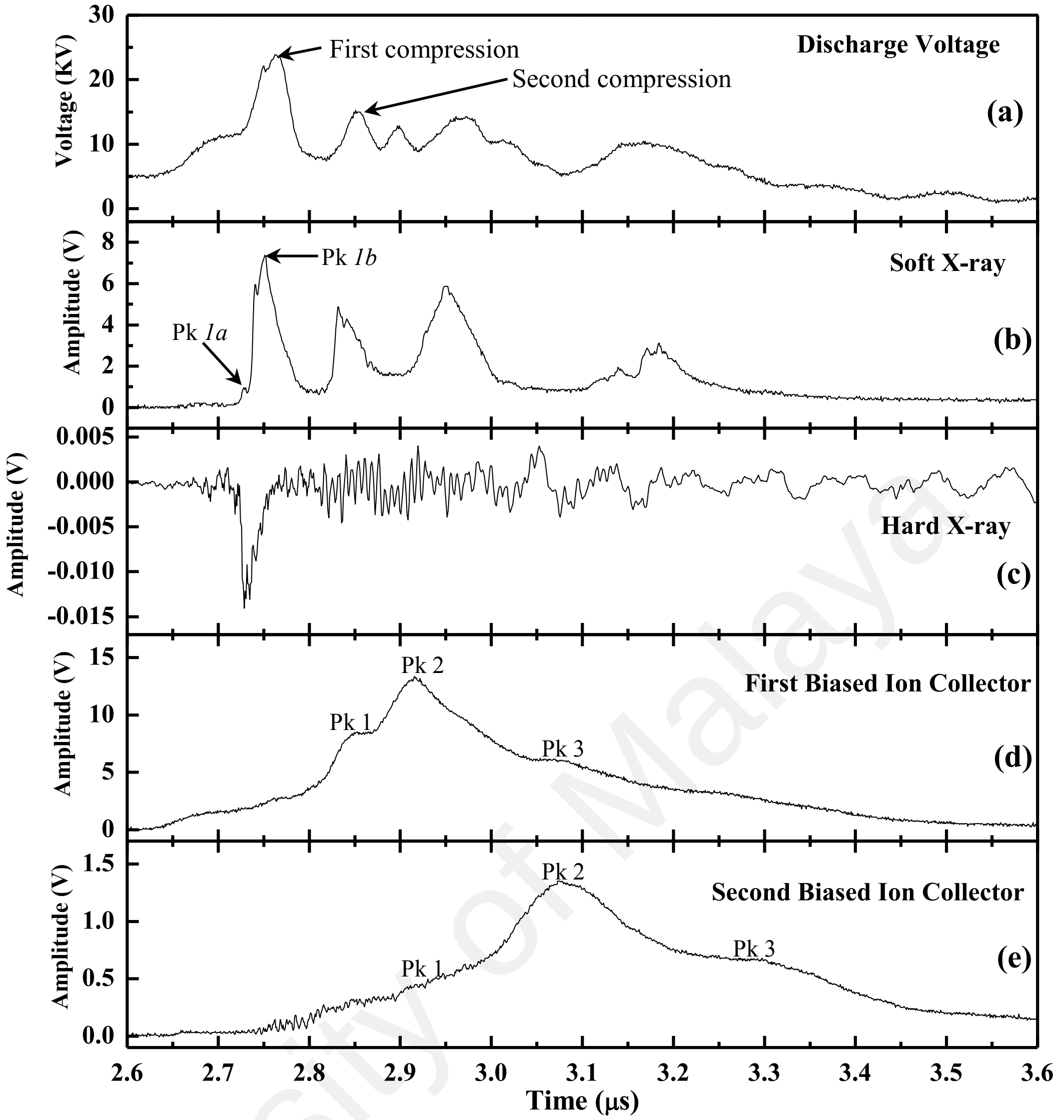

Figure 5.54: Time resolved signal of all diagnostics in 1 μs window at 0.3 mbar. From top to bottom traces are (a) discharge voltage signal, (b) soft X-ray recorded by PIN diode, (c) hard X-ray signal recorded by scintillator-photomultiplier tube detector, (d) & (e) time of flight ion beam signals recorded by biased ion collector

5.8 Correlation of Radiation Emission and Discharge Parameters

The correlations between the radiation emissions and the discharge and pinch dynamics are summarized to give a better understanding on the inter-correlation between different type of radiation emission and effect of discharge parameters to the radiation output.

A) Ion beam energy versus discharge voltage

The highest ion beam energy was obtained from every shot and correlated to the amplitude of the corresponding voltage spike. Figure 5.55 shows the summarized results of all the shots in the pressure range of 0.1 - 0.8 mbar. It is discernible that the ion beam energy is closely related to the voltage spikes and operating pressures. As the voltage spike measured the plasma inductance and the sudden increase in the plasma resistance during pinch, its amplitude represent the rapid change of the plasma impedance. During the pinch, the increment of the plasma impedance resulted a localized high electric field that is responsible for the ion beam acceleration, thus resulted high energy ion beam.

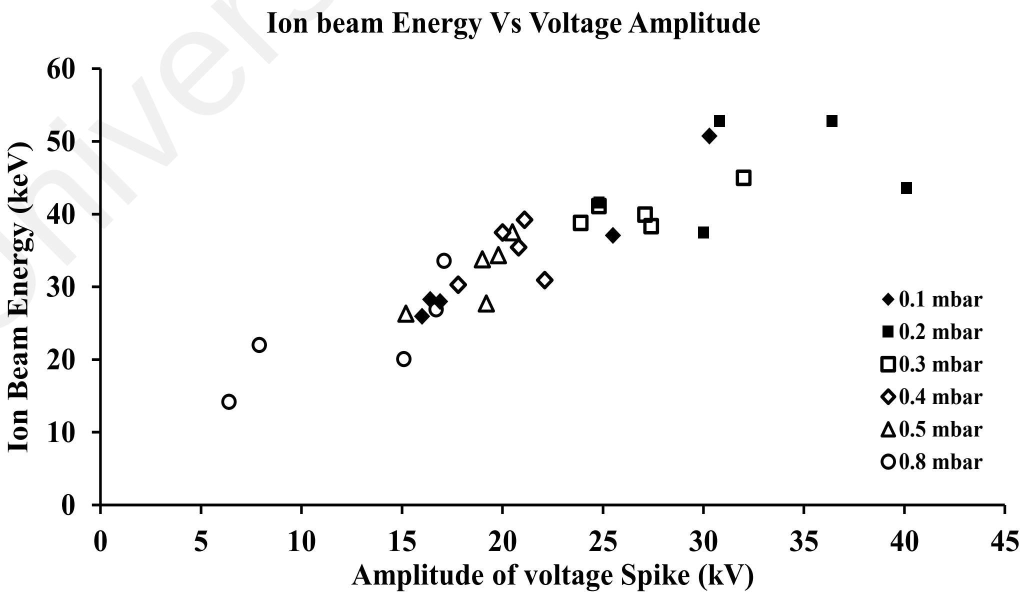

Figure 5.55: Ion beam energy as a function of voltage amplitude

On the other hand, both ion beam energy and amplitude of voltage spikes were found increasing with reduced pressure. This implied that the ion beam emission is strongly dependent on the dynamics of the plasma pinch. To have better picture of the ion beam energy with amplitude of voltage spike and operating pressure, average reading of the ion beam energy and the corresponded voltage amplitude at each operating pressure was analyzed and illustrated in Figure 5.56. It is quite pronounced that almost a linear correlation between the ion beam energy and amplitude of voltage spike is obtained. Low ion beam energy with low amplitude of voltage spike has been obtained at 0.8 mbar due to weak focusing discharge whereas the highest ion beam energy due to highest amplitude of voltage spike was obtained at 0.2 mbar. At pressure of 0.1 mbar, the amplitude of voltage spike decreased and thus resulted in lower ion beam energy production. This is because the pinching at 0.1 mbar occurred much earlier before the discharge current reaches to the maximum. It has also been observed at this pressure a poor pinching of plasma and smaller voltage spike.

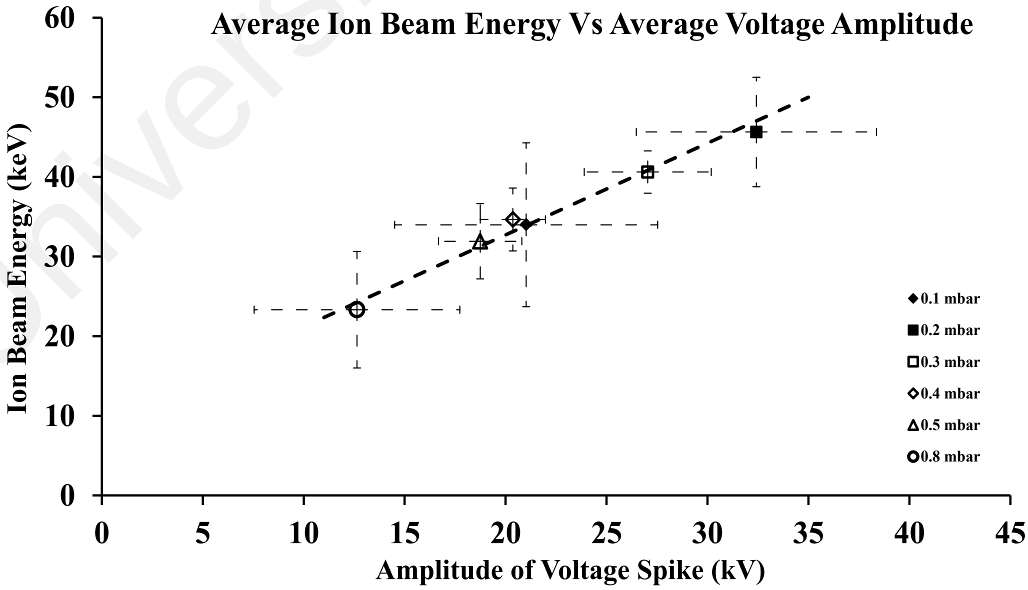

Figure 5.56: Average ion beam energy Vs average amplitude of voltage spike at each pressure

B) **Ion beam energy versus focused energy**

The focused energy is the energy transferred into the plasma during the pinching. It has been calculated from the discharge voltage and current signals (method refers to 5.1.2). Figure 5.57 explains the dependency of the ion beam energy on the focused energy. During pinch phase, variety of pinch phenomena and radiation emission were taking place. As discussed in section 5.7 that ion beam emitted at the moment of maximum compression and accelerated due to various possible mechanisms. Therefore correlation of ion beam energy with the plasma focused energy is presented here.

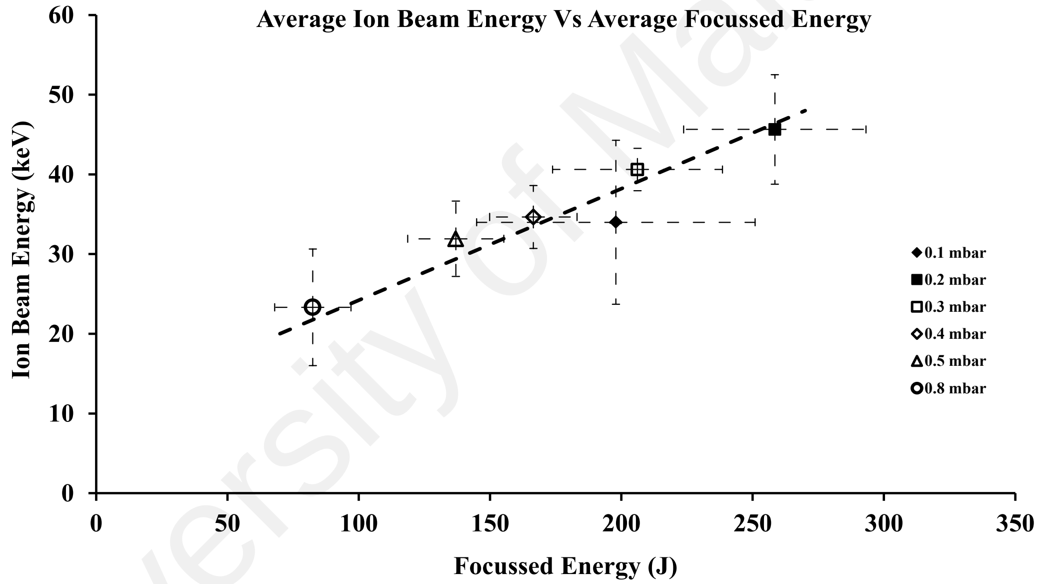

Figure 5.57: Average ion beam energy versus average focused energy

It is shown that the focused energy is generally larger for discharges producing higher ion beam energy. Energy transferred into the pinch heats up the plasma and increase the kinetic energy of deuterons. The energy is shared by the deuterons, thus higher focused energy resulted higher ion beam energy.

C) Ion beam energy versus current drop

The current drop registered in the current signal during the pinch with respect to the operating pressures has been discussed in Section 5.1.3. It is related to the anomalous resistivity effect for plasma focus device of high inductance ≥ 100 nH (Lee et al., 2011) and operated in low pressure regime of less than 1 mbar. Variations of the ion beam energy versus the current drop at different operating pressures were summarized in Figure 5.58. The scattered points from the many shots show the shot to shot variation but at the same time pointed to a positive correlation of the dependency of the ion beam energy to the current drop (Figure 5.59).

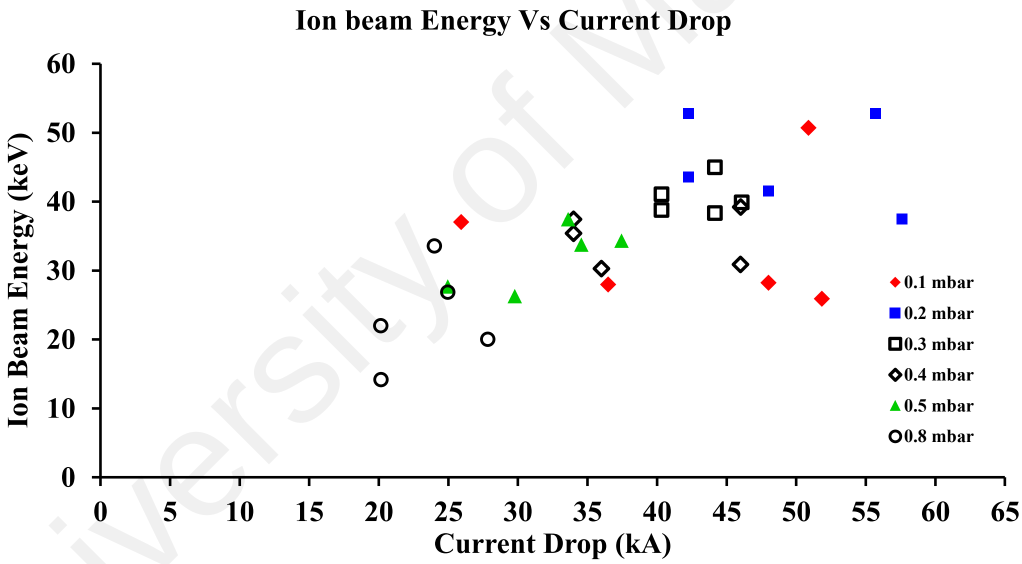

Figure 5.58: Variation of ion beam energy with respect to current drop at all pressures

It has been reported by Behbahani et al. that the current drop is related to the effect of anomalous resistance which is arisen from the onset of different types of instabilities and micro turbulences (Behbahani & Aghamir, 2012). Thus, the fundamental parameter that determines the duration and amount of the current drop in a discharge is characterized by the energy transferred into the plasma during the pinching process. The larger current drop implies that greater amount of energy has been transferred to the plasma column.

Therefore, expected the ions in the pinched plasma would gain more energy and thus accelerated to higher energy.

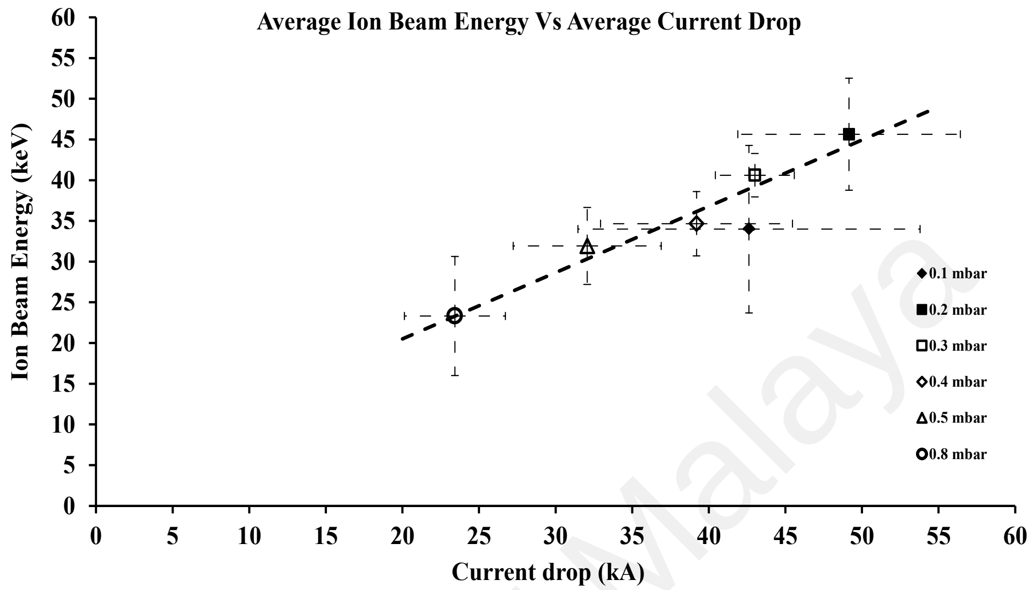

Figure 5.59: Average ion beam energy and corresponded average current drop at different pressure

D) Hard x-ray intensity versus discharge voltage

The hard X-ray intensity in terms of signal amplitude is plotted against the voltage amplitude for all the measured shots with hard X-ray emission. The voltage amplitude was taken from the voltage spike corresponded to the instant of hard X-ray emission. Hard X-ray intensity in the end on direction was analyzed. Figure 5.60 showed the dependence of the hard X-ray intensity on the voltage amplitude. The hard X-ray intensity is found correlated to the amplitude of voltage spike as well as the pressure. Similar pattern was also observed for the hard X-ray measured experimentally at side on direction.

Essentially, the production of hard X-ray is originated from the interaction of electron beam from the plasma column with the anode target through bremsstrahlung process. In this way, the intensity of the hard X-ray emission is attributed with the energy of the emitted electron beam. The high induced accelerating field reflected in the high amplitude of voltage spike has resulted the energetic electron beam and upon striking the anode produced intense emission of hard X-ray. Highest hard X-ray intensity obtained at 0.2 mbar is consistent with the highest ion beam energy measured at the same pressure.

It is also important to note that there is a threshold in the amplitude of voltage spike for the hard X-ray emission. No hard X-ray signals were registered for amplitude of voltage spike below 15 kV. It is interesting to note that the charging voltage of each discharge is fixed at 13.5 kV but hard X-ray signal was only observed when the amplitude of voltage spike is beyond 15 kV. Thus, hard X-ray signal was not observable at pressure beyond 0.5 mbar where the amplitude of voltage spike is mostly less than 15 kV. This may be due to the limitation of the diagnostics technique to register hard X-ray signals for discharge with amplitude of voltage spike below 15 kV.

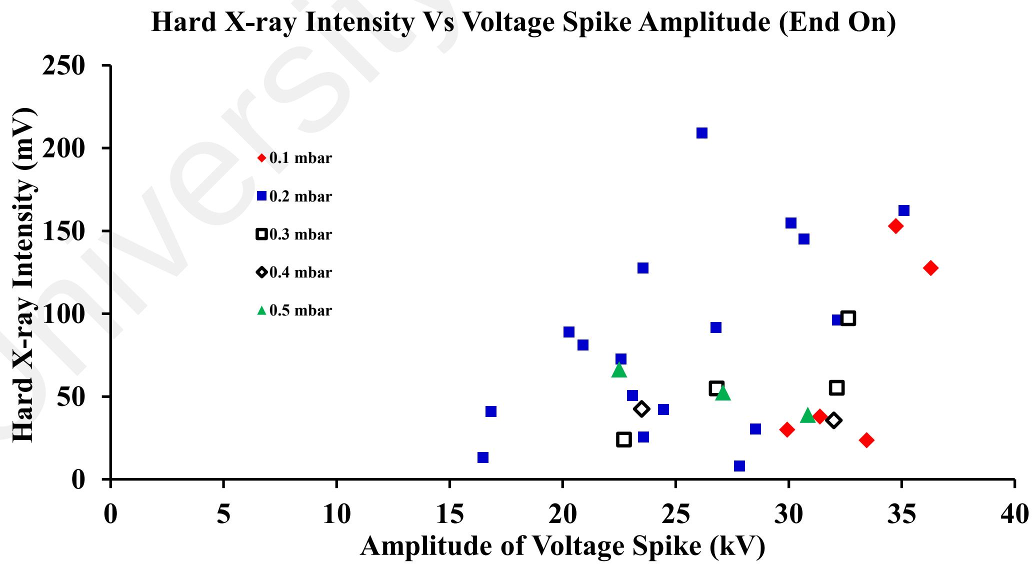

Figure 5.60: Hard X-ray intensity versus corresponded voltage amplitude at all pressure

E) Hard X-ray intensity vs ion beam energy

In previous section, it has been shown that the hard X-ray intensity is strongly dependent on the amplitude of voltage spike. The amplitude of voltage spike is a gross indicator for the strength of induced electric field that is necessary to accelerate the electron beams in the plasma column for the production of hard X-ray by bremsstrahlung process upon bombarded with the anode surface. Therefore, higher intensity of hard X-ray emission indicates higher energy of the electron beam which is not measured in current project. Nevertheless, the ion and electron beam were found to be accelerated and originated from the same instant as discussed in Section 5.7. In other words, higher energy ion beam and hence electron beam shall produce hard X-ray of higher intensity as summarized in Figure 5.61.

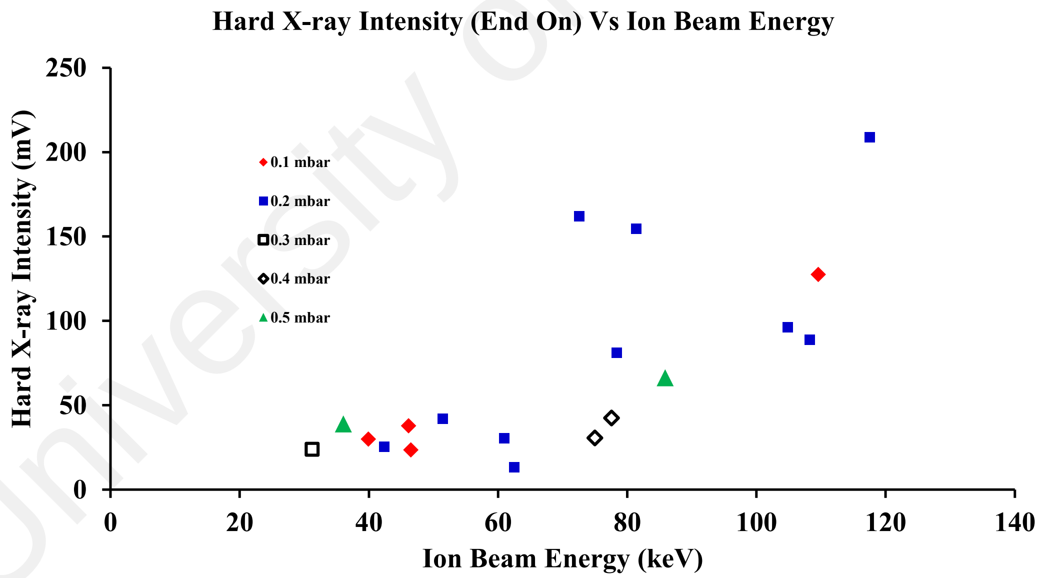

Figure 5.61: Hard X-ray intensity as a function of ion beam energy

It is worth to mention that the induced electric field must exceed the critical electric field, E_c which is given as:

$$E_c[\mathrm{Vm^{-1}}] \approx 3.9X10^{-10}\frac{n[\mathrm{cm^{-3}}]}{kT[\mathrm{eV}]} \quad \textbf{(5.3)}$$

where n is the electron density and kT is the electron temperature (Barbaglia et al., 2009). This phenomena is known as Dreicer condition for electron runaway in plasmas (Dreicer, 1959) for the production of hard X-rays.

The induced electric field E can be calculated from the voltage drop (V_p) and length of plasma column (Z_p) where ($E = V_p/Z_p$). The method to determine voltage drop has been reported elsewhere (Bruzzone et al., 2006). Despite the parameters required for the verification of the Dreicer condition are not available for the present work, nevertheless the correlation between hard X-ray intensity and ion beam energy does show an important finding. In the light of this fact, comparison between induced electric field in the plasma column and critical electric field is believed to help in verified the evidence of Dreicer condition for electron runaway in plasma focus device which shall demand a further study in future work.

F) Ion beam fluences vs hard X-ray yield

It is a challenge to give a clear clarification on number of electrons that is responsible for the emission of hard X-ray due to the constrained in the diagnostics tools and the lack of reproducibility in the hard X-ray production. However, by virtue of the fact that electron and ion beam are mutually correlated, there is reason for expecting a strong correlation between ion beam and the hard X-ray emission. Thus, the influence of electrons beam fluences represented in terms of ion beam fluences on the hard X-ray yield is investigated.

Assuming singly charged ion, fluence of electron beam is taken as same as the ion beam. Hard X-ray yield was calculated in terms of area under the hard X-ray signal with respect to time for the whole period of hard X-ray emission. Correlation of hard X-ray yield with ion beam fluences was established on a statistical basis and is showed in Figure 5.62. Each data point was taken from the same discharge where the ion beams and hard X-ray emission was measured simultaneously. The results show that the hard X-ray emission does not depend solely on the electron beam fluence (ion beam fluence) but also the operating pressure. A conclusion may be extracted from this results is that at beam optimized mode the device is not only optimizes for ion beam production but also hard X-ray generation via electron beam – anode target mechanism.

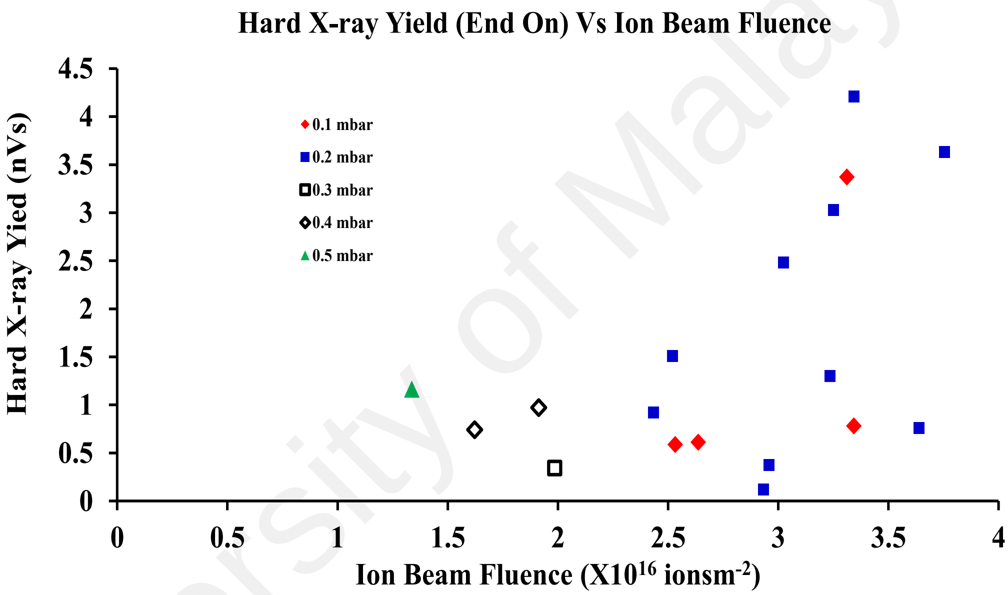

Figure 5.62: Variation of hard X-ray yield with ion beam fluences

CHAPTER 6: CONCLUSIONS & SUGGESTIONS FOR FURTHER WORK

6.1 Conclusion

In the present study, exploration in low pressure regime on the pulsed radiation emission produced by a 30 μF, 13.5 kV plasma focus device has been experimentally investigated and reported. Mainly we are focus on ion beam emission with the attempt to study the mechanism of ion beam production and its correlation with other emissions and discharge parameters.

A systematic studies have been carried out at pressure of 0.1 – 1.0 mbar with deuterium filling only. Two types of focusing discharge were obtained, i.e. discharge with single voltage spike and discharge with multiple voltage spikes. Discharge with single voltage spike was more readily to be obtained at higher pressure meanwhile more than 80 % of the total discharges showed multiple voltage spikes in these pressure range. The origin of this multiple voltage spikes in the focusing discharge is suggested to be correlated with micro-instabilities and turbulences occurred in the plasma pinching

Analysis of discharge voltage and current signals showed that focusing discharge which occurs at time slightly before the maximum of the discharge current is favourable for a good plasma pinch associated with high ion beam emission. This is the case for the plasma focus discharge at operating pressure of 0.2 mbar. It is believed that under this condition, the magnetic piston is still able to transfer energy to the pinched plasma during the pinch phase. Thus, a stronger pinching and hotter plasma is formed. Accordingly, more energies are shared between particles in the pinched plasma and produced higher energy ion beam.

The performance of the plasma focus discharges evaluated from the discharge voltage and current signals indicates that an average energy of (290 ± 40) J are transferred into the pinched plasma in the low pressure operation. This corresponds to an efficiency of about 9 % considered the maximum discharge energy of 2.7 kJ. The discharge current signals with multiple current dips and prolong duration showed that several important mechanisms taking place after the current sheath collapses to the axis. Fitting using six phase Lee model code showed that anomalous resistivity effect could explain the characteristic of the current drop and multiple current dips during the pinch phase.

Anomalous Resistance ascribed to the growth of various types of instabilities and micro turbulence has the significant effect on the pinched plasma and thus the radiation emissions. Onset of instabilities and micro turbulence during the pinch phase was found to be more profound at low pressure which play a dominant role in the mechanism of energy transfer to the pinched plasma and also in the enhancement of ion beam as well as hard X-ray emission.

Comparison of various diagnostic techniques for ion beam measurement showed that 0.2 mbar is the optimum operating pressure for highest ion beam fluence and beam energy production. At pressure range of 0.1 – 0.5 mbar, intense ion beam emission with great reproducibility has been measured. At pressure beyond 0.5 mbar, weaker focusing discharge is obtained and thus the ion beam emission becomes less significant. Intense pulsed ion beam emission with average energy of 21 – 53 keV are consistently obtained at operating pressure between 0.1 – 0.5 mbar with ion beam fluence in the order of 10^{15} ions/m^2.

In addition to ion beam signal, plasma jet was also observed but at a later time with relatively low intensity. The average velocity of the plasma jet was measured to be about 0.87 cm/µs. We found that the bombardment of plasma jet on the biased ion collector can be reduced significantly by using a 2 mm aperture which was located before the biased ion collector.

The solid state nuclear detectors were used to measure the angular distribution of the ion beam emission. The ion beam emission is highly anisotropy and emitted mainly in the forward direction. Saturated ion tracks were obtained at the end on (0^o) and 30^o angular position, and spread out to about 30^o. The exposed solid state nuclear track detector was etched in 6M of NaOH for different duration and it was found that 5 - 7 hours etching time is suitable to show clear ion tracks.

Ion beam population has also been deduced from measurement using solid state nuclear track detectors (CR-39). Two group of ion tracks were found where ion tracks with smaller crater diameter (1 - 3 µm) is more abundance than the larger ones (3 – 5 µm), suggesting there are more ions of lower energy. The density of the ion tracks was measured to be 6.3×10^{10} ions/m^2. The overall distribution of ion tracks according to the track sizes is in the Maxwell distribution where 76 % of the total population of ions tracks lies between 2 – 4 µm.

At charging voltage of 13.5 kV, ion beam signals with multiple peak structures and energies in the range of 18 – 350 keV were resolved using two biased ion collectors by time of flight technique. This suggested there could be few mechanisms that generates the accelerating field responsible for the energetic ion beam production. Time resolved measurement of ion beam, soft X-ray, hard X-ray and discharge voltage indicated that the ion beams were emitted at different instances during the pinch phase. Majority of the ion beam was emitted at the moment of maximum compression and some after the onset of instability. The ion beam emitted due to $m = 0$ instability has higher energy. The growth of instabilities induce higher localized electric field which was also indicated in the voltage spike. Analysis from the hard X-ray signal confirms that the ion beam and the electron beam were emitted corresponded to a same localized high electric field.

Lee model was used to generate comparable plasma focus discharges numerically and the results on the ion beams were intended to explain the experimentally observed data. Comparison of the ion beam measurement with Lee model code showed a fair agreement in terms of ion beam energy. Ion beam emission from the plasma focus discharge to a large extend is believed to be accelerated by the high voltage produced during the pinch like a plasma diode action. The plasma diode action was modelled in Lee Model by taking the acceleration voltage to be three times the maximum voltage induced by the radially collapsed current sheath. This gave the energy of ion beam in the range of 35 to 70 keV to match the measured data.

The ion beam fluence on the other hand is calculated by assuming the focusing action remain effective without considering Magnetic Reynold Number (MRN) effect in increasing pressures, thus the number of ions increases in higher pressures. The measured data shown the realistic trend of ion beam fluence versus pressures which is depending on the plasma focusing action. Magnetic Reynold Number effect becomes significant at higher pressure due to lower current sheath speed. Thus, resulting in diffusive current sheath structure and weaker electromagnetic drive mechanism. Therefore, the computed ion beam fluence and number of ions from the model failed to explain the measured data.

In reality, not all the ions are compressed into the pinch and ejected as ion beam (This is the art of PF).

In the present configuration of long electrode, the operating pressure used was relatively low compared to normal pressure regime of several mbar. Since neutron yield is strongly dependent on operating pressure, thus the neutron yield is expected to be low. Neutron yield in the order of 1 x 10^6 neutrons per shot at the pressure of 0.2 mbar was measured, which is two order of magnitude lower than the 10^8 measured at normal pressure discharge. The time of flight measurement using pair of scintillator-photomultiplier detectors give the neutron energy of 3.31 MeV at the end on direction suggesting the existence of beam-target mechanism for neutron production.

Hard X-ray emission was registered in about half of the discharge at 0.2 mbar. The hard X-ray emission correlated to the ion beam emission and increases with the ion beam energy. This is explained as energetic electron and ion beam are generated in opposite direction, and the electron beam bombardment onto the anode resulted the hard X-ray emission. The soft X-ray registered was also strongly dominated by copper line radiation such as copper K_α and copper K_β with the copper vapour introduced from the anode. In measurement where copper X-rays emission is less, the electron temperature of the deuterium plasma was estimated in the range of 3 – 5 keV.

Time resolved studies and numerical computation showed that there is no single ion acceleration model that could stand alone to explain our results where ion beam emission has been shown to produce by different mechanism. Nevertheless, ion beam acceleration model concerning an anomalous resistivity effect in conjunction with plasma diode action could be more appropriate for explaining the enhanced ion beam emission in low pressure regime.

The plasma focus with static inductance of more than 100 nH operated in low pressure is a new regime conducive to higher ion beam production, in contrast to the high pressure operation which was conventionally optimized for neutron emission at several mbar of deuterium. In other words, at low pressure operation the plasma focus is operated in ion beam enhanced mode. The current setup therefore is potentially a versatile pulsed deuteron beam source for the application in breeding fissile fuels (Kazunari, 1982) and beam-target neutron production using beryllium target (Ajzenberg, 1952; Whittlestone, 1977).

6.2 Suggestion for Further Work

Present work reported a comprehensive results of ion beam and associated radiation emission in low pressure plasma focus operation. The discussions have enhanced our understanding on the plasma dynamics and the ion acceleration mechanisms, while also posting some deeper questions. Some suggestions for further work are proposed and discussed below.

The Faraday cup used in present work was a flat plate collector design where it may suffer from the demerits of low signal to noise ratio and the secondary electron emission upon registration of ion beam. Thus, this design of Faraday cup can be modified into version of deep cup collector to improve the efficiency of the diagnostic. A charge collector material that minimizes the emission of secondary electrons such as graphite is suggested to replace the copper metal plate. This design will enable a fast nanosecond response of the diagnostic while register ion beam with a broad range of energy from few keV to hundreds of keV.

The determination of ion beam angular distribution has been based on the method using solid state nuclear track detectors. This method has the drawback of long processing time to get the information from the exposed detector where an exposed detector need to be etched for few hours and analysed under optical microscope. On the other hand, a multiple Faraday cup assembly can be developed for measuring the angular distribution of the pulsed ion beam. This method does not require protection of the detector against ion beam irradiation during conditioning shots while the information of the ion beam angular distribution can be obtained upon careful analysis from the measured ion beam signal without long etching procedure.

To anticipate the plasma focus device for application as an intense pulsed ion beam source, it is very important to understand the ion beam acceleration mechanism. The time resolved measurement in present work can be improved by investigate simultaneously the ion beam emission with electron, soft X-ray, hard X-ray and electrical discharge signal. The measurements could also give meaningful results when correlates to the imaging of the pinching evolution that shall verified the ion beam emission chronology.

Plasma focus operated at low pressure regime of below 1 mbar seems to be optimized for ion beam production. In these pressure regime, a very significant dip and long duration of current drop can be observed in the discharge current signal. This phenomena is believed to be due to the effect of anomalous resistivity which was attributed to the set in of various plasma instabilities and micro turbulence. To substantiate this argument, time resolved imaging of the plasma pinch and pinch structure from a single discharge using gated micro-channel plate or streak camera could be carried out. This kind of time resolved image with frame separation of a few nanoseconds would give a better insight in understanding the plasma dynamics at low pressure. This could also help in investigate the determining factor in optimizing the ion beam emission.

It has been shown in previous chapter where the whole of the soft X-ray emission period was dominated by copper X-ray line emission due to evaporation of copper material from the anode. This in turns has caused the determination of the electron temperature for deuterium plasma to be uncertain. Therefore, to improve the electron temperature measurement of the plasma, electrode material with the characteristic of high resistant to ablation such as stainless steel can be employed to replace the copper anode. Anode with hollow geometry to reduce the contamination due to electron beam bombardment on the anode surface is suggested.

In this project only pure deuterium gas was used. Doping with high *Z* gas of different concentration in the deuterium discharge can be conducted in future work which may induce radiative collapse phenomena resulting in stronger compression and tighter pinch. This could lead to an increase in the interaction time between the energetic ions and pinched plasma and thus enhances the neutron production. Different mechanism for ion beam and neutron production may exist for plasma focus operated with gas admixture compared to pure filling. Therefore, such investigation may establish a better correlation between the ion beam and neutron yield in resolving the questions of neutron production mechanism from a plasma focus of whether it is predominantly thermonuclear or of beam-target origin.

Other than doping with high Z gases, deuterium mixed with tritium gas is proposed to enhance the neutron yield. Since the cross section for deuterium-tritium reaction is about 100 times more than the deuterium-deuterium reaction, typical neutron production increased by two orders of magnitude is anticipated. Therefore, with current plasma focus neutron yield of 10^6 per shot, it will be possible to achieve 10^8 neutron per shot. The enhanced neutron yield can be explored for the application in neutron radiography and detection of hidden illegal objects due to the high penetrating power and activation properties of this ionizing radiation.

In order to examine the feasibility of the plasma focus as pulsed ion beam source, the experiments with deuterated target for application in beam target neutron production can be explored. Research into this area is also vital in the sense that it may lead to the development as a pulsed neutron source via beam-target scheme for application in the test of first wall material of fusion reactor.

REFERENCES

Abdollahzadeh, M., & Sadat, K. S. M. (2010). Time dependent behavior of neutron emission in Dena plasma focus. *Journal of Fusion Energy, 29*(3), 218-222.

Agarwala, P., Annapoorni, S., Srivastava, M. P., Rawat, R. S., & Chauhan, P. (1997). Magnetite phase due to energetic argon ion irradiation from a dense plasma focus on hematite thin film. *Physics Letters A, 231*(5-6), 434-438.

Aghamir, F. M., & Behbahani, R. A. (2011). Current sheath behavior and its velocity enhancement in a low energy Mather-type plasma focus device. *Journal of Applied Physics, 109*(4), 043301.

Ahmad, S., Hussain, S. S., Sadiq, M., Shafiq, M., Waheed, A., & Zakaullah, M. (2006). Enhanced and reproducible neutron emission from a plasma focus with pre-ionization induced by depleted uranium (U238). *Plasma Physics and Controlled Fusion, 48*(6), 745-755.

Ajzenberg, F. (1952). Deuteron Bombardment of Be 9 and Classification of Levels of B 10. *Physical Review, 88*(2), 298-304.

Akel, M., Alsheikh, S. S., Ismael, S., Saw, S. H., & Lee, S. (2014). Interaction of the high energy deuterons with the graphite target in the plasma focus devices based on Lee model. *Physics of Plasmas, 21*(7), 072507.

Akel, M., Salo, S. A., Ismael, S., Saw, S. H., & Lee, S. (2017). Comparison of measured and computed beam ion current densities emitted from two 2 kJ plasma focus machines. *Vacuum, 136*, 163-167.

Akel, M., Salo, S. A., Saw, S. H., & Lee, S. (2014). Properties of ion beams generated by nitrogen plasma focus. *Journal of Fusion Energy, 33*(2), 189-197.

Al-Hawat, S. (2004). Axial velocity measurement of current sheath in a plasma focus device using a magnetic probe. *IEEE Transactions on Plasma Science, 32*(2), 764-769.

Amrollahi, R., Habibi, M., & Shahshenas, S. (2009). Correlation between plasma pinch intensity, current sheath symmetry, and HXR yield by APF plasma focus device. *Plasma Devices and Operations, 17*(1), 1-7.

Angeli, E., Tartari, A., Frignani, M., Mostacci, D., Rocchi, F., & Sumini, M. (2005). Preliminary results on the production of short-lived radioisotopes with a Plasma Focus device. *Applied Radiation and Isotopes, 63*(5-6 SPEC. ISS.), 545-551.

Atkinson, R. d. E., & Houtermans, F. G. (1929). Zur Frage der Aufbaumöglichkeit der Elemente in Sternen. *Zeitschrift für Physik, 54*(9), 656-665.

Auluck, S. K. H. (2014). Bounds imposed on the sheath velocity of a dense plasma focus by conservation laws and ionization stability condition. *Physics of Plasmas, 21*(9), 090703.

Ayash, S., Alshoufi, K., Soukieh, M., & Al-Hawat, S. (2016). Al2O3/Y2O3/ZrO2 ceramic composite properties investigation by plasma focus device. *Journal of Fusion Energy, 35*(3), 567-572.

Bailey, L. E. (1963). Fluorescent yield in the phosphor NE‐102 for x-rays from 4 to 17 keV. *Journal of Applied Physics, 34*(10), 3008-3009.

Bar, A. E., & Porath, Y. (1975). The use of a dense plasma focus accelerator in nuclear physics. *Nuclear Instruments and Methods, 123*(1), 5-9.

Barbaglia, M., Bruzzone, H., Acũa, H., Soto, L., & Clausse, A. (2009). Experimental study of the hard x-ray emissions in a plasma focus of hundreds of Joules. *Plasma Physics and Controlled Fusion, 51*(4), 045001.

Bayley, J. M., Decker, G., Kies, W., Mälzig, M., Müller, F., Röwekamp, P., . . . & Sidelnikov, Y. V. (1991). Observations of soft x‐ray production in the speed 2 plasma focus. *Journal of Applied Physics, 69*(2), 613-617.

Beckner, E. H., Clothiaux, E. J., & Smith, D. R. (1969). Dominant source of soft x radiation from coaxial discharge tubes. *Physics of Fluids, 12*(1), 253-254.

Beg, F. N., Krushelnick, K., Gower, C., Torn, S., Dangor, A. E., Howard, A., . . . & Gillespie, J. R. (2002). Table-top neutron source for characterization and calibration of dark matter detectors. *Applied Physics Letters, 80*(16), 3009-3011.

Beg, F. N., Ross, I., Lorenz, A., Worley, J. F., Dangor, A. E., & Haines, M. G. (2000). Study of x-ray emission from a table top plasma focus and its application as an x-ray backlighter. *Journal of Applied Physics, 88*(6), 3225-3230.

Behbahani, R. A., & Aghamir, F. M. (2011). Anomalous resistivity effect on multiple ion beam emission and hard x-ray generation in a Mather type plasma focus device. *Physics of Plasmas, 18*(10), 103302.

Behbahani, R. A., & Aghamir, F. M. (2012). Correlation of current drop, filling gas pressure, and ion beam emission in a low energy Mather-type plasma focus device. *Journal of Applied Physics, 111*(4), 043304.

Bennett, N., Blasco, M., Breeding, K., Constantino, D., DeYoung, A., DiPuccio, V., . . . & Yuan, V. (2017). Development of the dense plasma focus for short-pulse applications. *Physics of Plasmas, 24*(1), 012702.

Bennett, W. H. (1934). Magnetically self-focussing streams. *Physical Review, 45*(12), 890-897.

Benzi, V., Mezzetti, F., Rocchi, F., & Sumini, M. (2004). Feasibility analysis of a plasma focus neutron source for BNCT treatment of transplanted human liver. *Nuclear Instruments and Methods in Physics Research Section B: Beam Interactions with Materials and Atoms, 213*, 611-615.

Bernard, A., Bruzzone, H., Choi, P., Chuaqui, H., Gribkov, V., Herrera, J., . . . & Zoita, V. (1998). Scientific status of plasma focus research. *Journal of the Moscow Physical Society, 8*, 93-170.

Bernard, A., Cloth, P., Conrads, H., Coudeville, A., Gourlan, G., Jolas, A., . . . & Rager, J. P. (1977). The dense plasma focus — A high intensity neutron source. *Nuclear Instruments and Methods, 145*(1), 191-218.

Bernard, A., Coudeville, A., Jolas, A., Launspach, J., & De Mascureau, J. (1975). Experimental studies of the plasma focus and evidence for nonthermal processes. *Physics of Fluids, 18*(2), 180-194.

Bernard, A., Garconnet, J., Jolas, A., Le Breton, J., & De Mascureau, J. (1979). Turbulence caused by the interaction between plasma and electric current in the focus experiment. *Proceedings of the Seventh International Conference, 2*, 159-172.

Bernstein, M. J. (1970a). Acceleration mechanism for neutron production in plasma focus and z-pinch discharges. *Physics of Fluids, 13*(11), 2858-5866.

Bernstein, M. J. (1970b). Deuteron acceleration and neutron production in pinch discharges. *Physical Review Letters, 24*(13), 724-727.

Bernstein, M. J., & Comisar, G. G. (1972). Neutron energy and flux distributions from a crossed-field acceleration model of plasma focus and Z-pinch discharges. *Physics of Fluids, 15*(4), 700-707.

Bernstein, M. J., & Hai, F. (1970a). Evidence for neutron production via enhanced resistivity in a plasma focus. *Physical Review Letters, 25*(10), 641-642.

Bernstein, M. J., & Hai, F. (1970b). Evidence for nonthermonuclear neutron production in a plasma focus discharge. *Physics Letters A, 31*(6), 317-318.

Bernstein, M. J., Meskan, D. A., & Van Paassen, H. L. L. (1969). Space, time, and energy distributions of neutrons and x rays from a focused plasma discharge. *Physics of Fluids, 12*(10), 2193-2202.

Bethe, H. A. (1939). Energy production in stars. *Physical Review, 55*(5), 434-456.

Bhuyan, H., Favre, M., Valderrama, E., Avaria, G., Guzman, F., Chuaqui, H., . . . & Paulraj, M. (2007). Effect of high energy ion irradiation on silicon substrate in a pulsed plasma device. *Applied Surface Science, 254*(1 SPEC. ISS.), 197-200.

Bhuyan, H., Favre, M., Valderrama, E., Chuaqui, H., & Wyndham, E. (2006). Experimental studies of ion beam anisotropy in a low energy plasma focus operating with methane. *Journal of Physics D: Applied Physics, 39*(16), 3596.

Bhuyan, H., Mohanty, S. R., Neog, N. K., Bujarbarua, S., & Rout, R. K. (2003). Magnetic probe measurements of current sheet dynamics in a coaxial plasma accelerator. *Measurement Science and Technology, 14*(10), 1769-1776.

Bhuyan, M., Neog, N. K., Mohanty, S. R., Rao, C. V. S., & Raole, P. M. (2010). Studies on ion emission from the plasma focus device by using ion collector and track detector. *Journal of Fusion Energy, 29*(2), 177-180.

Bhuyan, M., Neog, N. K., Mohanty, S. R., Rao, C. V. S., & Raole, P. M. (2011). Temporal and spatial study of neon ion emission from a plasma focus device. *Physics of Plasmas, 18*(3).

Bienkowska, B., Paduch, M., Scholz, M., Stepniewski, W., & Tomaszewski, K. (2005). Study of the pinch structure in PF1000 plasma-focus device by high speed photography and MHD numerical modeling. *IEEE Transactions on Plasma Science, 33*(2 I), 450-451.

Bilbao, L., Bruzzone, H. A., Kelly, H., & Esper, M. (1985). Structure of a plasma focus current sheath from magnetic and optical measurements. *IEEE Transactions on Plasma Science, PS-13*(4), 202-206.

Bing, S., Pau, L., Mahe, L., & Sing, L. (2000). Improving energy efficiency of plasma focus. *Singapore Journal of Physics, 16*(1), 25-36.

Bogolyubov, E. P., Bochkov, V. D., Veretennikov, V. A., Vekhoreva, L. T., Gribkov, V. A., Dubrovskii, A. V., . . . & Zhang, G. X. (1998). A powerful soft x-ray source for x-ray lithography based on plasma focusing. *Physica Scripta, 57*(4), 488-494.

Borowiecki, M., Bieńkowska, B., Jednoróg, S., Karpiński, L., Paduch, M., Scholz, M., & Sadowski, M. J. (2006). Investigation of pinch dynamics in plasma-focus discharges by means of fast-streak-and fast-frame-cameras. *Czechoslovak Journal of Physics, 56*(SUPPL. 2), B184-B191.

Bostick, W. H., & Prior, W. (1972). X-ray fine structure of dense plasma in a co-axial accelerator. *Journal of Plasma Physics, 8*(01), 7-20.

Bruzzone, H., Acũa, H., Barbaglia, M., & Clausse, A. (2006). A simple plasma diagnostic based on processing the electrical signals from coaxial discharges. *Plasma Physics and Controlled Fusion, 48*(5), 609-620.

Bruzzone, H., Acũa, H., & Clausse, A. (2007). The lift-off stage of plasma focus discharges. *Plasma Physics and Controlled Fusion, 49*(2), 105-112.

Bruzzone, H., & Grondona, D. (1997). Magnetic probe measurements of the initial phase in a plasma focus device. *Plasma Physics and Controlled Fusion, 39*(9), 1315-1326.

Bruzzone, H., & Vieytes, R. (1993). The initial phase in plasma focus devices. *Plasma Physics and Controlled Fusion, 35*(12), 1745-1754.

Bures, B. L., Krishnan, M., & James, C. (2012). A plasma focus electronic neutron generator. *IEEE Transactions on Plasma Science, 40*(4), 1082-1088.

Burkhardt, L. C., Dunaway, R. E., Mather, J. W., Phillips, J. A., Sawyer, G. A., Stratton, T. F., . . . & Tuck, J. L. (1957). Pinch effect. *Journal of Applied Physics, 28*(5), 519-521.

Burns, E. J. T., Falacy, S. M., Hill, R. A., Thacher, P. D., Koehler, H. A., Davis, B., & Shafer, R. E. (1988). A high neutron output dense plasma focus. *Physics Letters A, 133*(3), 144-148.

Castillo-Mejia, F., Herrera, J. J. E., Rangel, J., Golzarri, J. I., Espinosa, G., Horowitz, Y. S., & Oster, L. (2002). Neutron angular distribution in a plasma focus obtained using nuclear track detectors. *Radiation Protection Dosimetry, 101*(1-4), 557-560.

Castillo-Mejía, F., Milanese, M. M., Moroso, R. L., Pouzo, J. O., & Santiago, M. A. (2001). Small plasma focus studied as a source of hard x-ray. *IEEE Transactions on Plasma Science, 29*(6), 921-926.

Castillo, F., Herrera, J. J. E., Rangel, J., Alfaro, A., Maza, M. A., Sakaguchi, V., . . . & Golzarri, J. I. (2002). Neutron anisotropy and x-ray production of the FN-II dense plasma focus device. *Brazilian Journal of Physics, 32*(1), 3-12.

Castillo, F., Milanese, M., Moroso, R., & Pouzo, J. (2000). Evidence of thermal and non thermal mechanisms coexisting in dense plasma focus D-D nuclear reactions. *Journal of Physics D: Applied Physics, 33*(2), 141-147.

Castillo, M. F., Milanese, M., Moroso, R., & Pouzo, J. (1997). Some experimental research on anisotropic effects in the neutron emission of dense plasma-focus devices. *Journal of Physics D: Applied Physics, 30*(10), 1499-1506.

Chernyshova, M., Gribkov, V. A., Kowalska-Strzeciwilk, E., Kubkowska, M., Miklaszewski, R., Paduch, M., . . . & Matejicek, J. (2016). Interaction of powerful hot plasma and fast ion streams with materials in dense plasma focus devices. *Fusion Engineering and Design, 113*, 109-118.

Choi, P., Wong, C. S., & Herold, H. (1989). Studies of the spatial and temporal evolution of a dense plasma focus in the X-ray region. *Laser and Particle Beams, 7*(4), 763-772.

Chow, S. P., Lee, S., & Tan, B. C. (1972). Current sheath studies in a co-axial plasma focus gun. *Journal of Plasma Physics, 8*(01), 21-31.

Conrads, H. (1990). Dense plasma focus as a neutron source for fusion research. *Nuclear Science and Engineering, 106*(3), 299-307.

Conrads, H., Cloth, P., Demmeler, M., & Hecker, R. (1972). Velocity distribution of the ions producing neutrons in a plasma focus. *Physics of Fluids, 15*(1), 209-211.

Corallo, D. M., Creek, D. M., & Murray, G. M. (1980). The x-ray calibration of silicon p-i-n diodes between 1.5 and 17.4 KeV. *Journal of Physics E: Scientific Instruments, 13*(6), 623-626.

Decker, G., Flemming, L., Kaeppeler, H. J., Oppenlander, T., Pross, G., Schilling, P., . . . & Trunk, M. (1980). Current and neutron yield scaling of fast high voltage plasma focus. *Plasma Physics, 22*(3), 245-260.

Decker, G., Kies, W., & Pross, G. (1983). The first and the final fifty nanoseconds of a fast focus discharge. *Physics of Fluids, 26*(2), 571-578.

Decker, G., & Wienecke, R. (1976). Plasma focus devices. *Physica B+C, 82*(1), 155-164.

Deeney, C., Douglas, M. R., Spielman, R. B., Nash, T. J., Peterson, D. L., L'Eplattenier, P., . . . & Struve, K. W. (1998). Enhancement of x-ray power from a Z pinch using nested-wire arrays. *Physical Review Letters, 81*(22), 4883-4886.

Deutsch, R., & Kies, W. (1988a). Ion acceleration and runaway in dynamical pinches. *Plasma Physics and Controlled Fusion, 30*(3), 263-276.

Deutsch, R., & Kies, W. (1988b). Manifestation of an ion acceleration mechanism in computer simulations and plasma-focus experiments. *Plasma Physics and Controlled Fusion, 30*(8), 921-934.

Donges, A., Herziger, G., Krompholz, H., Rühl, F., & Schönbach, K. (1980). The breakdown phase in a coaxial plasma gun. *Physics Letters A, 76*(5–6), 391-392.

Dreicer, H. (1959). Electron and ion runaway in a fully ionized gas. I. *Physical Review, 115*(2), 238-249.

Durrani, S. A., & Bull, R. K. (1985). Solid state nuclear track detection: Principles, methods, and applications *Solid State Nuclear Track Detection: Principles, Methods, And Applications*. Oxford: Pergamon Press.

El-Aragi, G. M. (2010). Neutron and ion beams emitted from plasma focus (112.5 J) device. *Plasma Science and Technology, 12*(1), 1-5.

Etaati, G. R., Amrollahi, R., Habibi, M., & Baghdadi, R. (2011). Angular distribution of argon ions and x-ray emissions in the Apf plasma focus device. *Journal of Fusion Energy, 30*(2), 121-125.

Etaati, G. R., Amrollahi, R., Habibi, M., Mohammadi, K., Baghdadi, R., & Roomi, A. (2010). Study of the soft and hard x-ray emitted by APF plasma focus device in different pressures. *Journal of Fusion Energy, 29*(5), 503-507.

Farahani, N. D., Davani, F. A., & Rad, Z. S. (2011). X-ray measurement and enhancement of SBUPF1 plasma focus device in different Ar pressures and operating voltages. *Journal of Fusion Energy, 30*(6), 466-472.

Favre, M., Lee, S., Moo, S. P., & Wong, C. S. (1992). X-ray emission in a small plasma focus operating with H2-Ar mixtures. *Plasma Sources Science and Technology, 1*(2), 122-125.

Feugeas, J. N., Llonch, E. C., De González, C. O., & Galambos, G. (1988). Nitrogen implantation of AISI 304 stainless steel with a coaxial plasma gun. *Journal of Applied Physics, 64*(5), 2648-2651.

Fleischer, R. L., Price, P. B., & Walker, R. M. (1965). Ion explosion spike mechanism for formation of charged particle tracks in solids. *Journal of Applied Physics, 36*(11), 3645-3652.

Gaillard, S., Fuchs, J., Renard-Le Galloudec, N., & Cowan, T. E. (2007). Study of saturation of CR39 nuclear track detectors at high ion fluence and of associated artifact patterns. *Review of Scientific Instruments, 78*(1), 013304-013304-013313.

Ghareshabani, E., & Sobhanian, S. (2016). Deposition of alumina films on Si (1 0 0) substrate using a low energy dense plasma focus device. *Journal of Fusion Energy, 35*(3), 573-578.

Gonzalez, J. H., Brollo, F. R., & Clausse, A. (2009). Modeling of the dynamic plasma pinch in plasma focus discharges based in Von Karman approximations. *IEEE Transactions on Plasma Science, 37*(11), 2178-2185.

Goudarzi, S., Sadat Kiai, S. M., Morshedian, N., Nasiri, A., & Amrollahi, R. (2005). Experimental study of the neutron emission mechanisms in a Filippov-type plasma focus device. *Czechoslovak Journal of Physics, 55*(1), 45-53.

Gratton, R., Kelly, H., Milanese, M., & Pouzo, J. (1977). On the upper pressure limit for the efficient operation of a plasma focus device. *Physics Letters A, 62*(6), 422-424.

Gribkov, V., & Orlova, M. (2004). On various possibilities in pulsed radiation biochemistry and chemistry. *Radiation and Environmental Biophysics, 43*(4), 303-309.

Gribkov, V. A., Banaszak, A., Bienkowska, B., Dubrovsky, A. V., Ivanova, S. I., Jakubowski, L., . . . & Tomaszewski, K. (2007). Plasma dynamics in the PF-1000 device under full-scale energy storage: II. Fast electron and ion characteristics versus neutron emission parameters and gun optimization perspectives. *Journal of Physics D: Applied Physics, 40*(12), 3592 - 3607.

Gribkov, V. A., Pimenov, V. N., Ivanov, L. I., Dyomina, E. V., Maslyaev, S. A., Miklaszewski, R., . . . & Zatekin, V. V. (2003). Interaction of high temperature deuterium plasma streams and fast ion beams with stainless steels in dense plasma focus device. *Journal of Physics D: Applied Physics, 36*(15), 1817-1825.

Gribkov, V. A., Srivastava, A., Keat, P. L. C., Kudryashov, V., & Lee, S. (2003). Operation of NX2 dense plasma focus device with argon filling as a possible radiation source for micro-machining. *IEEE Transactions on Plasma Science, 30*(3 II), 1331-1338.

Gross, R. A. (1967). Thickness of a shock wave in hydrogen. *Physics of Fluids, 10*(8), 1853-1855.

Gullickson, R. L., & Sahlin, H. L. (1978). Measurements of high energy deuterons in the plasma-focus device. *Journal of Applied Physics, 49*(3), 1099-1105.

Gupta, R., Mohanty, S. R., Rawat, R. S., & Srivastava, M. P. (2000). Current sheath dynamics and x-ray emission studies from sequential dense plasma focus device. *IEEE Transactions on Plasma Science, 28*(4), 1263-1270.

Gupta, R., Srivastava, M. P., Balakrishnan, V. R., Kodama, R., & Peterson, M. C. (2004). Deposition of nanosized grains of ferroelectric lead zirconate titanate on thin films using dense plasma focus. *Journal of Physics D: Applied Physics, 37*(7), 1091-1094.

Habibi, M., Amrollahi, R., & Etaati, G. R. (2010). Experimental study of hard x-ray emission with different anode tips in APF plasma focus device. *Journal of Fusion Energy, 29*(1), 49-54.

Habibi, M., & Laktarashi, A. (2016). Investigation of nimonic alloy: Plasma interaction in different plasma pulses using a small plasma focus device. *Journal of Fusion Energy, 35*(2), 452-458.

Haines, M. G. (1983). Ion beam formation in an m = 0 unstable Z-pinch. *Nuclear Instruments and Methods In Physics Research, 207*(1-2), 179-185.

Haines, M. G. (1996). Fifty years of controlled fusion research. *Plasma Physics and Controlled Fusion, 38*(5), 643-656.

Haines, M. G., Sanford, T. W. L., & Smirnov, V. P. (2005). Wire-array z-pinch: a powerful X-ray source for ICF. *Plasma Physics and Controlled Fusion, 47*(12B), B1-B11.

Harries, W. L., Lee, J. H., & McFarland, D. R. (1978a). Space and time resolved emission of hard x-rays from a plasma focus. *Plasma Physics, 20*(9), 963-969.

Harries, W. L., Lee, J. H., & McFarland, D. R. (1978b). Trajectories of high energy electrons in a plasma focus. *Plasma Physics, 20*(2), 95-106.

Haruki, T., Yousefi, H. R., Masugata, K., Sakai, J. I., Mizuguchi, Y., Makino, N., & Ito, H. (2006). Simulation of high energy particle production through sausage and kink instabilities in pinched plasma discharges. *Physics of Plasmas, 13*(8), 082106.

Heo, H., & Park, D. K. (2002). Correlations between argon ion beams and x-rays in a plasma focus. *Japanese Journal of Applied Physics, 41*(5 A), 3120-3124.

Herziger, G., Krompholz, H., Michel, L., Schleiferböck, D., & Schönbach, K. (1978). Hard x-ray emission from the plasma focus. *Physics Letters A, 69*(1), 37-38.

Hirano, K., Yamamoto, T., Shimoda, K., & Nakajima, H. (1989). Production of a highly ionized ion beam by a plasma focus. *Journal of the Physical Society of Japan, 58*(10), 3591-3599.

Hubbell, J., & Seltzer, S. (1996). Tables of x-ray mass attenuation coefficients and mass energy-absorption coefficients 1 keV to 20 MeV for elements z = 1 to 92 and 48 additional substances of dosimetric interest. Retrieved 07 March 2016, from Ionizing radiation division, Physics Laboratory, National Institute of Standards and Technology, Gaithersburg, MD, USA https://www.nist.gov/pml/x-ray-mass-attenuation-coefficients

Hübner, K., Bruhns, H., & Steinmetz, K. (1978). Fusion reaction rate for a plasma boiler moving in an ambient plasma. *Physics Letters A, 69*(4), 269-272.

Imshennik, V. S., Osovets, S. M., & Otroschenko, I. V. (1973). The dynamics of plasma constrictions and electromagnetic acceleration of ions. *Soviet Physics—JETP, 37*(6), 1037-1044.

Jaeger, U., & Herold, H. (1987). Fast ion kinetics and fusion reaction mechanism in the plasma focus. *Nuclear Fusion, 27*(3), 407-423.

Jahoda, F. C., Little, E. M., Quinn, W. E., Sawyer, G. A., & Stratton, T. F. (1960). Continuum radiation in the x-ray and visible regions from a magnetically compressed plasma (Scylla). *Physical Review, 119*(3), 843-856.

Jalufka, N. W., & Lee, J. H. (1972). Current sheet collapse in a plasma focus. *Physics of Fluids, 15*(11), 1954-1958.

Johnson, D. J. (1974). Study of the x-ray production mechanism of a dense plasma focus. *Journal of Applied Physics, 45*(3), 1147-1153.

Kalaiselvi, S. M. P., Tan, T. L., Talebitaher, A., Lee, P., & Rawat, R. S. (2013). Optimization of neon soft x-rays emission from 200 J fast miniature dense plasma focus device: A potential source for soft X-ray lithography. *Physics Letters A, 377*(18), 1290-1296.

Kato, Y., & Be, S. H. (1986). Generation of soft x rays using a rare gas-hydrogen plasma focus and its application to x-ray lithography. *Applied Physics Letters, 48*(11), 686-688.

Kato, Y., Ochiai, I., Watanabe, Y., & Murayama, S. (1988). Plasma focus x‐ray source for lithography. *Journal of Vacuum Science & Technology B, 6*(1), 195-198.

Kazunari, I. (1982). Plasma Focus Breeder. *Japanese Journal of Applied Physics, 21*(1), 125-127.

Kelly, H., Lepone, A., Márquez, A., Lamas, D., & Oviedo, C. (1996). Coating on metallic samples produced by a small energy plasma focus. *Plasma Sources Science and Technology, 5*(4), 704-709.

Kelly, H., Lepone, A., Marquez, A., Sadowski, M. J., Baranowski, J., & Skladnik-Sadowska, E. (1998). Analysis of the nitrogen ion beam generated in a low energy plasma focus device by a faraday cup operating in the secondary electron emission mode. *IEEE Transactions on Plasma Science, 26*(1), 113-117.

Klir, D., Kubes, P., Paduch, M., Pisarczyk, T., Chodukowski, T., Scholz, M., . . . & Tomaszewski, K. (2011). Experimental evidence of thermonuclear neutrons in a modified plasma focus. *Applied Physics Letters, 98*(7), 071501.

Kondoh, Y. (1984). A model of charged particle accelerations in the plasma focus. *Journal of the Physical Society of Japan, 53*(12), 4200-4209.

Kondoh, Y., & Hirano, K. (1978). Numerical study of an ion acceleration in a z-pinch type plasma focus. *Physics of Fluids, 21*(9), 1617-1622.

Kotov, Y. A., & Sokovnin, S. Y. (2000). Overview of the application of nanosecond electron beams for radiochemical sterilization. *IEEE Transactions on Plasma Science, 28*(1), 133-136.

Krompholz, H., Neff, W., Rühl, F., Schönbach, K., & Herziger, G. (1980). Formation of the plasma layer in a plasma focus device. *Physics Letters A, 77*(4), 246-248.

Krompholz, H., Rühl, F., Schneider, W., Schönbach, K., & Herziger, G. (1981). A scaling law for plasma focus devices. *Physics Letters A, 82*(2), 82-84.

Kubes, P., Klir, D., Kravarik, J., & Rezac, K. (2009). Neutron production at the small plasma focus device with antianode. *IEEE Transactions on Plasma Science, 37*(9), 1786-1791.

Kubes, P., Kravarik, J., Klir, D., Rezac, K., Scholz, M., Paduch, M., . . . & Schmidt, H. (2006). Correlation of radiation with electron and neutron signals taken in a plasma-focus device. *IEEE Transactions on Plasma Science, 34*(5 III), 2349-2355.

Kwek, K. H., Tou, T. Y., & Lee, S. (1990). Current sheath structures of the plasma focus in the run-down phase. *IEEE Transactions on Plasma Science, 18*(5), 826-830.

L., V. P. H. L. (1971). A time resolved ross filter system for measuring x-ray spectra in Z-pinch plasma focus devices. *Review of Scientific Instruments, 42*(12), 1823-1824.

Lee, J. H., Shomo, L. P., & Kim, K. H. (1972). Anisotropy of the neutron fluence from a plasma focus. *Physics of Fluids, 15*(12), 2433-2438.

Lee, J. H., Shomo, L. P., Williams, M. D., & Hermansdorfer, H. (1971). Neutron production mechanism in a plasma focus. *Physics of Fluids, 14*(10), 2217-2223.

Lee, P., Feng, X., Zhang, G. X., Liu, M. H., & Lee, S. (1997). Electron lithography using a compact plasma focus. *Plasma Sources Science and Technology, 6*(3), 343-348.

Lee, R., & Lampe, M. (1973). Electromagnetic instabilities, filamentation, and focusing of relativistic electron beams. *Physical Review Letters, 31*(23), 1390-1393.

Lee, S. (1969). *Tranverse ionizing shock waves in a planar electromagnetic shock tube.* (PhD. thesis), Australian National University, Australia.

Lee, S. (2013). Radiative dense plasma focus computation package:RADPF Retrieved 10 August 2015 http://www.intimal.edu.my/school/fas/UFLF

Lee, S., & Saw, S. H. (2008). Neutron scaling laws from numerical experiments. *Journal of Fusion Energy, 27*(4), 292-295.

Lee, S., & Saw, S. H. (2012). Plasma focus ion beam fluence and flux—Scaling with stored energy. *Physics of Plasmas, 19*(11), 112703.

Lee, S., & Saw, S. H. (2013). Plasma focus ion beam fluence and flux—For various gases. *Physics of Plasmas, 20*(6), 062702.

Lee, S., Saw, S. H., Abdou, A. E., & Torreblanca, H. (2011). Characterizing plasma focus devices—Role of the static inductance—Instability phase fitted by anomalous resistances. *Journal of Fusion Energy, 30*(4), 277-282.

Lee, S., Saw, S. H., Lee, P., Rawat, R. S., & Devi, K. (2013). Magnetic reynolds number and neon current sheet structure in the axial phase of a plasma focus. *Journal of Fusion Energy, 32*(1), 50-55.

Lee, S., & Serban, A. (1996). Dimensions and lifetime of the plasma focus pinch. *IEEE Transactions on Plasma Science, 24*(3), 1101-1105.

Lee, S., Tou, T. Y., Moo, S. P., Eissa, M. A., Gholap, A. V., Kwek, K. H., . . . & Zakaullah, M. (1988). A simple facility for the teaching of plasma dynamics and plasma nuclear fusion. *American Journal of Physics, 56*(1), 62-68.

Leonard, S. L. (1965). Basic macroscopic measurements. In R. H. Huddlestone & S. L. Leonard (Eds.), *Plasma Diagnostic Techniques* (pp. 7-67). New York, London: Academic Press Inc. (London) Ltd. .

Lerner, E. J., Murali, S. K., Shannon, D., Blake, A. M., & Roessel, F. V. (2012). Fusion reactions from > 150 keV ions in a dense plasma focus plasmoid. *Physics of Plasmas, 19*(3), 032704.

Lim, L. K., Yap, S. L., Lim, L. H., Neoh, Y. S., Khan, M. Z., Ngoi, S. K., . . . & Lee, S. (2015). Parametric optimisation of plasma focus devices for neutron production. *Journal of Fusion Energy, 35*(2), 274-280.

Lim, L. K., Yap, S. L., Wong, C. S., & Zakaullah, M. (2013). Deuteron Beam Source Based on Mather Type Plasma Focus. *Journal of Fusion Energy, 32*(2), 287-292.

Liu, M., Feng, X., Springham, S. V., & Lee, S. (1998). Soft x-ray yield measurement in a small plasma focus operated in neon. *IEEE Transactions on Plasma Science, 26*(2), 135-140.

Malinowski, K., Skladnik-Sadowska, E., & Sadowski, M. J. (2005). Comparison of responses of LR-115A, CR-39 and PM-355 track detectors to pulsed low-energy proton streams. *Radiation Measurements, 40*(2-6), 371-374.

Malinowski, K., Skladnik-Sadowska, E., Sadowski, M. J., & Czaus, K. (2009). Application of PM-355 track detectors for investigation of the spatial structure of plasma–proton streams. *Radiation Measurements, 44*(9–10), 865-869.

Mankowski, J., & Kristiansen, M. (2000). A review of short pulse generator technology. *IEEE Transactions on Plasma Science, 28*(1), 102-108.

Mather, J. W. (1965). Formation of a high density deuterium plasma focus. *Physics of Fluids, 8*(2), 366-377.

Mather, J. W. (1966). High density deuterium plasma. *Proceedings of a Conference on Plasma Physics and Controlled Physics Research Nuclear Fusion Research, 2*, 389-404.

Mather, J. W., Bottoms, P. J., Carpenter, J. P., Williams, A. H., & Ware, K. D. (1969). Stability of the dense plasma focus. *Physics of Fluids, 12*(11), 2343-2347.

Mathuthu, M., Zengeni, T. G., & Gholap, A. V. (1996). Measurement of magnetic field and velocity profiles in 3.6 kJ United Nations University/International Center For Theoretical Physics plasma focus fusion device. *Physics of Plasmas, 3*(12), 4572-4576.

Michel, L., Schönbach, K. H., & Fischer, H. (1974). Neutron emission from a small 1-kJ plasma focus. *Applied Physics Letters, 24*(2), 57-59.

Milanese, M., Moroso, R., & Pouzo, J. (2003). D-D neutron yield in the 125 J dense plasma focus Nanofocus. *European Physical Journal D, 27*(1), 77-81.

Milanese, M., & Pouzo, J. (1985). Critical analysis of plasma focus design based on the implications of an upper pressure limit. *Nuclear Fusion, 25*(7), 840 - 846.

Mohammadi, M. A., Sobhanian, S., Wong, C. S., Lee, S., Lee, P., & Rawat, R. S. (2009). The effect of anode shape on neon soft x-ray emissions and current sheath configuration in plasma focus device. *Journal of Physics D: Applied Physics, 42*(4), 045203.

Mohanty, S. R., Bhuyan, H., Neog, N. K., Rout, R. K., & Hotta, E. (2005). Development of multi Faraday cup assembly for ion beam measurements from a low energy plasma focus device. *Japanese Journal of Applied Physics, 44*(7 A), 5199-5205.

Mohanty, S. R., Srivastava, M. P., & Rawat, R. S. (1997). Study of x-ray emission of dense plasma focus device in the presence of external magnetic field. *Physics Letters A, 234*(6), 472-476.

Moo, S. P., Chakrabarty, C. K., & Lee, S. (1991). An investigation of the ion beam of a plasma focus using a metal obstacle and deuterated target. *IEEE Transactions on Plasma Science, 19*(3), 515-519.

Moreno, C., Raspa, V., Sigaut, L., Vieytes, R., & Clausse, A. (2006). Plasma focus based tabletop hard x-ray source for 50 ns resolution introspective imaging of metallic objects through metallic walls. *Applied Physics Letters, 89*(9), 091502.

Moreno, J., Silva, P., & Soto, L. (2003). Optical observations of the plasma motion in a fast plasma focus operating at 50 J. *Plasma Sources Science and Technology, 12*(1), 39-45.

Neda, S., Babak, S. B., & Hosein, P. (2017). Development of a radiographic method for measuring the discrete spectrum of the electron beam from a plasma focus device. *Plasma Science and Technology, 19*(7), 075101.

Neff, W., Eberle, J., Holz, R., Lebert, R., & Richter, F. (1989). The plasma focus as soft x-ray source for microscopy and lithography. *1140*, 13-20.

Neff, W., Krompholz, H., Rühl, F., Schönbach, K., & Herziger, G. (1980). Subnanosecond MeV electron beams from the plasma focus. *Physics Letters A, 79*(2), 165-166.

Neog, N. K., & Mohanty, S. R. (2007). Study on electron beam emission from a low energy plasma focus device. *Physics Letters, Section A: General, Atomic and Solid State Physics, 361*(4-5), 377-381.

Neog, N. K., Mohanty, S. R., & Borthakur, T. K. (2008). Time resolved studies on x-rays and charged particles emission from a low energy plasma focus device. *Physics Letters A, 372*(13), 2294-2299.

Newman, C. E., & Petrosian, V. (1975). Production of hard x rays in a plasma focus. *Physics of Fluids, 18*(5), 547-551.

Ng, C. M., Moo, S. P., & Wong, C. S. (1998). Variation of soft x-ray emission with gas pressure in a plasma focus. *IEEE Transactions on Plasma Science, 26*(4), 1146-1153.

Ngoi, S. K., Yap, S. L., Goh, B. T., Ritikos, R., Rahman, S. A., & Wong, C. S. (2012). Formation of nano-crystalline phase in hydrogenated amorphous silicon thin film by plasma focus ion beam irradiation. *Journal of Fusion Energy, 31*(1), 96-103.

Northrup, E. F. (1907). Some newly observed manifestations of forces in the interior of an electric conductor. *Physical Review (Series I), 24*(6), 474-497.

Oliphant, M. L. E., Harteck, P., & Rutherford, L. (1934). Transmutation effects observed with heavy hydrogen. *Proceedings of the Royal Society of London. Series A, Containing Papers of a Mathematical and Physical Character, 144*(853), 692-703.

Oppenlander, T., Pross, G., Decker, G., & Trunk, M. (1977). The plasma focus current in the compression phase. *Plasma Physics, 19*(11), 1075-1083.

Patran, A., Tan, L. C., Stoenescu, D., Rafique, M. S., Rawat, R. S., Springham, S. V., . . . & Lee, S. (2005). Spectral study of the electron beam emitted from a 3 kJ plasma focus. *Plasma Sources Science and Technology, 14*(3), 549-560.

Peter Gary, S. (1974). Ion acceleration in a plasma focus. *Physics of Fluids, 17*(11), 2135-2137.

Peter, G. S., & Hohl, F. (1973). Ion kinematics in a plasma focus. *Physics of Fluids, 16*(7), 997-1002.

Pheng, M. S., Chakrabarty, C. K., & Sing, L. (1989). Half-life measurement of 116In using plasma focus neutrons. *Jurnal Fizik Malaysia, 10*(2), 57-59.

Pimenov, V. N., Dyomina, E. V., Ivanov, L. I., Maslyaev, S. A., Gribkov, V. A., Miklaszewski, R., . . . & Szydlowski, A. (2002). Damage of structural materials for fusion devices under pulsed ion and high temperature plasma beams. *Journal of Nuclear Materials, 307-311*(1 SUPPL.), 95-99.

Piriaei, D., Yousefi, H. R., Mahabadi, T. D., Elahi, A. S., & Ghoranneviss, M. (2017). The effects of pre-ionization on the impurity and x-ray level in a dense plasma focus device. *Physics of Plasmas, 24*(2), 022509.

Pollock, J. A., & Barraclough, S. H. (1905). Note on a hollow lightning conductor crushed by the discharge. *Journal and Proceedings of the Royal Society of New South Wales, XXXIX*, 131-138.

Potter, D. E. (1971). Numerical studies of the plasma focus. *Physics of Fluids, 14*(9), 1911-1924.

Pouzo, J., Milanese, M. M., Cortázar, O. D., & Moroso, R. (2005). Images of the dense plasma focus phenomenon in the 2-kJ PACO device. *IEEE Transactions on Plasma Science, 33*(2 I), 438-439.

Rafique, M. S., Lee, P., Patran, A., Rawat, R. S., & Lee, S. (2010). Radiation emission correlated with the evolution of current sheath from a deuterium plasma focus. *Journal of Fusion Energy, 29*(3), 295-304.

Rapezzi, L., Angelone, M., Pillon, M., Rapisarda, M., Rossi, E., Samuelli, M., & Mezzetti, F. (2004). Development of a mobile and repetitive plasma focus. *Plasma Sources Science and Technology, 13*(2), 272-277.

Raspa, V., Moreno, C., Sigaut, L., & Clausse, A. (2008). Hard x-ray spectrum emitted by a plasma focus optimized for flash radiography. *Physica Scripta, T131*, 014034.

Raspa, V., Sigaut, L., Llovera, R., Cobelli, P., Knoblauch, P., Vieytes, R., . . . & Moreno, C. (2004). Plasma focus as a powerful hard x-ray source for ultrafast imaging of moving metallic objects. *Brazilian Journal of Physics, 34*(4B), 1696-1699.

Rawat, R. S., Chew, W. M., Lee, P., White, T., & Lee, S. (2003). Deposition of titanium nitride thin films on stainless steel-AISI 304 substrates using a plasma focus device. *Surface and Coatings Technology, 173*(2-3), 276-284.

Rawat, R. S., Srivastava, M. P., & Mohanty, S. R. (1994). Study of current sheath dynamics in dense plasma focus in the presence of axial magnetic field using laser shadowgraphic technique. *IEEE Transactions on Plasma Science, 22*(5), 967-972.

Rawat, R. S., Zhang, T., Phua, C. B. L., Then, J. X. Y., Chandra, K. A., Lin, X., . . . & Lee, P. (2004). Effect of insulator sleeve length on soft x-ray emission from a neon-filled plasma focus device. *Plasma Sources Science and Technology, 13*(4), 569-575.

Rishi, V., Rawat, R. S., Lee, P., Krishnan, M., Springham, S. V., & Tan, T. L. (2009). Experimental study of neutron emission characteristics in a compact sub-kilojoule range miniature plasma focus device. *Plasma Physics and Controlled Fusion, 51*(7), 075008.

Robouch, B. V., & Rager, J. P. (1973). Filter method and silicon detectors to measure the temperature of a hot dense thermal deuterium plasma from its quantum bremsstrahlung. *Journal of Applied Physics, 44*(4), 1527-1533.

Roomi, A., Saion, E., Habibi, M., Amrollahi, R., Baghdadi, R., Etaati, G. R., . . . & Iqbal, M. (2011). The effect of applied voltage and operating pressure on emitted X-ray from nitrogen (N2) gas in APF plasma focus device. *Journal of Fusion Energy, 30*(5), 413-420.

Roshan, M. V., Lee, P., Lee, S., Talebitaher, A., Rawat, R. S., & Springham, S. V. (2009). Backward high energy ion beams from plasma focus. *Physics of Plasmas, 16*(7), 074506.

Roshan, M. V., Lee, P., Pan, Z., Verma, R., Rawat, R. S., & Springham, S. V. (2010). Correlation analysis of intense and high energy deuteron beam, pinch images, and neutron yield. *IEEE Transactions on Plasma Science, 38*(9), 2434-2438.

Roshan, M. V., Springham, S. V., Rawat, R. S., & Lee, P. (2010). Short-lived pet radioisotope production in a small plasma focus device. *IEEE Transactions on Plasma Science, 38*(12), 3393-3397.

Sadiq, M., Shafiq, M., Waheed, A., Ahmad, R., & Zakaullah, M. (2006). Amorphization of silicon by ion irradiation in dense plasma focus. *Physics Letters A, 352*(1-2), 150-154.

Sadowski, M., ebrowski, J., Rydygier, E., Herold, H., Jäger, U., & Schmidt, H. (1985). Multi spike structure of ion pulses generated by plasma focus discharges. *Physics Letters A, 113*(1), 25-31.

Sadowski, M., Herold, H., Schmidt, H., & Shakhatre, M. (1984). Filamentary structure of the pinch column in plasma focus discharges. *Physics Letters A, 105*(3), 117-123.

Sadowski, M., Skladnik-Sadowska, E., Baranowski, J., Zebrowski, J., Kelly, H., Lepone, A., . . . & Pouzo, J. (2000). Comparison of characteristics of pulsed ion beams emitted from different small PF devices. *Nukleonika, 45*(3), 179-184.

Sadowski, M., Zebrowski, J., Rydygier, E., & Kucinski, J. (1988). Ion emission from plasma focus facilities. *Plasma Physics and Controlled Fusion, 30*(6), 763 - 769.

Sánchez, G., & Feugeas, J. (1997). The thermal evolution of targets under plasma focus pulsed ion implantation. *Journal of Physics D: Applied Physics, 30*(6), 927-936.

Sauerbrey, R., Zhu, Y., Millar, P., Tittel, F. K., & Jr., W. L. W. (1987). Improved laser pumping by intense electron beams via a backscattering reflector. *Journal of Applied Physics, 61*(10), 4740-4743.

Saw, S. H., & Lee, S. (2011). Scaling the plasma focus for fusion energy considerations. *International Journal of Energy Research, 35*(2), 81-88.

Schmidt, A., Tang, V., & Welch, D. (2012). Fully kinetic simulations of dense plasma focus Z-pinch devices. *Physical Review Letters, 109*(20), 205003.

Schneider, R. F., Rhee, M. J., & Smith, J. R. (1985). Experimental study of the electron beam produced by a plasma focus accelerator. *IEEE Transactions on Nuclear Science, 32*(5), 3536 - 3538.

Scholz, M., Bieńkowska, B., Ivanova-Stanik, I., Karpiński, L., Miklaszewski, R., Paduch, M., . . . & Sadowski, M. J. (2004). The physics of a plasma focus. *Czechoslovak Journal of Physics, 54*(3), C170-C185.

Scholz, M., Bienkowska, B., Ivanova-Stanik, I. M., Karpinski, L., Paduch, M., Tomaszewski, K., . . . & Vitulli, S. (2004). Correlation between pinch dynamics, neutron and X-ray emission from megajoule plasma focus device. *Vacuum, 76*(2-3), 361-364.

Schönbach, K., Krompholz, H., Michel, L., & Herziger, G. (1977). Microinstabilities in the plasma focus. *Physics Letters A, 62*(6), 430-432.

Serban, A., & Lee, S. (1997). Soft x-ray emission from a small plasma focus operated in deuterium. *Plasma Sources Science and Technology, 6*(1), 78-85.

Serban, A., & Lee, S. (1998). Experiments on speed-enhanced neutron yield from a small plasma focus. *Journal of Plasma Physics, 60*(1), 3-15.

Shirani, B., Abbasi, F., & Nikbakht, M. (2013). Production of 13N by 12C(d,n)13N reaction in a medium energy plasma focus. *Applied Radiation and Isotopes, 74*, 86-90.

Siegbahn, K. (1965). *Alpha-Beta and Gamma-ray spectroscopy* (Vol. 1). Amsterdam: North-Holland Publishing Company.

Silva, P., Moreno, J., Soto, L., Birstein, L., Mayer, R. E., & Kies, W. (2003). Neutron emission from a fast plasma focus of 400 Joules. *Applied Physics Letters, 83*(16), 3269-3271.

Skladnik, S. E., Baranowski, J., & Sadowski, M. (2001). Low energy ion measurements by means of CR-39 nuclear track detectors. *Radiation Measurements, 34*(1-6), 337-339.

Skladnik, S. E., Czaus, K., Malinowski, K., & Sadowski, M. J. (2005). Study of spatial structure and energy spectrum of ion beams by means of LR 115A and PM-355 nuclear track detectors. *Radiation Measurements, 40*(2-6), 475-478.

Smith, A. J., Suryadi, Jasbir, S., & Lee, S. (1986). *A simple high current switch.* Paper presented at the Second Tropical College on Applied Physics: Laser and Plasma Technology, University of Malaya, Malaysia.

Springham, S. V., Lee, S., & Moo, S. P. (2002). Deuterium plasma focus measurements using solid state nuclear track detectors. *Brazilian Journal of Physics, 32*(1), 172-178.

Springham, S. V., Lee, S., & Rafique, M. S. (2000). Correlated deuteron energy spectra and neutron yield for a 3 kJ plasma focus. *Plasma Physics and Controlled Fusion, 42*(10), 1023-1032.

Springham, S. V., Moo, S. P., Lee, P., Rawat, R. S., Patran, A. C., & Lee, S. (2005). Imaging of fusion protons from a 3 kJ deuterium plasma focus. *Japanese Journal of Applied Physics, Part 1: Regular Papers and Short Notes and Review Papers, 44*(6A), 4117-4121.

Srivastava, M. P., Mohanty, S. R., Annapoorni, S., & Rawat, R. S. (1996). Diode like behaviour of an ion irradiated polyaniline film. *Physics Letters A, 215*(1–2), 63-68.

Stratton, T. F. (1965). X-ray Spectroscopy. In R. H. Huddlestone & S. L. Leonard (Eds.), *Plasma diagnostic techniques* (pp. 359-397). New York, London: Academic Press Inc.

Stygar, W., Gerdin, G., Venneri, F., & Madrekas, J. (1982). Particle beams generated by a 6 - 12. 5 kJ dense plasma focus. *Nuclear Fusion, 22*(9), 1161-1172.

Sumini, M., Mostacci, D., Rocchi, F., Frignani, M., Tartari, A., Angeli, E., . . . & Cucchi, G. (2006). Preliminary design of a 150 kJ repetitive plasma focus for the production of 18-F. *Nuclear Instruments and Methods in Physics Research, Section A: Accelerators, Spectrometers, Detectors and Associated Equipment, 562*(2), 1068-1071.

Szydlowski, A., Banaszak, A., Bienkowska, B., Ivanova-Stanik, I. M., Scholz, M., & Sadowski, M. J. (2004). Measurements of fast ions and neutrons emitted from PF-1000 plasma focus device. *Vacuum, 76*(2-3), 357-360.

Szydłowski, A., Sadowski, M., Czyżewski, T., Jaskóła, M., & Korman, A. (1999). Comparison of responses of CR-39, PM-355, and PM-600 track detectors to low-energy hydrogen, and helium ions. *Nuclear Instruments and Methods in Physics Research Section B: Beam Interactions with Materials and Atoms, 149*(1–2), 113-118.

Szydlowski, A., Scholz, M., Karpinski, L., Sadowski, M., Tomaszewski, K., & Paduch, M. (2001). Neutron and fast ion emission from PF-1000 facility equipped with new large electrodes. *Nukleonika, 46*(SUPPL.1), S61-S64.

Talaei, A., Sadat Kiai, S. M., & Zaeem, A. A. (2010). Effects of admixture gas on the production of 18F radioisotope in plasma focus devices. *Applied Radiation and Isotopes, 68*(12), 2218-2222.

Tan, T. L., Wong, D., Lee, P., Rawat, R. S., Springham, S., & Patran, A. (2006). Characterization of chemically amplified resist for x-ray lithography by Fourier transform infrared spectroscopy. *Thin Solid Films, 504*(1-2), 113-116.

Tanimoto, M., & Koyama, K. (1982). Resistive ion acceleration in a plasma focus. *Japanese Journal of Applied Physics, 21*(8), L491-L493.

Tarifeño, S. A., Pavez, C., Moreno, J., & Soto, L. (2011). Dynamics and density measurements in a small plasma focus of tens-of-joules-emitting neutrons. *IEEE Transactions on Plasma Science, 39*(2), 756-760.

Tartari, A., Da Re, A., Bonifazzi, C., & Marziani, M. (2004). Energy spectra measurements of x-ray emission from electron interaction in a dense plasma focus device. *Nuclear Instruments and Methods in Physics Research, Section B: Beam Interactions with Materials and Atoms, 213*, 206-209.

Tartari, A., Da Re, A., Mezzetti, F., Angeli, E., & De Chiara, P. (2004). Feasibility of x-ray interstitial radiosurgery based on plasma focus device. *Nuclear Instruments and Methods in Physics Research, Section B: Beam Interactions with Materials and Atoms, 213*, 607-610.

Tartari, A., Verri, G., Da Re, A., Mezzetti, F., Bonifazzi, C., & Rapezzi, L. (2002). Improvement of calibration assessment for gold fast-neutron activation analysis using plasma focus devices. *Measurement Science and Technology, 13*(6), 939-945.

Tiseanu, I., Mandache, N., & Zambreanu, V. (1994). Energetic and angular characteristics of the reacting deuterons in a plasma focus. *Plasma Physics and Controlled Fusion, 36*(3), 417-432.

Tou, T. Y. (1995). Multislit streak camera investigation of plasma focus in the steady state rundown phase. *IEEE Transactions on Plasma Science, 23*(5), 870-873.

Van, P. H. L. L., Vandre, R. H., & White, R. S. (1970). X-ray spectra from dense plasma focus devices. *Physics of Fluids, 13*(10), 2606-2612.

Verma, R., Rawat, R. S., Lee, P., Springham, S. V., & Tan, T. L. (2013). High performance high repetition rate miniature plasma focus device: Record time averaged neutron yield at 200 J with enhanced reproducibility. *Journal of Fusion Energy, 32*(1), 2-10.

Verma, R., Roshan, M. V., Malik, F., Lee, P., Lee, S., Springham, S. V., . . . & Rawat, R. S. (2008). Compact sub-kilojoule range fast miniature plasma focus as portable neutron source. *Plasma Sources Science and Technology, 17*(4), 045020.

Verri, G., Mezzetti, F., Da Re, A., Bortolotti, A., Rapezzi, L., & Gribkov, V. A. (2000). Fast neutron activation analysis of gold by inelastic scattering, 197Au(n,n′ γ)197Aum, by means of plasma focus device. *Nukleonika, 45*(3), 189-191.

Vikhrev, V. V., Ivanov, V. V., & Rozanova, G. A. (1993). Development of sausage-type instability in a Z-pinch plasma column. *Nuclear Fusion, 33*(2), 311.

Vikhrev, V. V., & Korolev, V. D. (2007). Neutron generation from Z-pinches. *Plasma Physics Reports, 33*(5), 356-380.

Whittlestone, S. (1977). Neutron distributions from the deuteron bombardment of a thick beryllium target. *Journal of Physics D: Applied Physics, 10*(13), 1715 - 1723.

Wong, C. S. (1978). *Some neutron measurements of the plasma focus.* (PhD. thesis), University of Malaya, Malaysia.

Yamada, Y., Kitagawa, Y., & Yokoyama, M. (1985). High energy deuteron beam generated by a plasma focus device. *Journal of Applied Physics, 58*(1), 188-192.

Yamamoto, T., Kondoh, Y., Shimoda, K., & Hirano, K. (1982). Measurement of electron and ion beam energies and currents in a plasma focus discharge. *Japanese Journal of Applied Physics, V 21*(N 4), 659-663.

Yamamoto, T., Shimoda, K., & Hirano, K. (1985). Neutrons, x-rays and charged particle beams emission in a 65 kV plasma focus. *Japanese Journal of Applied Physics, Part 1: Regular Papers & Short Notes, 24*(3), 324-327.

Yanagidaira, T., Sato, M., & Hirano, K. (1996). A streak mode soft x-ray imaging system. *Japanese Journal of Applied Physics, Part 1: Regular Papers and Short Notes and Review Papers, 35*(11), 5862-5865.

Yap, S. L., Wong, C. S., Choi, P., Dumitrescu, C., & Moo, S. P. (2005). Observation of two phases of neutron emission in a low energy plasma focus. *Japanese Journal of Applied Physics, Part 1: Regular Papers and Short Notes and Review Papers, 44*(11), 8125-8132.

Yousefi, H. R., Mohanty, S. R., Nakada, Y., Ito, H., & Masugata, K. (2006). Compression and neutron and ion beams emission mechanisms within a plasma focus device. *Physics of Plasmas, 13*(11), 114506.

Yousefi, H. R., Nakada, Y., Ito, H., & Masugata, K. (2006). Investigation of the neutron production mechanism in a 20 kJ plasma focus device. *Journal of Fusion Energy, 25*(3-4), 245-248.

Yousefi, H. R., Nakata, Y., Ito, H., & Masugata, K. (2007). Characteristic observation of the ion beams in the plasma focus device. *Plasma and Fusion Research, 2*, S1084-S1084.

Zakaullah, M., Akhtar, I., Waheed, A., Alamgir, K., Shah, A. Z., & Murtaza, G. (1998). Comparative study of ion, x-ray and neutron emission in a low energy plasma focus. *Plasma Sources Science and Technology, 7*(2), 206-218.

Zakaullah, M., Alamgir, K., Shafiq, M., Hassan, S. M., Murtaza, G., & Waheed, A. (2001). Improved temperature measurement in a plasma focus by means of a cobalt filter. *Plasma Sources Science and Technology, 10*(2), 295-301.

Zakaullah, M., Alamgir, K., Shafiq, M., Hassan, S. M., Sharif, M., & Waheed, A. (2001). Enhanced copper K-alpha radiation from a low energy plasma focus. *Applied Physics Letters, 78*(7), 877-879.

Zakaullah, M., Alamgir, K., Shafiq, M., Sharif, M., Waheed, A., & Murtaza, G. (2000). Low energy plasma focus as a tailored x-ray source. *Journal of Fusion Energy, 19*(2), 143-157.

Zakaullah, M., Imtiaz, A., Shafique, M., Murtaza, G., Yasin, M., & Beg, M. M. (1998). Correlation study of ion, electron and x-ray emission from argon focus plasma. *Physica Scripta, 57*(1), 136-141.

Zakaullah, M., Murtaza, G., Qamar, S., Ahmad, I., & Beg, M. M. (1996). Neutron and x-ray emission studies in a low energy plasma focus. *Physica Scripta, 53*(3), 360-363.

Zambreanu, V., & Doloc, C. M. (1992). An electrodynamical model for the ion behaviour in the final plasma focus stages. *Plasma Physics and Controlled Fusion, 34*(8), 1433-1442.

Zhang, T., Gan, T. K. S., Lee, P., Ramanujan, R. V., & Rawat, R. S. (2006). Characteristics of FeCo nano-particles synthesized using plasma focus. *Journal of Physics D: Applied Physics, 39*(10), 2212-2219.

Zhang, T., Lin, J., Patran, A., Wong, D., Hassan, S. M., Mahmood, S., . . . & Rawat, R. S. (2007). Optimization of a plasma focus device as an electron beam source for thin film deposition. *Plasma Sources Science and Technology, 16*(2), 250-256.

Zhang, T., Lin, X., Chandra, K. A., Tan, T. L., Springham, S. V., Patran, A., . . . & Rawat, R. S. (2005). Current sheath curvature correlation with the neon soft x-ray emission from plasma focus device. *Plasma Sources Science and Technology, 14*(2), 368-374.

Zhang, T., Rawat, R. S., Hassan, S. M., Lin, J. J., Mahmood, S., Tan, T. L., . . . & Lee, S. (2006). Drive parameter as a design consideration for Mather and Filippov types of plasma focus. *IEEE Transactions on Plasma Science, 34*(5), 2356-2362.

Zucker, O., Bostick, W., Long, J., Luce, J., & Sahlin, H. (1977). The plasma focus as a large fluence neutron source. *Nuclear Instruments and Methods, 145*(1), 185-190.

LIST OF PUBLICATIONS AND PAPERS PRESENTED

LIST OF PUBLICATIONS

1. **Lim, L. K.**, Yap, S. L., Wong, C. S., & Zakaullah, M. (**2013**). Deuteron Beam Source Based on Mather Type Plasma Focus. Journal of Fusion Energy, **32**(2), p. 287-292.

2. **Lim, L.K.**, Ngoi, S.K., Wong, C.S. & Yap, S.L., Diagnostics of ion beam generated from a Mather type plasma focus device. AIP Conference Proceedings, **2014**. 1588: p. 181-184.

3. Khan, M.Z., Yap, S.L, Ibrar, Y., Nitturi, N.K, **Lim, L.K.** & Wong, C.S., Low-Energy Plasma Focus Device as an Electron Beam Source. The Scientific World Journal, **2014**. p. 9.

4. Khan, M. Z., **Lim, L. K.**, Yap, S. L., & Wong, C. S. (**2015**). Imperative function of electron beams in low-energy plasma focus device. Pramana, 1-13. doi: 10.1007/s12043-015-0951-6.

5. Lim, L.H., S.L. Yap, **Lim, L. K.**, M.C. Lee, H.S. Poh, J. Ma, S.S. Yap, and S. Lee. (**2015**), Comparison of measured and computed radial trajectories of plasma focus devices UMDPF1 and UMDPF0. Physics of Plasmas, **22**(9): p. 092702.

6. **Lim, L.K.**, Yap, S. L., Lim, L. H., Neoh, Y. S., Khan, M. Z., Ngoi, S. K., Yap, S. S., and Lee, S. (**2015**), Parametric Optimisation of Plasma Focus Devices for Neutron Production, *Journal of Fusion Energy*, **35**(2): p. 274-280.

PAPERS PRESENTED AT NATIONAL AND INTERNATIONAL CONFERENCE

1. **Lim, L.K.**, Yap, S.L., & Wong, C.S., Enhancement of Ion Beam Emission from a Low Energy Plasma Focus Device, 8^{th} Mathematics and Physical Sciences Graduate Congress, Chulalongkorn University (Thailand), 8 – 10 December **2012**

2. **Lim, L.K.** & Yap, S.L., Ion beam and X-ray Production Based on Mather Type Plasma Focus Device, Joint ICTP-IAEA College on Plasma Physics, Trieste (Italy), 1 – 12 October **2012**

3. **Lim, L. K.**, Yap, S. L., and Wong, C. S., Diagnostic of Ion Beam Emission from a Mather Type Plasma Focus Device, Fourth International Meeting on Frontiers of Physics (IMFP2013), Genting Awana, Malaysia, Aug **2013**.

4. **Lim, L.K.** & Yap, S.L., Plasma Focus Based Ion Beam, Sixth HOPE Meeting with Nobel Laureates, Tokyo (Japan), 11 – 15 March **2014**

5. **Lim, L. K.** & Yap, S. L., Pulsed Ion Beam Production from a Mather Type Plasma Focus, Sokendai Asian Winter School, National Institute for Fusion Science, Toki (Japan), 1 - 4 December **2015**

6. **Lim, L. K.**, Yap, S. L., Khan, M. Z. and Yap, S. S., Ion Jet Produced By Anomalous Resistance In Plasma Focus Discharge, 43rd IEEE International Conference on Plasma Science, Banff, Alberta (Canada), 19 - 23 June **2016**